Development and characterization of algorithms for estimation of blood velocity with ultrasound

Schlaikjer, Malene

Publication date:
2001

Document Version
Publisher's PDF, also known as Version of record

Development and characterization of algorithms for estimation of blood velocity with ultrasound

Malene Schlaikjer

Ph.D. dissertation
February, 2001

Ørsted•DTU
Bldg. 348, Technical University of Denmark
DK-2800 Kgs. Lyngby, Denmark.

Preface

This dissertation is submitted in partial fulfillment of the requirements for obtaining the Ph.D. degree at the Technical University of Denmark, Denmark.

The research has been carried out mainly at the Department of Information Technology, Section of Electronics and Signal Processing, at the Technical University of Denmark. This group is now with the institute Ørsted•DTU at the Technical University of Denmark. A 5 months stay at University of Virginia, Virginia, USA with Professor Katherine W. Ferrara was included in this Ph.D. project. The research has been carried out over the period from January 1st, 1998 until February 14th, 2001. Within this period I was on leave for 6 weeks. Professor, Dr. Techn. Jørgen Arendt Jensen was my advisor.

Acknowledgments

I would like to express my thanks to every one, who have helped and supported me over the last three years. That covers quite a number of people.

A special thanks goes to my fiance Peter Holst Nielsen. You always support me, when I set my mind on living out another dream. You are always there for me and never complain, when I ”disappear” into my world of research. I owe you a lot, and I hope I will get a chance to pay you back sometime.

Thank you to all my colleagues in the Center for Fast Ultrasound Imaging and in the department for taking the time for scientific discussions, helping out with computer issues and daily matters, and proofreading of parts of my dissertation. A thank you goes to my advisor Jørgen Arendt Jensen for making it possible for me to carry out this research, as he has assured that the right environment (with respect to laboratory facilities and the Center for Fast Ultrasound Imaging) was present.

Professor Katherine W. Ferrara and her research group at the University of Virginia are thanked for accepting and including me in their research group and letting me use their laboratory facilities. I thank Dustin Kruse, Paul Dayton, James Chomas, John Allen, and Karen Morgan for helping me getting settled and helping out on daily matters during my stay.

My former officemate Ph.D. Peter Munk should be thanked for passing on some of his great expertise within ultrasound theory and ultrasound scanners.

I would like to thank my Ph.D. colleague MD Morten Høgholm Pedersen for taking the time and being patient, when I needed his expertise for generating images and acquiring *in-vivo* data for this dissertation.

I thank my engineer colleague Maja Skytte Jensen for taking the time to proofread part of my dissertation.

I also thank her for being a good friend.

Svetoslav Nikolov, Ph.D. student, has been of great help with respect to proofreading part of my dissertation. I thank him and promise to be there for him as well, when time comes.

I thank associate professor, Ph.D. Rasmus Larsen from the Department of Informatics and Mathematical Modelling at the Technical University of Denmark for introducing me to and discussing the theory on optical flow, which I used to develop a new filter for post-processing of the velocity estimates. I also thank him for taking the time to proofread the chapter on post-processing filters.

A number of people at B-K Medical A/S, Gentofte, Denmark, have been of great help by providing information about how scanners and transducers work in real live. I hereby thank Gert Seerup and Per Nygaard for taking the time and always being willing to help.

Again - thank you all.

Kongens Lyngby, February 2001

Malene Schlaikjer

Abstract

This Ph.D. project has been concerned with the development of new algorithms, which are to be used in the processing of medical ultrasound RF-signals. The aim of the processing is to obtain estimates of the blood velocities in the human cardiovascular system. Algorithms, which are related to 1) the pre-processing of the RF-signals prior to the estimation, 2) the actual estimation of the blood velocities, and 3) the post-processing of the estimates prior to display, have been developed.

Two pre-processing algorithms, which perform a classification of the signal segments in the RF-signals, have been developed. The aim of the classification is to determine those segments, which carry blood velocity information. This knowledge can be used to control the subsequent estimation, as only signal segments, which do carry blood velocity information, should be processed by the blood velocity estimator. If the estimation is performed on all segments, the outcome of the classification is used to determine, which of the computed estimates that should be displayed. A set of features have been determined, which distinguish segments, which do and do not carry blood velocity information. The features are I) the energy content in the segments before and after echo-canceling, and II) the amplitude variations between samples in consecutive RF-signals (acquired along the same line in the image) before and after echo-canceling. This gives a total of 4 features. The first discriminator employs maximum likelihood theory. The probability densities of the features, when they represent segments that do and do not carry blood velocity information, have been determined. Two joint probability densities are generated and based on the values hereof, it can be determined, how likely it is that the segment under investigation do or do not carry blood velocity information. The statistical discriminator has a success rate on correct classification of over 96 %, when the signal to noise ratio is above 0 dB. The second discriminator uses a neural network to perform the classification. The neural network determines a non-linear relation between the feature values. A SoftMax expansion of the network results in an output, which determines the likelihood of a segment carrying blood velocity information. The neural classifier has a success rate above 97 %. The two discriminators have been compared to a simple discriminator, which only uses the amplitude level in the segments. The classification is performed by comparing the amplitude level to a threshold value. The new discriminators out perform the simple discriminator significantly, as they have a success rate of 91-99 % on the segments, which do carry blood velocity information. The simple discriminator can only classify 42 % of these segments correct. The performance on the segments, which do not carry blood velocity information, is similar for all three discriminators, and the success rate is above 96 %. The incorporation of more features and the employment of more advanced algorithms have improved the basis for the discrimination. The discriminators are applicable on RF-signals acquired from the larger vessels in the human cardiovascular system.

Present blood velocity estimators do not employ the features of fluid mechanics, which predicts that the velocities in a temporally and spatially bounded neighborhood are correlated. A maximum likelihood estimator, which incorporates this feature, has been developed and evaluated. An a priori density function has been included in the distribution for a measure of the cross-correlation between segments in the RF-signals. The a priori density sets up restrictions for the allowed variations between the blood velocities in the bounded neighborhood. The functionality of the a priori density is to determine, if the velocity value under investigation is likely, when the velocities in a bounded spatial and temporal neighborhood are known.

The estimator has been named the CMLE estimator. Its performance has been evaluated on simulated data, which represent RF-signals from the carotid artery. The introduction of the correlation property has shown to be beneficial for the estimation process. A selection of previously developed estimators have been evaluated as part of this project. Most of them produce quite a few estimates, which deviate significantly from the true velocities. The number of deviating estimates range from 4-42 %. With the CMLE estimator no highly deviating estimates are produced. The CMLE estimator produces estimates, which follow the overall variations throughout the cardiac cycle well. The employment of the correlation property has improved the basis for the estimation.

A second blood velocity estimator has been developed. It combines the autocorrelation and the BST estimators in order to overcome the aliasing problem of the former estimator. An initial velocity estimate is determined with the autocorrelation estimator, and then a set of possible true phase shifts are evaluated with the BST estimator. The estimator has been named the AB estimator. The introduction of the subsequent analysis with the BST estimator both has a positive and negative effect on the estimation. The aliasing problem can be circumvented, but some estimates are generated, which deviate significantly from the true velocity. A total of 4 % of the estimations result in these deviating estimates for the employed data set. This number can be decreased by employing a post-processing filter. The combination of the two estimators have been beneficial. The obtained velocity estimates follow the variations across and throughout the vessel and throughout the cardiac cycle well. Investigations have shown that the AB estimator is able to out perform a large selection of the previously developed blood velocity estimators. Therefore the AB estimator should be considered used for blood velocity estimation.

A new post-processing filter based on optical flow theory, which incorporates the properties of fluid mechanics, has been developed. The post-processing is required, as the blood velocity estimates come with a level of inaccuracy. This results in a noisy and non-smooth appearance of the estimated velocity profiles, which is not consistent with the true profiles. The post-processing of the estimates should minimize this variation before the estimates are displayed. The correlation between the velocities in time and space makes it possible to set up restrictions for the allowed variations between the velocity levels in time and space. A posterior probability density has been determined, which incorporates the restrictions in an a priori density function, and the information given by the computed estimates in an observation specific density function. The relation for the filter is determined through maximization of the posterior density. A filter arises, which computes a new velocity estimate as a linear combination of the original velocity estimate and the velocities in a spatial and temporal bounded neighborhood of the original estimate. The filter coefficients weight the contributions from the different velocity estimates and allow for a difference in the spatial and temporal correlation. The values of the filter coefficients are dependent on the temporal and spatial resolution in the CFM images along with the temporal position in the cardiac cycle. The performance of the new post-processing filter has been evaluated on simulated and *in-vivo* data acquired from the carotid artery. The evaluation on the simulated data reveals that an improvement of 15-53 % on the RMS error can be obtained. The highest improvement was obtained at low SNRs. The resulting velocity profiles are more consistent with the true velocity profiles. The performance of the filter has been compared to the performance of median filters, which employ the original estimate and the spatial neighbors in the velocity image to compute the new velocity estimate. The improvement on the RMS error is a factor of 2-4 lower, when the median filters are employed. The velocity profiles obtained with the median filters are less smooth, and steep transitions are seen, which are not consistent with the true profiles. The incorporation of the correlation between the blood velocities in a temporal and spatial bounded neighborhood has shown to be beneficial for the post-processing of the velocity estimates.

Models for the tissue motion induced by breathing, the beating of the heart, and the pulsation of the vessel wall have been developed based on investigations of *in-vivo* data. These models are required to be able to create realistic simulated data, which contain as many properties of the *in-vivo* situation as possible. Thereby a proper basis for the evaluation of new algorithms is given. The investigations of the *in-vivo* data revealed that tissue motion is present, when scannings are performed at the carotid artery and in the

abdominal region. The motion level is on the order of a few millimeter per second. The analysis of the data revealed that the tissue motion is a function of time and space. The time dependence is determined by the motion pattern of the motion inducer. The spatial dependence is due to the damping of the tissue motion, as the distance from the motion inducer to the tissue region being scanned increases. In the models developed here, the dependence on time and space has been split up in two separate terms. A linear relation for the damping of tissue motion induced by breathing and the beating of the heart has been used. The temporal evolution of the motion is modeled with a sine function for these two motion inducers. A cosine function was used for the modeling of the damping of the tissue motion at the carotid artery, and an exponential weighted sine function was used for the temporal function. The parameters in the models are dependent on the scan site, the subject, and the physical state of the subject. The models were verified through simulations. The results hereof were compared with the *in-vivo* data, and a qualitatively agreement was seen. Tissue motion exists and can be modeled, and therefore this motion should be incorporated in the generation of realistic simulated RF-data.

Resumé (Abstract in danish)

Dette ph.d. projekt har omhandlet udvikling af nye algoritmer, der skal bruges i signalbehandlingen af medicinske ultralyds RF-signaler. Målet med signalbehandlingen er at opnå estimater af blodhastighederne i det menneskelige hjerte- og karsystem. Algoritmer, der er relateret til 1) forbehandlingen af RF-signalerne inden beregningen af estimaterne, 2) den egentlige beregning af blodhastighederne, og 3) efterbehandlingen af estimaterne inden visning, er blevet udviklet.

To forbehandlingsalgoritmer, som udfører en klassifikation af signalsegmenterne i RF-signalerne, er blevet udviklet. Målet med klassifikationen er at fastlægge de signalsegmenter, som indeholder information om blodets hastigheder. Denne viden kan bruges til at kontrollere den efterfølgende beregning af blodhastighederne, idet kun de segmenter, som indeholder denne information, skal behandles af blodhastighedsestimatoren. Hvis hastighedsestimationen udføres på alle signalsegmenterne, kan udfaldet af klassifikationen bruges til at fastlægge, hvilke hastighedsestimater der skal vises. Et sæt af karakteristiske egenskaber er blevet fastlagt, som adskiller segmenterne, der indeholder og ikke indeholder information om blodhastighederne. Egenskaberne er I) energien i segmenterne før og efter ekko-filtrering, og II) amplitudevariationerne mellem signalværdierne i efterfølgende RF-signaler (opsamlet langs den samme linie i billedet) før og efter ekko-filtrering. Dette giver sammenlagt 4 karakteristiske egenskaber. Den første diskriminator anvender maximum likelihood teori. Sandsynlighedstæthederne for de 4 egenskaber, når de henholdsvis repræsenterer segmenter med eller uden information om blodets hastigheder, er blevet fastlagt. De samlede sandsynligheder udregnes og på baggrund af disse værdier, kan det fastlægges, om det er sandsynligt, at det undersøgte signalsegment indeholder information om blodets hastigheder. Den statistiske diskriminator har en succes procent på korrekt klassifikation på 96 %, når signal-støj forholdet er over 0 dB. Den anden diskriminator anvender et neuralt netværk til at udføre klassifikationen. Det neurale netværk fastlægger en ikke-lineær relation mellem værdierne for de 4 egenskaber. En SoftMax udvidelse af netværket resulterer i et output, der fastlægger sandsynligheden for, om et segment indeholder information om blodets hastigheder. Det neurale netværk har en succes procent på over 97 %. De to diskriminatorer er blevet sammenlignet med en simpel diskriminator, der kun anvender amplitudeniveauet i segmenterne. Klassifikationen udføres ved at sammenligne amplitudeniveauet med en tærskelværdi. De nye diskriminatorer udkonkurrerer den simple diskriminator signifikant, idet de har en succes procent på 91-99 % på segmenterne, der indeholder information om blodets hastigheder. Den simple diskriminator kan kun klassificere 42 % af disse segmenter korrekt. Klassifikationsevnen på de segmenter, der ikke indeholder information om blodets hastigheder, er meget ens for alle tre diskriminatorer. Over 96 % af segmenterne klassificeres korrekt. Inkorporeringen af flere karakteristiske egenskaber samt anvendelsen af mere avancerede algoritmer har forbedret grundlaget for diskriminationen. Diskriminatorerne kan anvendes på RF-signaler opsamlet fra de større blodkar i hjerte- og karsystemet.

De nuværende blodhastighedsestimatorer anvender ikke egenskaber fra fluid mekanik, som udsiger at hastighederne i et tidsligt og rumligt afgrænset område er korrelerede. En maximum likelihood estimator, der inkorporerer denne egenskab, er blevet udviklet og evalueret. En a priori tæthedsfunktion er blevet inkluderet i fordelingen for et mål af krydskorrelationen mellem segmenter i RF-signalerne. Den a priori tæthed opstiller restriktioner på de tilladte variationer mellem blodhastighederne i et afgrænset område.

Funktionen af den a priori fordeling er at fastlægge, om den undersøgte hastighed er sandsynlig, når hastighederne i et tidsligt og rumligt afgrænset område er kendt. Estimatoren er blevet navngivet CMLE estimatoren. Dens estimationsevne er blevet evalueret på simulerede data, som repræsenterer RF-signaler omsamlet fra carotis. Introduktionen af korrelationsegenskaben har vist sig at være gavnlig for beregningen af blodhastighedsestimaterne. Et udvalg af de tidligere udviklede estimatorer er blevet evalueret som en del af dette projekt. De fleste producerer en hel del hastighedsestimater, der afviger signifikant fra de sande blodhastigheder. Antallet af afvigende estimater spænder fra 4-42 %. Med CMLE estimatoren bliver der ikke produceret nogle afvigende estimater. CMLE estimatoren fastlægger hastighedsestimater, der følger de overordnede variationer henover hjertecyklusen godt. Anvendelsen af korrelationsegenskaben har forbedret grundlaget for estimationen af blodets hastigheder.

Endnu en blodhastighedsestimator er blevet udviklet. Den kombinerer autokorrelations og BST estimatorerne med henblik på at overvinde aliaserings problemet for autokorrelations estimatoren. Et initielt hastighedsestimat fastlægges med autokorrelations estimatoren, og et sæt af mulige sande fase skift evalueres med BST estimatoren. Den nye estimator er blevet navngivet AB estimatoren. Introduktionen af den efterfølgende variansanalyse med BST estimatoren har både en positiv og negativ effekt på udregningen af estimaterne. Aliaserings problemet kan omgås, men et antal estimater beregnes, som afviger signifikant fra den sande hastighed. Fire procent af det samlede antal estimater for det anvendte data sæt afviger signifikant. Dette antal kan nedbringes ved efterbehandling af estimaterne. De beregnede estimater følger hastighedsvariationerne i karret og henover hjertecyklusen godt. Undersøgelser har vist, at AB estimatoren kan udkonkurrere et stort udvalg af de tidligere udviklede blodhastighedsestimatorer. Derfor bør det kraftigt overvejes at anvende AB estimatoren til beregning af blodhastighederne.

Et nyt efterbehandlingsfilter baseret på optisk flow teori, som inkorporerer egenskaber fra fluid mekanik, er blevet udviklet. Efterbehandling er nødvendig, idet estimaterne er behæftet med usikkerhed. Dette resulterer i en støjfyldt og ujævn fremtoning af de estimerede hastighedsprofiler, som ikke er i overensstemmelse med de sande profiler. Efterbehandlingen af estimaterne skal minimere denne variation, inden estimaterne vises. Korrelationen mellem blodets hastigheder i tid og rum gør det muligt at opstille restriktioner for de tilladte variationer mellem hastighedsniveauerne i tid og rum. En a posteori tæthedsfunktion er blevet fastlagt, som inkorporerer restriktionerne i en a priori tæthedsfunktion, og informationen fra de givne estimater i en observations specifik tæthedsfunktion. Udtrykket for det resulterende filter fastlægges ved maksimering af den posteori tæthedsfunktion. Et filter opstår, som udregner et nyt hastighedsestimat som en lineær kombination af det originale estimat og hastighedsestimaterne i et tidsligt og rumligt afgrænset område i forhold til det originale estimat. Filterkoefficienterne vægter bidragene fra de forskellige hastighedsestimater og tillader, at den tidslige og rumlige korrelation er forskellig. Værdierne af filterkoefficienterne afhænger af den tidslige og rumlige opløsning i CFM billederne samt den tidslige position i hjertecyklusen. Filtreringsevnen for det nye efterbehandlingsfilter er blevet evalueret på simulerede og *in-vivo* data opsamlet fra carotis. Evalueringen på de simulerede data viser, at en forbedring af RMS-fejlen på 15-53 % kan opnås. Den største forbedring opnås for lave værdier af signal-støj forholdet. De resulterende hastighedsprofiler stemmer mere overens med de sande profiler. Filtreringsevnen af det udviklede filter er blevet sammenlignet med filtreringsevnen af median filtre, som anvender det originale estimat samt de rumlige naboer i hastighedsbillederne til at udregne det nye hastighedsestimat. Forbedringen på RMS-fejlen er en faktor 2-4 lavere, når median filtrene udfører efterbehandlingen af hastighedsestimaterne. Hastighedsprofilerne, der opnås efter filtrering med median filtrene, er mindre jævne og bratte overgange eksisterer, som ikke er i overensstemmelse med de sande profiler. Inkorporeringen af korrelationen mellem blodhastighederne i et tidsligt og rumligt afgrænset område har vist sig at være gavnlig for efterbehandlingen af hastighedsestimaterne.

Modeller for vævsbevægelse frembragt af vejrtrækning, hjertets slag og pulsationen af karvæggene er blevet udviklet baseret på undersøgelser af *in-vivo* data. Disse modeller er nødvendige for at skabe realistiske simulerede data, som indeholder så mange egenskaber fra den *in-vivo* situation som muligt. Dermed skabes en forsvarlig basis for evalueringen af nye algoritmer. Undersøgelserne af de *in-vivo* data afslørede, at vævsbevægelse er tilstede, når skanninger foretages ved carotis og i underlivsregionen. Bevægelses-

niveauet ligger i størrelsesordenen et par millimeter per sekund. Analysen af data viste, at vævsbevægelsen er en funktion af tid og rum. Tidsafhængigheden er fastlagt af bevægelsesmønstret for organet, der genererer bevægelsen. Den rumlige afhængighed skyldes dæmpning af vævsbevægelsen, når afstanden mellem organet og vævet, der skannes, øges. I modellerne udviklet i dette projekt blev den tidslige og rumlige afhængighed opsplittet i to led. En lineær relation for dæmpningen af vævsbevægelsen frembragt af vejrtrækningen og hjerteslaget er blevet anvendt. Det tidslige forløb af bevægelsen er modelleret ved en sinus funktion. En cosinus funktion blev anvendt til modellering af dæmpningen ved carotis, og en eksponentiel vægtet sinus funktion blev brugt til at beskrive den tidslige funktion. Parametrene i modellerne afhænger af den vævsregion, der bliver skannet, patienten, samt den fysiske tilstand for patienten. Modellerne blev verificeret ved simulationer. Resultaterne fra simuleringerne blev sammenlignet med de *in-vivo* data, og en kvalitativ overensstemmelse blev fastlagt. Vævsbevægelse er tilstede og kan modelleres, og derfor skal denne bevægelse inkorporeres i genereringen af realistiske simulerede RF-data.

Table of Contents

List of Figures

List of Tables

Nomenclature

c	:	Sound velocity.
d	:	Dilation.
f_{prf}	:	Pulse repetition frequency.
f_0	:	Center frequency of emitted pulse.
r	:	Acquired RF-signal.
r_b	:	Acquired RF-signal for B-mode imaging.
r_{cfm}	:	Acquired RF-signal for blood velocity estimation.
$r_{c,cfm}$	:	Complex representation of acquired RF-signal for blood velocity estimation.
r_{echo}	:	RF-signal after echo-canceling.
r_{env}	:	Envelope detected RF-signal.
SNR	:	Signal to Noise Ratio.
t	:	Time.
T_{prf}	:	Time between pulse emissions.
TGC	:	Time Gain Compensation.
v	:	Velocity.
v_z	:	Velocity along propagation direction.

Chapter 1

Introduction

Techniques for imaging of the internal organs in the human body have developed a great deal in the 20th century. Employment of X-rays gave the first pictures. Unfortunately X-rays have the disadvantage of exposing the patient to ionizing radiation. The 3D volume examined is projected onto a 2D plane. Each pixel in the image is the sum of contributions from the tissue structures, which are located along the propagation path from the source to the X-ray film. This feature limits the information extractable from the images. Magnetic Resonans Imaging (MRI) evolved in the 1970's. Volume images became available, but the electronic capabilities at that time limited its usability. Hours were spent on acquiring and processing responses from a small volume, which made the imaging process very cumbersome. The time issue has been addressed today with the advances within electronics. The MRI scanners still have some disadvantages, as they are very expensive and non-mobile. The research into employment of ultrasound for imaging started around the same time as for MRI. Medical ultrasound deals with the mentioned disadvantages of X-ray and MRI. A movable scanner on wheels is standard, which makes it possible to move the same scanner between examination rooms and theaters depending on the need. Two dimensional images are constructed from reflected acoustic waves, which have been emitted into the body. Three dimensional information is obtained by moving the transducer around in space and thereby scan different planes. No health risk has been reported, so the health issue of performing scannings is considered non-existing. Several examinations can be performed without considering the trade off between the information obtainable by doing another scan and the health risk. The initial costs are a factor of 40 lower compared to an MRI scanner (according to price levels in Denmark [1],[2]).

Medical ultrasound is employed intensively in modern hospitals for diagnosing diseases in all soft tissue structures in the body. Grey-level B-mode images are used for anatomical studies, and velocity images are employed for diagnosing diseases in the cardiovascular system. Fast image formation can be performed, which makes it possible to both follow flow dynamics in real-time and give an immediate diagnosis. This is of great importance for diagnosing cardiovascular diseases. The flow conditions tell something about the pathological conditions:

- If the vessel lumen is constricted (due to *e.g.* plaque), the blood will flow at higher velocities as it passes the constriction.
- The flow to and in the kidneys determines the functionality of the kidneys.
- The flow in the heart and the coronary arteries determines the functionality of the heart.
- Cancerous tissue requires an increased supply of oxygen. Therefore increased blood flow in the tissue (*e.g.* breast tissue) might be an indicator for cancer.

The advantages and capabilities of medical ultrasound has made it one of the fastest growing and mostly used scanning modalities today.

This project aims at improving the estimation of the blood velocities in the human cardiovascular system. The estimation is performed on acquired ultrasound RF-signals. Proper processing schemes must be employed to extract the valuable information in the RF-signals and compute the velocity estimates. The research carried out in this project aims at improving some of the processing schemes. This involves the pre-processing prior to blood velocity estimation, the actual estimation of the blood velocities, and the post-processing prior to displaying the computed estimates. In the following the different parts of the project will be described in more detail.

The development of new algorithms includes an evaluation phase, where the performance of the algorithms is determined. This requires access to well-defined data, where the true outcome of the processing is known a priori. In medical ultrasound this includes knowing the exact location of the tissue structures and the blood vessel(s), along with the true values of the blood velocities. Simulated data are often used, but it requires that as many features of the *in-vivo* situation are incorporated as possible. Especially the features that will influence the performance of the algorithms should be incorporated, so the evaluation is performed on a realistic basis. One feature of importance in blood velocity estimation is the motion in the tissue surrounding the vessel. The movement induced by breathing, the beating of the heart, and the pulsation of the vessel walls degrades the ability to detect slow moving blood. Determination and modeling of these motions will enable us to create more realistic simulated data, so a proper evaluation of algorithms can be performed. Investigations into these motions and modeling hereof are carried out in this project.

The acquired RF-signals are pre-processed prior to performing the velocity estimation. The pre-processing includes de-noising of the signals along with processing, which improves the basis for the estimation and the subsequent display of the blood velocity estimates. Only the blood velocity estimates are of interest in blood velocity estimation, but non-zero estimates are obtained for both the blood and the tissue regions in the image. A discrimination must be performed that determines, which parts of the RF-signals that carry blood velocity information. The output of the discrimination can be used to control the subsequent processing, as the blood velocity estimation only should be carried out on segments, which carry blood velocity information. The discriminator must use features extractable from the RF-signals. The ability to determine features will be investigated, and a set of discriminators will be developed in this project.

A number of blood velocity estimators have been proposed in the past. An investigation and evaluation of some of these are carried out to determine their capabilities and shortcomings. This gives a basis for developing new estimators. In present velocity estimators the fact that spatial and temporal correlation exist between the blood velocities is not incorporated into the estimators. The mechanics of fluid flow predicts that the velocity profile in a vessel can be described as a continuous function in time and space. This sets up limitations to the possible variations in the velocity levels between the velocities in a spatially and temporally bounded neighborhood. A situation with a sudden change from high positive to high negative velocity within a short time indicates an error in the calculations of the velocity. The incorporation of flow characteristics into the estimators makes it possible to improve the estimates. The estimator processes data from a spatially and temporally bounded neighborhood in the present and previous images. A new estimator based on maximum likelihood theory, which incorporates the temporal and spatial correlation, will be developed and evaluated.

The computed blood velocity estimates come with a level of inaccuracy, so the estimates in the images vary about the true velocities. A noisy and non-smooth appearance of the velocity distribution is obtained, which is not consistent with the actual velocities in the vessel. The variations will disturb the eye, when a sequence of images are shown right after each other at a high frame rate. Post-processing should be applied to minimize the variation prior to displaying the estimates. The correlation between the velocities in time and space can also be used in the post-processing. A post-processing filter will be derived and evaluated in

this study, which incorporates the correlation property.

Organization of dissertation

The organization of the dissertation is listed in the following:

Chapter 1 : This chapter contains a short introduction to this dissertation and a project description.

Chapter 2 : The basic theory of acoustics and the employment of transducers are introduced.

Chapter 3 : The cardiovascular system and properties hereof are introduced. A relation between the internal pressure in the carotid artery and the induced tissue motion from pulsation is derived. Womersley's model for the blood flow in the carotid and femoral artery is introduced. The common imaging modes are described. The information is employed in the subsequent chapters.

Chapter 4 : This chapter is concerned with the generation of realistic simulated data, which incorporate the tissue motion. The presence of tissue motion is investigated through inspection of *in-vivo* data. The possibility of generating simulated RF-data, which include the tissue motion, is investigated. Models are derived for motion related to the pulsation, breathing, and the beating of the heart. Simulations are performed to verify the models.

Chapter 5 : The pre-processing of the acquired RF-signals is the topic of this chapter. A filter for denoising is introduced. The pre-processing also includes elimination of the tissue components, and two echo-canceling filters will be introduced. The discrimination process is investigated, and three discriminators are discussed and evaluated. The last two discriminators represent new approaches. A set of features, which determine when a segment of the RF-signal carry blood velocity information, are derived. The new discriminators are based on maximum likelihood theory and neural networks, respectively.

Chapter 6 : After the pre-processing the actual estimation can be carried out. This chapter introduces and evaluates a selection of blood velocity estimators. The capabilities and shortcomings of each are determined. Two new estimators are derived and evaluated. The first estimator combines two existing estimators. The second estimator makes use of maximum likelihood theory and incorporates the correlation property between the velocities.

Chapter 7 : This chapter introduces and evaluates the performance of two post-processing filters. The last filter represents a new approach, which incorporates the temporal and spatial correlation between the velocities in the blood vessels. The filter is based on Bayesian image analysis.

Chapter 8 : The work and the results obtained in this project are summarized in this chapter.

A number of papers, which contain some of the results obtained within this Ph.D. project, have been presented and published. Copies of the papers are enclosed in Appendix A of this dissertation.

Chapter 2

Basic acoustics

The generation of medical ultrasound images is based on transmission of an acoustic wave into the human body, which is followed by a measurement of the reflected and scattered wave due to the interactions with the tissues. An example of an ultrasound image of the fetus is given in Fig. 2.1. The image contains spatial information in 2 dimensions, so individual structures can be distinguished. The skull, the spinal cord, and the heart can be recognized fairly easy. The spatial resolution is obtained by emitting a wave that has a finite extent in time and space. Ultrasound waves with frequencies in the range 1-10 MHz are used in diagnostic clinical ultrasound to image the human anatomy [3]. The wavelengths, λ, span the range from 150 μm to 1540 μm, which makes it possible to visualize organs, but not the micro structures - the cells, fibers *etc*.

This chapter introduces the basic theory of wave propagation and the interaction with media, the concepts and limitations of using transducers of finite size, and the aspect of beamformation. A more comprehensive discussion of these topics is obtainable from a number of books on acoustics [4], [5], arrays [6], and medical ultrasound [3].

2.1 Generation of waves

The first aspect to understand is the generation of waves. When observing a medium in its ambient state, no waves are propagating. Applying a force causes a pressure change, so the medium is perturbed. The pressure acts on the medium and results in a displacement of the particles next to the point of interaction. The displaced particles subsequently act on their neighboring particles and displace them. This interaction between neighbors continues, and like the Domino-effect the pressure and displacement travel through the medium. A propagating wave has been generated. An example of wave propagation that one can relate to is speech. The vocal cords apply a pressure to the air particles in the trachea. Due to the Domino-effect the generated displacement travels up and out of the mouth and propagates into space. The proof of the propagation is that other people can hear you talking! In medical ultrasound the wave propagates in body fluids and soft tissues. In these media longitudinal waves can exist, and the theory is derived for these waves. The particle displacement is parallel to the direction of the wave propagation in this case.

2.2 Wave propagation

Upon generation of the wave it will propagate through the medium. The propagation is a function of both time and space. In the following the characteristics of the propagation will be described briefly. The propa-

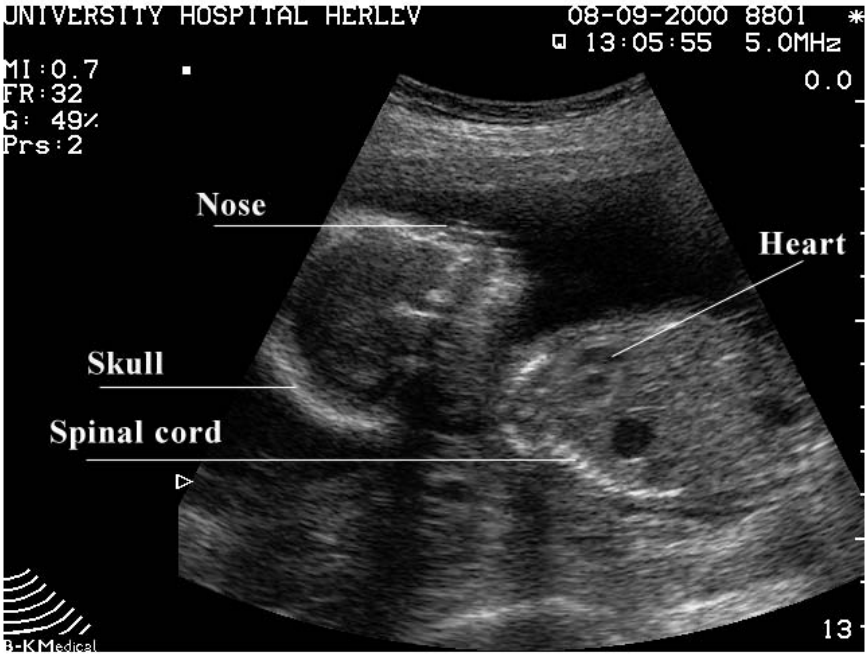

Figure 2.1: Gray tone (B-mode) image of a 17 week old fetus.

gation has both linear and non-linear properties.

Many factors influence the propagation. The interaction between the wave and the medium is one factor, and the composition of the medium is another on a long list of factors. A comprehensive mathematical description of the propagation becomes very complicated, and will not be derived in this context (see [4], [5]). In this section the nature of linear and non-linear propagation is discussed. In the following sections some of the factors that influence and alter the wave, as it propagates and interacts with the medium, will be discussed.

2.2.1 Linear wave equation

A mathematical relation that describes the linear property of the propagation can be derived. In the derivation it is assumed that the medium is a homogeneous, lossless, and elastic fluid. The applied pressure disturbance is assumed small relative to the equilibrium pressure, so only small density variations and displacements occur. The last assumption does not apply to medical ultrasound. High pressures are applied (1-10 MPa) that causes additional non-linear propagation (see Section 2.2.2). The derivation of an equation, which describes the linear propagation, is based on three well known relations from mechanics:

1. *Equation of state :* When a pressure p is applied, particles are displaced an amount$\vec{\varepsilon}$ in space. This causes a change in the density (ρ). The linear relation between pressure and density variation is [4]:

$$p = B\frac{\rho - \rho_0}{\rho_0} = Bs, \tag{2.1}$$

where B is the adiabatic bulk modulus [4]. The variation in density relative to the equilibrium density ρ_0 is termed condensation, s. The equation holds, when the condensation is small, $|s| << 1$. The relation is referred to as the "Equation of state".

2. *Conservation of mass:* The derivation of a relation between the pressure and the particle displacement is based on the property of conservation of mass [4]. Based on this property another linear relation is

Tissue					
Water	Air	Blood	Fat	Kidney	Muscle
1480	333	1566	1446	1567	1542-1626

Table 2.1: Sound velocities ([m/s]) for various body tissues.

obtained:

$$p = -B\nabla \cdot \vec{\varepsilon}, \tag{2.2}$$

where ∇ is the three-dimensional Laplacian operator.

3. *Force relation (Euler's equation):* As the force is applied, the particles, which span a volume with a certain mass, will accelerate according to Newton's second law. A relation between the particle velocity $\vec{u}$ and the applied pressure can be derived [4]:

$$\rho_0 \frac{\partial \vec{u}}{\partial t} = -\nabla p, \tag{2.3}$$

where t represents time. By proper combination of the above three equations the wave equation is obtained. It describes the course of the wave propagation in a homogeneous medium as a function of time and space. The relation is:

$$\nabla^2 p = \frac{1}{c^2}\frac{\partial^2 p}{\partial t^2}, \tag{2.4}$$

where c is the propagation velocity for the longitudinal wave - usually termed the sound velocity. The sound velocity is material dependent. In Table 2.1 the sound velocity is listed for different tissues and fluids of interest in medical ultrasound [3]. Due to the linear relation between pressure, condensation, and density, the wave equation can also be expressed as a function of the latter variables [4].

A set of solutions to the wave equation are the harmonic waves. The plane wave is one solution, and the mathematical description is:

$$p(t,\vec{r}) = A\exp(j(\omega t - \vec{k}\cdot\vec{r})), \tag{2.5}$$

where $\vec{r}$ is a vector representing the spatial coordinates (x,y,z), A is the amplitude, and ω is the oscillation frequency. $\vec{k}$ is the wavenumber, and the orientation of the vector determines the direction of propagation of the plane wave. Its magnitude is related to the sound velocity and the oscillation frequency through $|\vec{k}| = \frac{\omega}{c}$. The phase front of the plane wave is characterized by being constant perpendicular to the propagation direction.

Another solution of importance in medical ultrasound is the spherical wave:

$$p(t,r) = \frac{A}{r}\exp(j(\omega t - kr)). \tag{2.6}$$

The wave propagates symmetrical in all directions, and constant phase fronts occur as spheres at points in space with equal radial distances to the source. Due to the nature of the wave it is usually described in polar coordinates with r being the radial distance from the source to a point in space. The requirement of conservation of energy results in the amplitude drop off with increased distance. Spherical waves therefore have a finite propagation range. Far away from the source (in the far-field) the curvature of the spherical wave decreases and can be considered as a plane wave over a limited distance.

When only the linear propagation is considered, any wave can be described by a linear combination of plane waves [7]. If more than one wave are propagating in the medium, the total pressure in any point in space is the sum of the contributions from the individual waves. This property is usually named the superposition principle.

Up until now the source and the boundary conditions have not been defined and included. To solve the equation for a particular situation these conditions must be incorporated [4].

2.2.2 Non-linear effects

In medical ultrasound the applied pressures can reach 1-10 MPa, which results in non-linear wave propagation. Through investigation of the relations between the sound velocity, the applied pressures, the density variations, and the particle velocities one will learn the following [3]:

- positive particle velocity results in an increase in the effective sound velocity,
- negative particle velocity results in a decrease in the effective sound velocity.

The particle velocity is related to the pressure, which causes the wave to propagate faster during a positive period of pressure, and slower during a negative period. The waveform thereby gets distorted. The distortion results in generation of higher harmonics. In the last few years imaging based on higher harmonics has been developed and is now widely used [8], [9]. The image quality is improved, since an increase in contrast and resolution is obtained.

A comprehensive description of wave propagation therefore contains both the linear and non-linear effects.

2.3 Interaction with the medium

In the above it is assumed that the wave was propagating in a homogeneous and lossless medium. No real media are completely homogeneous and lossless, so the wave will interact with the medium and be altered as it propagates.

2.3.1 Refraction

If the object under investigation consists of a set of bounded regions of different media, the wave will get altered as it reaches the plane boundaries. All media can be characterized by the product of the sound velocity and the density. This property is designated the acoustic impedance, and the parameter determines, if two media are different. As the wave interacts with the boundary, part of the wave will get reflected, whereas the remaining part will continue propagating (see Fig. 2.2). The splitting of the wave is termed refraction. The acoustic impedance of the two media determines the ratio of pressure amplitude and energy contained in the transmitted and reflected wave. The propagation direction of the transmitted wave (θ_t) is determined by the incidence angle (θ_i) and the sound velocities in the different media. Snell's law determines the relation [3], [4]:

$$\frac{\sin(\theta_i)}{c_i} = \frac{\sin(\theta_t)}{c_t}, \tag{2.7}$$

where c_i and c_t are the sound velocities in the two media. In the human body only a few plane boundaries exist such as the vessel walls, the diaphragm, and some of the organ boundaries. If only the refraction effects were present in the human body, medical ultrasound would only be able to map the boundaries. Fortunately other effects are present, which cause an interaction and reflection continuously as the wave propagates.

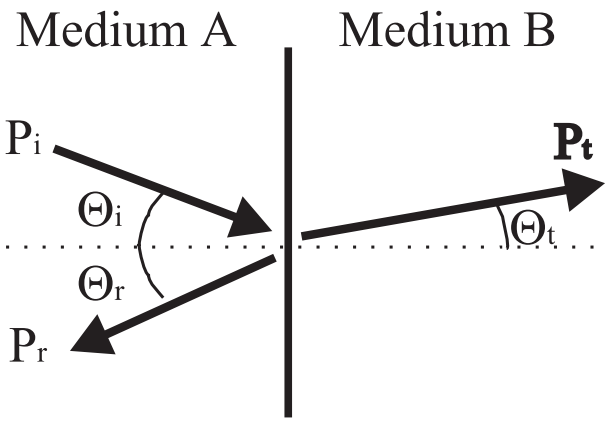

Figure 2.2: Refraction of a wave at the boundary between two media with different acoustic impedance.

2.3.2 Scattering

The soft tissues in the human body are non-homogeneous. When investigating small (infinitesimal) volumes of tissue one will observe that the density and tissue composition vary slightly between neighboring volumes. The soft tissues therefore are characterized by having varying properties on a continuous basis. Due to these variations in the acoustic impedance the propagating wave will interact continuously with the volumes along its propagation direction. As a result reflected waves will be generated continuously. Again the amplitude and energy of the reflected wave is determined by the acoustic impedance of the neighboring volumes. Each reflected wave thereby carries information of the anatomical structures present in that area.

The observed interaction is not a mere refraction process but a phenomenon termed scattering [3]. Analysis of the soft tissues reveals that they consist of components (cells, fibers, connective tissues *etc.*) smaller in size than the wavelength of the wave. The propagating wave interacts with all these small structures termed scatterers. Scattering is a very complex phenomena, and a comprehensive description hereof is out of the scope of this discussion. The discussion in the following will point out some features of scattering from small, hard structures. When the propagating wave interacts with the scatterers, each scatterer absorbs part of the energy of the wave, and re-radiates it in all directions. The scatterers thereby act as a source radiating spherical waves. Due to the size of the scatterers, the measured reflected signal is the constructive and destructive interference of scattered signals from all the small structures. When visualizing the measured signal a speckle appearance will occur. It does not visualize the individual scatterers but the contributions from a group of scatterers [3]. The fraction of absorbed and thereby re-radiated acoustic energy is still dependent on the tissue characteristics (the acoustical impedance), so variations in the appearance of the speckle pattern reveal different anatomical and pathological structures. An example is shown in Fig. 2.3, which shows a B-mode image of the liver (left) and the kidney (bottom right).

Estimation of the blood velocities in the cardiovascular system also rely on the scattering of the wave as it interacts with the blood. The blood constituents are the plasma fluid and the blood cells, which are termed platelets, leukocytes (white blood cells), and erythrocytes (red blood cells). The dimensions of the individual particles are more than a factor of 10 smaller than the wavelength, which causes Rayleigh scattering [3], [10]. As the particles are displaced by the propagating pressure wave a change in compressibility occurs, which gives rise to the emission of a spherical wave re-radiating energy in all directions. This effect is known as monopole scattering [3]. The simultaneous occurrence of density variations results in a dipole scattering, where the re-radiated energy mainly propagates forward or backwards along the direction of propagation [3]. The scattering ability is described by the backscattering coefficient and the backscattering cross-section, σ_{bsc} [3]. The backscattering cross-section depends on:

Figure 2.3: B-mode image of liver (left) and kidney (bottom right).

- the density and compressibility fluctuations,
- the inverse of the wavelength to the power of 4,
- the size of the erythrocytes,
- the fraction of the volume filled with the erythrocytes (the hematocrit value), and
- a packing factor determining the level of independence of the erythrocytes. As the volume fraction of erythrocytes increases, their location and orientation becomes dependent on the neighboring erythrocytes. The backscattering from the individual erythrocytes get correlated, which seems to introduce destructive interference between the scattered waves [3].

Investigation of the backscattering from blood reveals that the amplitude level is 10-500 times smaller than that from tissue.

The majority of the anatomical structures in the human body can be imaged employing ultrasound due to the scattering characteristics of soft tissues and blood. Imaging of bone structures and the air in the lungs are limited, as most of the wave is reflected at the boundary. This effect influences the ability to image soft tissues lying directly beneath air and bone structures.

Although scattering results in energy re-radiated in all directions, a measurement of the signals is performed with a sensor of finite size. One should therefore be aware that only part of the scattered waves is measured.

2.3.3 Attenuation

The human tissues are lossy media, and therefore acoustic energy is dissipated. Usually the term attenuation is used to describe this effect. The linear wave equation does not govern this. Additional terms should be

Tissue				
Liver	Fat	Kidney	Blood	Bone
0.6-0.9	1.0-2.0	0.8-1.0	0.17-0.24	16.0-23.0

Table 2.2: Attenuation ([dB/(MHz cm)]) values for a selection of soft body tissues and the blood.

included in the basic equations, and a new set of equations must be solved [4]. The majority of the energy loss (70-90 % [3]) is due to absorption, where the acoustical energy is converted into thermal energy. The following effects cause this conversion [4]:

- the viscous losses due to the shearing viscosity of particles with different velocities, and the bulk viscosity losses from the compression and dilation of volumes,
- heat exchange due to temperature gradients, and
- molecular energy exchange, where the kinetic energy is converted into other energy forms such as potential and vibrational energy.

The level of attenuation is tissue and frequency dependent and is usually expressed in dB/[MHz cm]. The amplitude level of the wave decreases with increased distance from the source to a point in space. For high oscillation frequencies the amplitude drop off is higher, than is the case for a wave oscillating at a lower frequency. The distance dependence causes the wave to have a finite propagation range. A trade off between penetration depth, resolution, and level of backscattered energy is thereby introduced. In cardiovascular imaging it is desirable to emit a wave with a high frequency to obtain high resolution. This limits the imaging depth and thereby the number of vessels that can be imaged. Table 2.2 lists attenuation values for a selection of soft tissues and the blood in the human body [3].

In medical ultrasound the emitted wave spans a band of frequencies. Due to the nature of the attenuation the higher frequency components are attenuated more than the lower frequencies. This results in a change of the emitted wave as it propagates. Often a linear relation between attenuation in dB, distance, and frequency is assumed. In ultrasound imaging, compensation is attempted by performing an amplification upon measuring. The amplifier characteristics change over time to compensate for the depth dependence. More or less advanced amplifiers can be implemented. Often a mere amplitude amplifier is used, where the signal amplitude is increased by multiplication by a factor, which is dependent on depth. The amplification process is termed the ”Time Gain Compensation” - TGC for short.

2.3.4 Alteration of the emitted wave

Two more effects cause alteration of the emitted waveform. As the wave propagates through different tissues, the speed of propagation varies. Since different parts of the wave propagate through different tissues, some wave segments travel faster or slower than other segments. A temporal misalignment of the wave segments occurs, which causes a distortion of the waveform. This effect is termed phase aberration [6].

If the propagating wave passes through a medium in motion such as blood, the center frequency will change due to the Doppler effect [3]. The relation between the velocity of the medium v and the change in frequency - the Doppler shift f_d - is given by:

$$f_d = -\frac{2v}{c} f_0, \tag{2.8}$$

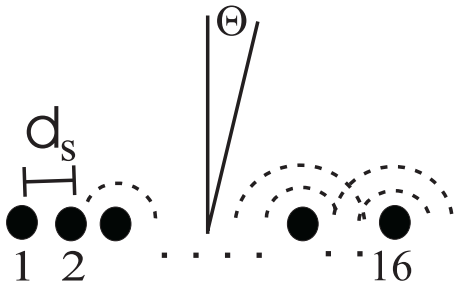

Figure 2.4: Plot of 1D linear array of 16 point sources.

where f_0 is the temporal center frequency of the wave. In the human body both blood and the tissue lying next to moving or pulsating organs (heart, lungs, and arteries) carry motion and thereby cause a Doppler shift.

2.4 Employment of transducers

The characteristics of wave propagation and the interaction with media have been discussed so far. The generation of the wave and the measuring of the scattered signals for imaging requires a device that can convert two energy forms in a controlled manner. A transducer is used for this purpose. It can convert voltage to pressure (and vice versa), and thereby emit a specific pressure waveform, and subsequently measure the scattered signals. Real physical transducers have a limited spatial extent and consist of an array in 1D or 2D of one or more elements. The individual elements can be flat or curved. The different types of transducers have different characteristics. The choice of the transducer to use in a particular situation depends on what one wants to emit and measure. A finite sized transducer - an aperture - introduces spatial windowing and sampling. Waves can only be emitted and received at a set of predefined locations determined by the aperture size and location, and the element size and spacing. Each of the elements in the aperture emit a wave. Investigation of the generated wave field and its distribution in space reveals that the distribution of energy is dependent on the geometry and element spacing of the aperture. This property can be described fully by an aperture function, which can be computed for any transducer geometry [4]. The function describes the distribution of energy as a function of direction in the far field. In the acoustics literature the term beampattern is used. Medical ultrasound scanning is performed in the near field, but the aperture function still can be used to give an indication of the energy distribution.

In Fig. 2.4 a linear array is shown, which consists of 16 point sources spaced a distance d_s apart. The direction is determined by the angle θ, which is measured relative to the unit normal vector for the transducer surface. The beampattern is plotted in Fig. 2.5 (a), (b), and (c) for d_s equal to $1.5\lambda, 0.5\lambda$, and 0.25λ, respectively. Continuous waves are emitted from each element. As the distance d_s decreases, the replica of the major and minor lobes is removed from the so called visible region, which is the space bounded by the range $\theta \in [-90^o, 90^o]$. These grating lobes are a result of the spatial sampling, which is determined by the choice of d_s. If the replicas are not removed, signals from several regions in space will contribute to the measured signal. The different regions cannot be distinguished, so the spatial resolution is limited. Decreasing d_s unfortunately has the effect of widening the mainlobe, when the number of elements are kept constant. Although the insonification area has been narrowed by removing the grating lobes, the finite width of the mainlobe results in insonification of a volume of scatterers. As the mainlobe width increases, the resolution along the direction perpendicular to the transducer surface decreases. Infinite resolution is therefore not obtainable.

The parameters in the aperture function include the wave frequency, which makes the aperture function dependent on the wavelength. The grating lobes will not be present in the visible region, if the following

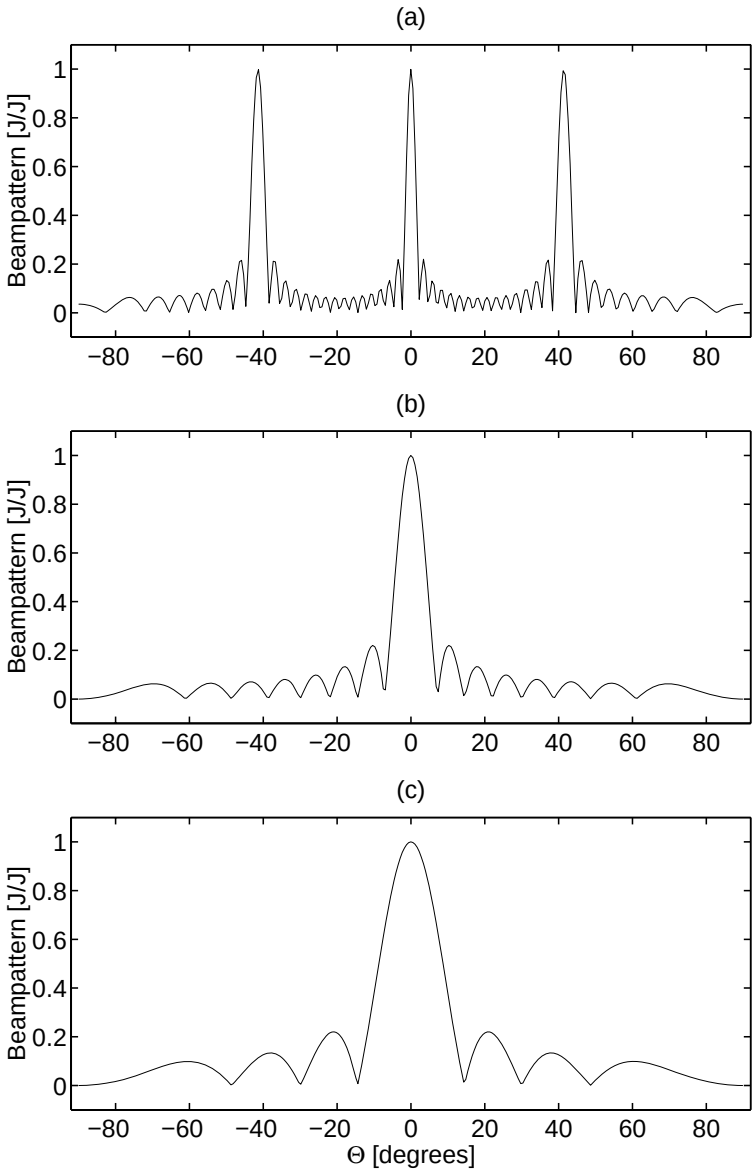

Figure 2.5: Plot of the beampattern for different choices of spacing between the sources. Top : $d_s = 1.5\lambda$. Middle : $d_s = 0.5\lambda$. Bottom : $d_s = 0.25\lambda$. The center frequency is 3 MHz, and the sound velocity equals 1540 m/s.

constraint is obeyed: $d_s \leq \lambda/2$ [4]. During reception the aperture function causes scattered signals from certain directions to be favored over other directions. Thereby directional sensitivity is obtained both in transmission and reception. As discussed above the width of the mainlobe determines the resolution perpendicular to the direction of propagation (usually termed the lateral resolution). By increasing the number of elements the mainlobe can be narrowed and the resolution increased. So by proper design of the geometry and working frequency the lateral resolution can be increased. In medical ultrasound the apertures should be handy to work with, which limits the size and thereby the resolution.

So far a square spatial windowing function has been assumed, where the individual signals from each element contribute equally. Introduction of a weighting function on the aperture, which weights the contributions from the individual elements, improves the resolution. The mainlobe becomes wider but the sidelobe levels decrease. The weighting (apodization) function should have the following properties [6]:

- the amplitude should have its maximum in the center of the aperture,
- the amplitude should drop off and go towards zero with increased distance to the center element.

2.5 Beamforming

As each of the elements can emit and receive independently, the propagation characteristics of the waves can be incorporated in the emission and reception scheme to improve resolution at some location. The latter is done by introducing focusing. The definitions of focusing in emission and reception respectively are as follows:

- the ability to direct waves in a desired direction and concentrate energy in a spatial location,
- the ability to receive energy from a desired spatial location and compensate for different travel times.

The focusing scheme is usually termed beamformation. The focusing schemes discussed in the following are only possible for multi-element transducers.

2.5.1 Emission

A spherical wave (approximately) is emitted from each of the elements. By assuming a constant sound velocity throughout the medium, the propagation time from the element to a spatial location can be computed for the individual waves. Concentration of the energy in a particular location requires that the individual waves constructively interfere at that point. By delaying the time of emission of the individual waves, the differences in travel time can be compensated for. A delay function over the elements is introduced, and a focusing of energy and thereby a higher resolution at the point of focus is obtained. This focusing method resembles the conventional focusing in transmission and is limited to having only one transmit focus. By varying the delay function the focus point can be moved around in space.

This focusing scheme is not fully valid due to the existence of phase aberration. Different research groups investigate the issue of phase aberration correction [11], [12], [13], [14]. Different methods are currently being developed employing synthetic apertures to obtain multiple foci in transmission [15], [16].

2.5.2 Reception

The scattering of energy results in the emission of a spherical wave. The distance from a point in space to each of the elements varies, which causes a delayed arrival of the constant phase fronts on the elements. As the distance is known, the travel time to each of the elements can be calculated. An alignment of the individual signals can be obtained by introducing a delay function in the reception phase. A dynamic focusing along the scan direction can be performed by letting the delay function vary as a function of time (and thereby depth).

2.6 Summary

With the theoretical basis given above it can be concluded that it is possible to emit waves in predefined directions with a level of spatial resolution, along with measurement of the acoustical response from the interaction between the wave and the tissue structures. Information about the investigated media can be extracted by means of proper processing of the signals. The subsequent chapters will describe some of the processing schemes employed in more detail.

Chapter 3

The cardiovascular system and imaging modes

After having introduced the acoustical basis for medical ultrasound in Chapter 2, an introduction to the cardiovascular system and some of the imaging modes will be given in this chapter. The introduced terminology and the properties are used in the following chapters.

First, a short introduction to the cardiovascular system and its properties is presented in Section 3.1. A relation between the internal pressure in the carotid artery and the induced motion of the vessel wall and the surrounding tissue is introduced in Section 3.1.1. Womersley's model for the blood velocities as a function of time and position along the radius of the vessel is introduced in Section 3.1.2. The model applies for the carotid and femoral artery, and the set of model parameters for these arteries are listed. The properties of the cardiovascular system and the models will be employed for generating simulated data, which resemble the *in-vivo* situation.

Some of the typical images that are generated from the recorded signals are discussed in Section 3.2.

3.1 The cardiovascular system

The cardiovascular system supplies the organs and the tissue in the body with oxygen and removes waste products (such as CO_2). This requires a network of branching and interconnected pipes, in which blood flows out into the body and back to the heart. The heart initiates the outgoing flow by pumping oxygenated blood out into the arteries. The blood propagates in the body through the branching arterioles and capillaries. At the capillary level the exchange of oxygen and waste products between blood and tissue takes place. The capillaries collect into venulaes, which connect to the veins. The de-oxygenated blood is lead back to the heart through them. Re-oxygenation is performed by passing the blood through the lungs. The four chamber structure of the heart ensures that de-oxygenated and oxygenated blood are kept separate, and pumped to the lungs and into the arteries, respectively. A more thorough discussion of the cardiovascular system is given in [17].

Table 3.1 lists flow and dimensions characteristics for a selection of arteries and veins from the human cardiovascular system [18]. Fig. 3.1 shows an anatomical drawing of a subset of the arteries and veins in the human body.

Vessel	Internal diameter [cm]	Wall thickness [cm]	Length [cm]	Young's modulus [N/m$^2 \cdot 10^5$]
Ascending aorta	1.0-2.4	0.05-0.08	5	3-6
Descending aorta	0.8-1.8	0.05-0.08	20	3-6
Femoral artery	0.2-0.8	0.02-0.06	10	9-12
Carotid artery	0.2-0.8	0.02-0.04	10-20	7-11
Inferior vena cava	0.6-1.5	0.01-0.02	20-40	0.4-1.0

Vessel	Peak velocity [cm/s]	Mean velocity [cm/s]	Reynolds number (peak)	Pulse propagation velocity [cm/s]
Ascending aorta	20-290	10-40	4500	400-600
Descending aorta	25-250	10-40	3400	400-600
Femoral artery	100-120	10-15	1000	800-1030
Carotid artery				600-1100
Inferior vena cava	15-40		700	100-700

Table 3.1: Dimensions and flow characteristics for a selection of arteries and veins in the cardiovascular system.

3.1.1 A relation between blood pressure and tissue motion

The pumping heart generates a pulsating blood flow in the arteries, which induces a time varying pressure acting on the arterial wall [19]. Due to the elastic property of the vessel, a radial motion of the wall (relative to the center of the vessel) and the surrounding tissue [19] is induced. As a result hereof the radius of the vessel varies throughout the cardiac cycle - it pulsates. The change in radius is usually termed dilation d, and it is defined as the change in radius R relative to the inner radius R_i at diastolic pressure:

$$d = R - R_i. \tag{3.1}$$

A mathematical relation between the pressure and the dilation for the carotid artery is introduced in the following. The relation assumes a vessel with no pathological conditions. The amount of dilation depends on the elastic properties of the vessel wall (such as stiffness which increases with age), and the exercise level. The levels of pressure throughout a cardiac cycle in the carotid artery are normally within a range of 80-160 mmHg [19]. A relation between the internal pressure in the vessel and the resulting dilation can be derived using the theory on deformable pipes [20], [21]. The human vessels are approximated by a cylinder with a finite wall thickness, which are subjected to uniformly distributed internal and external pressures. This results in a symmetrical deformation about the center axis of the vessel. The vessel wall must be considered as thick, since the thickness of the wall is large compared to the inner vessel radius [3], [21]. The level of displacement varies along the radius. The motion of the outer vessel wall is of interest in order to relate the motion of the surrounding tissue to the internal pressure. When the outer wall moves, the tissue next to the wall will move with it. The pulsation induces motion in the tissue. Based on the above assumptions the following relation arises:

$$d(t) = \frac{1}{E} \frac{2R_o}{(\frac{R_o}{R_i})^2 - 1} p(t), \tag{3.2}$$

where $p(t)$ is the time-varying internal pressure in the vessel, R_o is the outer radius at diastolic pressure, and E is Youngs modulus for the vessel wall. The relation is independent of the external pressure, since it is assumed that no pressure variations occur outside the vessel. A relation between pressure and dilation

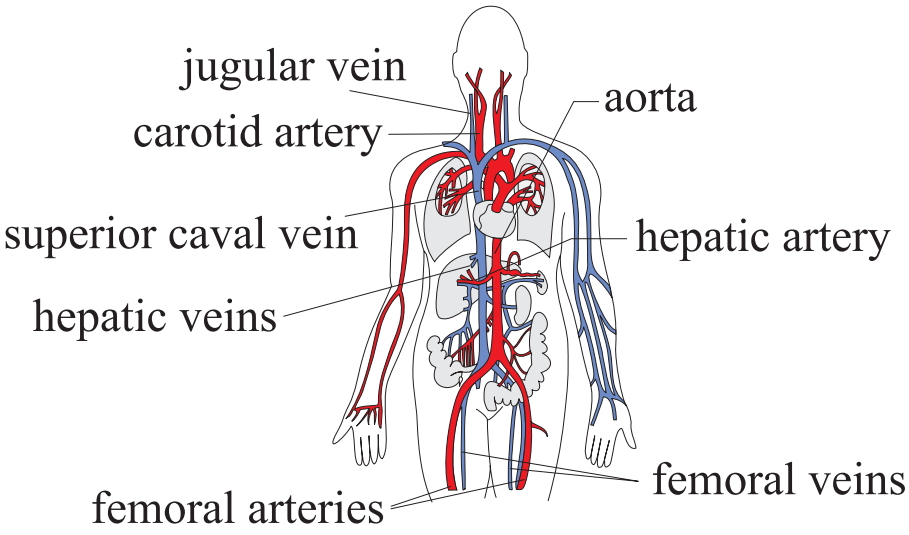

Figure 3.1: Drawing of part of the human cardiovascular system.

has not been derived for pathological conditions. By introducing a measure of the elasticity that varies as a function of angular position on the wall, a relation approximating the dilation for a diseased vessel might be obtainable.

Based on (3.2) a relation between the internal pressure and the volumetric flow rate, Q_F, can be obtained. The volumetric flow rate at any time instant, t, is defined as the integral of the velocity v over the cross-section of the vessel [3]. By introducing related parameters the relation can be derived:

$$\begin{aligned} Q_F(t) &= \int_x \int_y v(x,y,t)dxdy \\ &= A(t)\bar{v}(t) \\ &= \bar{v}(t)\pi R^2(t) \\ &= \bar{v}(t)\pi(R_i + d(t))^2 \\ &= \bar{v}(t)\pi(R_i + \frac{1}{E}\frac{2R_o}{(\frac{R_o}{R_i})^2 - 1}p(t))^2, \end{aligned} \tag{3.3}$$

where (x,y) are the spatial coordinates, A is the cross-sectional area of the vessel, $\bar{v}$ is the spatial mean blood velocity over the cross-section, and $R(t)$ is the radius of the vessel as a function of time. The volumetric flow rate ([m^3/s]) will in practical systems be computed by summing the estimated velocities within the vessel. Given a measure of the parameters $\bar{v}, R_o, R_i$, and E an estimate of the internal pressure can be obtained. The feasibility of using this relation to make an estimate of the internal pressure has not been considered in this study.

3.1.2 Womersley's model for blood flow

Investigations of the motion of the blood particles throughout a cardiac cycle have resulted in equations, which describe the velocity of the scatterers as a function of time and position relative to the center of the vessel. The results are based on the assumption that the blood fluid is Newtonian [3], [19]. This is approximately true for larger vessels, as the dependence between viscosity and the shear stresses (the force per unit area) decreases. It is assumed that the fluid flows in a straight pipe, and no patholocigal conditions are present. The flow profile can then be described as a linear combination of a set of sinusoidal components [3], [19]. The model parameters are found from the spatial mean velocity over the vessel cross-section as a

function of time. This signal is Fourier decomposed and the spatial and temporal velocity in the vessel can be computed from the coefficients. The Fourier decomposed version of the model [19] is given by:

$$v(t, r_d/R) = 2v_0 \left(1 - \left(\frac{r_d}{R}\right)^2\right) + \sum_{m=1}^{\infty} |V_m||\psi_m(r_d)| \cos(m\omega t - \phi_m + \chi_m(r_d)), \tag{3.4}$$

where r_d is the radial distance from the center to a position along the radius of the vessel, and v_0 is the mean velocity. V_m and ψ_m are the Fourier amplitude and phase term, respectively. ω is the fundamental heart frequency. The parameters ϕ and χ are dependent on the vessel characteristics (density ρ, viscosity μ) and the radial position. They are defined by:

$$\begin{aligned} \tau_m &= j^{3/2} R \sqrt{\frac{\rho}{\mu}\omega m} = \alpha j^{3/2} \\ \psi_m(r_d/R, \tau_m) &= \frac{\tau_m J_0(\tau_m) - \tau_m J_0(\frac{r_d}{R}\tau_m)}{\tau_m J_0(\tau_m) - 2J_1(\tau_m)} \\ \chi_m &= \angle\psi_m(r_d/R, \tau_m), \end{aligned} \tag{3.5}$$

where $J_n(x)$ is the n^{th} order Bessel function, and $\angle\psi_m(r_d/R, \tau_m)$ denotes the angle of the complex function ψ. Table 3.2 lists the model parameters for the carotid and femoral artery [22], [23]. The unit bpm is an abbreviation for beats per minute. In Fig. 3.2 the velocity profile for the carotid artery is plotted for a full

Common femoral					Common carotid				
Diameter	=	8.4 mm			Diameter	=	6.0 mm		
Heart rate	=	62 bpm			Heart rate	=	62 bpm		
Viscosity	=	0.004 kg/[m · s]			Viscosity	=	0.004 kg/[m · s]		
m	f	α	$\frac{\lvert V_m\rvert}{v_0}$	ϕ_m	m	f	α	$\frac{\lvert V_m\rvert}{v_0}$	ϕ_m
0	-	-	1.00	-	0	-	-	1.00	-
1	1.03	5.5	1.89	32	1	1.03	3.9	0.33	74
2	2.05	7.7	2.49	85	2	2.05	5.5	0.24	79
3	3.08	9.5	1.28	156	3	3.08	6.8	0.24	121
4	4.10	10.9	0.32	193	4	4.10	7.8	0.12	146
5	5.13	12.2	0.27	133	5	5.13	8.7	0.11	147
6	6.15	13.4	0.32	155	6	6.15	9.6	0.13	179
7	7.18	14.5	0.28	195	7	7.18	10.3	0.06	233
8	8.21	15.5	0.01	310	8	8.21	12.4	0.04	218

Table 3.2: Fourier model parameters for the carotid and femoral artery.

cardiac cycle as a function of time and radial distance relative to the radius of the vessel. The mean velocity is 0.15 m/s, and R=0.003 m. Due to the fluid laws arising from flow physics, the velocity must converge to 0 at the vessel wall [24]. The profile is symmetric about the center axis of the vessel.

The common carotid artery branches into two, the external and internal carotid, half way up the neck. The latter supplies the brain, whereas the former supplies the muscles and the other organs in the head. The velocity profile for the internal carotid has an offset velocity different from zero, as the brain needs a continuous flow of oxygen. The muscles and organs do not require this, so in this case the offset velocity equals zero. The velocity profile from the common carotid artery thereby gets altered at the level of branching, and the two profiles in the branches are different.

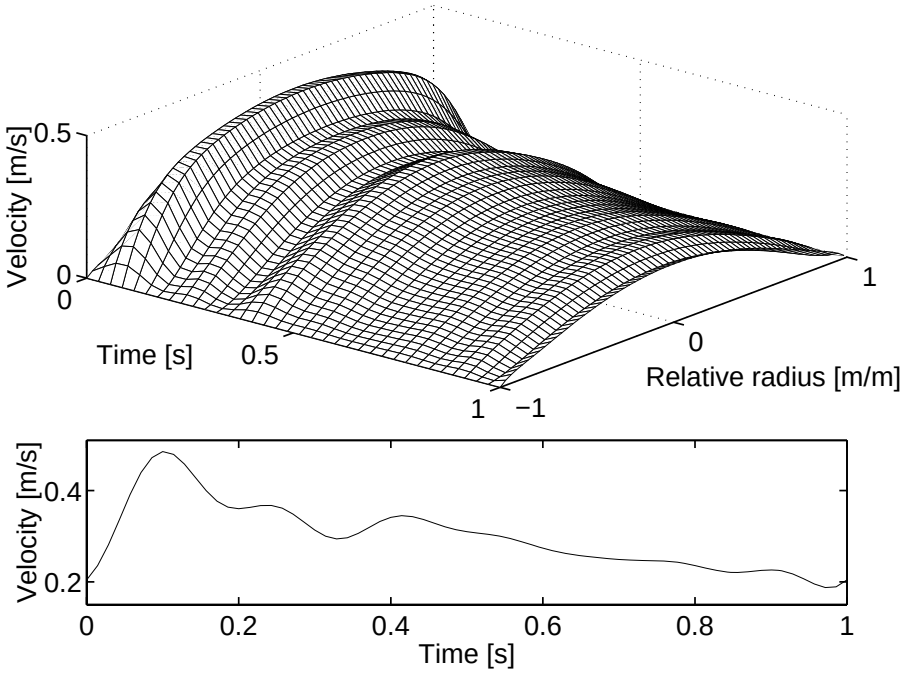

Figure 3.2: Plot of the velocity profile for the carotid artery.

3.2 Imaging modes in medical ultrasound

Medical ultrasound is used to extract information of diagnostic value. Depending on the aim of the examination different strategies with respect to the frequency and temporal extent of the emitted pulse, the volume scanned *etc.* are used. After acquisition of the signals - usually termed RF-signals - processing is performed to extract and present the valuable information to the clinicians. The subsequent presentation of the information depends on the aim. In the following a short discussion of some of the commonly used visualization modes [3], [25] will be presented. The introduced terminology will be used in the subsequent chapters.

3.2.1 B-mode imaging

An image of the anatomical structures in the scanned volume can be created due to the varying acoustic impedances of the tissue components. The information about the different tissue structures is extracted from the recorded RF-signals. A high level of resolution is obtained by emitting a temporally short pulse (a few cycles). The exact resolution level is dependent on the frequency and increases, as the frequency is increased. As the attenuation increases with increased frequency, a trade off between axial resolution and imaging depth exists.

By emitting and receiving from a number of directions a 2D image can be generated. Each recorded RF-signal, r, is:

- envelope detected according to (3.6), where l is the line number in the image, and n is time in number of samples. One RF-signal is acquired for each line in the image. The operator H represents the Hilbert transformation,
- logarithmically compressed to a dynamic amplitude range of 60-80 dB. Gray-tone values are assigned for the chosen range.

$$r_{env,l}(n) = |r_l(n) + jH\{r_l(n)\}|. \tag{3.6}$$

An alignment of the lines to a 2D rectangular grid along with an interpolation is performed, before the image is displayed on the screen. This process is usually termed scan conversion. The resulting 2D image is termed a B-mode image. An example is shown in Fig. 3.3(a).

3.2.2 CFM-mode imaging

Diseases in the cardiovascular system can be diagnosed through inspection of the spatial blood velocity distribution and the magnitudes hereof. Estimates of the blood velocities are obtainable after proper processing of a number of RF-signals (see Chapter 6) acquired along the same direction. The B-mode image is still needed to guide the scanning and determine pathological conditions for the tissue regions. Therefore the blood velocity estimates are overlaid onto the B-mode image, and different colors are used to represent the velocity levels. This scan mode is termed Color Flow Mapping (CFM for short). An example is shown in Fig. 3.3(b). The length of the emitted pulse is dependent on the processing scheme used to determine the blood velocities. Both long and short pulses are used (see Chapter 6). When a long pulse is used, an alternation between emission of pulses and acquisition of the RF-signals for B-mode and CFM-mode is performed. Different schemes can be used, and they vary for different scanners and for the scan settings (center frequency, pulse emission frequency, size of scanned area with respect to blood velocity estimation *etc*.). In CFM-mode more lines have to be acquired before a full image can be displayed. The frame rate (the number of images presented per second) therefore decreases. The frame rate is inversely proportional to the size of the 2D B-mode and the 2D CFM-mode image, and the number of lines used in the blood velocity estimation.

In the following chapters RF-signals for blood velocity estimation will be referred to with the variable r_{cfm}, whereas the signals for B-mode imaging will be named r_b. The terms RF-signal(s) and RF-line(s) will be used alternately throughout this dissertation. They both denote the acquired signal response, which arises, when the emitted pulse has interacted with the scanned medium.

3.2.3 Spectral Doppler mode

The temporal evolution of the blood velocity in a specified spatial point is also used to extract information of diagnostic value. The scanners show this information, when they run in Spectral Doppler mode. The velocity or the corresponding frequency value is plotted as a function of time on the screen. The temporal sequence is termed a sonogram. The lower plot in Fig. 3.3(a) shows an example of a sonogram.

3.3 Summary

Some of the properties of the cardiovascular system were presented in this chapter. An approximative model between the pressure variations in the carotid artery and the induced tissue motion was introduced. Womersley's model for the velocity profiles in the carotid and femoral artery was introduced, and it will be employed in the subsequent chapters. A selection of the imaging modes were introduced, and the terminology here fore will be used throughout the dissertation.

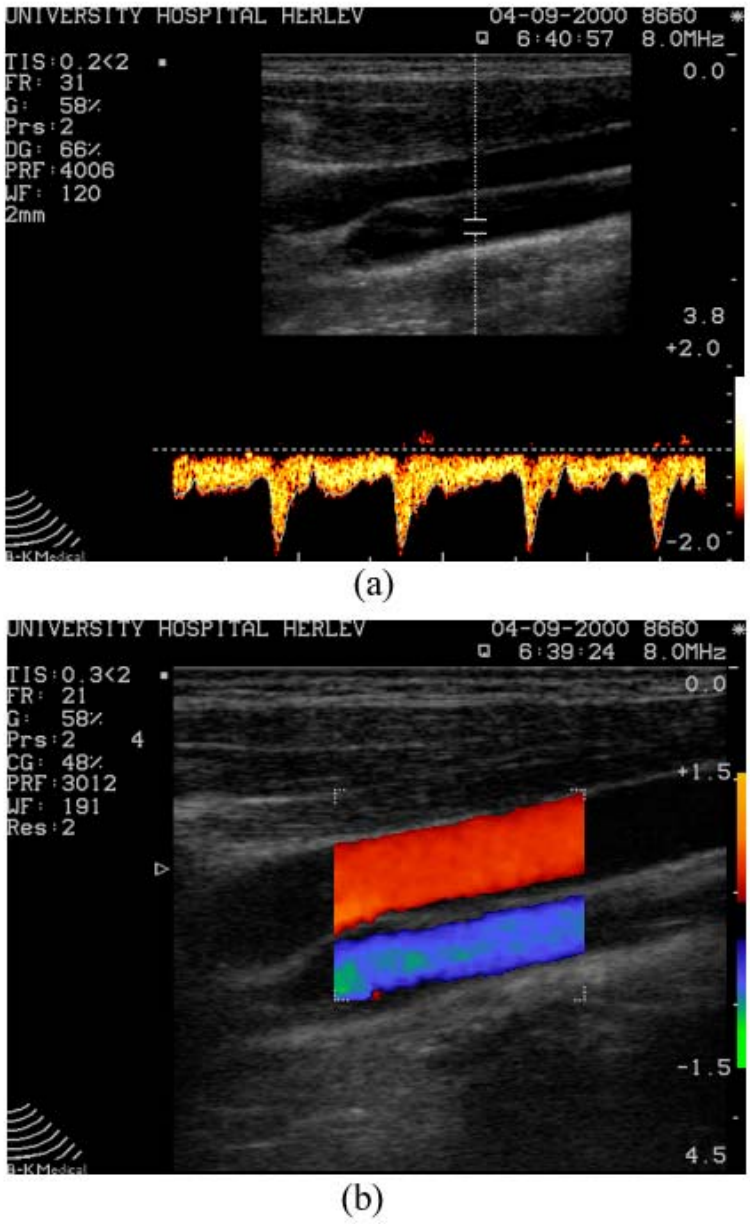

Figure 3.3: Examples of some of the common imaging modes in ultrasound. (a) The upper plot is a B-mode image of the carotid artery and the jugular vein, and the lower plot is the sonogram of the flow in the center of the carotid artery. (b) CFM-mode image of the carotid artery and the jugular vein.

Chapter 4

Incorporation of tissue motion in simulated RF-data

A testing phase is included in any development of new techniques, where the performance of the methods is evaluated. The evaluation must be performed on a well-defined setup. When developing algorithms for blood velocity estimation, a well-defined setup is characterized by RF-data, where 1) the location of the signal components from the interactions with the tissue structures, the vessel wall, and the blood are given, and 2) the true blood velocity distribution and magnitudes in the vessels are known. Data obtained from *in-vivo* measurements are not well-defined, since these requirements are not met. Measurements on phantoms come close to being well-defined, as the location of the tissue mimicking structures often are fixed and therefore known. A level of uncertainty is present on the velocities of the blood mimicking fluid. The flow situation is dependent on the capabilities and the precision of the flow pump and the tubing to and from the phantom. Turbulence might be generated, and then the actual flow profile will not be consistent with the expected profile. Data from phantom measurements are therefore not completely well-defined. Simulated data, which resemble the *in-vivo* situation, are often employed instead. The computation of simulated data requires:

- modeling of the transducer (1D/2D array, number of elements, geometry and spacing of elements), the excitation pulse, the impulse response of the transducer, and the focusing and apodization schemes,
- generation of a distribution of point scatterers in space. Each scatterer is assigned a value, which determines its scattering ability and thereby the nature of the scatterer (tissue or blood),
- modeling of the propagation forth and back of the generated waves,
- determination of the interaction between the wave and the scatterers.

These requirements are fulfilled with the simulation program Field II, which has been developed by Jensen [26], [27]. Any array transducer, focusing and apodization scheme, and transducer excitation can be handled, and the simulation model can easily be expanded to any imaging method and flow situation. The Born approximation [10], which excludes multiple scattering, is applied. The simulated system is assumed to be a linear system, so the non-linear propagation is not incorporated.

Generation of realistic data, which resemble the *in-vivo* situation over time, includes the incorporation of the movements of the scatterers between acquisitions. The blood moves, as it propagates through the cardiovascular system. Motion in the tissue structures are also present and must be incorporated. The aspect of tissue motion is the topic of this chapter. The nature hereof is discussed in Section 4.1. The presence

of tissue motion is investigated through inspections of *in-vivo* data and subsequently modeled in Sections 4.2-4.4. A verification of the models is presented in Section 4.5, and the results are summarized in Section 4.6.

4.1 The nature of tissue motion

The tissue motion is induced by breathing, the beating of the heart, and the pulsation of arterial vessel walls. These motions are present, when measurements are performed on major arteries and in the abdominal region. A large group of echo-canceling filters (see Chapter 5) are based on the assumption that the tissue is stationary. As this is not the case they fail to perform well on *in-vivo* data. With simulated data incorporating tissue motion a proper basis for developing and evaluating these filters is present.

The motion in the surrounding tissue is a result of a change in position of one or more organs (lungs and heart), and the vessel walls lying close to the region of interest (ROI). The motion changes the position of the ROI and can also change the size of the different components in the region (*e.g.* increased diameter of vessel because of pulsation). The motion repeats itself due to the periodic nature of breathing and the beating of the heart. The repetition rate, and thereby duration of the motion, usually varies for the individual motion contributors. The heartbeat frequency is about 60 bpm on average, and the respiratory frequency is 12 breaths/min (when resting). These values vary among individuals and their physical state. The level of tissue motion at a particular scan site is dependent on 1) the distance from inducers to the ROI, and 2) the motion level of the inducers (*e.g.* breathing level: superficial or deep). All these factors should be incorporated in the simulation. The above motions are generated by the subject being scanned. A fourth motion arises, when the transducer is hand held during the scan session. It is most likely that the clinician, which performs the scanning, cannot keep the hand and probe steady over a longer period of time. The applied pressure against the skin and/or the angulation will vary (slightly) during a scan session. The level of motion is highly dependent on the clinician and impossible to predict. Over short periods of time its contribution will be negligible. This study will not investigate and model the fourth motion but will focus on the motions induced by the subject.

Several authors have investigated tissue motion previously. Badawi et al. [28] studied the tissue motion due to pulsation of the heart and neighboring arteries in normal and diseased livers. The diseased livers suffer from schistosomiasis, which results in changes of the elastic properties of the liver tissue. Variations in the level of tissue motion were found among the different states of the disease.

Induced motion of the breast tissue due to cardiac pulsation and respiration was investigated by El-Fallah et al. [29]. The ability to minimize the tissue motion - leaving only the blood motion - by proper positioning (dorsal, lateral, or ventral decubitus) of the subject was studied. A dependence between position and the level of tissue motion was proven. The level of motion was also shown to depend on depth and varied among the examined subjects. In both studies the velocity of the motion was determined to be on the order of millimeters per second.

Changes in the motion properties of the vessel wall due to stenoses was studied by Bonnefous [30]. Diameter variations of the vessel throughout a cardiac cycle were determined for normal and stenotic arteries. The dilation sequences had different characteristic properties dependent on the pathological condition.

The above studies focused on obtaining some pathological information from tissue motion or minimization hereof. The issue of tissue motion modeling for simulation of realistic RF-data is addressed in this project. The focus is on scannings performed at the carotid artery and in the abdominal region. A model for each of the motion inducers (heart, lungs, and the pulsating vessel wall) is determined.

4.2 *In-vivo* measurements of motion

The development of models for the individual motion contributors were based on investigations of *in-vivo* RF-data. The RF-data were recorded with a 3.2 MHz probe. A dedicated real-time sampling system [31] interfaced to a B-K Medical 3535 scanner was used for data acquisition. The system was capable of sampling at 15 MHz, which limited the selection of the center frequency of the ultrasound probe. The sampling system could acquire 0.27 seconds of data along one line in the image. Measurements were performed on 10 healthy volunteers lying supine, and the probe was hand held throughout the measurements. Each measurement was repeated 10 times to cover the whole cardiac cycle and a total of 400 independent RF measurements of 950 pulse echo lines were recorded. It was not possible to synchronize the measurements to the ECG signal, and it could therefore not be guaranteed that the whole heart cycle was covered in the complete measurement set for each volunteer.

To obtain information about all the different motion contributors, a number of measurements at different positions and under various conditions were made. Table 4.1 lists the scan sites and the motions present during measurements.

Dataset	Vessel	Scan plane	Motion
C1	Carotid artery	Transverse scan angle 90^o	P,B
HV1	Hepatic vein	Right liver lobe intercostal scan	B,H (P)
HV2	Hepatic vein	Right liver lobe intercostal scan	H (P)
HV3	Hepatic vein	Left liver lobe epigastric scan	H (P)

Table 4.1: Measurement conditions for determination of motion due to pulsation (P), heartbeat (H), and breathing (B).

Measurements were taken at three different sites for a total of four different conditions:

C1. The common carotid artery was scanned in a transverse plane with an insonation angle between the blood flow and the ultrasound beam of 90^o. This site and insonation angle were chosen to obtain measurements, where all movement could be attributed to pulsation from the target artery.

HV1. An hepatic vein in the right liver lobe was scanned intercostally. The insonation angle was in the interval $34 - 66^o$, and the vessel was seen longitudinally. The subject was instructed to breathe shallowly during measurements in order to keep the vessel within the Doppler gate (size : 19 mm). During measurements the vessel moved back and forth, but was always inside the gate. This vessel was chosen to obtain measurements where movement could be attributed to both pulsation (venous pulsation of the vessel in question plus arterial pulsation from neighboring arteries and the heart) and respiratory movement (the vessel moved back and forth inside the gate).

HV2. The measurement in HV1 was repeated where the subject was asked to hold his breath to eliminate the influence of respiratory movement.

HV3. An hepatic vein in the left liver lobe was scanned longitudinally in the midline. The insonation angle was in the interval $0 - 65^o$ and the vessel was seen longitudinally. The subject was instructed to hold his breath during measurements. This vessel was chosen to obtain measurements, where movement could be attributed to pulsation (venous), and heartbeat (the left lobe of the liver moves with every heartbeat).

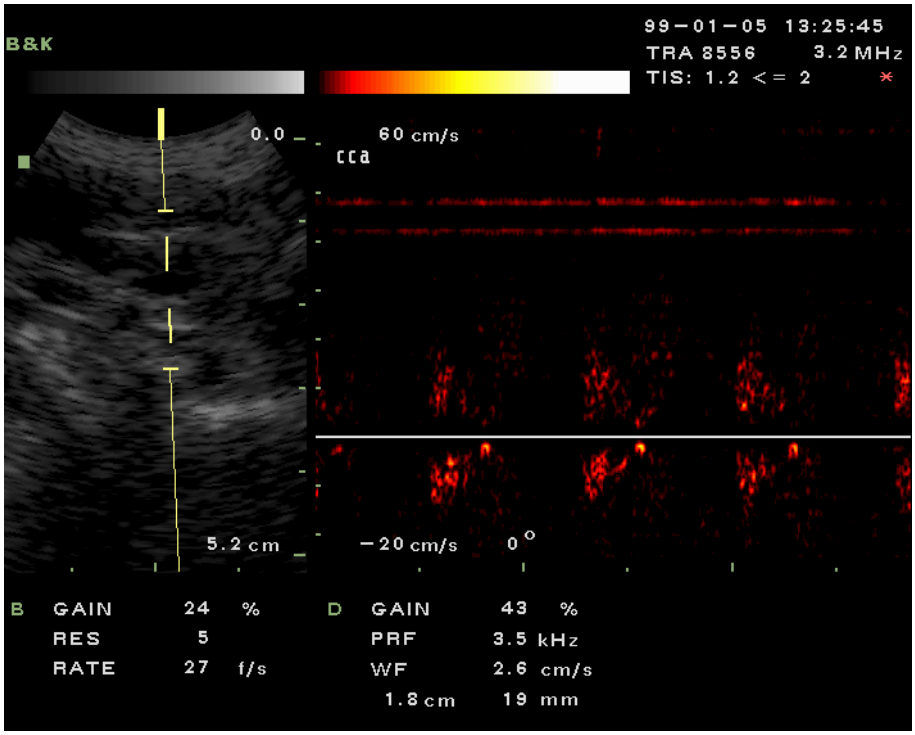

Figure 4.1: Duplex scan image from carotid artery (C1 scanning).

Duplex scan images from a C1 and a HV2 measurement are shown in Figures 4.1 and 4.2.

4.3 *In-vivo* velocity estimates

The acquired RF-data were bandpass filtered to minimize the noise content in the data. The tissue velocities were estimated by applying the autocorrelation estimator (see Section 6.3). Thirty-four consecutive RF-lines were used to obtain high-quality estimates. Tissue velocity estimates as a function of time and depth were computed for further investigation. The estimates revealed presence of tissue motion. The maximum velocities (v_{max}) for the individual volunteers (P_i) are listed in Table 4.2. Differences are seen among these due to anatomical variations, variations in heartbeat frequency, and level of shallow breathing. No HV3-data were obtained from subject P4 due to anatomical limitations. The maximum estimates were computed

Volunteer	Investigation site			
	C1	HV1	HV2	HV3
P1	6.3	3.1	3.1	17.0
P2	6.2	4.9	3.9	10.2
P3	9.1	13.2	5.3	9.6
P4	10.6	5.4	2.9	-
P5	9.4	4.9	2.2	9.7
P6	5.7	4.0	2.4	6.2
P7	5.9	11.8	7.7	7.7
P8	7.6	5.8	4.8	11.8
P9	18.1	4.3	4.9	9.3
P10	9.6	4.7	4.3	9.6

Table 4.2: Maximum velocities (in mm/s) for each volunteer for the 4 scan conditions.

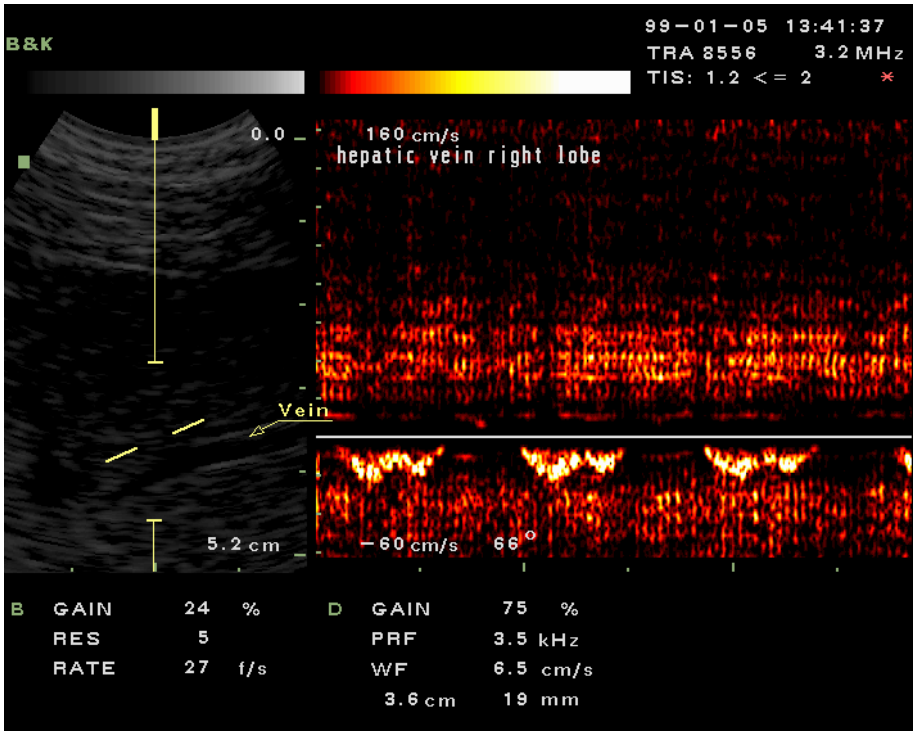

Figure 4.2: Duplex scan image from the right liver lobe (HV2 scanning).

by two different methods for the carotid artery and the hepatic vein. Tissue and blood motion must be continuous in both time and space, which precludes the possibility of having neighboring estimates that differ significantly in value. The estimates of the blood velocities are encumbered with uncertainty due to measurement noise, velocity spread, and signal alteration introduced by the de-noising and echo-canceling filters (see Chapter 5). A non-smooth velocity distribution arises. As only the velocity level is of interest, no post-processing filter is applied to smoothen the distribution. A few estimates - the outliers - differ significantly from the smooth surface and should be removed.

For the hepatic vein the maximum velocity estimate at each estimated position in the signal was determined for each measured file of RF-signals. Any of these maximum estimates were determined as outliers, if they had a value outside the interval $[\mu_{max} \pm 3\sigma_{max}]$, where μ and σ are the mean and standard deviation of the computed maximum estimates. Since some outliers were very dominant the elimination process was repeated, until μ and σ did not change between iterations. After elimination of the outliers the maximum velocity was found as the maximum (absolute) velocity estimate among all estimates. For the carotid artery a different approach was chosen based on the following observations. Within the blood vessel non-zero estimates occur, although theoretically this should not be the case with a scan angle of 90°. Tissue motion due to pulsation is at its highest close to the vessel and is then damped throughout the tissue. To incorporate this feature and eliminate outliers the maximum values were determined by applying a spatial median filter of length 5. The filter operated on the estimates along the scan direction, and the maximum velocity was found as the maximum output (absolute value) of the median filter for all estimates. The maximum velocity estimates (v_{max}) averaged over the 10 volunteers and the standard deviation (σ_v) among these are listed in Table 4.3.

Insonation angle correction of the motion direction relative to the transducer were not performed on the estimates from the hepatic vein. The motion angle for the heart and lungs cannot be determined, and will most probably not be the same. The above velocity estimates are a measure of the resulting velocity vector. This vector is the sum of the individual motion vectors from each contributor projected onto the scan direction. This is not a limitation of this simulation model, as it is the actual scan situation that should be

	C1	HV1	HV2	HV3
v_{max}	8.9	6.2	4.2	10.1
σ_v	3.7	3.4	1.7	3.0

Table 4.3: Maximum velocities (in mm/s) and corresponding standard deviations obtained for the 4 scan conditions, when averaged over all the volunteers.

modeled here. The goal is to create realistic simulated data - not to estimate the exact motion and motion directions of the heart and lungs.

The tissue velocities are small compared to the usual velocity levels seen in the center of an artery (see Chapter 3). As the blood velocities go to zero at the vessel wall, the blood and tissue velocities have similar levels at the boundary. Distinguishing the signals from the blood and the tissue is therefore complicated.

The maximum velocities quantify

- the level of motion,
- the influence from the different motion contributors, and
- the dependence on distance between scan site and the location of the motion generator(s).

The last two properties in the list will be investigated in the following. The obtained maximum velocities from each volunteer for the different scan sites are compared using a Wilcoxon test [32]. The Wilcoxon test compares two data sets to determine, whether a pair (x,y) differs in magnitude. The hypothesis is that the difference $(d_W = x-y)$ between the members of each pair (x,y) in the data set has a median value of 0. The test is used, since only few data are available and the distributions of x and y are unknown. The outcome of the test is a probability value - p - stating the probability of the hypothesis to be true. For p-values below 0.05 the hypothesis will be rejected, and the pairs are different in magnitude. Comparing HV1 and HV2 gives a p-value of 0.01, so the heart influences the motion at the right liver lobe, and the presence of respiration adds to the motion. The dependence on distance from the heart can be determined by testing HV2 against HV3. A p-value of 0.004 indicates that the level of tissue motion due to heart motion increases as the measurements are obtained closer to the heart.

4.4 Motion estimates and its modeling

Based on the above investigations, it can be concluded that tissue motion is present and should be incorporated into the simulation program to obtain realistic simulated data. The three motions are modeled individually, since the analysis showed that their contribution to the total motion depends on the scan site and the type of motion. The desired simulation model should then include both blood and tissue motion. Assuming no correlation between the individual motions, the accumulated tissue motion at a given scan site can be computed by adding the individual motion vectors.

Development of the tissue motion models are based on plots of velocity and motion estimates as a function of time and depth. The movement m is computed by a time summation of the estimated velocities at each depth:

$$m(n_e\Delta T, z) = \sum_{i=0}^{n_e} v(i\Delta T, z)\Delta T, \tag{4.1}$$

where n_e is the estimate number, ΔT is the time between estimates, $v(..)$ is the estimated velocities, and z is the (radial) depth. Figures 4.3, 4.4, and 4.5 show examples of motion plots, which illustrate features of the

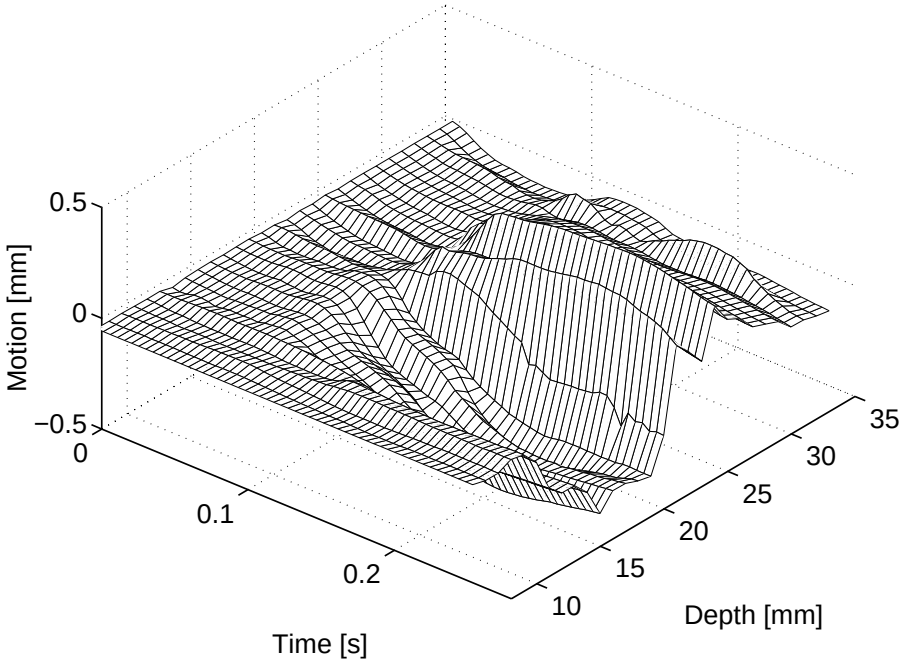

Figure 4.3: Example of motion found from *in-vivo* data from the carotid artery as a function of depth in tissue and time. Pulse rate: 60 bpm.

three different motions as a function of time and depth. The motion is positive, if the scatterers move away from the transducer relative to an initial position, and negative if movement is towards the transducer. A full motion sequence cannot be observed, since the sampling system only acquires RF-data in a time interval of 0.27 seconds. The time duration of pulsation and the heartbeat is approximately 1 second, whereas it is about 4-5 seconds for breathing. An estimate of the maximum value of the motion therefore cannot be determined. By combining the recorded sequences an idea of the maximum motion and the course of the motion can be obtained. One should bear in mind that the value of the maximum motion will vary among individuals and scan sites.

4.4.1 Pulsation

In Fig. 4.3 motion estimates from the carotid artery are shown. A motion due to pulsation will - in the plots - show up as two motion sequences moving in opposite directions relative to the center of the vessel. With this in mind the motion in Fig. 4.3 is due to pulsation. The nature of pulsation [19] gives that the position change of tissue scatterers has to be controlled by a change in radius relative to the center of the vessel. The time sequence of the dilation rises fast and then decreases and returns to the initial value. The motion is damped radially. Less dilation is seen for increased radius relative to the center. The model is therefore a function of time and depth. When no correlation between time and depth is assumed, the motion model becomes a product of two functions - one describing the time sequence, and the other describing the depth dependence. The latter dependence will be modeled as a damping function, which can take the values from 0 to 1. A damping value of zero at some depth is equal to no motion present at this depth. A value of one results in no damping, and therefore the scatterers will move an amount described by the temporal motion model. Close to the transducer (for low axial values) hardly any tissue motion is seen, as the transducer is maintaining a pressure on it. This limits the tissues ability to move around.

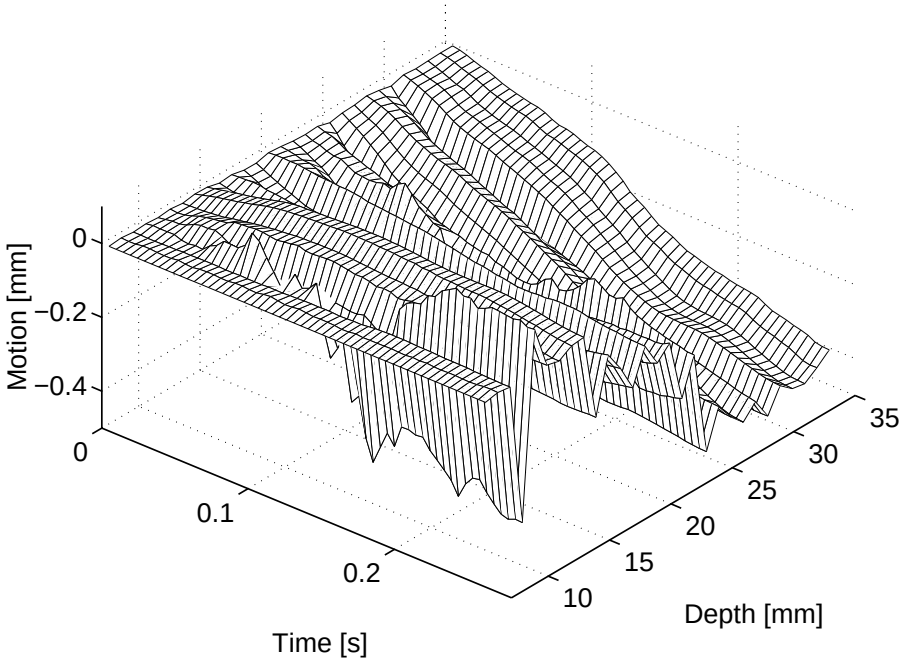

Figure 4.4: Example of breathing motion at carotid artery obtained from *in-vivo* data.

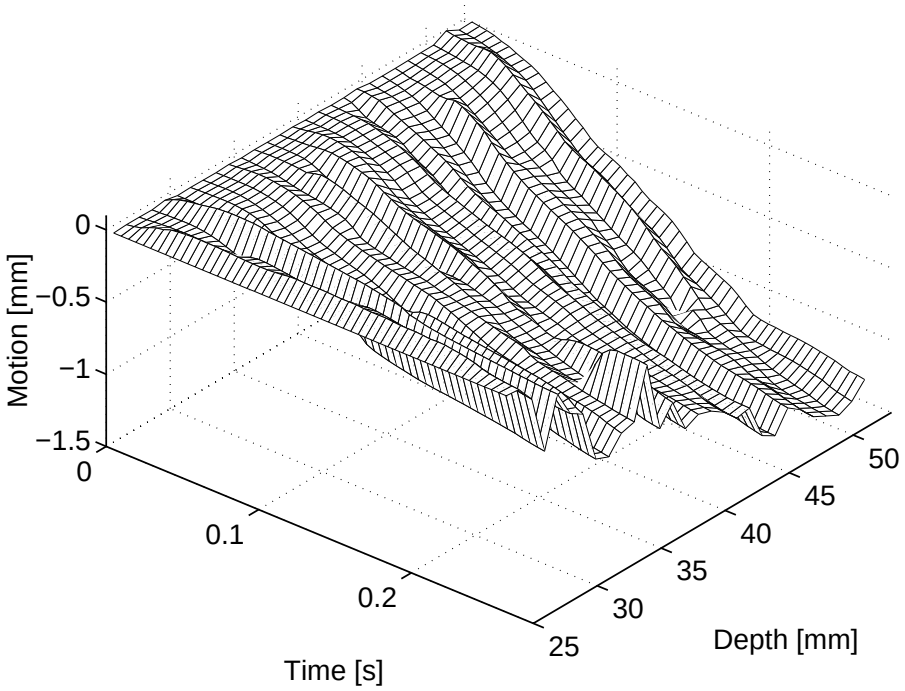

Figure 4.5: Example of motion due to heartbeat (HV3) at hepatic vein obtained from *in-vivo* data.

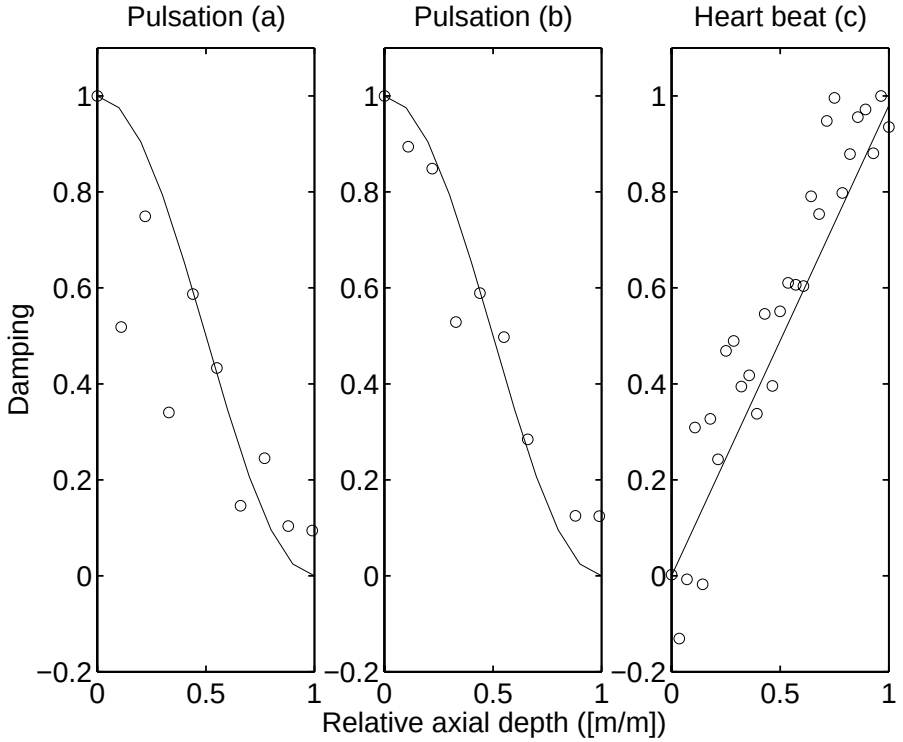

Figure 4.6: The damping functions associated to motions from pulsation (a), (b) and heartbeat (c). Solid lines (–) indicate the model values, and the circles (o) represent the *in-vivo* data.

The damping radially is described by a cosine damping function:

$$\alpha_p(r_d) = \begin{cases} 1 & r_d = R \\ 0.5(\cos(\pi\frac{r_d - R}{R_l - R}) + 1) & R < r_d \leq R_l, \\ 0 & r_d > R_l \end{cases} \tag{4.2}$$

where α_p is the damping level at a given radius r_d relative to the center of the vessel, R is the radius of the vessel, and R_l is the maximum radial distance at which motion will be seen. Beyond R_l the damping function is equal to zero. In Fig. 4.6(a)-(b) the damping model is compared to two sets of *in-vivo* damping sequences. The sequences have been computed by temporal averaging of the estimates and a normalizing with the maximum dilation. No filtering has been performed on the estimates to eliminate wrong estimates and thereby smoothen the motion estimates. Therefore the *in-vivo* data contain some variations in the damping sequence, which is not expected to be due to tissue properties. One damping estimate has been left out in the plot, since it originates from an outlier, which is significantly wrong.

To match the fast rise and the slower decay of the temporal dilation, the following model for the dilation has been chosen:

$$d(t) = a_p \sin(\pi t / T_{pulse}) \exp(-b_p t / T_{pulse}) \quad 0 \leq t \leq T_{pulse}, \tag{4.3}$$

where a_p is the amplitude, and b_p is the decay term, which is dependent on the heartbeat frequency. The variable T_{pulse} represents the period of pulsation. In Fig. 4.7(a) the temporal model for dilation due to pulsation is shown. The parameters T_{pulse} and b_p are equal to 1 s and 4.7, respectively. This model matches the *in-vivo* dilation estimates obtained by Bonnefous [30], where a maximum radial dilation of 0.35 mm was estimated. Assuming a vessel radius of 4 mm for the carotid artery, a lumen increase of 20% will occur at the time of maximum dilation.

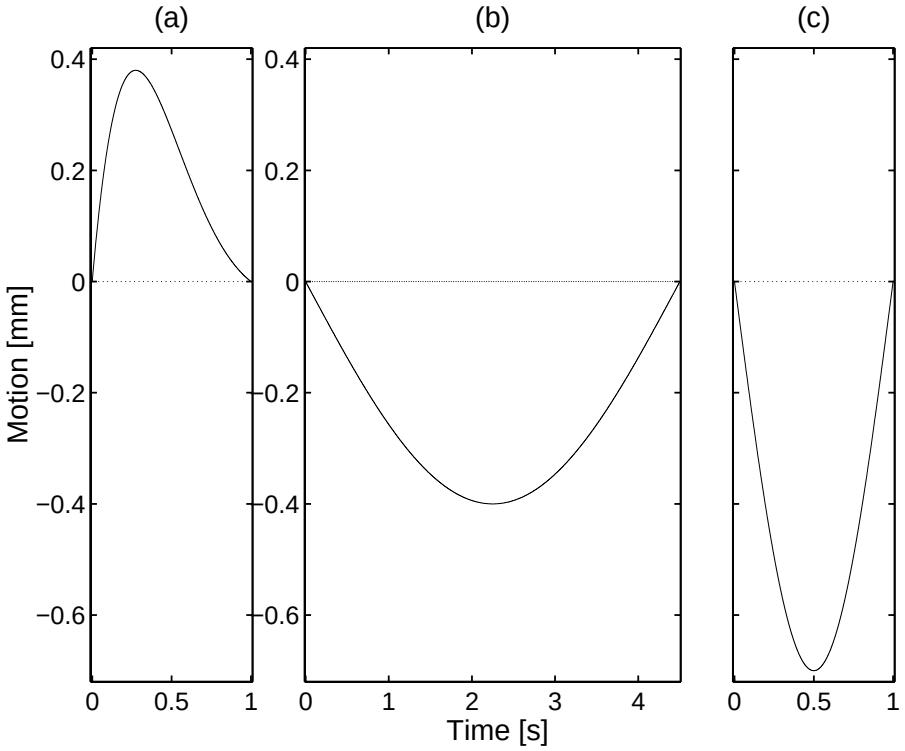

Figure 4.7: Temporal models of motion due to pulsation (a), breathing (b), and heartbeat (c). Frequency of breath: 13 breaths/min. Frequency of pulsation and heartbeat: 60 bpm.

4.4.2 Breathing

Tissue motion from breathing is the only motion contributor, which can be eliminated by asking the subject to hold their breath. In long examination sessions this cannot be done by the subject, so RF-data with motion due to breathing can occur. Therefore the ability to simulate this should be investigated. In abdominal recordings the lung is positioned deeper than the scanned region. The tissue will be pushed towards the transducer as the lungs expand. The absolute level of motion increases as a function of (radial) depth. The exact motion direction of the lung wall (relative to the transducer axis) is unknown, so the motion is modeled as acting along the radial axis - corresponding to what is seen in the motion plot. Motion due to breathing is a much slower process than pulsation due to the respiration frequency. Breathing can be modeled as a product of a time and a damping dependent function, when they are assumed independent. The temporal motion model $m_b(t)$ is shown in Fig. 4.7(b) with a respiration frequency of 0.22 breaths/s. The mathematical relation is given by:

$$m_b(t) = -a_b \sin(\pi t / T_{breath}) \quad 0 \leq t \leq T_{breath}, \tag{4.4}$$

where a_b is the amplitude, and T_{breath} is the respiration period. The model has a negative sign, since the motion is acting in the opposite direction of the positive motion axis (z-axis). The damping function α_b is modeled as a linear function of depth (decreasing damping for increasing depth):

$$\alpha_b(z) = \begin{cases} 0 & z \leq z_b \\ k_b(z - z_b) & z_b < z < z_{max}, \\ 1 & z = z_{max} \end{cases} \tag{4.5}$$

where k_b determines the rate of decay, z_b is the depth, where no motion due to the breathing can be seen, and z_{max} is the distance to the motion inducer.

4.4.3 Heartbeat

The contractions of the heart induce motion in the surrounding tissue. A sequence of motion due to the heart beating is shown in Fig. 4.5. It contains the same features as for breathing in terms of position of motion generator and damping, but the repetition frequency is higher - on average 60 bpm. The linear model for the damping is used (see (4.6)). The model has been compared to an *in-vivo* data sequence, and the plot in Fig. 4.6(c) shows a good agreement. Since heart contractions are the driving force of the blood pulsation in the arteries, one could suspect that the temporal model for tissue motion induced by the heart would be the same as the model for pulsation. Investigations of motion plots of *in-vivo* and simulated data have shown that this is not the case. It is presumed to be due to the more complex motion pattern (translation as well as rotation) of the heart. The motion induced on the surrounding tissue is still time-varying, but more equally divided throughout the heartbeat cycle. The temporal model for the tissue motion is plotted in Fig. 4.7(c). It is assumed that the motion is acting in the radial direction. The sequence matches the temporal model for breathing, if T_{breath} is replaced with T_{heart} - the period for one heartbeat (see (4.6)).

$$\begin{aligned} m_h(t) &= -a_h \sin(\pi t / T_{heart}) \quad 0 \le t \le T_{heart} \\ \alpha_h(z) &= \begin{cases} 0 & z \le z_h \\ k_h(z - z_h) & z_h < z < z_{max} \\ 1 & z = z_{max} \end{cases} \end{aligned} \tag{4.6}$$

All the models developed contain the same features regarding time and depth dependence, but the repetition time, amplitude of motion, and damping vary with scan site and for the individual motion types. Additionally, these model parameters vary among individuals.

4.5 Simulation of motion

Simulations have been performed to verify the developed models. Simulations for the carotid artery (C1) and the hepatic vein (HV3) have been performed. The transducer was modeled as a 3.2 MHz convex, elevation focused array with 58 elements. A focusing and apodization scheme matching the used scan probe for the *in-vivo* measurements has been incorporated. The point scatterers were given amplitude properties of tissue or blood. Some scatterers were positioned explicitly to resemble the vessel wall. Any angle orientation of the vessel relative to the transducer can be chosen. In the following equations this angle dependence is left out to make them easier to read. A mathematical description of the motion $\vec{m}$ for each scatterer is:

$$\vec{m}_j(iT_{prf}) = \vec{m}_j((i-1)T_{prf}) + T_{prf}\vec{v}_j(iT_{prf}, j), \tag{4.7}$$

where $\vec{m}_j$ is the position of scatterer j in a 3D coordinate system, i is the discrete time index, T_{prf} is the time between pulse emissions, and $\vec{v}_j$ is the velocity of scatterer j. It is assumed that accelerations occur, but the level of acceleration multiplied by T_{prf} is small compared to the magnitude of the velocity. The velocity profiles for blood and tissue motion can therefore be assumed continuous within the time interval T_{prf}. Motion due to pulsation results in a motion of the scatterers outside the vessel. All scatterers inside and outside of the vessel are affected, when motion due to breathing and the beating of the heart is present. In the simulation all scatterers are assigned an initial position $\vec{m}_j(0)$. This is used to compute the scatterers positions at any given time by adding the contributions from the individual motions. As an example, the mathematical relation for the computation of the position for scatterers outside the vessel is:

$$\vec{m}_j(iT_{prf}) = \vec{m}_j(0) + \vec{d}(iT_{prf})\vec{\alpha}_p(r) + \vec{m}_h(iT_{prf})\vec{\alpha}_h(z) + \vec{m}_b(iT_{prf})\vec{\alpha}_b(z), \tag{4.8}$$

where each product term is a vector multiplication. The motion of the blood scatterers for the carotid artery is determined by Womersley's pulsatile flow model (see Chapter 3). RF-data for 5 seconds have been

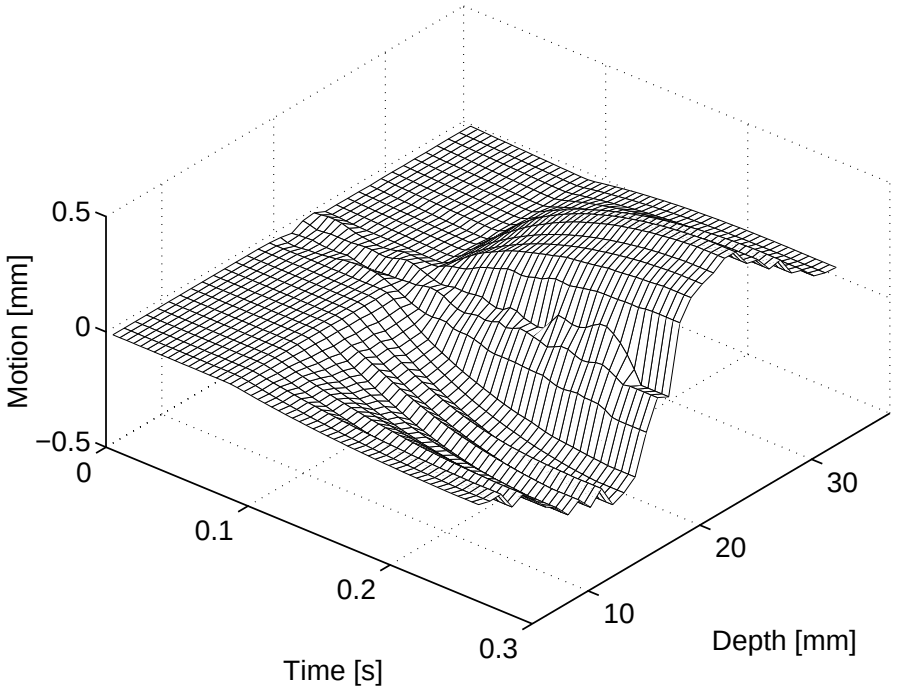

Figure 4.8: Estimates of motion from simulated data mainly due to pulsation at the carotid artery. Pulse rate: 60 bpm.

simulated to generate data containing the full effect of pulsation, heartbeat, and breathing. In Fig. 4.8 an example of simulated dilation for the carotid artery is shown. Motion from pulsation and breathing motion has been incorporated. The damping was modeled by the cosine damping function (4.2) with R_1 equal to 20 mm. The scan angle was 90^o. The breathing motion is at this point in the simulation not very dominant. Comparison with Fig. 4.3 reveals a good agreement between the two motions.

For the hepatic vein the blood motion was modeled as a steady flow superimposed on a time varying flow modeled by Womersley flow model. The diameter was set to 0.6 cm. Simulations for 1 second have been performed, since only motion due to the heartbeat is present. The damping function in (4.6) was used. The result of simulation is plotted in Fig. 4.9, and the comparable measured data are plotted in Fig. 4.5. Comparison reveals a good agreement between the motions. Simulation of realistic data for the abdominal region is thus possible.

The amplitude levels of the individual motion contributors are variables that change relative to scan site, respiration and pulsation level, and the subject. These can be set in the simulation model. In the plot of *in-vivo* motion at the carotid artery some motion is present within the vessel (center of vessel at depth equal to 19 mm) - probably because the scan angle was not exactly 90^o.

In Fig. 4.10 a comparison of *in-vivo* and simulated RF-data as a function of time is shown. The insonation angle is 45^o. The tissue motion is seen as the slow varying signal component, and on top of that is the blood signal. Again the simulated and *in-vivo* data agree qualitatively. The simulated RF-data thereby contain both the tissue and blood motion present in *in-vivo* RF-data.

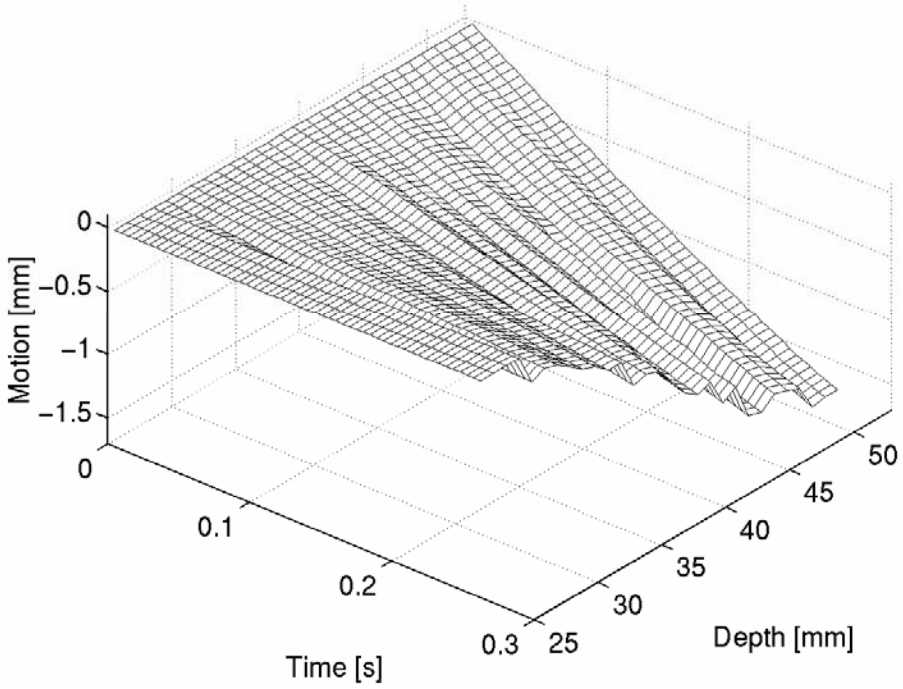

Figure 4.9: Motion estimates based on simulated data resembling the HV3 recordings. Pulse rate: 60 bpm.

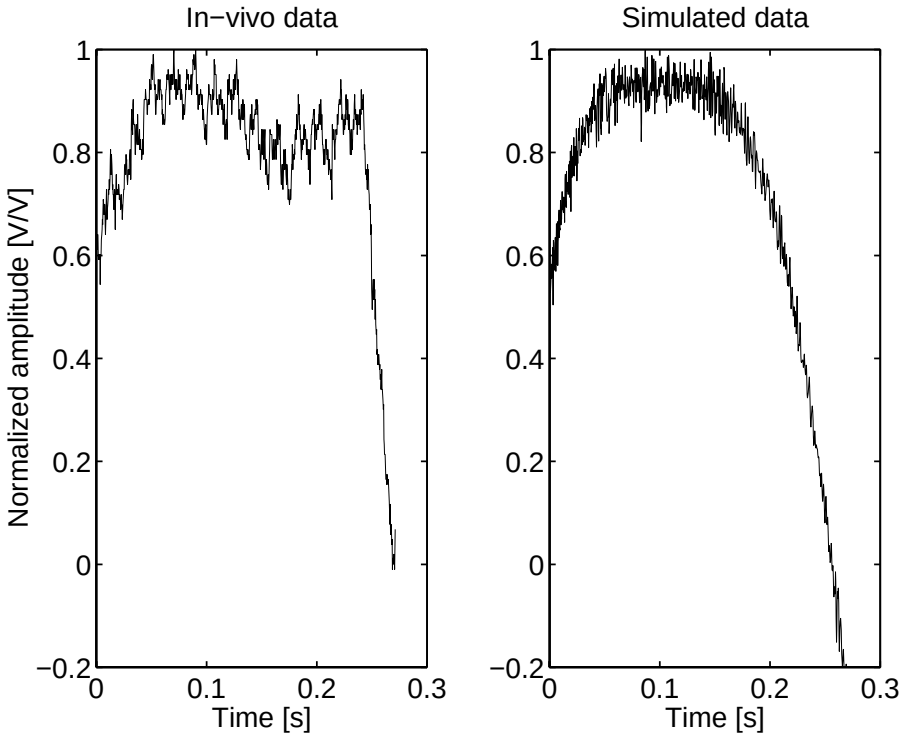

Figure 4.10: A measured (left) and simulated (right) RF-signal at the carotid vessel wall at one depth as a function of time.

4.6 Summary

Based on the above investigation it can be concluded that tissue motion is present, and should be incorporated into the simulation to create realistic simulated data. The motions induced by breathing, the beating of the heart, and pulsation at the carotid artery and in the abdominal region have been investigated. The motion takes values in the millimeters per second range. It is possible to model tissue motion and incorporate it into a simulation program. The models contain two terms. The first determines the temporal course of the motion next to the inducer, which is related to the motion pattern of the moving organ. The motion gets damped in space, and the second term defines the course of the damping. The simulated RF-data agree well with *in-vivo* RF-data. This makes the simulation a realistic and powerful tool in optimizing ultrasound echo-canceling filters and blood velocity estimators. The repetition frequency of the individual motions and model amplitudes vary among subjects and scan sites. Therefore choices for these parameters have to be made and set in every simulation.

4.7 Acknowledgment

MD Søren Torp-Pedersen, Gentofte University Hospital, Denmark, and Ph.D. Paul Stetson are acknowledged for helping out with acquiring the data.

Chapter 5

Pre-processing of RF-data

A clinical examination with ultrasound aims at extracting information of diagnostic value. The acquired RF-signals must be processed to extract the valuable information present. The processing goes through a number of steps, and the steps related to blood velocity estimation are discussed in this and the subsequent chapters. The steps can be divided into three parts: 1) the pre-processing of the acquired signals, 2) the actual estimation of the blood velocities, and 3) the post-processing of the estimates, which must be performed prior to displaying the computed estimates. This chapter discusses the pre-processing step, and the estimation and post-processing are discussed in Chapter 6 and 7, respectively.

The acquired signals are contaminated with noise, so a de-noising of the signals must be performed at first. De-noising with a matched filter is discussed in Section 5.1.

Blood velocity estimation aims at determining the velocity of the blood only. The acquired signals contain the responses from both blood and the tissue structures. The blood velocity estimation is complicated by the presence of the tissue responses, and it is desirable to remove them prior to performing the actual blood velocity estimation. Filters have been derived for this purpose, and they are usually referred to as clutter and echo-canceling filters. Two of these filters are introduced in Section 5.2.

A complete elimination of the noise and the tissue components is not possible, and non-zero velocity estimates are computed outside the vessels. Only the blood velocities should be displayed in the CFM image. By some means it must be determined, which segments of the RF-signals that carry blood velocity information. In Section 5.3 three algorithms are introduced, which perform this discrimination. Two of the discriminators represent new approaches.

5.1 Minimization of SNR with matched filter

As the recorded RF-signals are contaminated with noise (electrical and acoustical), pre-processing is performed to minimize the noise content prior to applying any other algorithms. The process of minimizing the noise content will be referred to as de-noising. In medical ultrasound the de-noising is often performed with the matched filter $h_d(t)$ [33], [34], which is the time reversed of the signal of interest $s(t)$:

$$h_d(t) = s(T_0 - t), \tag{5.1}$$

where T_0 is the temporal length of $s(t)$. In this case the signal of interest is the emitted signal. In reality only the excitation signal is known exact, whereas the impulse response of the transducer is less well defined. An idea of the transducers impulse response can be obtained by testing the transducer. The matched filter

is then the time reversed of the convolution of the excitation pulse $e(t)$ with the impulse response in both transmit ($h_t(t)$) and receive ($h_r(t)$):

$$\begin{aligned} s(t) &= h_r(t) * (h_t(t) * e(t)) \\ h_d(t) &= s(T_0 - t). \end{aligned} \tag{5.2}$$

The matched filter matches the signal bandwidth of the signal. When applied, the filter performs a bandpass filtering determined by the original, emitted signal. As the noise also has components within the pass band, only part of the noise is removed. The effect of attenuation and thereby alteration of the emitted signal should be considered and incorporated, if the best performance of the filtering should be obtained at all temporal positions along the RF-signal. This aspect will not be considered in the following, and the filter defined above will be employed on the entire signal. This choice implies that the filtered signals will be somewhat more noisy than data filtered with the ”optimum” filter.

5.2 Echo-canceling filters

The acquired RF-signals consist of the interactions with the different tissue structures and blood. The sections of the RF-signals originating solely from the interaction with the tissue are of no interest in blood velocity estimation. When imaging small vessels, the diameter of the vessel is comparable to the axial extent of the pulse, so a major part of the signal carrying blood velocity information is overlaid by the high amplitude response from the surrounding tissue and vessel wall. This complicates the blood velocity estimation, and it is therefore desirable to remove the tissue components prior to performing the estimation. Several clutter and echo-canceling filters have been developed for removing the tissue components [3], [35], [36], [37] [38]. A thorough discussion and evaluation of these filters are out of the scope of this project. Two echo-canceling filters will be introduced and commented on in the following. Their influence on the blood velocity estimation on a synthetic data set will be evaluated in Chapter 6.

5.2.1 Stationary echo-canceling with high-pass filters

If the tissue surrounding the blood vessels is assumed stationary, the tissue scatterers will be located at the same spatial position every time a pulse interacts with them. The part of the RF-signal representing the interaction with the tissue scatterers will be identical in consecutively recorded RF-signals, when no noise is present. This assumption is the basis for the high-pass echo-canceling filters, which act on the samples from consecutive RF-lines at the same temporal location relative to the pulse emission. The frequency spectrum of a constant signal is the DC value. Removal of the stationary tissue therefore requires a high-pass (HP) filter that filters out the DC value and lets all other frequencies pass unchanged. As the blood is moving, the frequency spectrum lies at non-zero frequencies and will not be removed by this filter. In Fig. 5.1(a) a sketch of the spectra is plotted. In reality the tissue is non-stationary due to motion induced by the pulsating vessels, the heart, and from breathing (see Chapter 4). The presence of noise adds a random signal to the responses from the blood and tissue. The values of the samples in consecutive RF-lines vary, which correspond to non-zero frequency components in the tissue spectrum (see Fig. 5.1(b)). The tissue and blood spectra now overlap, which complicates the separation process. No ideal solution exists. If the filter is designed to remove the tissue completely, the low blood frequency components are also removed. Estimation of the low blood velocities close to the vessel wall is then not possible. If the filter is designed to preserve all blood information, the tissue components will not be removed completely, and non-zero velocities will be estimated both inside and outside the vessel.

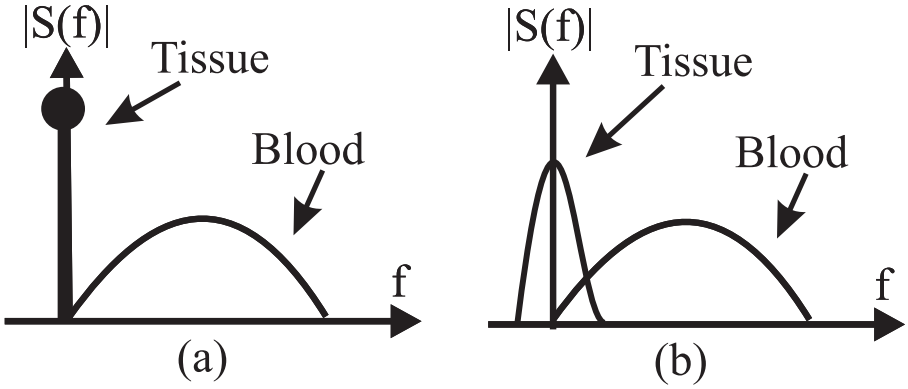

Figure 5.1: Frequency spectrum of tissue and blood components, when the tissue is not moving (a) and moving (b).

The general transfer function for an N^{th} order high-pass echo-canceling filter is [3]:

$$\begin{aligned} H_{HP}(f,l) &= \sum_{i=1}^{N} a_{i,l} \exp(-j2\pi(i-l)f/f_{sh}) \\ f_{sh} &= \frac{c}{2v_z} f_{prf}, \end{aligned} \tag{5.3}$$

where the $a_{i,l}$'s denote the filter coefficients, l specifies the line currently being filtered, and f_{prf} is the pulse repetition frequency. N consecutive RF-lines are employed in the filtering. A total of N_l consecutive RF-lines have been acquired, which put an upper limit to N: $N \leq N_l$. The f_{sh} term is related to the axial velocity, v_z, of the scatterers and determines the spectrum properties of the HP-filter. Employment of a finite number of lines result in a HP-filter, which has a transition band of finite extent between stop and pass band. The width of the transition band decreases as the number of lines increase. With this in mind as many lines as possible should be used in the filtering. The presence of the transition band results in alteration of the lower frequencies in the spectrum, which represent low velocities. The low frequency tissue motion gets filtered and partly removed, which is desirable. Unfortunately the blood close to the vessel wall also moves at low velocities, and these signals get altered. Valuable information is removed by the filter, and the accuracy on the subsequent estimate decreases due to the employed HP-filter. The HP-filter uses samples from N lines to compute one filtered sample. The number of lines available after filtering are therefore $N_l - N$, which limits the amount of data available for the blood velocity estimation. A trade off between the performance of the HP-filter and the need for several lines for blood velocity estimation exists.

The simplest HP-filter is a 2^{nd} order filter, where a mere subtraction of two samples in two consecutive lines is performed:

$$r_{echo,cfm}(n,l) = \frac{1}{2}(r_{cfm}(n,l) - r_{cfm}(n,l-1)). \tag{5.4}$$

The variable n represents the temporal location (in number of samples), and $r_{echo,cfm}$ is the echo-canceled output of the filter. Only one line is lost in the filtering, so $N_l - 1$ lines are available for the subsequent estimation. A 2^{nd} order HP-filter will be employed and evaluated, when different blood velocity estimators are evaluated in Chapter 6. The simple filter is easy to implement and employ, but a wide transition band is obtained. The acquired signals consist of the response from the blood, the tissue structures, and additive noise. At low velocities the response from blood and tissue will be almost identical in consecutive acquisitions, so the subtraction results in an almost complete cancellation of the response. The filtering causes a decrease in amplitude of the response. The random noise component will still be present, and the signal to noise ratio (SNR) decreases in the resulting signal after filtering [3]. The limitations of the HP-filter laid ground for development of more advanced filters [36], [37] [38], and one of them [35] will be introduced in the following.

5.2.2 Echo-canceling with regression line filter

The drawbacks of the HP-filter with respect to the loss of valuable RF-lines and the course of the transition phase between stop and pass band were the driving force for Hoeks et al. [35] to develop a new echo-canceling filter. The aim was to develop a filter, where no RF-lines were lost, and the transition band was narrowed.

Scatterers (blood or tissue) moving at low velocities will move little between two RF-line acquisitions. Within the time frame of the acquisition of a limited set of RF-lines (usually few milliseconds) the movement will also be small. Plotting the samples at a given temporal location as a function of line number will reveal that the movement approaches a straight line. Stationary tissue will give a flat line with a zero slope. The low velocity components can therefore be removed by fitting a regression line, y, to the set of samples. The filtering is carried out by subtracting the regression line from the samples. The deviations from the line remain and will be passed on to the subsequent velocity estimation. The equation for the regression line is:

$$\begin{aligned} y(t,l) &= m_t + l \cdot s_t \\ l &= -(N_l-1)/2, \ldots, 0, \ldots, (N_l-1)/2 \\ & \quad N_l \text{ odd}, \end{aligned} \tag{5.5}$$

where m_t expresses the mean of the samples at the temporal location t being investigated, and s_t determines the slope. An odd number of lines are employed, and the numbering of the lines go from $-(N_l-1)/2$ to $(N_l-1)/2$ rather than from 1 to N_l. Several approaches can be employed to determine the slope but one should keep the aim in mind: the low velocities should be suppressed, and the high velocities should pass unaltered. This can be achieved by requiring that the sum of deviations for a negative line index equals the sum of the deviations for a positive line index [35]:

$$\sum_{l=1}^{(N_l-1)/2} (r_{cfm}(t,-l) - (m_t - s_t \cdot l)) = \sum_{l=1}^{(N_l-1)/2} (r_{cfm}(t,l) - (m_t + s_t \cdot l)) \tag{5.6}$$

The relation determining the slope becomes:

$$s_t = 4 \sum_{l=1}^{(N_l-1)/2} (r_{cfm}(t,l) - r_{cfm}(t,-l))/(N_l^2-1) \tag{5.7}$$

The output of the echo-canceling filter is $r_{echo,cfm}(n,l) = r_{cfm}(n,l) - y(n,l)$, where n indicates the temporal location in number of samples.

A regression line is determined and applied for each temporal location. The filtering can only be performed after all N_l RF-lines have been acquired, so storage space must be set aside for storing the RF-lines. The performance and influence of the regression line, echo-canceling filter on blood velocity estimation will be evaluated in Chapter 6.

5.3 Display algorithms

In CFM-mode the blood velocity estimates are overlaid onto the B-mode image. Motion is present within the vessels as well as in the surrounding tissue, so non-zero velocity estimates will be computed in both regions. The presence of noise (measured as well as filter generated) adds a random signal variation on top of the RF-signals, so the responses from non-moving tissue structures will not be identical in consecutive RF-lines. Non-zero velocity estimates will be computed in these regions too. Prior to displaying the computed estimates a discrimination algorithm is needed to determine, which estimates should be displayed. If the

discrimination is performed prior to the estimation, it can be determined, which segments that carry blood velocity information and therefore should be processed by the blood velocity estimator. This approach will lower the computational load of the blood velocity estimation. Whether the discrimination is performed before or after the velocity estimation, an algorithm must be developed to perform the discrimination.

A comparison of the values of the velocity estimates within and outside the vessels reveals that the estimates cannot be discriminated by means of their amplitude. A wide and overlapping range of velocities are computed within as well as outside the vessel. The discriminator must employ other features to perform the discrimination. In the following 3 discriminators will be introduced and evaluated. The last two represent new approaches. Ideally the discriminator should be applicable in all scan situations with respect to tissue types, SNR, and vessel diameter. In this study the SNR is defined relative to the signal level in the section of the RF-signals, which only contain responses from the blood. Only preliminary investigations have been performed, so all the scan related issues have not been addressed. Therefore this study is only to be seen as indicative. Further investigations must be performed before any finite conclusions can be made, but hopefully the discussion can inspire future work.

The discriminators use information extractable from the acquired and de-noised RF-signals. This study focuses at the amplitude and energy variations in the RF-signals, along with the signal variations between consecutive RF-lines. Each RF-line is divided into a set of segments, which consist of a set of consecutive samples. The number of segments are equivalent to the number of velocity estimates that can be displayed for each line. The discriminator determines, which segments that carry blood velocity information and non-blood velocity information, respectively. In the following these two segment types will be referred to as BV and NBV segments. A segment is assigned as a BV segment if more than 66 % of the samples lie within the vessel. The discrimination process could also be termed a classification, as the segments are classified as either BV or NBV segments. Both terms will be used in the following.

5.3.1 Amplitude discriminator

The first discriminator to be introduced and evaluated is the amplitude discriminator. It is a very simple discriminator and has been used in scanners. As discussed in Chapter 2 the scattering from tissue is much stronger than from the blood. When imaging larger vessels (*e.g.* the carotid artery), this shows up as amplitude differences in the recorded RF-signals. It is not the amplitude at any temporal location in the RF-signal, which is considered, but the peak amplitude levels over a temporal range equaling a couple of wavelengths. An example is plotted in Fig. 5.2(a). The amplitude difference also shows up in the envelope detected signal as shown in Fig. 5.2(b). This property makes it possible to develope a discriminator. The amplitude level in the regions, which relate to the interactions with tissue, is higher, than the amplitude level in the region, which represents the interactions with the blood alone. A high amplitude signal originating from the interaction with tissue and vessel wall overlaps the blood signal just inside the vessel. The amplitude property is therefore not present here. The amplitude differences in the envelope detected data are used to discriminate BV and NBV segments in RF-signals obtained from larger vessels. A discrimination threshold is determined, and a decision is made by a mere comparison between the threshold and the amplitude in the segment. The segment amplitude is computed as the average amplitude over the samples in the segment and the number of acquired lines:

$$A(i_{seg}) = \frac{1}{\sigma}\frac{1}{N_s N_l}\sum_{l=1}^{N_l}\sum_{k=1}^{N_s} r_{env,cfm}(l, k + i_{seg}N_s), \tag{5.8}$$

where i_{seg} represents the segment number, and N_s is the number of samples in the segment. The normalization factor $(N_s N_l)^{-1}$ ensures that $A(i_{seg})$ is independent of the sampling frequency and the number of acquired CFM lines. The normalization factor σ is introduced to make the feature value independent of the representation of amplitude (*e.g.* mV or quantized levels according to the number of bits used). The

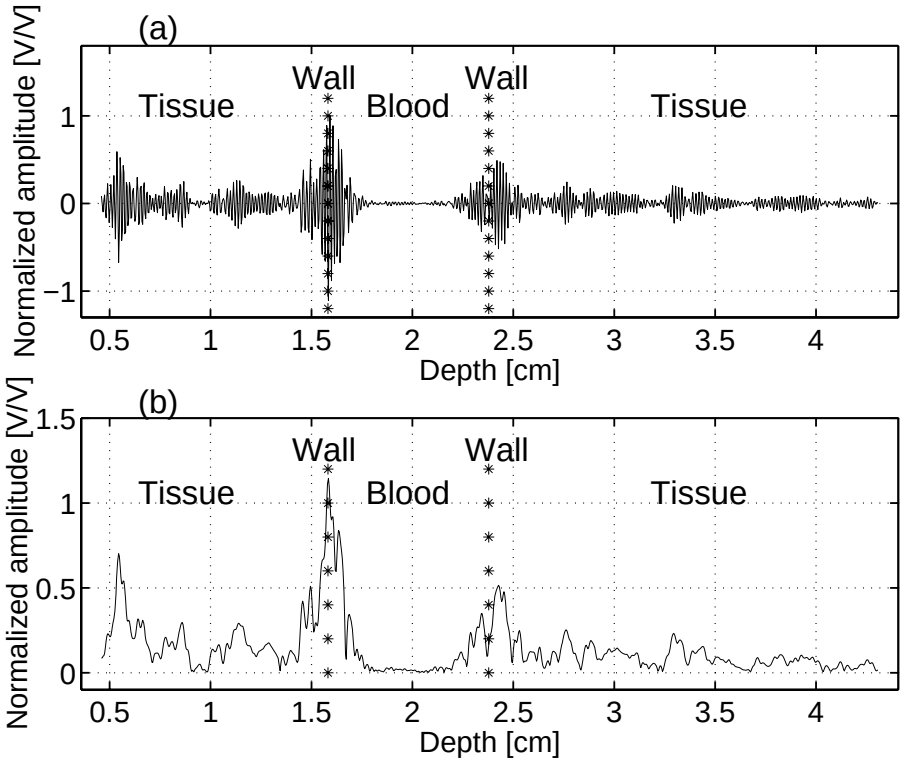

Figure 5.2: Example of an RF-line (a) and the envelope detected signal (b) from the carotid artery. The vertical lines indicate the location of the anterior and posterior vessel wall.

constant is computed as the average value of the standard deviation in a set of acquired RF-signals. The discrimination is performed on the de-noised RF-signals acquired for CFM-mode imaging. Ideally a short pulse should be emitted to minimize the overlap between the tissue and the blood signals at the vessel wall, which makes the discrimination difficult at this point.

The threshold varies as a function of depth and center frequency, when no compensation for the attenuation is performed. A continuous or discrete implementation of the threshold function can be used. The latter allows for a simple implementation with a short lookup table and will be employed in the following. The amplitude decay over distance and center frequency is assumed to be an exponential decaying function, and the discrete threshold function is modeled as a step function.

The performance of the amplitude discriminator has been evaluated on a set of simulated data, which resemble RF-data from the carotid artery. The simulation program Field II [26], [27] is used. A focusing and apodization scheme matching the setup of a B-K Medical 3535 scanner has been employed. The transducer is modeled as a linear array. Three cardiac cycles were simulated. Tissue motion due to pulsation along with blood motion were included (see Chapter 4). Table 5.1 lists the choices of simulation parameters. Eight RF-lines were acquired at each lateral position. RF-data were simulated for the full lateral imaging range of the transducer (3.6 cm) to cover a wide range of different RF-signals (*e.g.* location of vessel, location of vessel close to/far from/at the transmit focus). This gives a frame rate of 4 frames/s. The number of segments extractable from each line are 61, and a total of 97 imaging lines are present in each of the 13 2D images generated.

The threshold value changes every 1.2 cm (equal to 38 wavelengths). The step function, which gives the best classification, for the given data set was determined by generating a range of exponential functions, converting them into a step function, performing the discrimination, and then evaluating the performance. The number of correctly classified segments over all frames relative to the total number of segments are

Parameter	Value
Transducer center frequency	5.0 MHz
No. of elements	128
Pulse length	6 cycles
Geometric focus	17 mm
Pulse repetition frequency	4 kHz
Sampling frequency	40 MHz
Radius of vessel	3 mm
Angle between vessel and transducer	35^o

Table 5.1: Choice of parameters for the simulated data used in the performance evaluation of the amplitude discriminator.

used as an objective measure of performance. The overall and class specific performance are of interest, so the following three performance values are computed:

- the number of correctly classified segments in total relative to the total number of segments: N_T (independent of classes),
- the number of correctly classified BV segments relative to the total number of BV segments: N_{BV}, and
- the number of correctly classified NBV segments relative to the total number of NBV segments: N_{NBV}.

The values range from 0 to 1, and a high performance value is desirable. Before determining the threshold function, which gives the best performance, a discussion and definition of the expression ”best performance” is required. About 84 % of the segments in the employed data set are NBV segments. The value of N_T therefore mainly represents the performance on the NBV segments. The question arises, if it is reasonable to determine the discriminator from this value. Doing so implies that the NBV segments are considered a lot more important than the BV segments. It is of more concern to perform well on NBV segments than BV segments. In this case a discriminator could be chosen that performs perfect on NBV segments but does not perform at all on the BV segments. As the aim is to perform blood velocity estimation and subsequent visualization hereof, this result does not give the best performance. The performance on the two segment types - N_{BV} and N_{NBV} - should be used instead. Both values are normalized with the number of segments in the class, so the favoring of either of the classes is eliminated. This choice still leaves some unanswered questions about how to determine the discriminator though. It is likely that the maximum of N_{BV} and N_{NBV} do not occur simultaneously, so this criteria cannot be employed. Then one must ask: which segment type is more important to classify correct? What is the cost of making a wrong classification? The latter represents the issue of false positives (type 1 error) and true negatives (type 2 error) from statistics. A type 1 and 2 error represent the situations, where a true hypothesis is rejected, and a false hypothesis is accepted, respectively. In the discrimination process this resembles classifying the segments wrong. A BV segment is classified as an NBV segment, and vice versa. The issue then is: how does one determine, which is more important to classify correct? The answer to this is not simple and unambiguous. It is dependent on the aim of the scanning. This statement becomes more clear, when the following two scan situations are considered:

Situation 1
Upon a kidney transplant the blood flow conditions in the new organ are monitored. A lack of flow indicates that the body is rejecting the organ. Countermeasures must be taken. Ultrasound imaging is used to determine the flow conditions. Under these circumstances the cost of classifying a BV segment as an NBV

segment is high. The clinician will wrongly draw the conclusion that the kidney is rejected. Under these circumstances it is important to put emphasis on a high success rate on classifying the BV segments.

Situation 2
Increased flow in the breast tissue could be an indicator of breast cancer. The cost of showing flow, where there is no flow, is therefore high. The consequence could be a false diagnosis of breast cancer. In this situation the emphasis should be put on classifying as many NBV segments correctly as possible.

The expression "the best performance" is not unambiguous. The basis, which should be used to determine the threshold function for the discriminator, is therefore dependent on the situation. A set of solutions exist. The scanner must alternate between solutions as the aim of the scanning changes. Determination of the aim requires an input from the clinician, as it will be very complicated to make any automatic procedure to determine the anatomical location being scanned.

The goal of the discriminator is to classify as many BV and/or NBV segments correctly relative to the cost. The maximum of a weighted combination of N_{BV} and N_{NBV} is employed in this study to determine the discriminator, which gives the best performance:

$$\hat{\Upsilon} = \arg\max_{\Upsilon}(aN_{BV} + bN_{NBV}), \tag{5.9}$$

where a and b are the weights, and the following properties exist: $a+b=1$ and $(a,b) > 0$. The latter property is introduced to eliminate the discriminator that only works on BV or NBV segments. Υ represents the parameters in the exponential function. The weights determine the cost of making a wrong classification. A high value states that the cost is high, if a wrong decision is made with respect to this segment type. The discriminator, which gives the best performance, has been determined for three combinations of the weight values: $(a,b) = [(0.7,0.3);(0.5,0.5);(0.3,0.7)]$. The first and last combination could represent the kidney and breast cancer scenario, respectively. The influence of noise was determined by employing data sets, where the SNR was 0, 10, 20, and 30 dB. This gives a total of 12 combinations, and the discriminator has been determined for each combination. In Fig. 5.3(a) the normalized exponential function and the resulting discriminator (the step function) for the case of $(a,b) = (0.5,0.5)$ and a SNR of 10 dB are plotted. The normalization factor equals the maximum value of the exponential function. Fig. 5.3(b) shows the best discriminator and an example of the computed average amplitudes (see (5.8)) for an RF-line. Tables 5.2-5.4 list the values of N_{BV}, N_{NBV}, and N_T (in %) for the discriminators. The results show that the amplitude discriminator is stable to a variation in the SNR. The slight variations result in minor differences of the parameters in the exponential function, when (a,b) is equal to (0.3,0.7) and (0.5, 0.5). The performance values N_{BV}, N_{NBV}, and N_T vary according to the choice of weights and thereby the cost of drawing a wrong conclusion. The choice of discriminator to use varies according to the costs.

SNR (dB)							
0		10		20		30	
N_{NBV} / N_{BV}	N_T	N_{NBV} / N_{BV}	N_T	N_{NBV} / N_{BV}	N_T	N_{NBV} / N_{BV}	N_T
98.8 / 39.3	89	98.6 / 39.7	88.9	98.5 / 39.8	88.8	98.5 / 39.8	88.8

Table 5.2: Amplitude discriminator: Number of correctly classified segments (in %) for different SNRs, when the weights equal $(a,b) = (0.3,0.7)$.

Some general comments on the performance of the amplitude discriminator can be drawn from the tables. The N_{NBV} value is a factor of 1.8-2.5 higher than N_{BV}, so the discriminator works better at classifying the

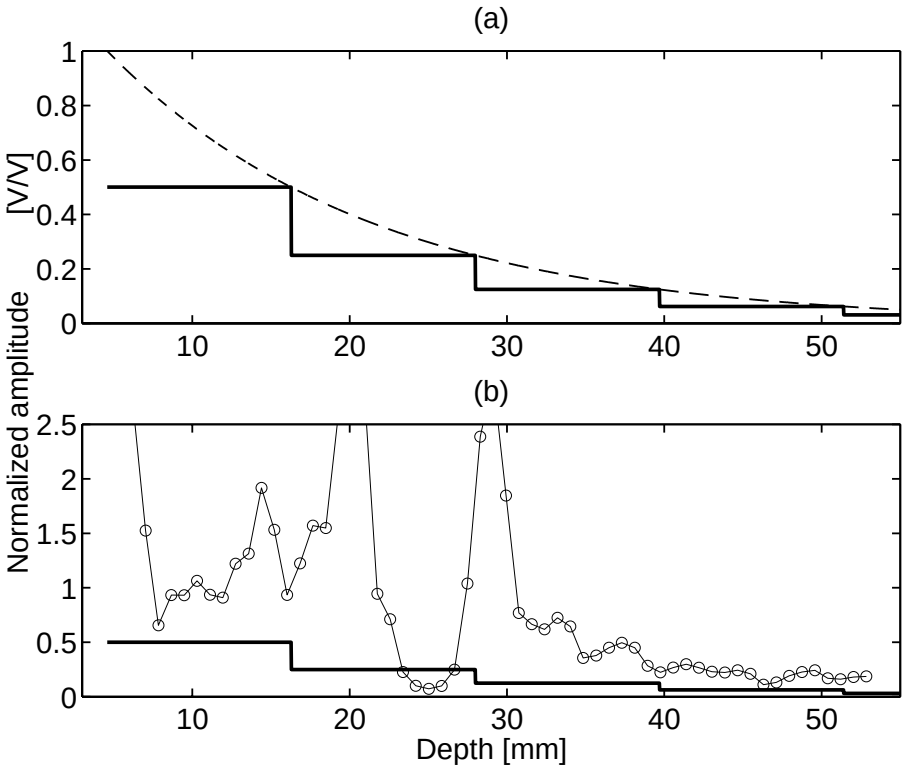

Figure 5.3: Plot of the best discriminator (a), and an example of the discrimination of an RF-line (b). The dashed line (- -) indicates the exponential function, the solid line (—) indicates the threshold function, and the circles (o) indicate the averaged amplitude values computed along an RF-line. The SNR is 10 dB, and the weights $(a, b) = (0.5, 0.5)$.

SNR (dB)							
0		10		20		30	
N_{NBV} / N_{BV}	N_T	N_{NBV} / N_{BV}	N_T	N_{NBV} / N_{BV}	N_T	N_{NBV} / N_{BV}	N_T
97.1 / 42.6	88.2	97.1 / 42.1	88.1	97 / 42.3	88	97 / 42.3	88

Table 5.3: Amplitude discriminator: Number of correctly classified segments (in %) for different SNRs, when the weights equal $(a,b) = (0.5, 0.5)$.

SNR (dB)							
0		10		20		30	
N_{NBV} / N_{BV}	N_T	N_{NBV} / N_{BV}	N_T	N_{NBV} / N_{BV}	N_T	N_{NBV} / N_{BV}	N_T
90.1 / 47.5	83.1	88.1 / 47.9	81.5	88 / 48	81.4	87.9 / 48	81.4

Table 5.4: Amplitude discriminator: Number of correctly classified segments (in %) for different SNRs, when the weights equal $(a,b) = (0.7, 0.3)$.

NBV segments than the BV segments. Less than half of the BV segments are classified correctly. In Fig. 5.4 the output of the discriminator is plotted along with the true discrimination (2 upper plots). Inspection of the blood velocity levels in this frame reveals that it contains the systolic phase of the cardiac cycle. The SNR is 10 dB, and (a,b) are (0.5,0.5). The images reveal that the majority of the misclassified BV segments are positioned next to the vessel wall, and the misclassification occurs at both the anterior and posterior vessel wall. The extent of the vessel is therefore always underestimated. This comes as no surprise due to the overlaid high amplitude tissue signal in this part of the RF-signal. The majority of the BV segments in the center of the vessel are classified correct. The misclassified NBV segments are spread out over the 2D image. Inspection reveals that quite a few of the misclassified NBV segments in one frame will show up again in the consecutive frame. This does not mean that the same misclassifications show up in all frames, but in two consecutive frames some systematism is present. The performance on a frame, which contains the diastolic phase, is plotted in the bottom two plots in Fig. 5.4. The performance on the BV segments is poorer, and it is especially pronounced in the part of the vessel in the lower right part of the image (far from the transducer). Hardly any of the BV segments are classified correct, which must be considered a major problem. The trends for the classification are similar, when the weights are $(0.7, 0.3)$ and $(0.3, 0.7)$. Of course the number of misclassified BV and NBV segments increase/decrease, as the focus of the discriminator - by means of the cost - is changed.

The amplitude discriminator described above is a simple method for discrimination of the segments. The performance on NBV segments is good but one cannot say the same for the BV segments. The overlapping, high amplitude response from the tissue and the vessel wall is the reason for the poor performance. The above investigations were carried out on simulated data resembling a large vessel. The level of overlap will increase as the size of the vessel decreases, and the amplitude differences - and thereby the basis for the discriminator - will be less profound or non-existing. It is therefore most likely that the number of correctly classified BV segments will decrease as the diameter of the vessel decreases.

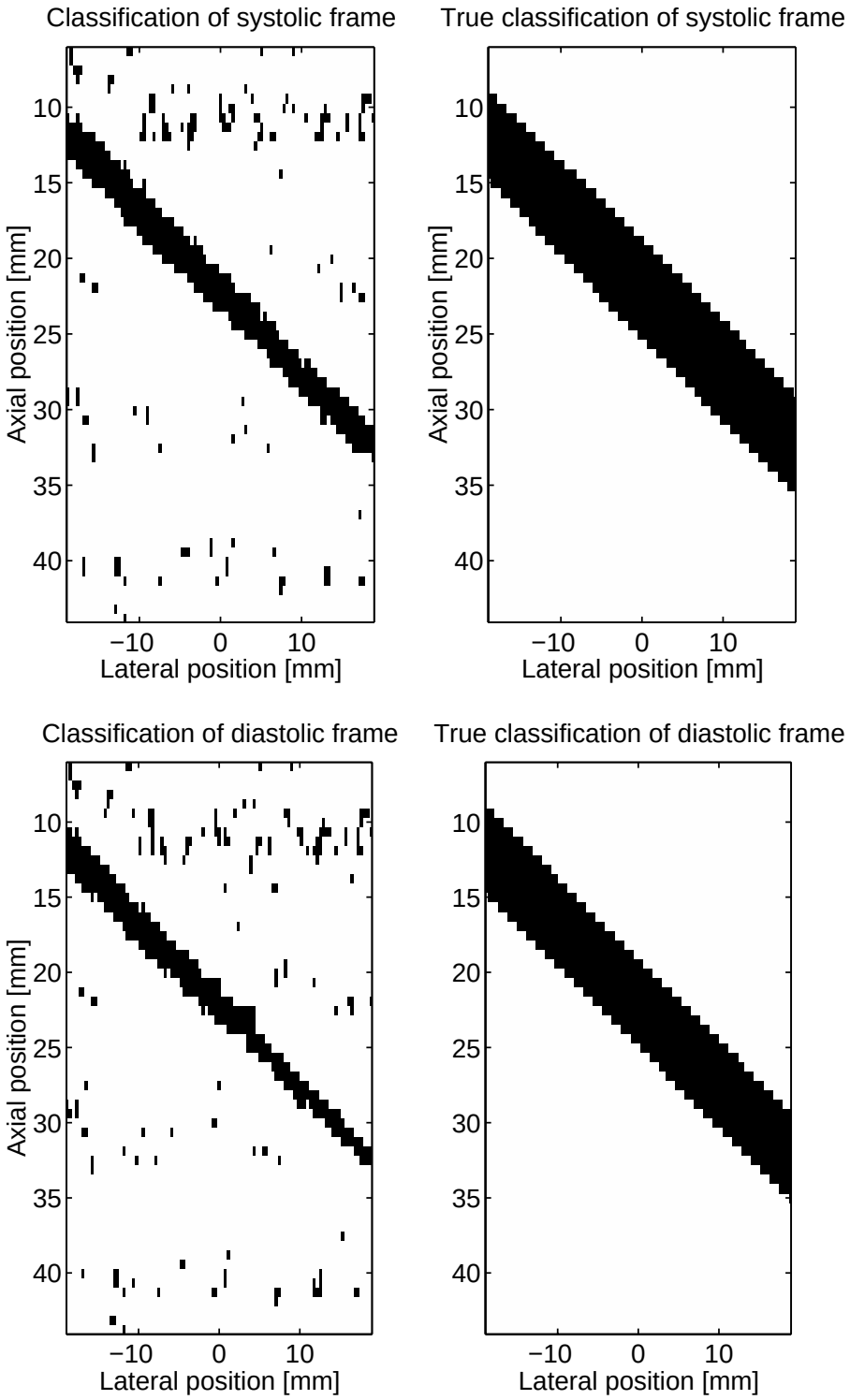

Figure 5.4: Performance of the amplitude discriminator on systolic frame (2 upper plots) and diastolic frame (2 lower plots), when $(a, b) = (0.5, 0.5)$, and the SNR is 10 dB. Black and white indicate BV and NBV segments, respectively.

5.3.2 Statistical discriminator

The amplitude discriminator only employs one feature of the signals, and it performs a mere comparison of the amplitude level with a threshold. Other approaches, which make use of more advanced algorithms and include more features to discriminate, should be developed. In the following a statistical discriminator will be considered and evaluated.

Features of RF-signals

Discriminators based on maximum likelihood statistics are of interest, if one can determine a set of features that makes it possible to distinguish the different segment types. A statistical discriminator can be obtained, if estimates of the probability density functions (PDFs) of the feature values for both the BV and NBV segments can be computed. The estimates can be obtained through a histogram analysis. In the following the PDFs for the BV and NBV segments will be denoted as $p_{f,BV}(X_f)$ and $p_{f,NBV}(X_f)$, respectively. The feature number is indicated with f ($f \in [1,..,F]$), and X_f is the feature value of the segment under investigation. A decision is made by choosing the segment type that is most likely. In statistics this can be determined by computing the joint probability densities:

$$\begin{aligned} p_{BV} &= p_{1,BV}(X_1) \cdot p_{2,BV}(X_2) \cdot p_{3,BV}(X_3) \cdot ... \cdot p_{F,BV}(X_F) \\ p_{NBV} &= p_{1,NBV}(X_1) \cdot p_{2,NBV}(X_2) \cdot p_{3,NBV}(X_3) \cdot ... \cdot p_{F,NBV}(X_F), \end{aligned} \tag{5.10}$$

where p_{BV} and p_{NBV} are the joint probability densities for the BV and NBV segments, respectively. This definition assumes that the individual features are independent. This is not the case for the features derived in this study, but the approach is used to ease the implementation with respect to storing the PDFs. The maximum value of the two joint probability densities determines the type of the segment. Investigation into this area has been initiated.

Feature 1

The basic assumption for the amplitude discriminator is that the distribution of amplitudes are different for the BV and NBV segments. The amplitude differences can also be expressed as a difference in the energy content in the segments. This measure is determined from the acquired RF-signals (no envelope detection performed). The first feature (feature 1 - F_1) to be used in the statistical discriminator is computed as:

$$F_1(i_{seg}) = \frac{1}{\sigma} \sum_{l=1}^{N_l} \sum_{k=1}^{N_s} (r_{cfm}(l, k + i_{seg} N_s))^2. \tag{5.11}$$

Again a normalization with σ is performed to make the feature independent on signal levels and representation. Normalization with the number of lines and samples has been left out here, as it merely performs a scaling of the values. These normalization factors will also be left out in the following. It should be included though in an implementation to make the method invariant of the sampling frequency and the number of lines.

Due to attenuation the energy level decreases as a function of depth and center frequency. This makes the probability density function dependent on the depth, and a set of density functions (as look-up tables) for each feature are required. This complicates the situation, and it has been decided to apply TGC compensation prior to computing the feature value to compensate for the attenuation. Two probability densities are determined and employed for each feature (one for the BV and the NBV segments, respectively).

Feature 1 is only valid for larger vessels, where the level of overlap between tissue and blood responses is small.

Feature 2

The energy content in the segments after echo-canceling is also worth considering as a feature. The energy content in the echo-canceled NBV segments is expected to be smaller than the same measure for the BV segments. A large portion of the tissue components has been removed or dampened a lot. The resulting signals will contain high amplitude samples mostly in the regions carrying blood velocity information. The probability density functions for the BV and the NBV segments will overlap to some extent due to the influence from noise, the moving tissue structures, and the characteristics of the echo-canceling filter. The level of overlap determines the suitability of this feature in the discrimination process. Feature 2 (F_2) is defined as:

$$F_2(i_{seg}) = \frac{1}{\sigma} \sum_{l=1}^{N_l-1} \sum_{k=1}^{N_s} (r_{echo,cfm}(l, k + i_{seg}N_s))^2. \tag{5.12}$$

At this point it should be noted that the echo-canceling in this study of the discriminators has been performed with the 2^{nd} order HP-filter discussed in Section 5.2.1 only. A major part of the tissue response, which is overlaid the blood response in smaller vessels, will be removed by the echo-canceling filter. It is therefore likely that this feature will be valid for both small and large vessels.

Feature 3

The RF-signal measured from non-moving scatterers will be identical in consecutive acquisitions, if no noise is present. The standard deviation on a set of samples from consecutive lines at a given temporal location will be zero. Moving structures (blood or tissue) will result in a non-zero standard deviation, as the sample values vary. The motion of the tissue structures is small, and in most cases smaller than the motion of the blood (see Chapter 4), so it is to be expected that the distributions of the standard deviation for the NBV and the BV segments differ quite a lot. This property becomes feature 3 in this study. Some overlap will inevitably exist, and the overlap determines the features suitability for discrimination. Feature 3 (F_3) is computed as:

$$F_3(i_{seg}) = \frac{1}{\sigma} \sum_{k=1}^{N_s} \sqrt{\frac{1}{N_l - 1} \sum_{l=1}^{N_l} (r_{cfm}(l, k + i_{seg}N_s) - \mu_{k+i_{seg}N_s})^2}, \tag{5.13}$$

where $\mu_{k+i_{seg}N_s}$ is the mean value of the set of samples from the set of consecutive lines at the temporal location $k + i_{seg}N_s$ (in samples). The level of overlap will increase, as the diameter of the vessel decreases, since the overlap between tissue and blood signals increases.

Feature 4

The idea behind feature 3 can also be used on the echo-canceled signals, and then it might also be feasible for smaller vessels. The standard deviation computed on the echo-canceled signals is used as feature 4 (F_4), and it is computed as:

$$F_4(i_{seg}) = \frac{1}{\sigma} \sum_{k=1}^{N_s} \sqrt{\frac{1}{N_l - 2} \sum_{l=1}^{N_l-1} (r_{echo,cfm}(l, k + i_{seg}N_s) - \mu_{echo,k+i_{seg}N_s})^2}. \tag{5.14}$$

A total of 4 features are suggested in this study. Feature 1 and 3 are probably only applicable for larger vessels, whereas feature 2 and 4 might also be usable for smaller vessels.

Generation of density functions

The estimation of the probability density functions for the different features has been carried out on simulated data resembling RF-signals obtained from the carotid artery. The same data set as the one employed in

the evaluation of the Amplitude Discriminator are used. The same basis material is thereby employed, and the performance of the two discriminators can be compared. In this study the distributions and performance on smaller vessels have not been evaluated.

The probability density functions are derived from a histogram analysis of the feature values. Two functions arise for each feature - one for the BV and the NBV segments, respectively. A finite number of equally spaced bins, n_{bins}, will be employed, which span the value range of the features. Each bin spans an interval $I_b, b \in [1,..,n_{bins}]$, of values. The estimated density functions are discrete, and they will be employed as such in the discrimination. The feature value X_f is assigned as belonging to a bin, I_b, and the probability of the feature value is then determined as the estimated probability of that bin. An empiric rule is used in statistics to determine the sufficient number of bins to be employed in the analysis [32]:

$$n_{bins} = 1 + \log_2(N_{segments}), \tag{5.15}$$

where $N_{segments}$ is the number of segments available for the analysis. A total of 67967 NBV segments and 13346 BV segments are extracted from the simulated data. The minimum requirement for the number of bins are 17.1 and 14.7, respectively. In this study a somewhat higher number of bins - 76 - have been used to increase the resolution in the feature values and thereby the ability to distinguish. The range of feature values spanned from 0 to 15, and this range was divided up into the 76 bins. Estimates of the probability density functions $p_{f,BV}$ and $p_{f,NBV}$ were obtained by performing the histogram analysis, and then dividing each bin value with the total number of BV and NBV segments, respectively. The computed estimates of the density functions for the features are plotted in Figures 5.5-5.8 for different levels of the SNR. A discussion of the PDFs for each feature follows. It will reveal if the assumptions made in the derivation of the features hold and to what extent.

Inspection of the PDFs for feature 1 in Fig. 5.5 reveals that the feature values of both segment types span the full value range. The probability mass is therefore spread out over the full range. In some regions the two segment types are more probable though, and these regions do not overlap much. Quite a few NBV segments lie in the region [0,1.5], whereas the BV segments are seen more often in the region [1.0,5]. The high amplitude signals inside and just outside the vessel, which originate from the wall (see Fig. 5.2), result in the non-zero probability at the high feature values for both segments. The plots show that feature 1 is stable to different SNRs. The suitability of employing feature 1 is limited by the spread and overlap of the probability mass.

The energy content after echo-canceling (feature 2) is concentrated in the low range of values. The PDFs in Fig. 5.6 overlap a lot for a SNR of 0 dB. At higher SNRs the NBV segments are highly concentrated around 0, whereas the BV segments span the range [0,1]. The inserted box in the plot represents a zoom of the PDF in the region 0 to 2. The density functions of feature 2 for BV and NBV segments differ to a high degree, and a discrimination based only on feature 2 will have a high rate of correct classified segments. Some misclassification will occur due to the overlap around 0. It is to be expected that more BV segments will be misclassified than NBV segments.

The probability density functions in Fig. 5.7 of feature 3 reveal that the properties of the BV and the NBV segments differ to a high degree, when the standard deviation property between samples in consecutive lines is employed to discriminate them. A level of overlap is present as expected but the level decreases as the SNR increases. The presence of noise makes the signals from non-moving structures appear to be moving to some extent (on a random basis), and therefore a non-zero value of the standard deviation is encountered. As the SNR decreases, this effect gets more pronounced, and it shows up in the PDFs. The probability densities for a SNR of 0 dB clearly show the effect. The feature value for the NBV segments are centered around 2 rather than 0 (equaling no motion). The effect also influences the BV segments but not as much. For the case of a SNR of 0 dB a high degree of overlap exists between the two density functions, which makes the discrimination process complicated under these conditions. For higher SNRs the level of overlap decreases, and the density function of the NBV segments narrows and moves toward 0. The probability

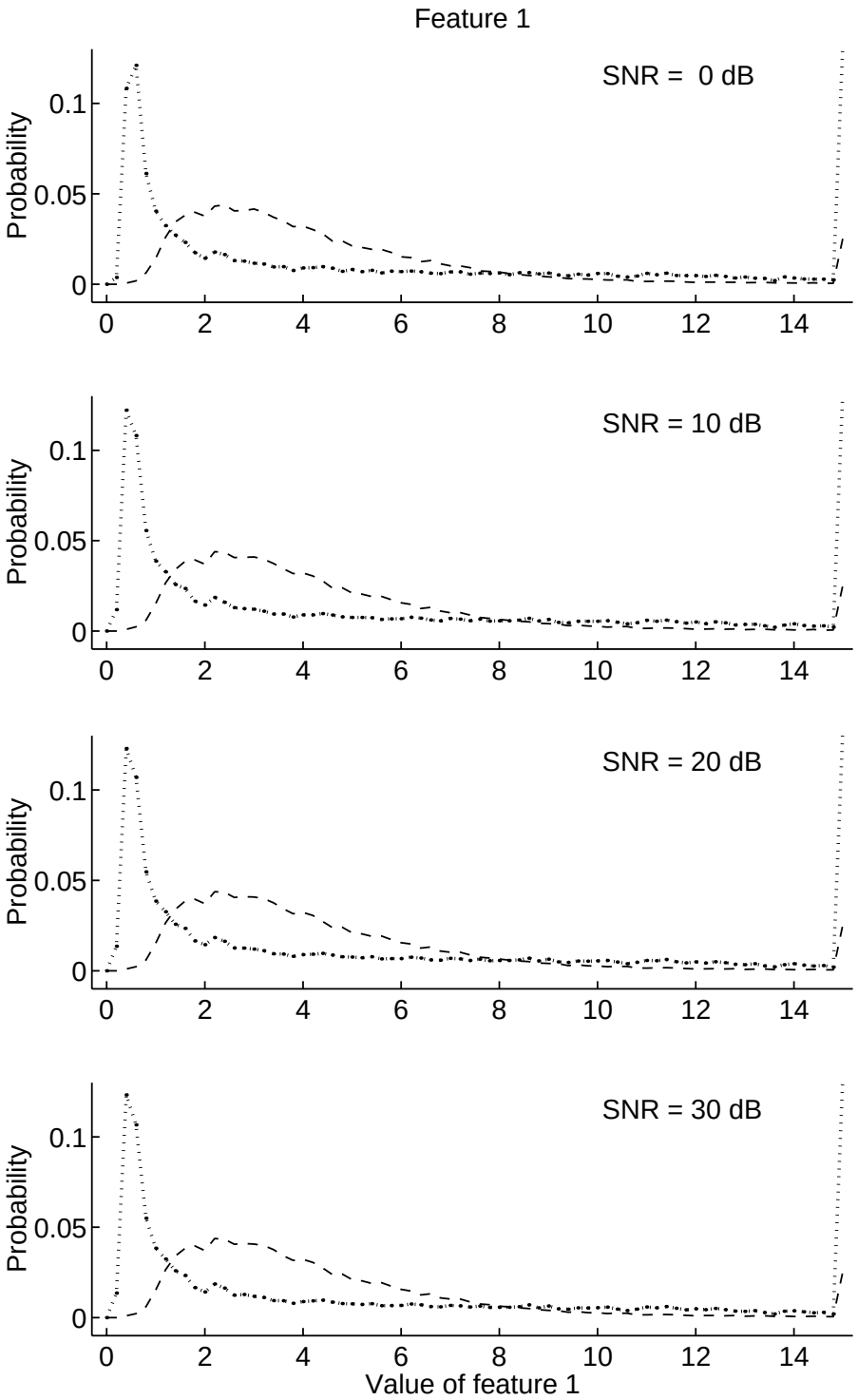

Figure 5.5: The probability density function for feature 1 for different SNRs. The densities for the BV and NBV segments are plotted with dotted (...) and dashed lines (- -), respectively.

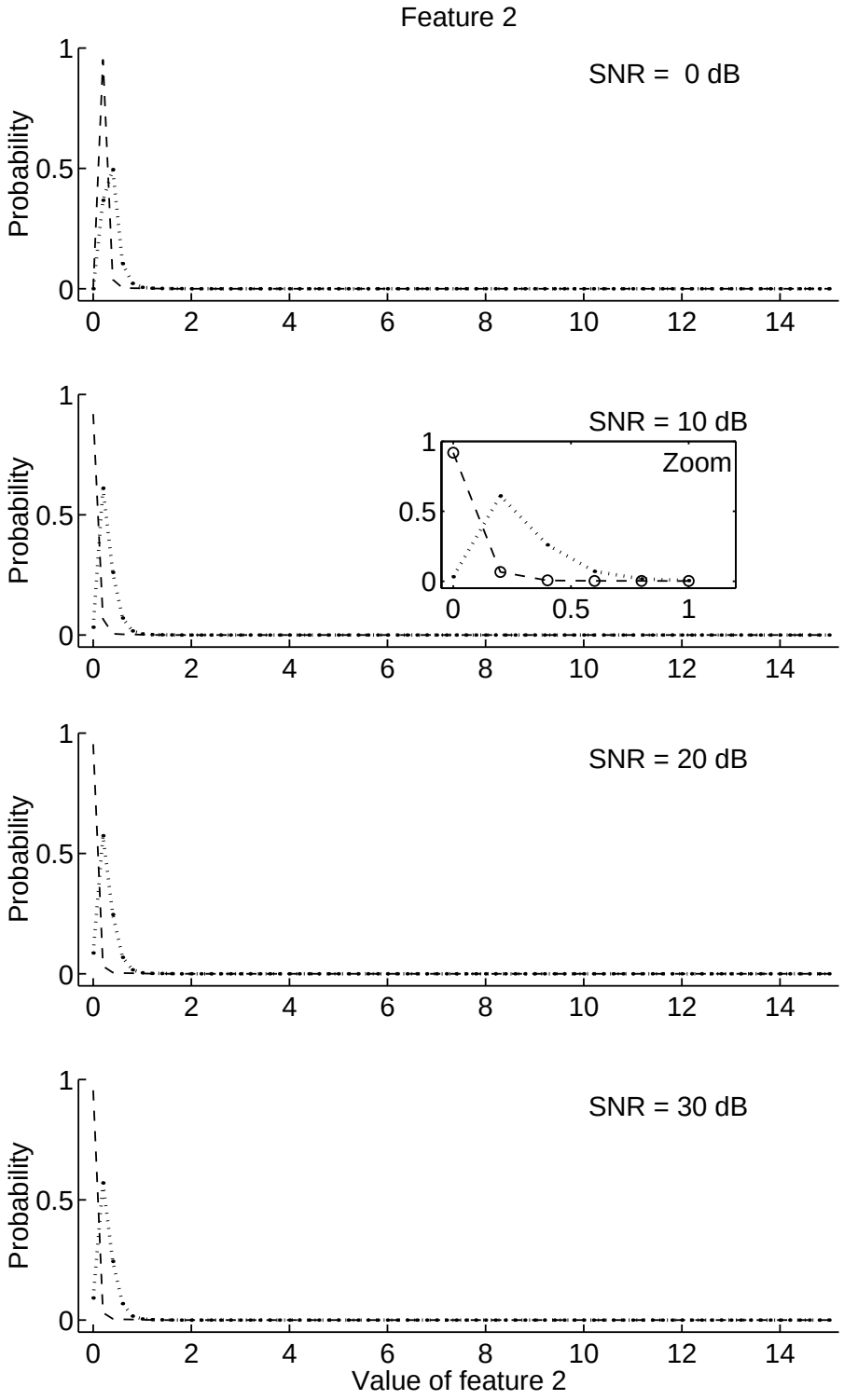

Figure 5.6: The probability density function for feature 2 for different SNRs. The densities for the BV and NBV segments are plotted with dotted (...) and dashed lines (- -), respectively.

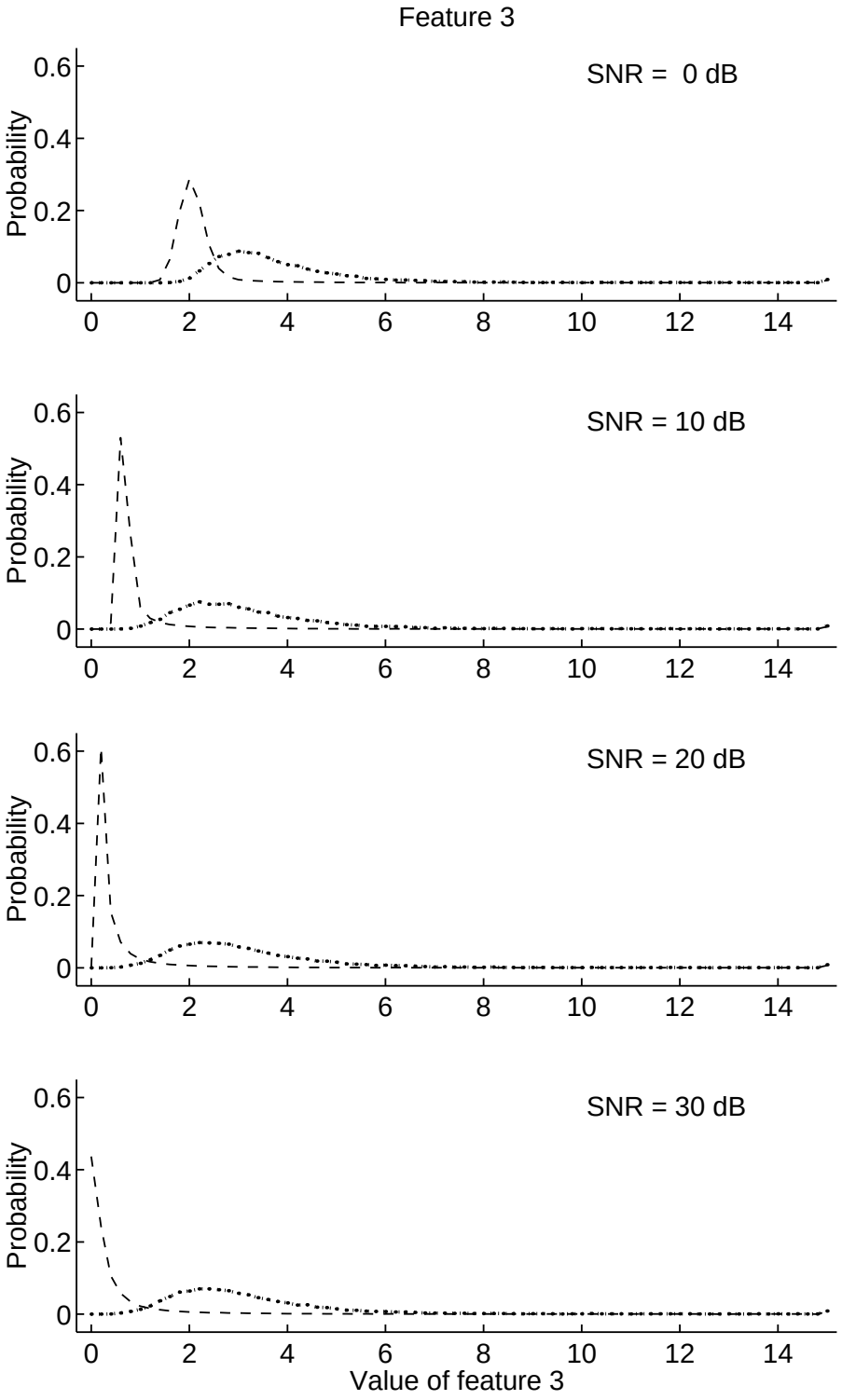

Figure 5.7: The probability density function for feature 3 for different SNRs. The densities for the BV and NBV segments are plotted with dotted (...) and dashed lines (- -), respectively.

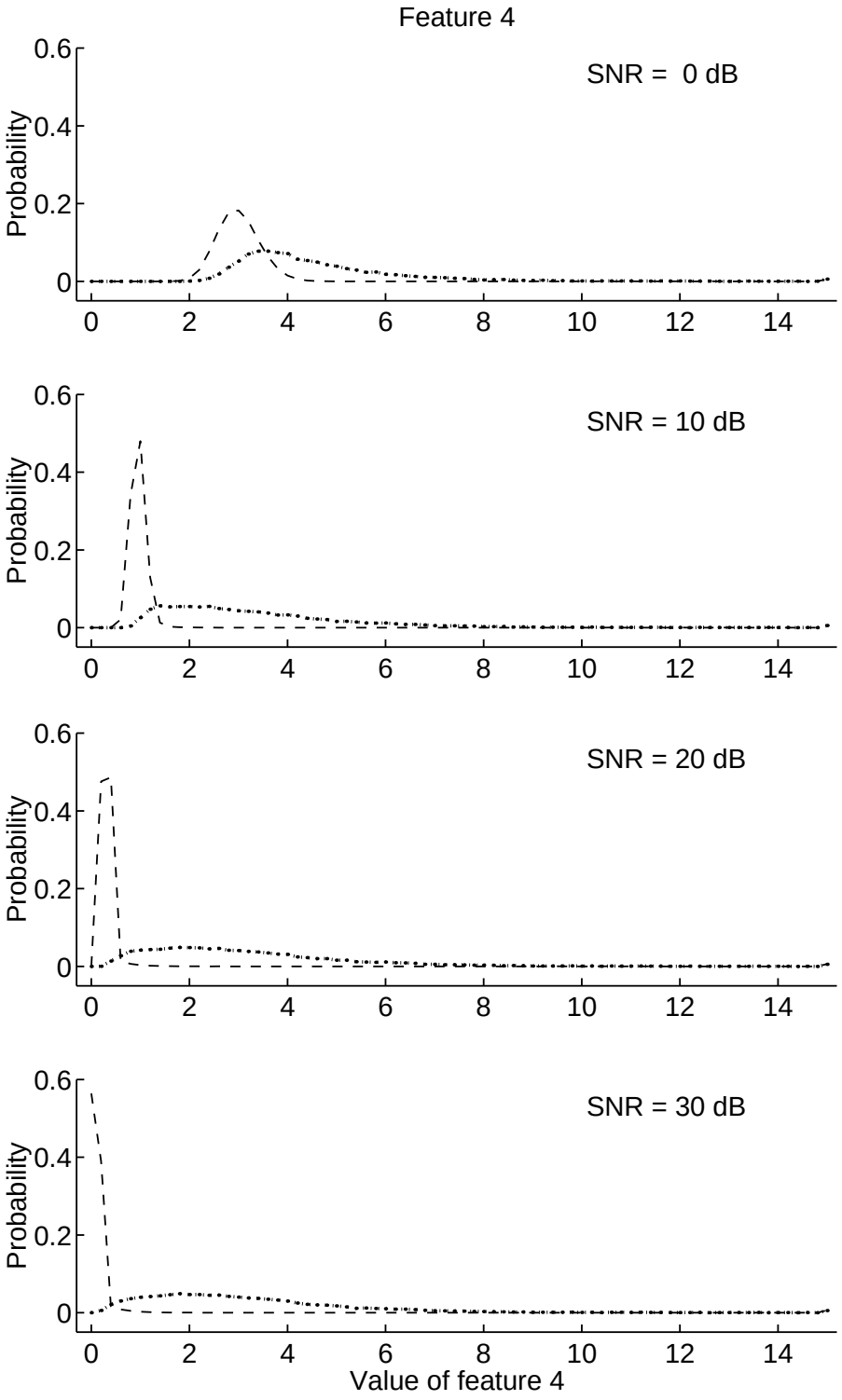

Figure 5.8: The probability density function for feature 4 for different SNRs. The densities for the BV and NBV segments are plotted with dotted (...) and dashed lines (- -), respectively.

density function for the BV segments is stable for SNRs over 10 dB, and spans the value range from 1 to 5. From these observations it seems as feature 3 carries some valuable information for the discrimination process. Its suitability depends on the level of overlap - just as is the case for feature 1 and 2.

The PDFs for feature 4 in Fig. 5.8 show most of the same characteristics as feature 3 but a few differences should be mentioned. The density function of the BV segments is spread out more and spans values from 1 to 6. At a SNR of 0 dB the two PDFs overlap quite a bit, which make the discrimination process very difficult. For all SNRs the level of overlap is increased, which makes this feature less suitable for discrimination compared to feature 3.

The above inspections of the PDFs show that overlap is present for all features, and the level hereof is dependent on the feature and the SNR. By computing the joint probability densities one can hope that the limitations of some features are counteracted by the other features. An example makes this statement more clear. The segment under investigation is an NBV segment, and the SNR is 10 dB. The value of F_1 is 1, which resembles a low energy content. The probability values $p_{1,BV}(1)$ and $p_{1,NBV}(1)$ take the values 0.04 and 0.02, respectively. If a classification was based merely on the PDFs for feature 1, this segment would be classified as a BV segment. No motion is present in the NBV segment, and the value of F_3 is 0.64. The probability values $p_{3,BV}(0.64)$ and $p_{3,NBV}(0.64)$ take the values 0.008 and 0.54, respectively. The joint probabilities p_{BV} and p_{NBV} become 0.00032 and 0.0108. It is therefore most likely that the segment is an NBV segment. The combination of feature 1 and 3 in the discrimination produced the correct classification despite the discrimination limitation of feature 1. The limitations of feature 1 have been counteracted by feature 3 for this particular segment.

The discriminator defined in (5.10) makes use of all features. In principal any combination of the features could be employed. In the above example the discriminator was based on the combination of feature 1 and 3 only. In the following all combinations of the 4 features (a total of 15) will be evaluated.

Results

The performance of the statistical classifiers are evaluated both objectively and subjectively. The objective measure is identical to the one employed in the evaluation of the amplitude discriminator. Table 5.5 lists the performance values (in %) for each of the classifiers for the different SNRs. Before determining the statistical discriminator, which gives the best performance, the results will be commented on. None of the classifiers can produce a 100 % correct classification, which is a result of the overlap between density functions. For a SNR of 0 dB the success rate on the classification of the BV segments ranges from 63.3-90.9 %, and the same measure for the NBV segments ranges from 86.2-95.2 %. The difference in performance on the two segment types spans the interval from -1.2 % to 31.9 %. Most often the success rate on NBV segments is higher than the same measure for the BV segments. As the SNR increases the success rate on classification increases for the BV segments. The overall success rate level for SNRs $>$ 0dB ends up around 90 % or more for most classifiers. The classifiers L - O use only one feature in the classification. The discussion in the following describes the results for SNRs $>$ 0 dB. Classifier L, which only uses feature 1 in the discrimination, has the poorest performance of all classifiers. This comes as no surprise, as the two probability density functions overlap quite a lot. Classifier N is stable to the variation in SNR, and the success rate is high. It performs really good on BV segments but has the second worst performance on NBV segments. The success rates of classifier M and O vary for the different SNRs, but the success rates are above 90 % for both BV and NBV segments. The features 2 and 4 contain valuable information for the discrimination. Actually classifier O out performs most of the other classifiers, which use two or more features. Unfortunately the performance of classifier O is very poor for a SNR of 0 dB, and therefore makes this classifer less usable as discriminator. Still, if a discriminator based on only one feature should be designed classifier O along with classifier M should be considered.

		SNR (dB)							
		0		10		20		30	
Classifier	Features	N_{NBV} N_{BV}	N_T	N_{NBV} N_{BV}	N_T	N_{NBV} N_{BV}	N_T	N_{NBV} N_{BV}	N_T
A	1,2,3,4	91.9 84.8	90.8	93.3 96.7	93.9	95.2 96.9	95.5	94.8 96.8	95.2
B	1,2,3	90.3 87.6	89.8	92.7 96.9	93.4	94.1 94.6	94.2	94.1 94.4	94.2
C	1,2,4	93.7 73.1	90.3	94.7 96.5	95	96.8 94.9	96.5	96.6 95.4	96.4
D	1,3,4	90.8 88.7	90.4	95.6 96.7	95.8	96.1 98.3	96.5	96 98.6	96.4
E	2,3,4	91.4 82	89.9	92.8 96.7	93.4	95.4 96	95.5	95 96.6	95.2
F	1,2	89.2 81.5	87.9	91.7 96.7	92.5	95.2 91.4	94.6	95.3 90.9	94.6
G	1,3	90.5 90.9	90.5	90.9 97	91.9	91 97.4	92	91 97.2	92.1
H	1,4	91 80.5	89.3	96.5 95.1	96.3	96.9 98.1	97.1	96.4 98.9	96.8
I	2,3	90.5 84.1	89.4	92.6 96.8	93.3	94.9 91.7	94.3	94.4 91.7	93.9
J	2,4	95 63.7	89.8	95.2 95.7	95.3	97.4 93.8	96.8	97.3 93.2	96.6
K	3,4	88.2 86.5	87.9	95.5 95.7	95.5	96.4 98.3	96.7	96 98.3	96.4
L	1	86.2 65.3	82.8	86 65.5	82.6	86 65.5	82.6	86 65.5	82.6
M	2	95.2 63.3	89.9	92 96.8	92.7	95.5 91.3	94.8	95.6 90.8	94.8
N	3	88.5 89.7	88.7	89.7 97.2	90.9	89.7 97.7	91	90 97.4	91.2
O	4	87.6 72.8	85.1	97.9 91.7	96.8	96.8 98.1	97	96 98.9	96.5

Table 5.5: Statistical discriminator: Number of correctly classified segments (in %) for the different classifiers at different SNRs.

Cost (a,b)	SNR (db) 0	10	20	30
(0.5,0.5)	G	D	H	H
(0.7,0.3)	G	D	H	H
(0.3,0.7)	G	H	H	H

Table 5.6: The best statistical classifier as a function of SNR and the cost.

Although the success rate is rather high for all classifiers, the classifier, which produces the best classification, should still be determined. This study focuses on features for larger vessels, and therefore all 15 classifiers are evaluated with respect to determining this classifier. As the features were defined, a comment was made on the likelihood of a feature being valid for both smaller and larger vessels. As no investigations on RF-data from a smaller vessel have been carried out, no conclusions will be drawn on the choice of classifier for small vessels in this context. The cost issue of taking a wrong decision must still be considered, and (5.9) must be employed to determine the discriminator. Table 5.6 lists the discriminators, which produces the best performance for the different SNR levels and the 3 combinations of the cost weights. A range of classifiers are to be employed dependent on the cost and the SNR. The discriminators use a combination of two or three features. The influence of the SNR requires that the SNR in the data is determined. From an implementation point of view this complicates the situation. The noise level should be determined prior to acquiring data for imaging. If this approach is not desirable, one discriminator must be determined. The choice hereof is based on the overall performance for the range of SNRs. The best classifier for the SNR range 10-30 dB is:

- classifier H, when the cost weights, (a,b), are (0.5,0.5),
- classifier D and H, when the cost weights, (a,b), are (0.7,0.3),
- classifier H, when the cost weights, (a,b), are (0.3,0.7).

At SNRs above 0 dB classifier H can be used for the discrimination independent of the choice of the cost weights. Determination of the best discriminator over the full range of SNRs (0-30 dB) gives the following results:

- classifier D, when the cost weights, (a,b), are (0.5,0.5),
- classifier D, when the cost weights, (a,b), are (0.7,0.3),
- classifier D, when the cost weights, (a,b), are (0.3,0.7).

The results show that the best performance for all the cost and noise situations is obtained with classifier D.

The objective performance measure does not tell anything about the distribution of the correctly classified and misclassified segments in the images. The misclassification should not be systematic or group together but rather be spread out over the images. Therefore a subjective performance evaluation is needed as well. Through inspection of the images of the classification the following can be learned:

- Often the misclassified NBV segments group together next to the vessel wall. This problem occurs as the systolic phase of the cardiac cycle starts. An example hereof is plotted in Fig. 5.9(a). The results originate from classifier D for a SNR of 0 dB. The true classification is given in Fig. 5.9(b).
- For some classifiers the misclassified BV segments group together in the vessel.

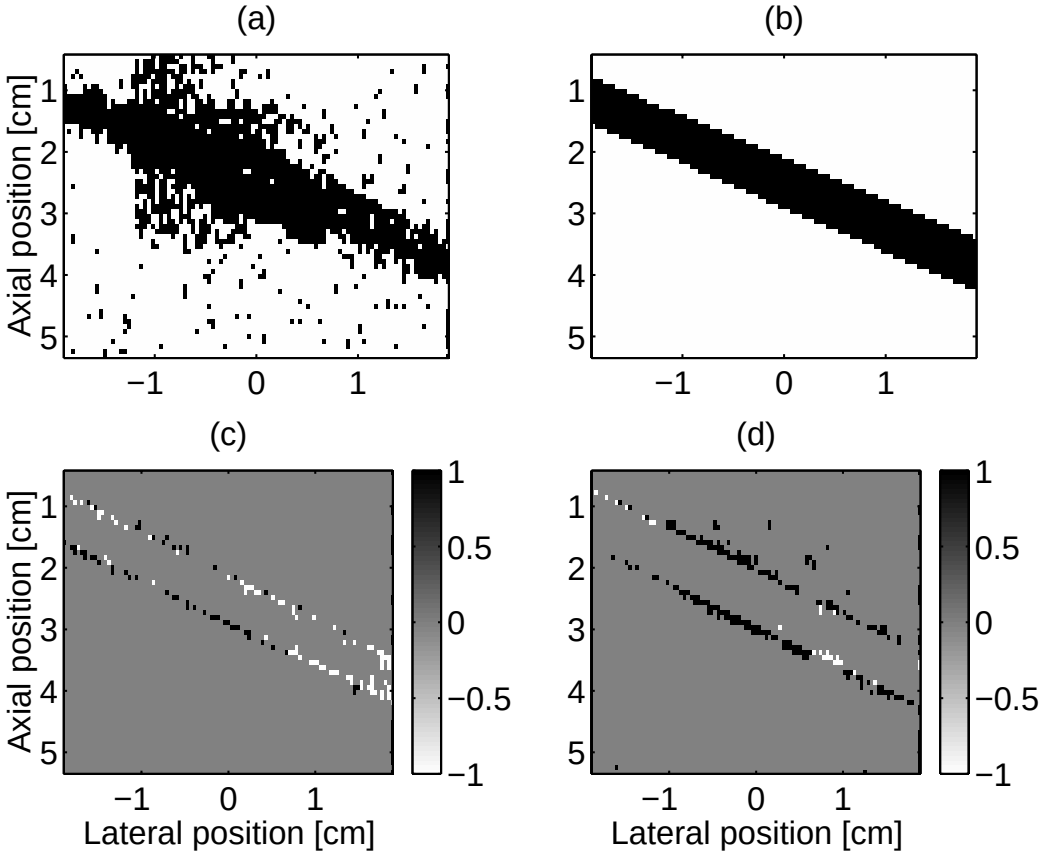

Figure 5.9: Plot of some of the problems encountered with the statistical classifiers. (a) Classification of systolic frame with classifier D for a SNR of 0 dB. (b) The true classification of the systolic frame in (a). Black and white pixels represent BV and NBV segments, respectively. (c)-(d) Examples of misclassification in the transition between segment types. Black indicates that a NBV segment has been classified as a BV segment, and vice versa for the white pixels.

- The transition between BV and NBV segments are not well-defined. The extent of the vessel is classified both to wide and narrow in the same frame as shown in Fig. 5.9(c). The misclassification of the transition some times extent several segments (see Fig. 5.9(d)).

So even though the objective measure expresses a high success rate on classification, the subjective inspection of the images reveals that discrimination problems are encountered. The problem in the systolic frames occurs as the cardiac pulsation starts, and the vessel walls and the surrounding tissue are pushed outward at high speed. The problem of the systematic misclassification of NBV segments in the systolic frames does not exist, when classifier H is employed. For a SNR of 0 dB the success rate on BV segments is 8.2 % lower than the same measure for classifier D, and the problem of grouped misclassified BV segments is increased. The inability to determine the exact extent of the vessels are not solved with classifier H or any of the other classifiers. In Fig. 5.10 the classification results on a systolic and a diastolic frame for the SNR 0-20 dB is plotted. Inspection of all the images in the cardiac cycle reveals that the plotted results do not represent the worst or best classification result but rather the average performance. The misclassification is fairly non-systematic and non-grouped. Though, some misclassifications repeat themselves in consecutive frames. This effect is mostly seen, when the SNR is 0 dB. The performance on the NBV segments is also at its lowest in this case. Overall this effect is much less pronounced than for the amplitude discriminator. All 15 statistical filters perform better than the amplitude discriminator with respect to the number of correctly classified segments (see Section 5.3.1). The amplitude discriminator has a high success rate on NBV segments, which exceeds quite a few of the statistical discriminators. The real achievement obtained

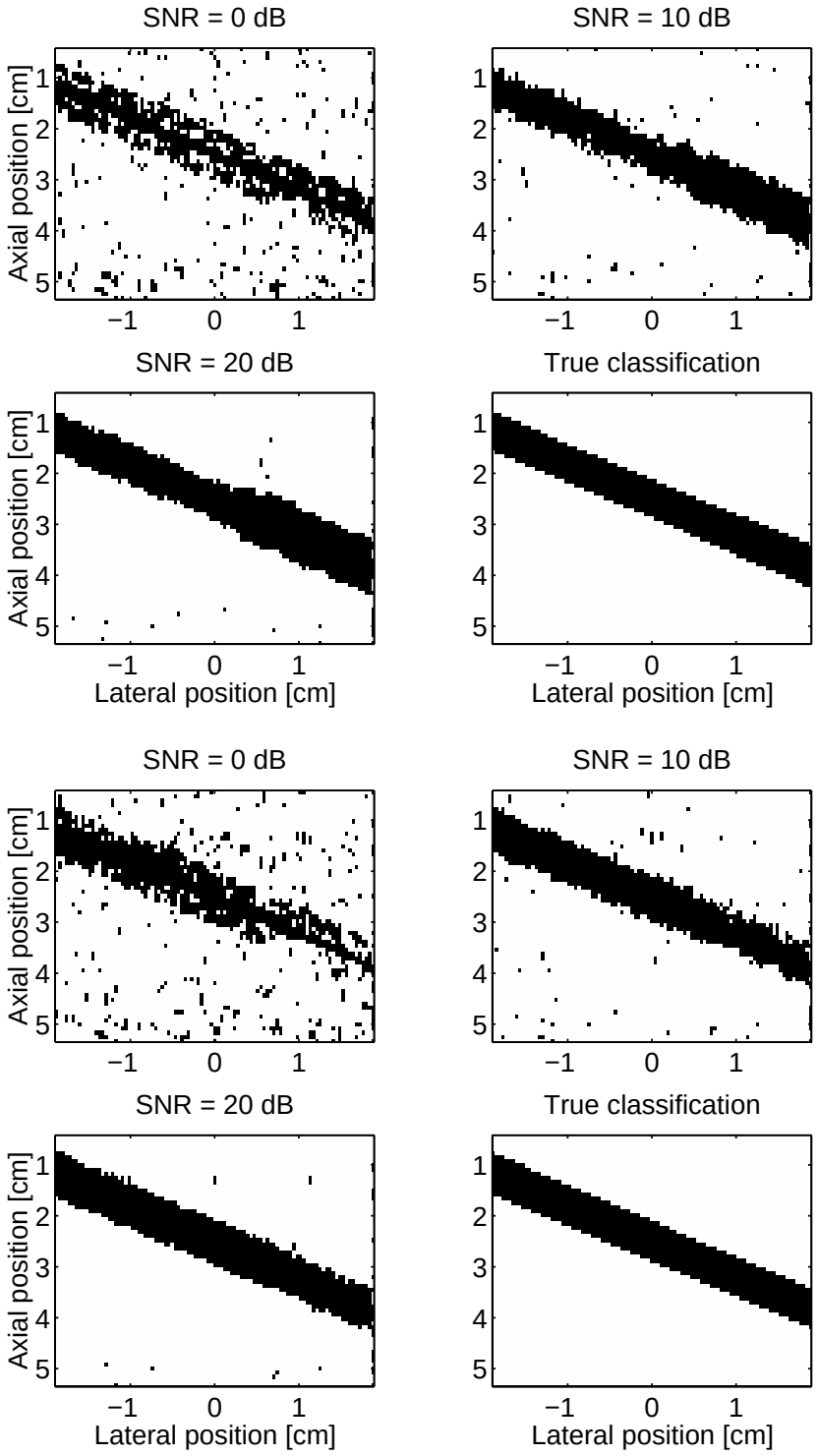

Figure 5.10: Performance of classifier H on systolic frame (4 upper plots) and diastolic frame (4 lower plots) for different values of the SNR along with the true classification. Black and white represent BV and NBV segments, respectively.

	SNR (dB) 0		10		20		30	
	N_{NBV} / N_{BV}	N_T	N_{NBV} / N_{BV}	N_T	N_{NBV} / N_{BV}	N_T	N_{NBV} / N_{BV}	N_T
Amp.	97.8 / 42.6	88.2	97.1 / 42.1	88.1	97 / 42.3	88	97 / 42.3	88
Stat.	91 / 80.5	89.3	91 / 95.1	96.3	96.9 / 98.1	97.1	96.4 / 98.9	96.8

Table 5.7: Performance comparison of the amplitude (Amp) and statistical (Stat) discriminator for $(a,b) = (0.5, 0.5)$.

by employing the statistical discriminator is the high success rate on classification of the BV segments. An improvement of a factor of 1.5-2.4 has been obtained. Table 5.7 shows these trends. The results for the amplitude discriminator (Amp) are the results for the best classifier for each SNR. The performance of classifier H as a function of SNR is listed as the best result for the statistical discriminator (Stat). The ideal situation of a 100 % correct classification has not been obtained but the statistical classifier is closer to this goal than the amplitude discriminator.

In the present study 4 features have been derived and evaluated. The results show that all 4 are valuable for the discrimination. More features are probably extractable for the RF-data, and other statistical classifiers will be obtained. From the above investigations it can be concluded that the acquired RF-data contain information of value for the discrimination. It is worth determining and including other features than the amplitude feature in the discrimination process.

5.3.3 Neural network

The statistical discriminator makes use of the joint probability of an outcome to classify the type of segment. Another approach would be to determine a parametric relation between the features, which produces an output that states the type of segment. The relation can be both linear and non-linear, and the contributions from the different features can be weighted. In the statistical classifier all features were assumed equally important for the discrimination. The span of possible relations are infinite. The process of determining the proper relation becomes to complicated and incalculable, unless the process is automated. In the following a classifier based on a neural network [39],[40] is investigated. The network simply describes a mathematical relation, and the complexity of the relation is dependent on the choice of structure. Looking into the literature of neural networks will reveal that many different network types exist. This study will not investigate which type is the optimum for the given situation. A 2-layered feed-forward neural network [39], [40] will be employed, and the suitability of employing this network for classification of the NBV and the BV segments will be investigated.

The literature shows that neural networks have been employed before for classification of RF-signals [41], [42], [43], [44]. The features employed in the classification were derived from filtered and processed data (*e.g.* audio data, envelope detected, and color-coded data). In the study by Kahl et al. [42] the filtered RF-signals were pre-segmented by a physician, so only signals in the region of interest (the myocardium) were filtered and processed before the features were derived. Feleppa et al. [44] employ a neural network to distinguish cancerous and non-cancerous tissue of the prostate, and the classification is performed on spectral parameters derived from the RF-signals. In general a set of features were derived and employed. The same approach will be used in this study. The aim is to discriminate between BV and NBV segments for CFM imaging.

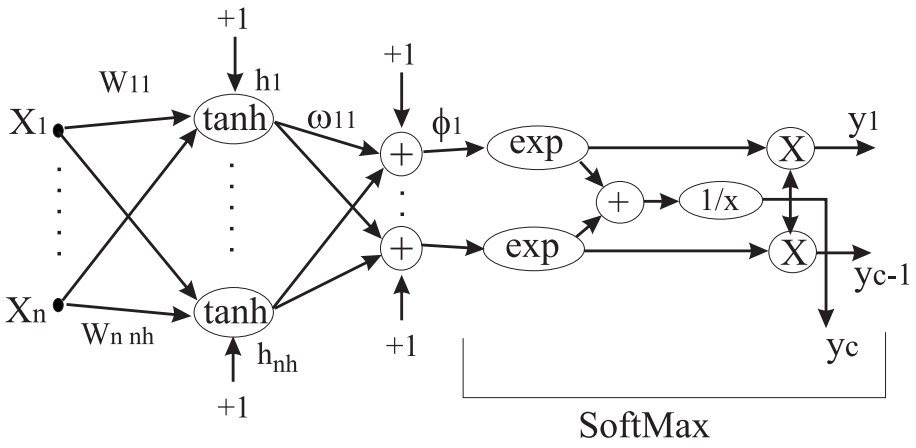

Figure 5.11: Architecture of a 2-layer feed-forward neural network expanded with a SoftMax function.

The lay-out of the network structure is given in Fig. 5.11. The feed-forward term refers to the fact that no feed-back loops are present. The flow of information is only in the forward direction. A set of input values, $x_1,..,x_{n_I}$, which represent features derived from the segment under investigation, are fed to the network and processed by the two layers in the network. The first layer is termed the hidden layer, where a set of "neurons", $h_1,..,h_{n_h}$, process the weighted sum of the inputs. The variables n_I and n_h determine the number of inputs and the number of hidden neurons, respectively. The w_{ij} indicates the weight multiplied onto input x_i, when it contributes to the sum at the hidden neuron h_j. The output of each hidden neuron is weighted by ω_{jl} and passed to the output layer. The contributions are summed, and the output values $\phi_1,..,\phi_{C-1}$ of the network are available. The variable C determines the number of classes (types of segments) in the classification, and ω_{jk} is the weight that is multiplied onto the value from hidden neuron h_j, when it contributes to the sum at the output neuron ϕ_k. To make the functionality of the 2-layer feed-forward network clearer the above description is exemplified by writing up some of the mathematical relations in the network. The relations giving the output of hidden neuron number 1, η_1, and the output number 1, ϕ_1, when four inputs are fed to the network, and two hidden neurons are present in the first layer, are:

$$\begin{aligned} \eta_1 &= \tanh(w_{11}\cdot x_1 + w_{21}\cdot x_2 + w_{31}\cdot x_3 + w_{41}\cdot x_4) \\ \phi_1 &= \omega_{11}\cdot\eta_1 + \omega_{21}\cdot\eta_2. \end{aligned} \tag{5.16}$$

From the output values, ϕ_k, it can be determined which class the segment under investigation belongs to. The level of certainty on the estimate is not given. A probability value of the segment belonging to a particular class contains this information. To interpret the output values as probabilities, the output values are passed through a normalized exponential transformation known as the SoftMax function [45]. This extension of the neural network is included in Fig. 5.11. A set of probabilities values, $y_1,...,y_{C-1},y_C$, result. The segment is assigned to the class with the highest probability.

The optimum weights w_{ij} and ω_{jk} for the problem at hand must be determined. It requires access to a data set, where the input values and the corresponding output values are known. Through minimization of an error cost-function the optimum weights are determined. Programs that can determine the weights have been developed, and one of them is employed in this study. The program is named Neural Classifier 1.0 [46], and it is written by Jan Larsen and Morten With Pedersen [47]. It uses a common optimization algorithm for feed-forward networks, which is named the pseudo Gauss-Newton scheme. The cost function is a negative log-likelihood function. The cost function determines the error on classification. Minimization of the error is performed on an iterative basis. After each iteration the weights are assigned new values, which cause the error to decrease some and thereby move toward the global minimum. The optimization schemes are manifold, but they all aim at reaching the global minimum fast without getting caught in local minima. A thorough discussion of these algorithms can be found in [39], [40].

The process of determining the network, which gives the best classification, is usually referred to as the training process. In this study the data set are divided into three subsets of equal size, and two of them are used to train the network. The ratio of NBV and BV segments are constant in the subsets. The third subset is used to evaluate the performance of the network, when the network has been determined. A choice has to be made on the number of hidden neurons in the network before the training can be performed. From an implementation point of view the network should be small, so the number of calculations are minimized. Still the network should have a certain size that allows for the generation of a relation, which can perform a good classification. The optimum number of hidden neurons are not known a priori, so a set of neural networks are evaluated for a range of values of n_h. The optimum network is determined according to a performance criteria. Initially all weights are assigned to randomly small values, which are Gaussian distributed [40]. When the training starts, the network has a fixed size, which is determined by the number of weights and the number of hidden neurons. This choice does not necessarily give the best performance, so algorithms have been developed to determine the importance of the weights. The least important weight is pruned away (set to zero) on an iterative basis, until all weights are zero. The least important weight is the one that causes the least change in the error value, when it is removed. The network is pruned by employing the algorithm Optimal Brain Damage (OBD) [40]. The error can increase or decrease in each iteration. The best choice of network - by means of the choice of number of non-zero weights - is determined by plotting the number of non-zero weights against the error. The training and pruning are performed on both the training and test set, so two curves are obtained. The joint minimum of the two determines, which network should be used for classification. The performance is then determined by letting the network classify the evaluation set, and then compare the outputs to the true outputs. Often the performance on the evaluation is (slightly) poorer than the performance on the test and training sets. This is not a surprise, as the network has been determined from the two latter sets and never has been introduced to the evaluation set.

In this study 5 networks are evaluated. The features determined for the statistical discriminator are used as inputs, so a total of 4 inputs are fed to the network. The results can thereby be compared to the results of the amplitude and statistical discriminator. The network has one output, as the number of classes are two (the BV and the NBV class). The networks differ on the number of hidden neurons, and a range from 4-20 in steps of four is investigated. The SNR in the data set was 20 dB. In Fig. 5.12 an example of the error curves for the training and test sets as a function of the number of non-zero weights are plotted. The network has 12 hidden neurons. The joint minimum occurs for 55, so the network, which produces the best classification, has 55 non-zero weights. For each network the optimization is performed. The results of the optimization are listed in Table 5.8. The first column specifies the number of hidden neurons. The initial size with respect to number of weights, n_w, is listed in the second column, and the final number of non-zero weights, $n_{w,opt}$ appear in column 3. The performance with respect to the number of correctly classified segments in each of the subsets and in total is listed in the last 4 columns. All the networks make use of a subset of the weights. No improvement in the classification of the training and test set is seen, when n_h is larger than 4. The performance on the evaluation set is slightly lower as expected. In the current investigation the difference is very little, so the networks have determined a relation that discriminates well. The overall performance increases as n_h increase. The performance with respect to correct classification of NBV and BV segments is listed in Table 5.9. The NBV segments are close to being classified 100 % correct, and no significant improvement on the classification is obtained for $n_h > 4$. The success rate on BV segments is also very high, and it increases as a function of n_h (except for $n_h = 16$). The best performance is obtained for $n_h = 20$. The performance of the networks with 12 and 20 hidden neurons is so similar that one would often choose to work with the smallest network to decrease the computational load. In Fig. 5.13 the structure of the neural network, which produces the best classification, for n_h equal to 12 is plotted. The middle layer represents the hidden layer. A line between two circles (o) tells that the weight is non-zero. The lack of a line between two circles tells that the weight is zero. All 12 hidden neurons play a role in the classification. All features contribute. Each of them is connected to 8 hidden neurons but none of them are connected to the same 8 hidden neurons. Fig. 5.14 shows plots of the classification on a systolic and diastolic frame along with the true classification, when the neural network with 12 hidden neurons is employed. The classification is very

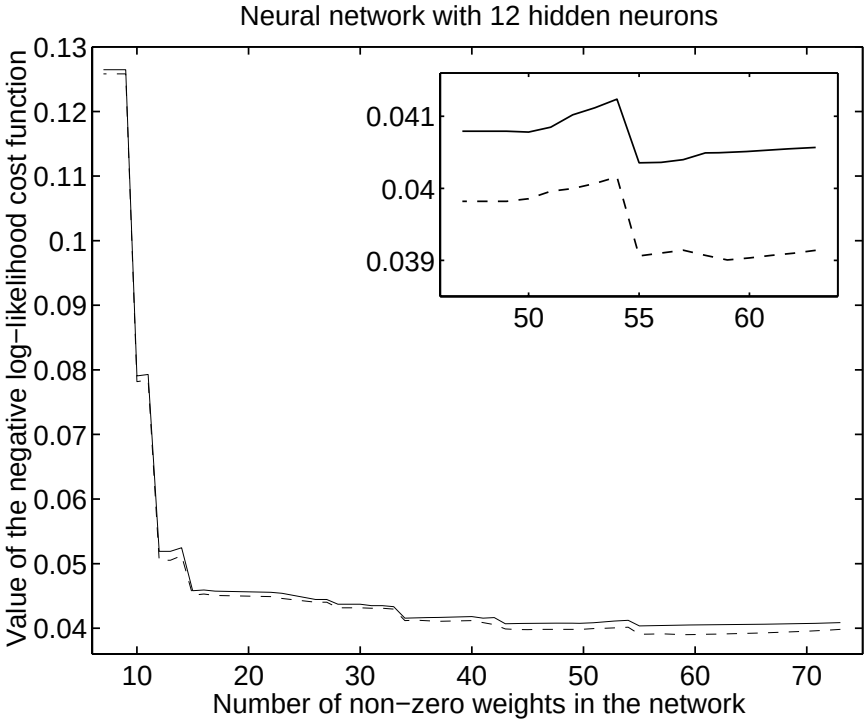

Figure 5.12: Plot of training (- -) and test (-) error as a function of the number of non-zero weights, when $n_h = 12$.

SNR = 20 dB

n_h	n_w	$n_{w,opt}$	TR	TE	EV	T
4	25	20	98.5	98.5	98.4	98.4
8	49	40	98.6	98.6	98.4	98.5
12	73	55	98.6	98.6	98.5	98.5
16	97	70	98.6	98.6	98.4	98.5
20	121	89	98.6	98.6	98.5	98.6

Table 5.8: The optimum size of the investigated neural networks along with the performance of the network on the training (TR), test (TE), and evaluation (EV) set. The overall performance (T) on the full data set is listed in the last column.

SNR = 20 dB

	4	8	12	16	20
N_{NBV}	98.9	99	99	99	99
N_{BV}	94.4	94.5	94.8	94.5	94.9
N_T	98.4	98.5	98.5	98.5	98.6

Table 5.9: Neural network: Number of correctly classified BV and NBV segments (in %) as a function of the number of hidden neurons.

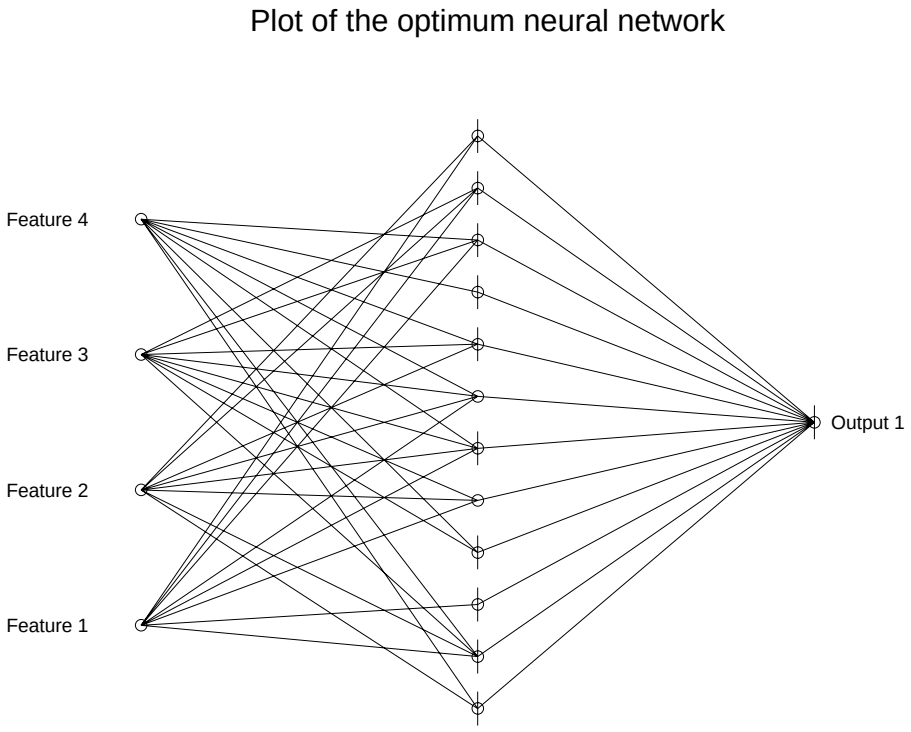

Figure 5.13: Plot of the optimum neural network, when n_h are 12, and the SNR is 20 dB.

good on both BV and NBV segments. The majority of the misclassified NBV segments appear around the vessel wall, when the extent of the vessel is overestimated. The misclassified BV segments also show up around the vessel wall, when the extent of the vessel is underestimated.

The investigations show that it is possible to determine a relation between the features, which can be used to discriminate BV and NBV segments, when the SNR is 20 dB. A range of SNRs must be investigated before any final conclusions can be made. This has been done for the network with 12 hidden neurons. The additional SNRs were 0, 10, and 30 dB. The networks, which produce the best performance, here fore have 56, 49, and 49 non-zero weights, and the network structures differ. For the 10 and 30 dB situation only 11 hidden neurons are present in the final network. In Table 5.10 (the last row) the performance on the BV and the NBV segments is listed for all investigated SNRs. At a SNR of 0 dB the success rate on classification of BV segments is below 80 %. For increasing SNRs the performance improves and gets beyond 90 %. The success rate on NBV segments is above 97 % for all SNRs. Plots of the classification reveal that the majority of misclassified segments are located in the region next to the vessel wall. The extent of the vessel is both over- and underestimated.

In Table 5.10 the results for the 3 different discriminators discussed in this chapter are summarized. Both the statistical and neural discriminator out perform the amplitude discriminator for all SNRs. The performance of the statistical discriminator and the neural network is very similar. Looking at the overall performance the statistical discriminator is to be preferred over the neural and the amplitude discriminator, as the statistical discriminator has the best overall performance on the BV segments.

5.3.4 Summary

The amplitude discriminator is a simple method for discrimination, but its performance is very poor on the BV segments. Only 42 % of these segments are classified correct. The success rate on the NBV segments is 97 %. More features should be determined, and more advanced algorithms must be used in order to make a

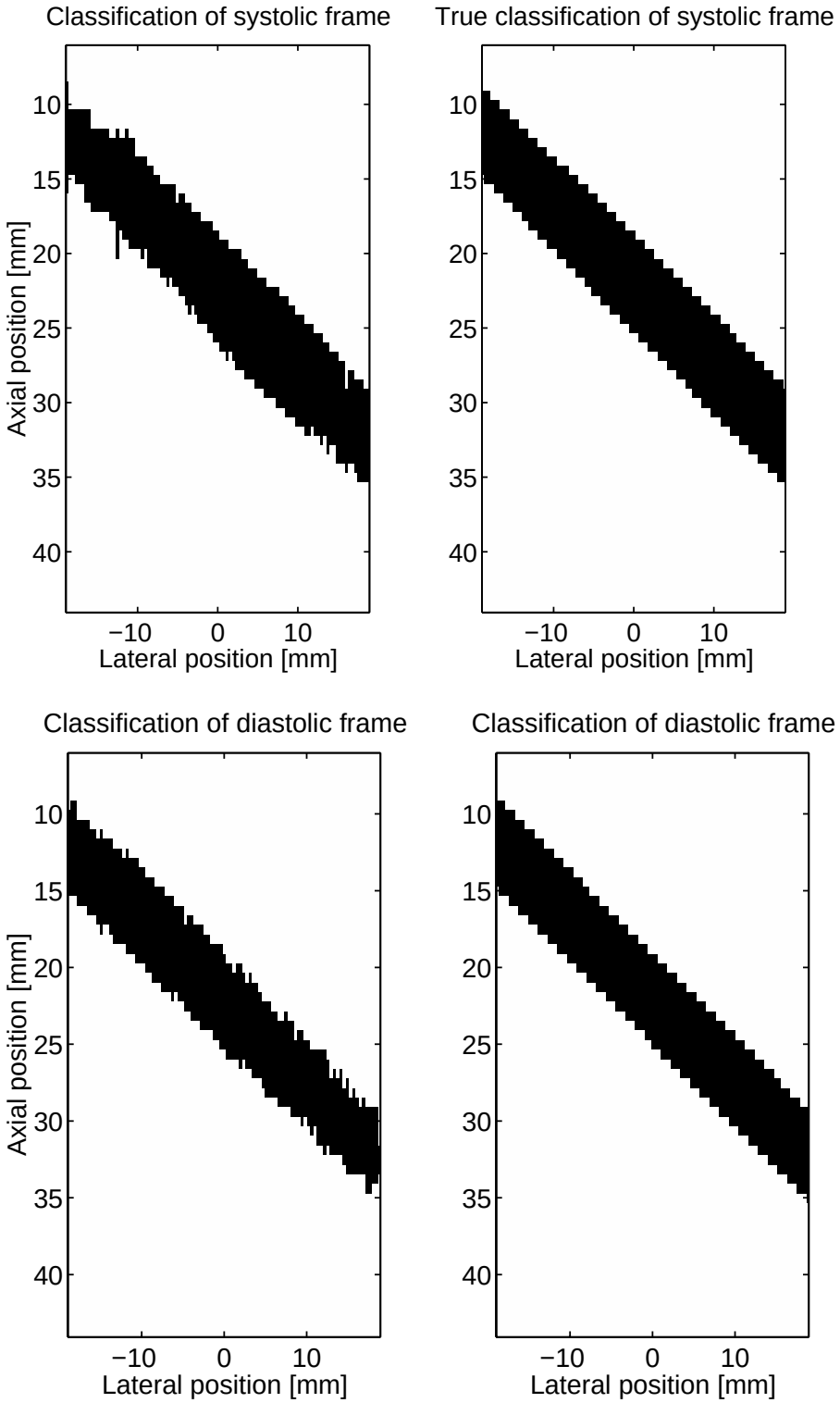

Figure 5.14: Classification with neural network of a systolic frame (2 upper plots) and a diastolic frame (2 lower plots).

	SNR (dB) 0		10		20		30	
	N_{NBV} / N_{BV}	N_T	N_{NBV} / N_{BV}	N_T	N_{NBV} / N_{BV}	N_T	N_{NBV} / N_{BV}	N_T
Amp.	97.8 / 42.6	88.2	97.1 / 42.1	88.1	97 / 42.3	88	97 / 42.3	88
Stat.	91 / 80.5	89.3	91 / 95.1	96.3	96.9 / 98.1	97.1	96.4 / 98.9	96.8
NN.	97.9 / 77.3	94.5	99.1 / 91.5	97.8	99 / 94.8	98.3	99 / 94.8	98.3

Table 5.10: Performance comparison of the amplitude discriminator (Amp), the statistical discriminator (Stat), and the neural network (NN) for $(a,b) = (0.5, 0.5)$.

good discrimination. This will result in better CFM images. Two new approaches - a statistical and a neural discriminator - have been investigated. They employ 4 new features, which were determined in this study. The features are the energy content in the segments before and after echo-canceling (a total of two features), and the variations in amplitude between consecutive RF-lines before and after echo-canceling (a total of two features). Both discriminators out perform the amplitude discriminator and come close to the optimum goal of being able to discriminate all BV and NBV segments correctly. The success rate on classification of the BV and NBV segments gets beyond 91 %, when the SNR is above 0 dB. The results only hold for larger vessels such as the carotid artery. Further investigations into using these methods on smaller vessels must be carried out.

More features probably exist and should be included, if they contribute positively to the performance of the discriminators. The class type of neighboring segments in time (between frames) and space (within frame) might carry valuable information. It is probably not very likely that a segment carries blood velocity information, if all its neighbors in time and space do not carry blood velocity information. Investigations into this aspect should be considered, included as one or more features in the discrimination process, and evaluated with respect to its influence on the performance.

What is to be learned from the investigations is that the RF-signals contain information applicable for discrimination. Several features should be derived and incorporated in advanced discrimination algorithms, which can combine the information at hand.

5.4 Summary

This chapter has been concerned with the pre-processing of the RF-signals prior to blood velocity estimation. A matched filter for minimization of the noise content in the RF-signals has been introduced in this chapter. It has been and will be employed for de-noising of the RF-signals in this and the subsequent chapters.

Echo-canceling must be performed prior to performing blood velocity estimation, and two filters here fore have been introduced. The influence of the filtering on the blood velocity estimation will be evaluated in the subsequent chapter. The evaluation is only carried out on a synthetic data set.

Non-zero velocity estimates are produced both inside and outside the vessel. Only the estimates, which relate to the motion of the blood, are of interest and should be displayed. Three discriminators have been derived and evaluated in this chapter. The first discriminator employs the variation in the amplitude levels in the envelope detected RF-signals. Less than 50 % of the segments, which carry blood velocity information,

were classified correct. Therefore other approaches for the discrimination were considered. In this study two new approaches were developed. One is based on maximum likelihood theory, and the other uses a neural network for the classification. Both approaches out perform the first approach. The new approaches included more features derived from the RF-signals in the discrimination. The features are the energy content in the segments before and after echo-canceling, and the signal variation between sample values in consecutive RF-lines (also computed before and after echo-canceling). The new discriminators are able to perform a correct classification of more than 91 % of the investigated BV segments. This is valid, when the SNR is above 0 dB. The performance on the NBV segments is similar for the three discriminators. The success rate reaches and gets beyond 91 %. The introduction of more features and the employment of more advanced algorithms have resulted in a better basis for discriminating the BV and the NBV segments. More features should be considered and incorporated. The segment types of neighboring segments in time and space could contain valuable information.

Chapter 6

Blood velocity estimators

The velocity distribution in the human vessels carries information of diagnostic value (see Chapter 1). Therefore methods for estimation of the blood velocities from the recorded RF-signals are desirable. If a continuous, monochromatic wave is emitted, an estimate of the average velocity in the medium can be determined from the acquired response due to the Doppler shift [3]. Estimates of the blood velocities with a level of spatial resolution along the propagation direction are not obtained with this approach. Other methods have been developed over the years to obtain images of the velocity distribution with a level of resolution. The resolution is achieved by emitting a wave of finite temporal extent instead. The resolution is inversely proportional to the length of the emitted pulse. An infinite resolution is not obtainable, as the excitation of the transducer with a Dirac delta impulse will result in an emitted pulse, which is a couple of cycles long. This is due to the impulse response of the transducer. A lower limit on the pulse length is therefore given and is transducer dependent. An infinite short pulse is not desirable, as all estimators discussed in the following use a set of samples to improve the accuracy on the estimate. The final choice of pulse length to use for blood velocity estimation depends on the estimator. The estimation is carried out on the acquired RF-signals. The signals are split up in a number of segments, and the velocity is determined for each of these. Employing a short pulse makes estimation based on the Doppler shift very difficult. The emitted pulse spans a band of frequencies (the bandwidth usually ranges from 60-100 % of the center frequency), and the attenuation in the medium changes the spectrum of the propagating pulse. This spectral change dominates over the change generated by the Doppler shift [3], so the effect of the Doppler shift is negligible and hardly detectable. The estimation therefore relies on other features of the acquired RF-signals, and these are discussed in Section 6.1.

A selection of estimators are presented and evaluated in Sections 6.3-6.9. The advantages and disadvantages will be pointed out. Two new estimators are presented in Section 6.7 and 6.9. The first combines two of the presented estimators, whereas the last is an expansion of the maximum likelihood estimator discussed in Section 6.8. The new maximum likelihood estimator incorporates properties of fluid mechanics, which predicts that the velocities are correlated in time and space.

The performance of the estimators is evaluated on two sets of data, which are defined in Section 6.2.

6.1 Properties of the RF-signals for blood velocity estimation

An understanding of the acquired RF-signals must be obtained prior to developing blood velocity estimators. The nature of the acquired RF-signals will be discussed in the following. The basic properties of wave propagation and the interaction with a medium were discussed in Chapter 2. A comprehensive model for

the received RF-signals will not be derived in this context. Instead, some features of the linear propagation and the linear interaction will be discussed and modeled, since the estimators introduced in the following rely on linear properties [3].

A pulse is emitted, and it propagates in the medium, which consists of a spatial distribution of scatterers. The pulse is reflected and scattered as it interacts with the medium. The acquired signal is influenced by:

- the distribution of scatterers and their scattering characteristics,
- the attenuation,
- the Doppler shift,
- the beam width of the emitted field,
- the noise, and
- the impulse response of the transducer in transmit and receive.

In the following discussion it is assumed that the properties of the scatterers are constant over the time of interaction with the emitted pulse. The velocity and the scattering properties of the scatterers are constant. The size of the scatterer is small compared to the length of the emitted pulse. Under these conditions the scatterers can be considered as point reflectors [34]. In the simple situation with only one, non-moving scatterer the acquired signal $r_c(t)$ will be a scaled version of the emitted signal $e(t)$ [3], [34]. The scaling depends on the scattering properties of the scatterer. The time of arrival determines the distance from the transducer to the scatterer. When the scatterer is moving, a frequency shift f_d is experienced due to the Doppler shift. This shows up as an expansion or compression of the time axis [3]. A simple model of the complex received signal $r_c(t)$ is [3], [34]:

$$\begin{aligned} e(t) &= \sqrt{E_t} f(t) \exp(j2\pi f_0 t) \\ r_c(t) &= S\sqrt{E_t} f(t - 2t_0 - \frac{f_d}{f_0} t) \exp(j2\pi(f_0 + f_d)(t - 2t_0 - \frac{f_d}{f_0} t)) + n(t), \end{aligned} \tag{6.1}$$

where E_t is the energy of the transmitted signal. The complex envelope of the emitted signal is represented by $f(t)$, and it is assumed that $\int f(t)^2 dt = 1$. The parameter S determines the scaling of the signal, which is introduced by the scattering. The effect of attenuation has not been included in this model, but it will be in the following. The time of arrival is equal to $2t_0$ and is determined by the distance R_0 from the transducer to the scatterer: $t_0 = R_0/c$. The influence of the noise is represented by the additive term $n(t)$. The noise is assumed random and Gaussian distributed.

When multiple scatterers are present, the acquired signal will consist of the sum of contributions from these scatterers [34], [48]. The individual contributions are influenced by the beam width and the attenuation. In medical ultrasound the width of the emitted wave is sought minimized in the directions perpendicular to the direction of propagation to increase resolution. Only scatterers lying within the spatial region bounded by the beam width will interact with the propagating wave and contribute to the acquired signal. The signal amplitude of the pulse varies over the extent of the beam, and the scattered signal is modeled as a scaled version of the emitted pulse. The effect of attenuation must also be included. As the attenuation is frequency dependent, the individual frequency components in the emitted signal experience different attenuation. Therefore the attenuation cannot be modeled as a mere amplitude scaling. A linear filter $g(t, t_0)$ is used instead [48], and the resulting signal is obtained by convolving the envelope of the emitted signal with $g(t, t_0)$ [3], [48]. The impulse response of the transducer influences the signal. In this discussion this effect is included in the envelope of the emitted signal. When only considering linear propagation and linear

interaction the simplified model for the acquired signal is [48]:

$$\begin{aligned} e(t) &= \sqrt{E_t} f(t) \exp(j2\pi f_0 t) \\ f_a(t - 2t_i - \frac{f_{d,i}}{f_0}t) &= g(t - 2t_0 - \frac{f_d}{f_0}t, t_i) * f(t - 2t_i - \frac{f_{d,i}}{f_0}t) \\ r_c(t) &= \sqrt{E_t}\sum_i S_i b_i(t_i) f_a(t - 2t_i - \frac{f_{d,i}}{f_0}t) \exp(j2\pi(f_0 + f_{d,i})(t - 2t_0 - \frac{f_d}{f_0}t)) + n(t), \end{aligned} \quad (6.2)$$

where the index i indicates the contribution from the i^h scatterer. The term $b_i(t_i)$ determines the scaling due to the beam width, and it is dependent on the spatial position indicated by t. It should be stressed again that this model is not complete and does not include all factors of the *in-vivo* situation. The model only indicates some features of the RF-signals. The modeling of the influence from the beam width as a mere scaling is an approximation to the real situation. It is assumed that the influence only depends on the spatial position, but in reality a temporal dependence also exists. The full description of the influence is determined by the so-called spatial impulse response [3], [49]. The influence gets to be a filtering rather than a scaling of the pulse. A thorough discussion of the spatial impulse response and the resulting filtering is out of the scope of this work. As discussed in the introduction to this chapter the Doppler shift and the attenuation changes the spectrum of the propagating pulse. The latter factor dominates, so the signal alteration due to the Doppler shift is negligible. The spatial location of the individual scatterers determines the temporal position of the contribution to $r_c(t)$ from each scatterer. The velocity information is not extractable from one RF-line, since t_i only determines the scatterers location in the signal. The change in position should be determined, and therefore a set of RF-lines must be acquired.

In medical ultrasound the set of RF-lines are acquired within a few milliseconds. Within this time frame the velocity of the scatterers can be assumed constant [50]. The movement of the scatterers between acquisitions is usually less than 1 mm even for high blood velocities [3]. The following example verifies this. The blood velocities take values up to 1-2 m/s. The time between acquisitions are determined by T_{prf}, which is usually less than a few milliseconds. For a velocity of 1 m/s and a T_{prf} of 1/4000 s the movement between acquisitions is equal to $z = v \cdot T_{prf} = 0.25$ mm. So the movement is very small. The beam width and beam profile can be assumed constant within this range [3]. The attenuation will be slightly different. Still the scattered response acquired from each scatterer is similar in consecutive acquisitions. The velocity of the individual scatterers vary, and therefore their relative distance changes between acquisitions. The sum of contributions from a group of scatterers in consecutive acquisitions is not identical. The change in distance between scatterers is very small due to the short time frame for acquisition of several RF-lines and the level of the blood velocities. If two neighboring scatterers move at a velocity of 0.4 and 0.5 m/s, the scatterers will move 0.1 and 0.125 mm, respectively. The distance between the scatterers changes by 0.025 mm between acquisitions, which can be considered small. The response from a group of scatterers are not identical but similar in a set of consecutive RF-lines. Similar patterns, which are temporally shifted, exist in the RF-lines. An example hereof is plotted in Fig. 6.1, where four consecutive RF-lines are plotted. The RF-lines have been generated with Field II [26], [27]. No noise is present in the signals. The plot clearly reveals that the RF-lines are not identical but fairly similar. The blood velocity estimators make use of this property and track the movements of the patterns. An estimate of the velocity can then be obtained.

The acquired RF-signals are a result of the contributions from a large number of scatterers. If the contributions from each of the scatterers are assumed independent, the Central Limit Theorem [51] states that the distribution of the amplitude in the RF-signals is Gaussian distributed. The blood particles cannot be assumed independent [3]. Still, investigations have shown that the amplitude distribution is approximately Gaussian distributed with a zero mean [3], [52]. The amplitudes follow a complex Gaussian distribution with zero mean, when the amplitudes are represented on complex form.

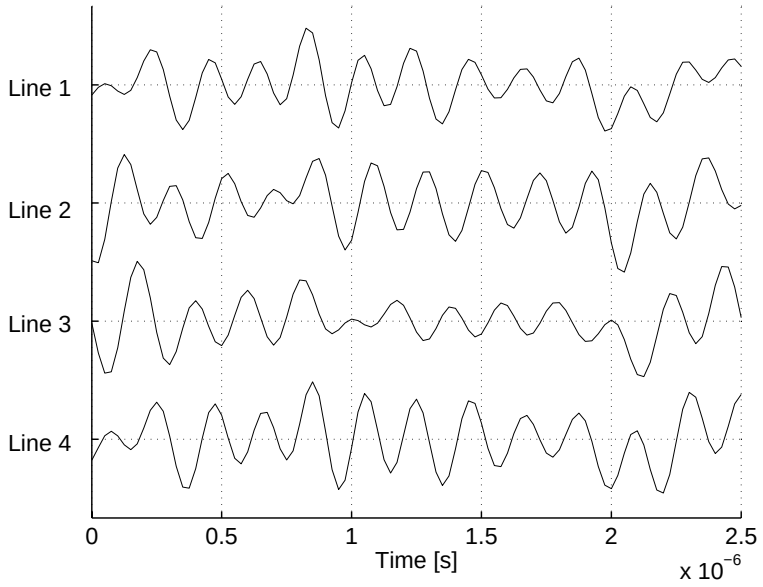

Figure 6.1: A set of consecutively acquired RF-lines, where scatterers have moved between acquisitions.

6.2 Evaluation data

Before moving on to the actual introduction and evaluation of a selection of estimators, the data sets used for the evaluation are defined. A performance evaluation requires access to a set of data, where the exact velocity distribution are known a priori. Many factors influence the performance of the estimators. Some are strictly related to the estimator algorithm, whereas others arise because of the properties of the RF-signals. An example of the latter is the velocity distribution of the scatterers. The individual scatterers move at different velocities relative to their spatial location in the vessel. *In-vivo* RF-data are characterized by carrying information for a spread of velocities within a set of samples due to the emission of a pulse of finite length and finite beam width. This complicates the estimation process as several samples are used. The increased inaccuracy is not due to the estimator itself but due to the properties of the RF-signals. Two types of data set - synthetic and simulated data - are used in the present study. The synthetic data set will determine the performance of the estimator itself, where the effect of beam width, velocity spread, and attenuation have been eliminated. The simulated data will resemble *in-vivo* RF-signals, where the properties of these signals thereby get to influence the performance.

6.2.1 Synthetic data

In this study a signal, which contains some of the features from the *in-vivo* situation, is employed in the generation of the synthetic data. A signal, which resembles the measured response from the interaction between the emitted pulse and a distribution of blood scatterers along a line, has been chosen. In this way the effect of beam width has been eliminated. The issue of velocity spread does not exist, if all scatterers move at the same constant speed. The blood scattering is modeled as a white, zero mean, random signal with a Gaussian amplitude distribution [3]. The transducer excitation pulse is a sine pulse, and the number of cycles are estimator dependent. Present estimators require either a short (1-2 cycles) or a long pulse (from about 6 cycles). The impulse response of the transducer is modeled as a Hanning weighted sine signal with 2 cycles. The interaction between the propagating pulse and the scatterers is described by a convolution, so the scattered signal is computed by convolving the blood and pulse signal. Noise is introduced and modeled as white, zero mean Gaussian noise. No correlation exists between the noise in consecutive lines.

This approach equals the method used by Jensen [3]. The generation of the synthetic data goes through the following steps:

- generate the scattered signal,
- convolve the scattered signal with the impulse response of the transducer in transmission and reception,
- time shift this signal according to the velocity, the pulse repetition frequency, and the line number. A set of consecutive lines are generated,
- add noise to each of the generated signals, and
- perform matched filtering to minimize the noise content.

For the data set generated here, the pulse repetition frequency is 4 kHz. Two set of signals are generated, where the length of the excitation pulse is 1.5 and 6 cycles, respectively. The generation process is repeated four times, as four velocities - $v = [10, 20, 30, 40]$ cm/s - are investigated. One hundred noise realizations are generated to make a statistical evaluation. The mean, μ, and the standard deviation, σ, on the velocity estimates are obtained.

Synthetic data, which can be employed for evaluating the performance of the individual estimators, have been generated. As will become clear in the following sections, the performance of the estimators is influenced by a number of factors and parameters. This influence is determined by performing an evaluation, where the factors and parameters are varied. The influence from the following factors and parameters will be evaluated:

- the number of RF-lines N_l available prior to echo-canceling,
- the number of samples N_s from an RF-line used in the estimation,
- the sampling frequency f_s,
- the signal to noise ratio : SNR $\in [0, 10, 20, 30]$ dB,
- the type of echo-canceling filter : no echo-canceling filter, the 2^{nd} order HP filter, or the regression line filter (see Chapter 5).

The possible range of values for N_l, N_s, and f_s are dependent on the estimator and echo-canceling filter and will be defined in each situation. In this study the number of samples used are stated in units of pulse lengths. A pulse length is defined as the length of the resulting pulse obtained, when the excitation pulse has been convolved with the transducers impulse response in transmit and receive. The number of samples within one pulse length are dependent on the sampling frequency. In Fig. 6.2 a section of two consecutive RF-lines are plotted, when a short and a long excitation pulse are used, respectively. Only one velocity estimate will be computed, and samples from the middle section of the RF-lines will be employed in the estimation. All RF-lines are de-noised with the matched filter (see Section 5.1) prior to performing the estimation.

6.2.2 Simulated data

Simulated data resembling RF-data acquired from the carotid artery have been generated with Field II [26], [27] (see Chapter 4). The *in-vivo* properties with respect to velocity spread, attenuation, and beam width are then present in the data and get to influence the estimation process. A focusing and apodization scheme

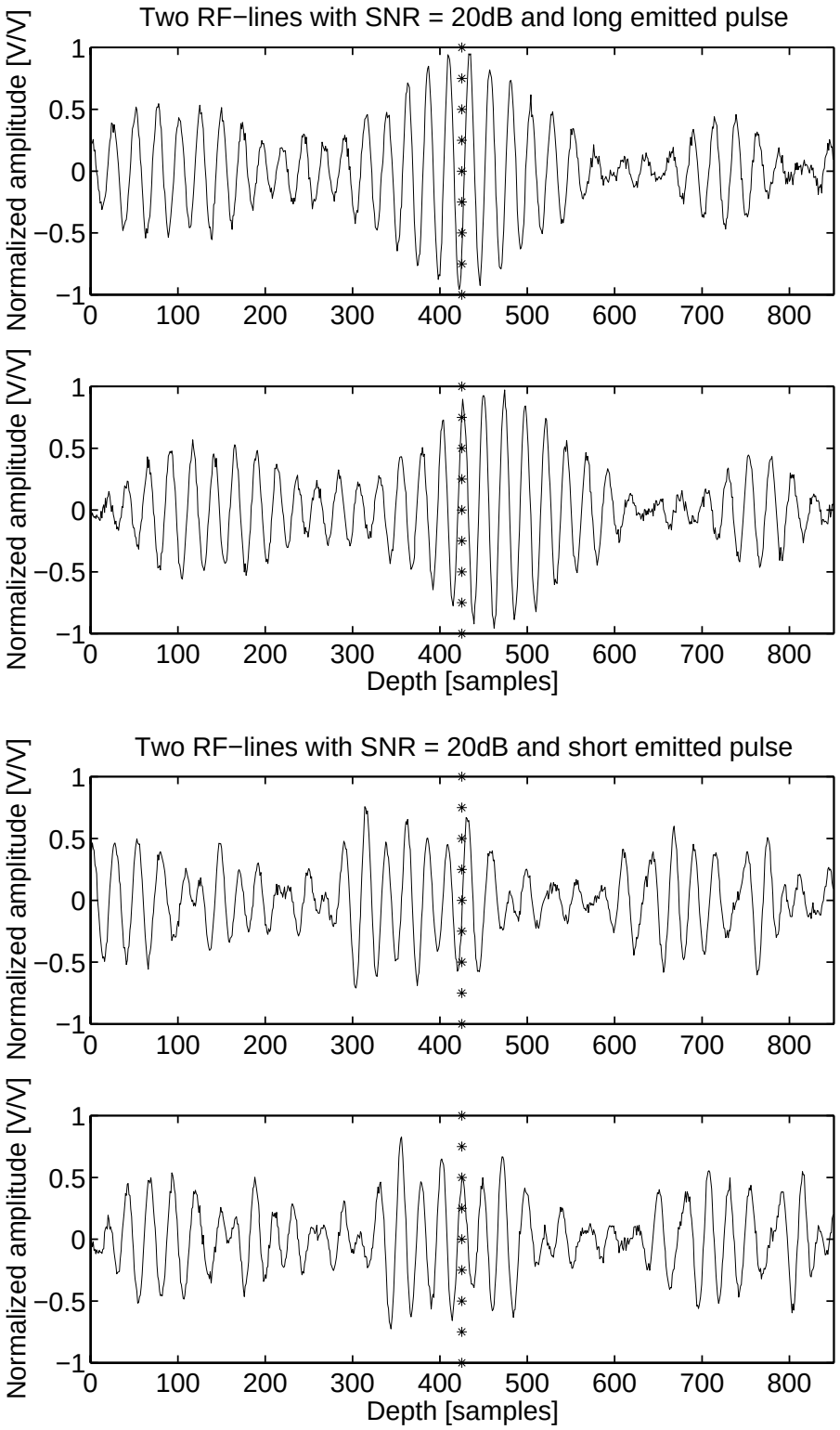

Figure 6.2: Examples of the synthetic data, when emitting a long (two upper plots) and short (two lower plots) pulse. A section of two consecutive RF-lines spaced 6 pulse emissions are plotted. The SNR is 20 dB.

Parameter	Value
Center frequency of pulse	5.0 MHz
No. of elements	128
Pulse length	1.5 / 6 cycles
Geometric focus	17 mm
Pulse repetition frequency	4 kHz
Sampling frequency	40 MHz
Radius of vessel	3 mm
Angle between vessel and transducer	35^o

Table 6.1: Choice of parameters for the simulated data used in the performance evaluation of the blood velocity estimators.

matching a B-K Medical 3535 scanner connected to a linear array with 128 elements has been used. The parameters for the current simulation are listed in Table 6.1. Both tissue motion (from pulsation) and blood motion are included (see Chapter 4). One cardiac cycle (one second) has been simulated. The lateral extent of the CFM image equals half the imaging range of the transducer. The pulsing strategy alternates between acquiring one RF-line for the B-mode image, and then 8 RF-lines for the blood velocity estimation. With this scan setup a frame rate of 10 frames/s is obtained for the CFM-mode image and 5 frames/s for the B-mode image. The low frame rate is of no concern in the current study, as the aim is to evaluate the performance of the estimators rather than displaying many images. The sound velocity is equal to 1540 m/s. The simulated data are de-noised with the matched filter. The echo-canceling is performed with the 2^{nd} order HP filter. The resulting, filtered signals are processed by the estimators. The velocity profiles in 10 consecutive frames can be determined from the data set.

6.3 Autocorrelation estimator

A group of scatterers traveling at a constant axial velocity of v_z will have moved a distance $z = v_z \cdot T_{prf}$ between two emissions. As the scatterers have moved, the time of interaction between the scatterers and the pulse is shifted. As discussed in Section 6.1, the part of the signal representing the interaction with this particular group of scatterers will (ideally) show up at a new temporal location ξ in the acquired response. The new location should be determined. The emitted signal and the acquired response are oscillating signals. Inspection of the acquired RF-signals from two consecutive emissions at the same temporal location will reveal that the movement can be approximated by a phase shift, ϕ, of the oscillating signal [3]:

$$\begin{aligned} r_{cfm}(t, l+1) &= r_{cfm}(t+t_s, l) \\ t_s &= \frac{\phi}{2\pi f_0} \\ \phi &= -2\pi f_0 \frac{2v_z}{c} T_{prf}, \end{aligned} \tag{6.3}$$

where l and $l+1$ indicate two consecutive lines, and f_0 is the center frequency. The movement and thereby velocity of the group of scatterers can be determined, if an estimate of the phase shift can be computed. For this to hold it is assumed that the velocity is constant within the time frame of the two emissions. This assumption is valid, when the time frame is less than 10 ms [50]. Different approaches can be employed to obtain an estimate of the phase shift [3]. The acquired RF-signals are sampled upon acquisition. The signals are therefore represented by a discrete set of samples. An estimation scheme applicable for this situation must be developed. Kasai et al. [53] derived a relation, which computes an estimate of the phase based on

the discrete samples. In order to determine the direction of the motion (towards/away from transducer) the complex signal is needed, which in the following will be represented by: $r_{c,cfm} = x + j \cdot y$. The imaginary part - the Q component - is the 90^o phase shift of the real part - the I component. In digital systems the Q component is determined by Hilbert transforming the RF-signal, since this transformation is capable of shifting all frequency components the desired 90^o. The estimate of the phase shift at a given temporal location in the RF-signal is [3]:

$$\hat{\phi} = \arctan\left(\frac{y(l)x(l-1) - y(l-1)x(l)}{x(l)x(l-1) + y(l)y(l-1)}\right). \tag{6.4}$$

The terms in the denominator and numerator correspond to the real and imaginary part of the discrete, complex autocorrelation function at lag 1, which is defined as [3]:

$$\hat{R}(1) = \frac{1}{(N_{l,e}-1)N_s} \sum_{l=1}^{N_{l,e}-1} \sum_{j=1}^{N_s} r^*_{c,cfm}(l,j) r_{c,cfm}(l+1,j), \tag{6.5}$$

where $*$ represents the complex conjugate operation. Averaging over a range of samples, N_s, and over a set of lines, $N_{l,e}$, has been introduced in (6.5) to improve the accuracy of the phase estimate. $N_{l,e}$ is the number of lines available for the estimation after echo-canceling. In reality the estimate of the phase shift is computed from the echo-canceled data. The subscript "echo" will be omitted here and in the following sections to make the equations easier to read. By combining the above equations an estimate of the velocity in a given temporal location can be computed. The estimate is:

$$v_z = -\frac{c}{2\pi f_0 2T_{prf}} \arctan\left(\frac{\mathrm{Im}\{\hat{R}(1)\}}{\mathrm{Re}\{\hat{R}(1)\}}\right), \tag{6.6}$$

where Im and Re denote the imaginary and real part, respectively. With this definition motion away from the transducer is positive, and motion towards the transducer is negative. This sign convention will be employed for all estimators. Equation 6.6 determines the velocity component along the propagation direction of the pulse. The true velocity is obtained by determining the projection angle and then compensating here fore.

The output of the inverse tangent operation is limited to the interval $]-\pi,\pi]$. This corresponds to a movement of half a wavelength. If the true phase shift is outside this interval, it will get projected into this interval. A bound on the maximum velocity that can be estimated correctly arises:

$$v_{max} = \frac{c}{4}\frac{1}{f_0 T_{prf}}. \tag{6.7}$$

The level can be varied by proper choice of the scan parameters. The maximum velocity bound is increased, if the pulse repetition frequency, $f_{prf} = 1/T_{prf}$, is increased, and/or a transducer with a lower center frequency is employed. The projection of phase shifts outside the interval follows a cyclic nature. A true phase shift of $\pi + \hat{\phi}$ will be aliased down to $-\pi + \hat{\phi}$.

The standard deviation, σ_v, on the velocity estimate computed from two consecutive lines is [3]:

$$\sigma_v = \sqrt{\frac{c}{4\pi^2 f_0^2}\frac{1}{T_{prf}T_p}|v_z|}. \tag{6.8}$$

It is a function of the center frequency, the time between emissions, the temporal length of the emitted pulse T_p, and the magnitude of the velocity. A longer pulse gives a better estimate. By decreasing the number of pulse emissions per second (f_{prf}) the standard deviation decreases. A trade off between the accuracy and the maximum detectable velocity thereby occur with respect to choosing T_{prf}. The same problem exists for the choice of f_0. The accuracy increases as the center frequency is increased, but the maximum detectable

velocity decreases. Averaging over several samples and lines decreases the variance. The expression for σ_v does not include the influence of the noise on the estimation.

The above velocity estimator is termed the autocorrelation estimator and determines the phase shift. The method is said to be a narrow band, frequency domain method. An oscillating signal arises, if the samples from consecutive lines are plotted as a function of the line number. The oscillation frequency is determined by the phase shifts. Estimation of ϕ equals estimation of the frequency. Therefore the method is referred to as a frequency method. The narrow band term refers to the employment of a long pulse in the emission.

A long pulse is required to obtain an estimate with a low standard deviation. Unfortunately then another issue gets to influence. In the human arteries the velocity varies as a function of spatial location (see Chapter 3). A long pulse will interact with a range of scatterers, which move at different velocities. The recorded RF-signal in a temporal interval equal to the pulse length therefore will contain information for a range of velocities due to the velocity spread. The estimated velocity for a given temporal position will be an average of the velocities. The variance on the estimate will increase for increasing spread. The expression in (6.8) does not take into account the velocity spread [3]. A finite pulse length has to be employed. The choice of pulse length depends on the desired resolution, but pulse lengths from 6 to 32 wavelengths are employed.

Although the recorded RF-signals are matched filtered to remove noise, the noise component within the frequency band of the RF-signal is not removed. The remaining noise will decrease the accuracy of the estimate. The presence of noise introduces a positive bias on the velocity estimate, when the echo-canceling is performed with the HP filter [3] or the regression line filter. This can be proven by splitting up the signal in two terms - the desired response and the noise - and passing them through the equations related to the echo-canceling and the estimation. The noise influence does not cancel out. The bias decreases as the SNR increases. The low velocities are degraded the most [3].

The autocorrelation estimator has the following disadvantages:

- a long pulse has to be emitted, which lowers the axial resolution and the accuracy of the estimate due to the velocity spread,
- the maximum detectable velocity is bounded, and aliasing errors occur if the velocity exceeds the boundary,
- the choice of the pulse emission frequency influences the estimate both positively and negatively, so a compromise must be made with respect to accuracy and maximum detectable velocity,
- the estimate is biased due to the noise influence.

The method is very popular though, as the computational load is low. The number of multiplications $N_{m,autocor}$ and additions $N_{a,autocor}$ performed to calculate the complex autocorrelation function $\hat{R}(1)$ are:

$$\begin{aligned} N_{m,autocor} &= 4N_s(N_{l,e}-1)+1 \\ N_{a,autocor} &= 3N_s(N_{l,e}-1). \end{aligned} \tag{6.9}$$

The determination of $N_{m,autocor}$ and $N_{a,autocor}$ are based on the definition of $\hat{R}(1)$ in (6.5). It is assumed that 4 multiplications are performed to compute the product of two complex numbers. The last multiplication comes from multiplying with the normalization term $1/(N_s(N_l-1))$. Implementation of the estimator requires that the variables in the equations are assigned a value. The variables are the number of lines N_l, the number of samples N_s, and the sampling frequency f_s.

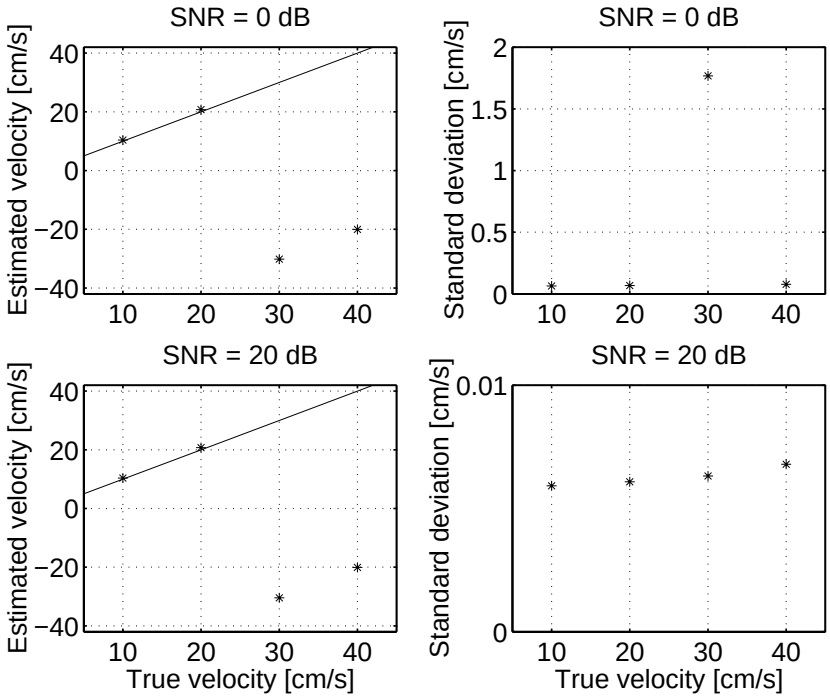

Figure 6.3: Performance of the autocorrelation estimator: the true (—) and estimated (*) velocities along with the standard deviation for a SNR of 0 and 20 dB. No echo-canceling filter was applied. Nine lines were employed. The sampling frequency equals 30 MHz, and the number of samples are equal to one pulse length.

6.3.1 Performance on synthetic data

The performance of the estimator on synthetic data has been determined, and the results are presented in the following. The estimator parameters were varied as follows:

- number of lines: $N_l \in [3, 6, 9, 12, 15, 18, 21, 24]$,
- sampling frequency: $f_s \in [15, 20, 30, 40, 60]$ MHz,
- number of samples: $N_s \in [0.25, 0.5, 0.75, 1.0, 1.25, 1.5, 1.75, 2.0]$ times the length of the emitted pulse. The length in samples is dependent on the sampling frequency.

When the regression line echo-canceling filter is employed, the number of lines employed in the estimation must be an odd number. In that situation the evaluation is only performed for the odd values of N_l. The maximum velocity detectable is 30.8 cm/s.

In Figures 6.3-6.11 the performance of the estimator is plotted, as the different parameters and factors (echo-canceling filters) are varied. The performance is determined by means of the mean and the standard deviation on the estimates over the 100 realizations. When one parameter is varied, the others are kept constant at: the SNR is 10 dB, N_s is equal to one pulse length, N_l are 9, and the sampling frequency is 30 MHz. Please refer to Appendix B for tables containing the performance for the range of combinations of the velocities, the parameter values, and the echo-canceling filters. The best performance is defined as the estimation, which produces the lowest standard deviation and still is able to compute a velocity estimate, which is within $\pm$ 2 cm/s of the true velocity. A good estimate has been determined, if the mean is within $\pm$ 2 cm/s of the true velocity, and the standard deviation is below 1 cm/s.

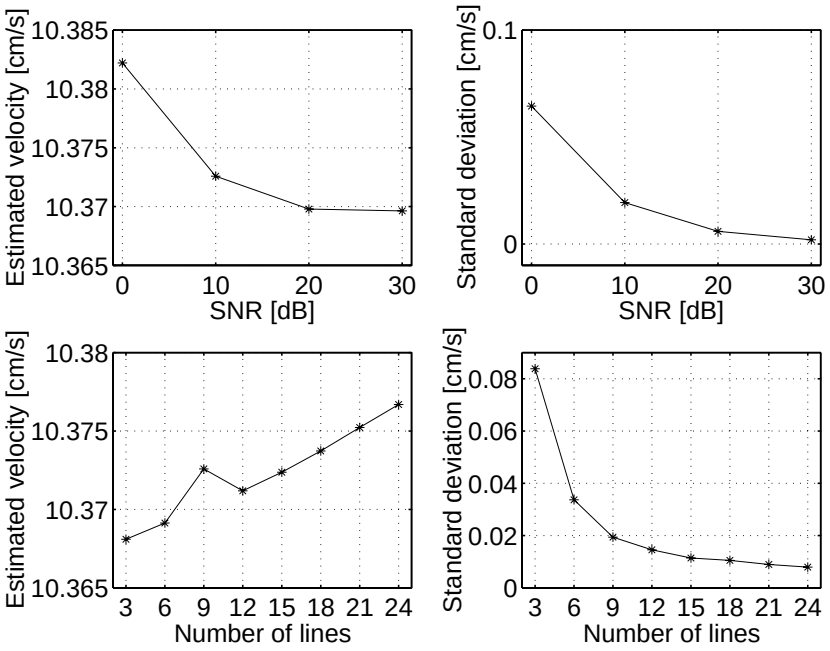

Figure 6.4: Performance of the autocorrelation estimator as a function of the number of lines and the SNR. No echo-canceling filter applied. The sampling frequency is 30 MHz, and the number of samples are equal to one pulse length. The true velocity is 10 cm/s.

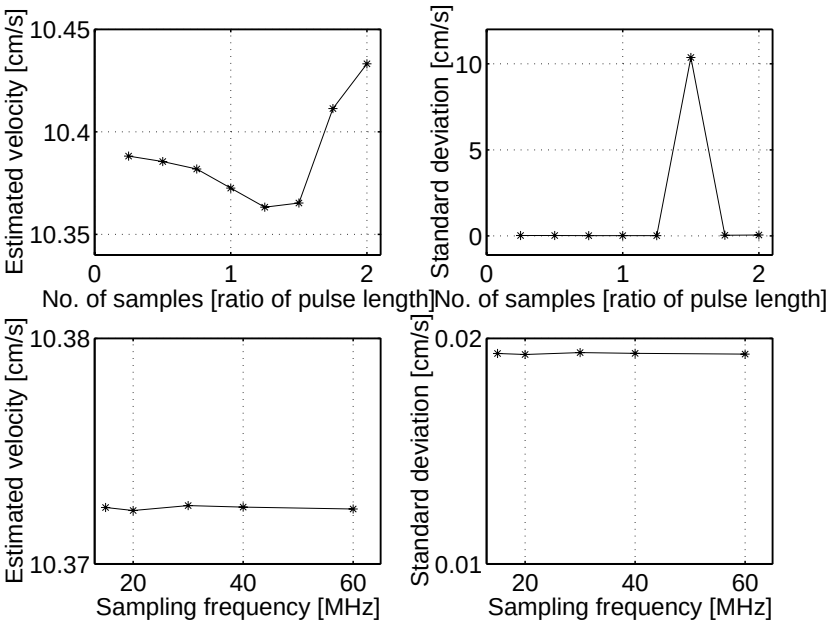

Figure 6.5: Performance of the autocorrelation estimator as a function of the number of samples and the sampling frequency. No echo-canceling filter applied. The SNR is 10 dB, and 9 lines were employed. The true velocity is 10 cm/s.

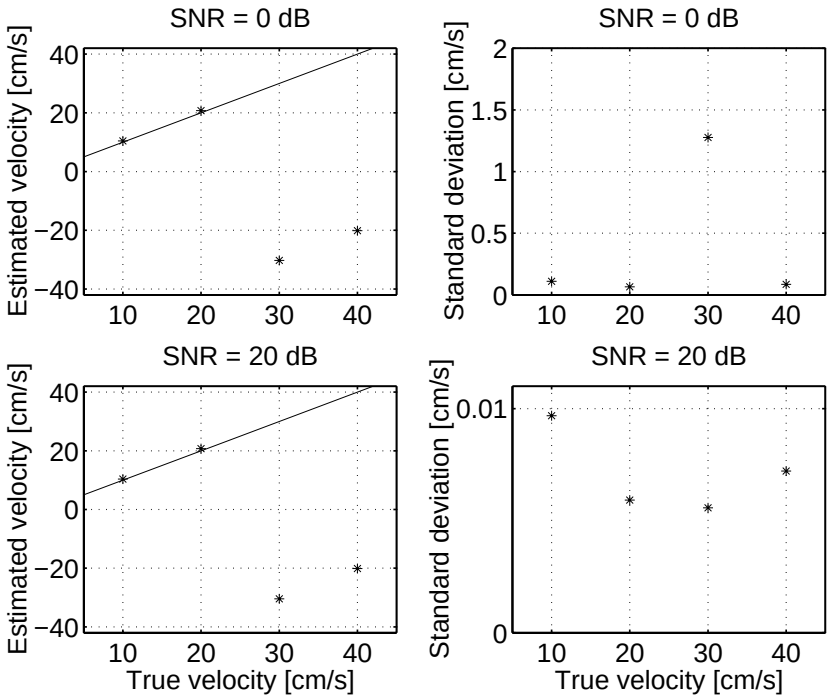

Figure 6.6: Performance of the autocorrelation estimator: the true (—) and estimated (*) velocities along with the standard deviation for a SNR of 0 and 20 dB. HP echo-canceling filter was applied. Nine lines were employed. The sampling frequency is 30 MHz, and the number of samples are equal to one pulse length.

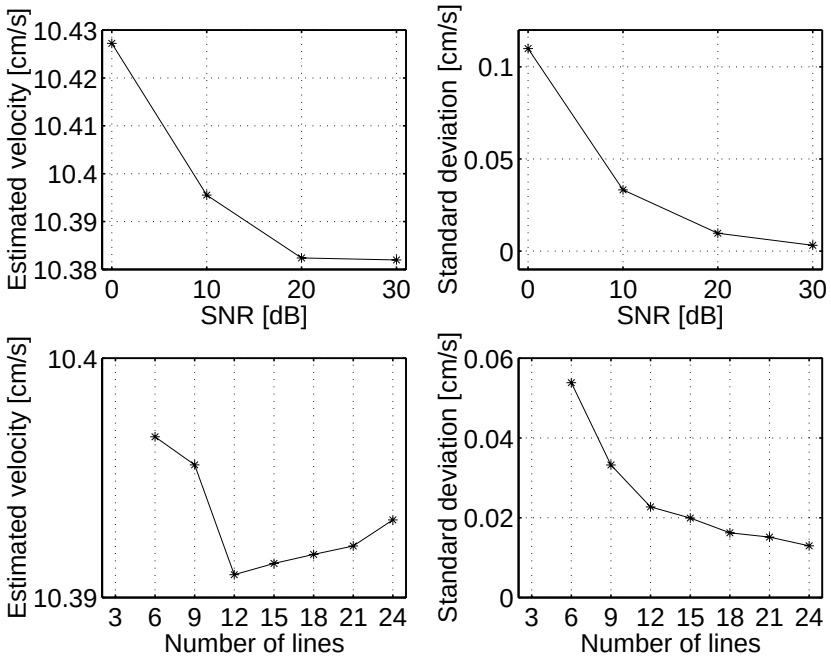

Figure 6.7: Performance of the autocorrelation estimator as a function of the number of lines and the SNR. HP echo-canceling filter applied. The sampling frequency is 30 MHz, and the number of samples are equal to one pulse length. The true velocity is 10 cm/s.

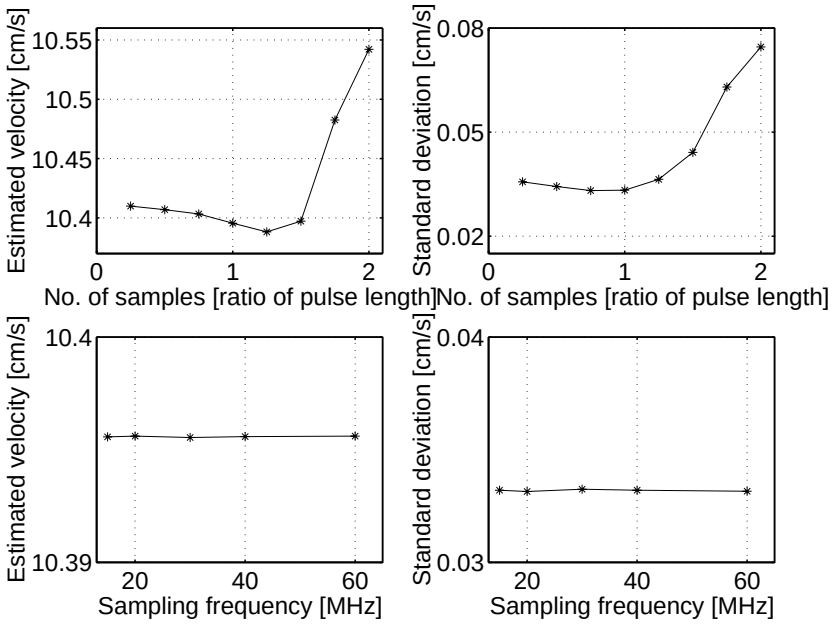

Figure 6.8: Performance of the autocorrelation estimator as a function of the number of samples and the sampling frequency. HP echo-canceling filter applied. The SNR is 10 dB, and 9 lines were employed. The true velocity equals 10 cm/s.

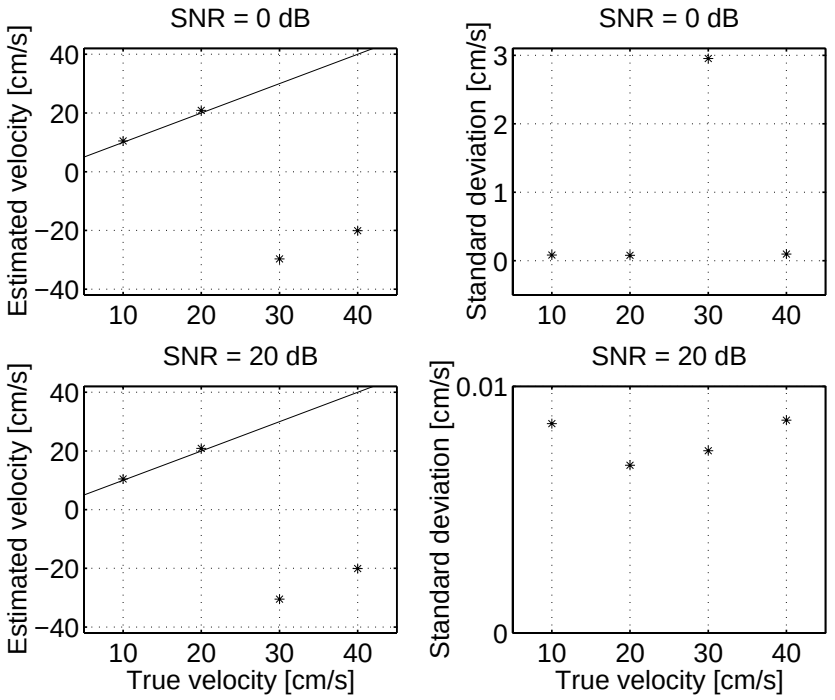

Figure 6.9: Performance of the autocorrelation estimator: the true (—) and estimated (*) velocities along with the standard deviation for a SNR of 0 and 20 dB. Regression line echo-canceling filter was applied. Nine lines were employed. The sampling frequency is 30 MHz, and the number of samples are equal to one pulse length.

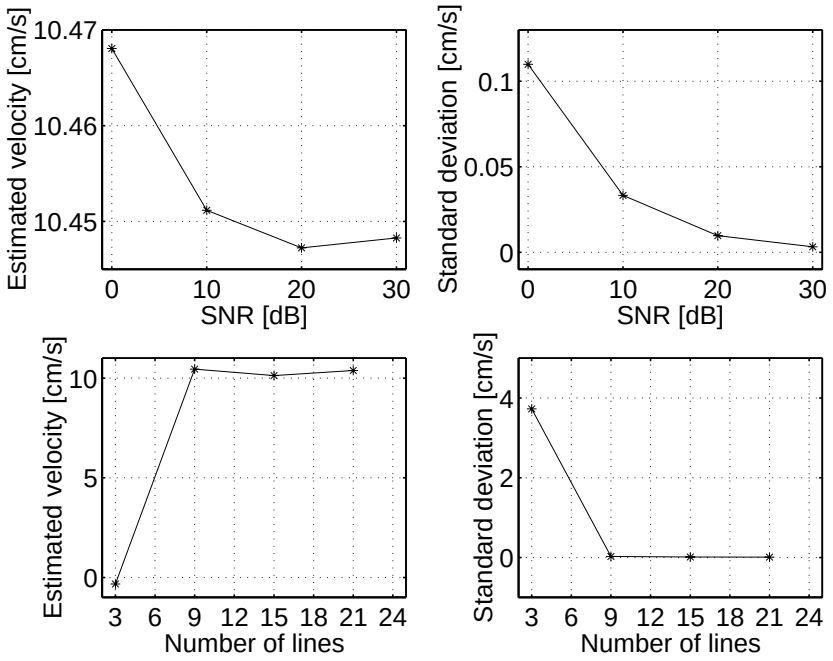

Figure 6.10: Performance of the autocorrelation estimator as a function of the number of lines and the SNR. Regression line echo-canceling filter applied. The sampling frequency is 30 MHz, and the number of samples are equal to one pulse length. The true velocity is 10 cm/s.

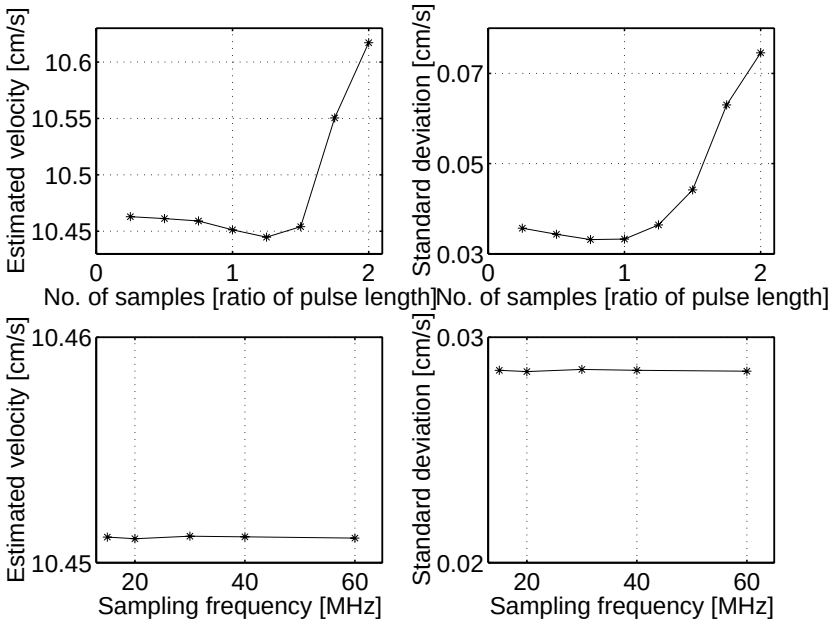

Figure 6.11: Performance of the autocorrelation estimator as a function of the number of samples and the sampling frequency. Regression line echo-canceling filter applied. The SNR is 10 dB, and 9 lines were employed. The true velocity is 10 cm/s.

The bound on the maximum velocity that can be estimated and the resulting aliasing show up clearly in Figures 6.3, 6.6, and 6.9. Although the bound is 30.8 cm/s, the velocity estimate of the scatterers moving at 30 cm/s is aliased due to the influence of the noise. The problem is usually rectified by increasing the pulse repetition frequency. Unfortunately this has the effect of decreasing the imaging depth. The results for the velocities 10 and 20 cm/s are discussed in the following. The estimator is biased, and the bias takes a positive value (as expected). The bias is dependent on the SNR, N_s, N_l, and the applied echo-canceling filter. The bias takes a value in the range from 1-10 % of the true velocity for the given data set. For some choices of N_s the bias increases as N_l increase, and vice versa. The first situation is present in Fig. 6.4. An oscillation between decreasing and increasing bias as a function of N_l is also seen (see Fig. 6.7). The following trends can be derived from the non-aliased results:

- the standard deviation decreases as the number of lines are increased,
- the standard deviation decreases as the SNR increases,
- the choice of N_s, which gives the best performance, is dependent on the SNR and the number of lines. The variation on the standard deviation for the span of parameter values is about a few millimeters per second in most cases, so the difference in performance is very small. The variation decreases as the SNR increases,
- the performance is independent of the sampling frequency.

The levels of the mean and the standard deviation vary, when the different echo-canceling filters are employed. The influence of the different filters is not unambiguous. It depends on the velocity level and the choice of N_l and N_s. The difference in the level of the standard deviations for the 3 filters is very small. The maximum variation is a few millimeters per second, but most often it is much less than 1 mm/s. A successful estimation can be obtained with either of them. This conclusion is valid, if more than 3 RF-lines are available. The regression line filter is not able to produce good estimates for any combination of the other parameters, if N_l are equal to 3 lines. The three data points do not contain enough information to make a good echo-canceling. The filtering alters the signal, and makes the subsequent estimation difficult (impossible).

The autocorrelation estimator performs well, as long as the velocities are below the aliasing bound. A non-zero, positive bias exists. Many lines should be employed to obtain the highest accuracy. The choice of the number of samples is dependent on the velocity level, the number of lines, and the SNR, but the variation is small for the span of values. Samples equal to one pulse length give an overall good performance.

6.3.2 Performance on simulated data

Other issues than optimum performance must be considered when implementing the estimator on a commercial scanner for CFM-mode imaging. An infinite number of lines cannot be used, as 1) the velocity can only be assumed constant within 10 ms, and 2) the frame rate goes down dramatically. In CFM-mode one wants to follow the temporal evolution of the velocities in a bounded spatial area. A finite number of lines must be employed, and the choice depends on the spatial extent of the CFM image and the desired frame rate. A lower limit also exists, as a certain level of accuracy on the estimation is required. Eight consecutive RF-lines are available for each lateral position in the simulated data, and the performance of the estimator will be evaluated for this situation. The HP echo-canceling filter will be applied. The investigations above showed that the estimates obtained were very similar for the different echo-canceling filters. Echo-canceling is necessary in *in-vivo* RF-signals. Since the HP filter is computationally simple, it has been preferred over the regression line filter. The velocity spread limits the number of samples that can be employed. The performance of the autocorrelation estimator on simulated data will be evaluated with N_s equal to one pulse

length. The choice of f_0 and T_{prf} ensures that no aliasing errors will occur. Thereby the autocorrelation estimators ability to perform on a span of velocities can be evaluated.

Figure 6.12 shows 2D plots of the estimated velocity profiles for a systolic and diastolic frame in the cardiac cycle. The true blood velocity image shows the true blood velocity values at the spatial position defined by the spatial location of the center of the pixel. The need for applying some kind of discrimination algorithm prior to displaying the estimates is evident, as non-zero velocity estimates occur in the tissue region. In the systolic frame the estimator is not able to produce good estimates along the anterior wall in the left half of the image. The vessel appears to be narrower than what is really the case. This problem does not show up to the same extent in the other frames. The true and estimated velocities are not identical. The trends with respect to the velocity levels are the same but some variation about the true values is present in the estimated values. This variation is due to the influence of the velocity spread, SNR, the echo-canceling filter, and the estimator parameters. In Fig. 6.13 two lines from the 2D plots are plotted as a function of depth. The variation about the true values shows clearly. The majority of the estimates in the upper half of the vessel (above the center axis of the vessel) are underestimated, whereas an overestimation is seen for quite a few of the estimates in the lower half of the vessel. This trend holds for all frames in the simulated cardiac cycle. The highest deviations from the true value are observed for the estimates along the posterior vessel wall. A few estimates in the last image line (to the right) take values below 0 m/s. This is not consistent with the true velocity values. The velocity profile for the carotid artery only takes positive values. The velocities range from 0 cm/s to 50 m/s for the current simulation of the blood flow. A measure of the estimates, which deviate significantly, has been determined. If the estimated velocities are outside the velocity range from -10 cm/s to 80 cm/s, they are considered as highly deviating. In the 10 frames given here 0.4 % of the estimates deviate significantly.

When the individual frames are combined into a movie, the noisy variation of the estimates about the true values disturbs the eye. Therefore post-processing (see Chapter 7) must be performed prior to displaying the results to minimize the variation. Still the autocorrelation estimator has captured the variations of the blood velocities within the cardiac cycle and throughout the vessel very well. The estimated velocities for each frame have been combined into one postscript-file, which is enclosed on CD-rom. Please refer to Appendix C for a description of how to locate and access the file.

The root-mean-square (RMS) error on the blood velocity estimation is used as the objective measure of performance. The RMS error is 0.06 m/s and 0.07 m/s for a SNR of 20 and 10 dB, respectively. As expected the performance improves as the SNR increases.

6.4 Cross-correlation estimator

As a group of scatterers move, the pattern in the RF-signal, which resembles the interaction between the pulse and these scatterers, moves (ideally) to a new temporal position expressed by t. An estimate of the temporal shift can be obtained by performing a cross-correlation analysis for a range of temporal shifts [3]. For each shift the original pattern is correlated with signal segments in the consecutively acquired RF-signals, which are shifted according to the temporal shift under investigation. The values of the resulting cross-correlation function give a measure of how similar the compared segments are. The cross-correlation function peaks, when the best match has been determined. The temporal shift, which relates to the maximum value of the cross-correlation function, is the estimate of $\hat{t}_s$. The estimator determines the time shift and therefore is said to be a time domain technique. The cross-correlation is performed on the recorded, real signals. The recorded RF-signals are split up in a number of segments i_{seg} with N_s samples in each segment.

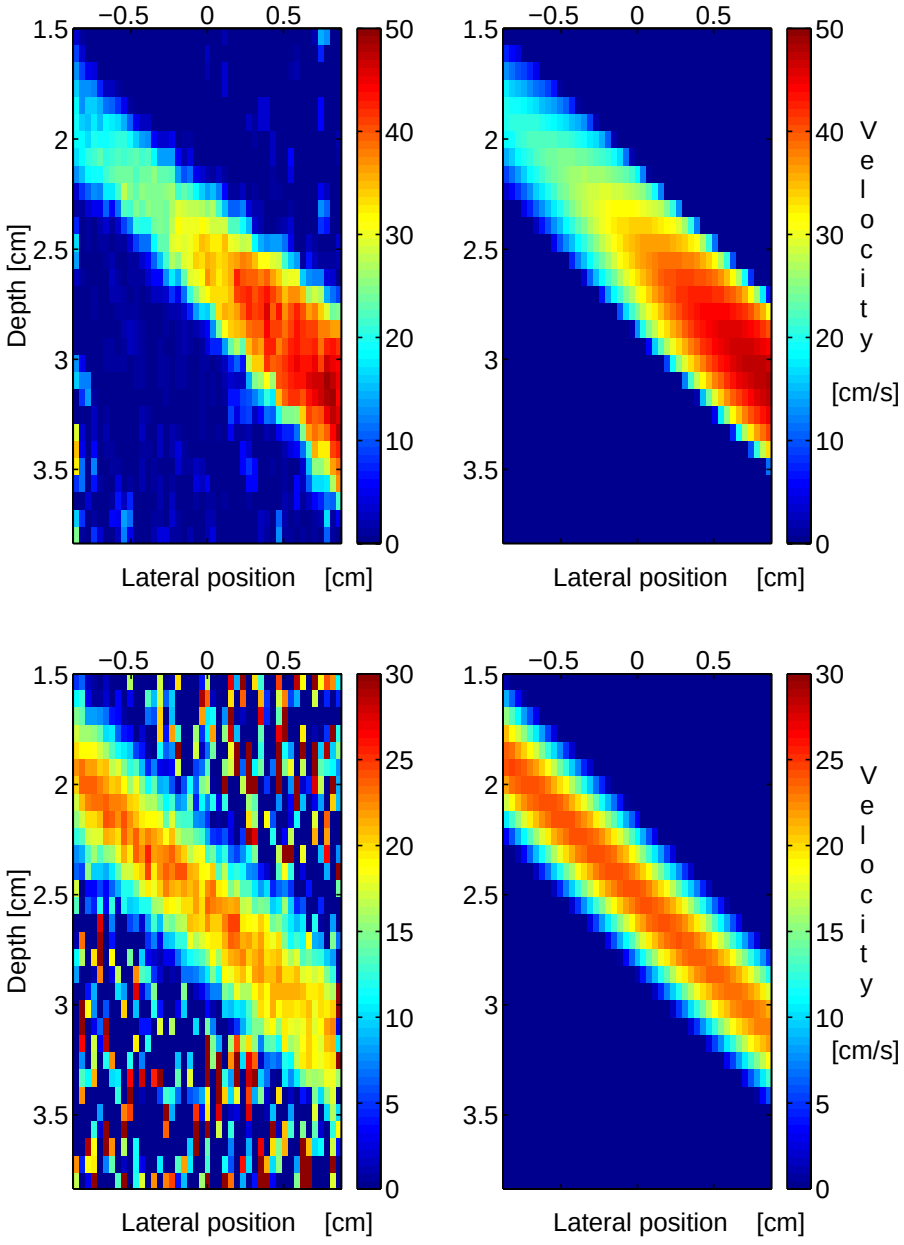

Figure 6.12: Autocorrelation estimator: The estimated (left) and the true (right) velocities for a systolic (upper two plots) and a diastolic frame (lower two plots). The SNR is 20 dB.

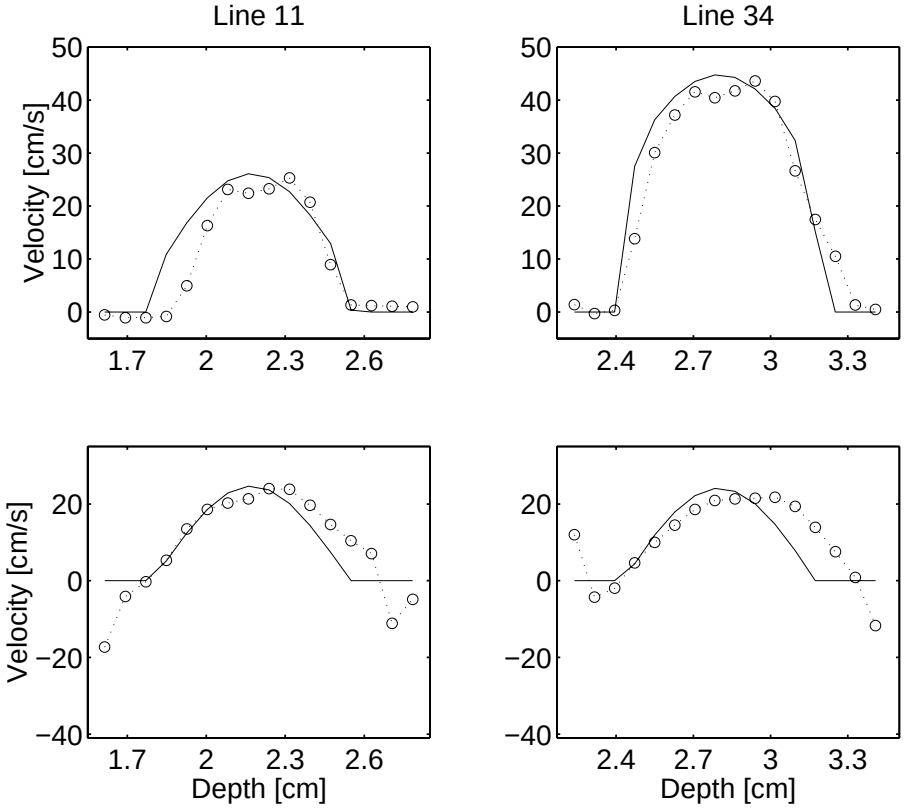

Figure 6.13: Autocorrelation estimator: Plot of line 11 and 34 in the images for the systolic (upper 2 plots) and diastolic frame (lower 2 plots). The SNR is 20 dB.

The velocity is determined for each segment. The cross-correlation is defined as [3]:

$$\hat{R}_{l,l+1}(n, i_{seg}) = \frac{1}{N_s} \sum_{k=0}^{N_s-1} r_{cfm}(l, k + i_{seg} N_s) r_{cfm}(l+1, k + i_{seg} N_s + n), \tag{6.10}$$

where n is the discrete time shift in number of samples. The computations are performed on the echo-canceled signals, but the subscript "echo" has been omitted in (6.10).

Employment of the cross-correlation estimator requires that a span of temporal shifts are investigated. This increases the computational load significantly compared to the autocorrelation estimator. Infinite time resolution is not implementable, so a set of discrete temporal shifts are investigated. A discrete cross-correlation function is computed, where the true maximum of the cross-correlation function is not necessarily present. The maximum can be determined by performing an interpolation of the cross-correlation function. This will increase the temporal resolution and increase the accuracy on the estimate of the time shift. The RF-signals are discrete signals. The discrete time shift is not necessarily an integer number of samples. Interpolation is required to determine the signal values for the temporal shift under investigation. This can be avoided though, if a discrete set of integer sample shifts are investigated instead. The accuracy on the cross-correlation estimate can be increased by averaging over a set of lines. In order for the discrete cross-correlation to be equivalent to the analog cross-correlation, the sampling frequency must be equal to four times the maximum frequency in the signal [3]. The estimate of the blood velocity is:

$$\hat{v}_z = \frac{c}{2T_{prf}} \hat{t}_s, \tag{6.11}$$

where $\hat{t}_s$ [s] is the estimated time shift.

In principle the correlation analysis can be carried out for any value of the temporal shift (and thereby any velocity). In practice the search range is limited, as the blood velocity levels are bounded. If n spans from $-N_s$ to N_s, the maximum detectable velocity is determined by the value of N_s. The minimum velocity is limited by the time quantization. The relations for the velocity bounds are:

$$\begin{aligned} v_{min} &= \frac{c}{2}\frac{f_{prf}}{f_s} \\ v_{max} &= \frac{c}{2}N_s\frac{f_{prf}}{f_s}. \end{aligned} \tag{6.12}$$

The sampling frequency influences both bounds. An increase in f_s will lower the bound on the minimum detectable velocity, but unfortunately also lower the bound on the maximum detectable velocity.

The employed relation for the cross-correlation does not include any normalization with the energies of the two segments. This makes the estimator vulnerable to the amplitude levels in the two segments, which are correlated. As the RF-signals are oscillating, similar patterns will show up a number of times throughout the signals. The amplitudes will vary, but the position of positive and negative values, and zero crossings will match between the signals. If one segment within the search range have a high amplitude compared to the amplitude of the original pattern, a high value of the cross-correlation will occur. This value will then be higher than the value of the cross-correlation for the true match of segments. An example will be given to make this point more clear. Consider the situation given in Fig. 6.14. In the top plot the original segment (solid line) and the true, matching segment from the consecutive line (indicated with circles) are plotted. The cross-correlation value is 37.4. In the bottom plot the original segment is compared with a different segment in the consecutive RF-line. Inspection of the plot clearly reveals that the two segments do not match in amplitude. The cross-correlation value is 38.9, which is higher than the value for the true match. The cross-correlation method states that the true time shift relates to the maximum value of the cross-correlation. In this case an incorrect estimate of the time shift and thereby velocity will be determined. The varying amplitude levels in the RF-signals introduce a level of uncertainty in the estimation and can result in false detection of the true time shift.

The accuracy on the velocity estimate is dependent on [3]:

- the noise level,
- observation time with respect to number of lines used in the estimation,
- beam width, since the acquired RF-signals will represent the interactions with a wider lateral range of scatterers (moving at different velocities), if the beam width is increased,
- velocity spread, and
- decorrelation between consecutive acquired RF-lines. As the scatterers move at different velocities the distance traveled between two emissions will be different. The summed responses will not give identical patterns in two consecutive lines, and this property is referred to as decorrelation.

An approximate expression for the variance on the estimate of the time shift, when two consecutive lines are employed, is [3]:

$$\sigma(\hat{t}_s) = \frac{1}{\pi B}\sqrt[4]{\frac{3}{4BT_s}}\sqrt[4]{1+\frac{1}{SNR^2}+\frac{1}{2SNR^4}}, \tag{6.13}$$

where B is the bandwidth of the emitted pulse, and T_s is the temporal length of the segment ($T_s = N_s/f_s$). A high bandwidth is preferred to minimize the variance. This is obtained by emitting a short pulse. The number of RF-lines available for estimation can be increased by one, if 1) the same excitation pulse is used to acquire RF-signals for the B-mode image and the velocity estimation, and 2) the emission strategy is

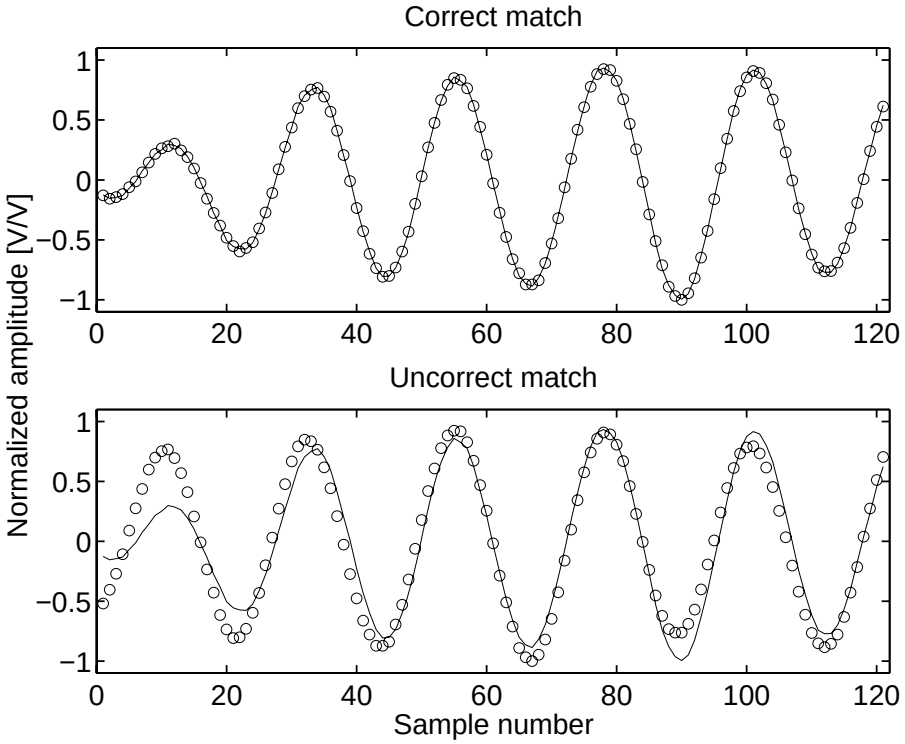

Figure 6.14: Comparison of the original segment (—) with two different segments (o) from the consecutive RF-line.

chosen properly. Averaging over a long segment (T_s high) is desirable to lower the variance on the estimate. The variance on the estimate decreases as the SNR increases.

The computational load of the estimator is high, since the computations in (6.10) have to be performed for each time shift evaluated. The number of multiplications, $N_{m,crosscor}$, and additions, $N_{a,crosscor}$, performed to calculate the cross-correlation function in (6.10) for $N_{v-steps}$ temporal shifts are:

$$\begin{aligned} N_{m,crosscor} &= N_s(N_{l,e}-1)N_{v-steps} \\ N_{a,crosscor} &= (N_s-1)(N_{l,e}-1)N_{v-steps}. \end{aligned} \tag{6.14}$$

The averaging over a set of lines is included in $N_{m,crosscor}$ and $N_{a,crosscor}$.

To decrease the computational load, Foster [54] and Bonnefous [55] suggested to perform the cross-correlation estimation using only the sign value of the samples. The sign can be represented by 1 bit, whereas the sampled signal values need 9 or 17 bit. The signs are assigned according to the following definitions:

$$r_{s,cfm}(n) = \begin{cases} 1 & r_{cfm}(n) \geq 0 \\ -1 & r_{cfm}(n) < 0 \end{cases} \tag{6.15}$$

where n indicates the sample number. The estimation follows the same procedure as the ordinary cross-correlation estimator. Only difference is that the RF-signals r_{cfm} are substituted with the signals $r_{s,cfm}$. The multiplication of signs can be implemented by a Boolean XOR operation [3].

6.4.1 Performance on synthetic data

The performance of the cross-correlation estimator has been evaluated on the synthetic data, where a short excitation pulse was used. A lower bound on the sampling frequency is introduced in order for the discrete

and analog cross-correlation function to be identical. The estimator parameters were varied as follows:

- number of lines: $N_l \in [3, 6, 9, 12, 15, 18, 21, 24]$,
- sampling frequency: $f_s \in [30, 40, 60, 120]$ MHz,
- number of samples: $N_s \in$: $[0.25, 0.5, 0.75, 1.0, 1.25, 1.5, 1.75, 2.0]$ times the length of the emitted pulse. The length in samples is dependent on the sampling frequency.

A good and stable performance is obtained, when the mean is within $\pm$ 2 cm/s of the true velocity, and the standard deviation is less than 2 cm/s. The velocity range from -50 cm/s to 50 cm/s was investigated in steps of 1 cm/s. Interpolation of the determined cross-correlation function is performed to increase the resolution on the estimates. The following trends can be derived from the results:

- the cross-correlation estimator does not suffer from aliasing problems,
- the segment length with respect to N_s must be 2 pulse lengths to ensure a stable estimation for all SNRs, values of N_l, f_s, and the velocity levels (for a few combinations of the parameters this is not valid). This conclusion holds, when no echo-canceling filter and the HP filter are applied. When the regression line filter is employed, a good performance can also be obtained, when N_s equal 1.75 pulse lengths. This is valid, if more than 3 lines are employed. The regression line filter cannot perform at all, when only 3 lines are used,
- the performance is slightly dependent on the sampling frequency but no unambiguous systematism has been determined,
- the velocities are estimated both to high and to low (relative to the true value), and the over-/underestimation do not follow any systematism,
- the standard deviation on the estimate decreases and approaches zero as the SNR increases.

In general only few combinations of the parameters produce good estimates. The influence of the different parameters is less unambiguous than was the case for the autocorrelation estimator. Only one thing is clear: a high number of samples should be used in the estimation of the cross-correlation. Both echo-canceling filters can be employed with success. Their influence on the estimation is dependent on the parameters. The output of the estimation after echo-canceling sometimes out perform the estimation with no echo-canceling filter. A lower standard deviation on the estimate is obtained in this case.

In Figures 6.15-6.17 examples of the performance of the estimator are plotted as the different parameters are varied. The HP echo-canceling filter was applied. When one parameter is varied, the others are kept constant at: the SNR is 10 dB, the number of lines are 9, the sampling frequency is 30 MHz, and the number of samples are equal to 2 pulse lengths. Tables, which contain the performance for the range of combinations of the parameters, the velocity values, and the echo-canceling filters, are enclosed in Appendix B.

The velocity estimates and the standard deviations obtained with the autocorrelation and the cross-correlation estimators have been compared for velocities below the aliasing limit of the autocorrelation estimator. The HP filter was applied and the estimator parameters are chosen to give stable performance. The results reveal the following trends:

- the difference between the true and the estimated velocity is often higher for the cross-correlation estimator than with the autocorrelation estimator,

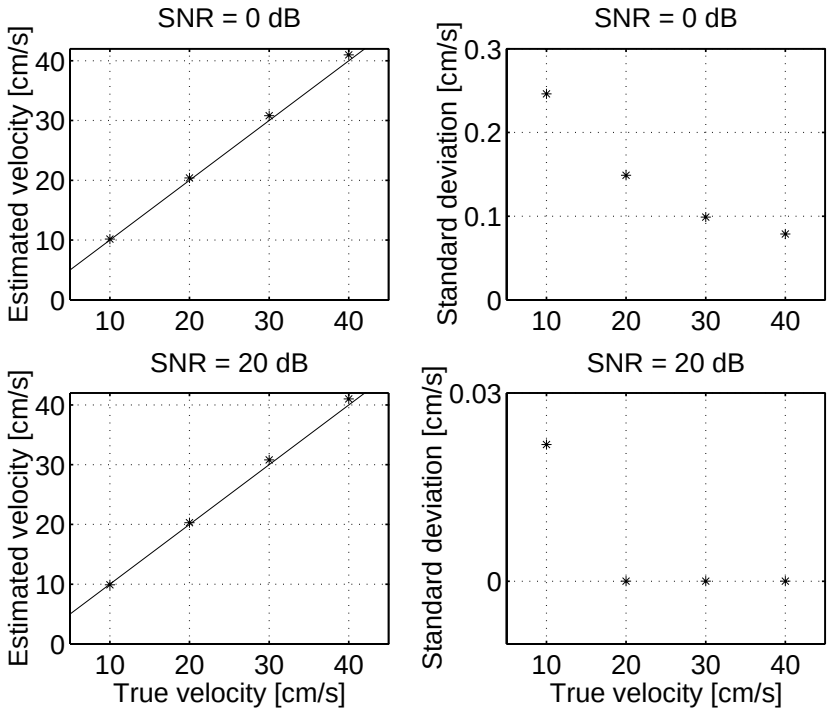

Figure 6.15: The cross-correlation estimator: the true (—) and the estimated (*) velocities along with the standard deviation for a SNR of 0 and 20 dB. HP filter applied for echo-canceling. The number of lines are 9, f_s is 30 MHz, and N_s are 2 pulse lengths.

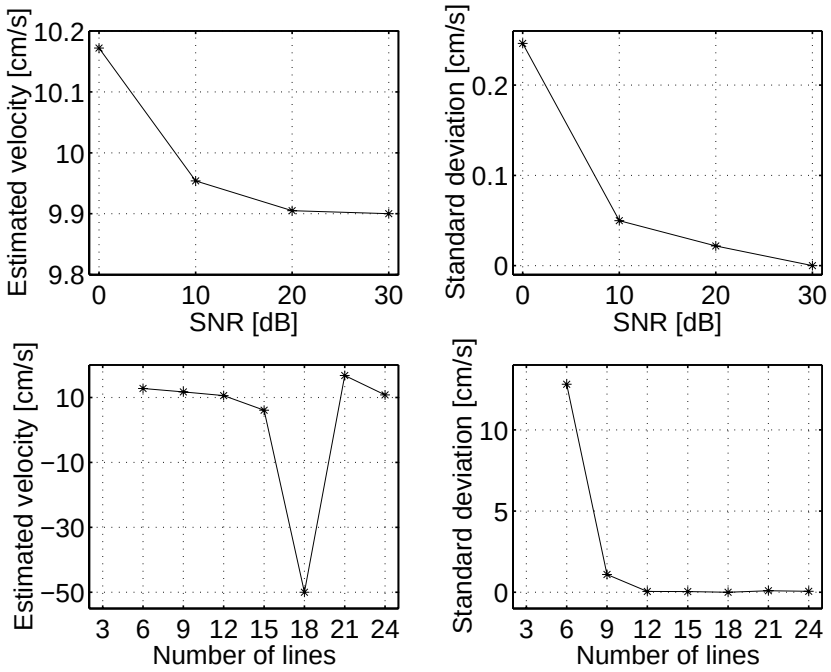

Figure 6.16: Performance of cross-correlation estimator as a function of the number of lines and the SNR. HP filter applied for echo-canceling. The sampling frequency is 30 MHz, and N_s are 2 pulse lengths. The true velocity is 10 cm/s.

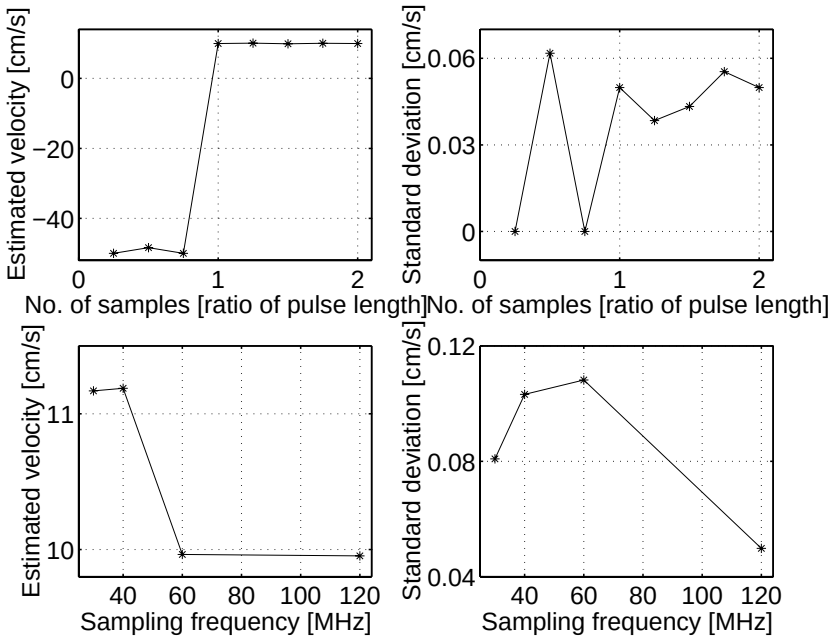

Figure 6.17: Performance of cross-correlation estimator as a function of the number of samples and the sampling frequency. HP filter applied for echo-canceling. The number of lines are 9, and the SNR is 10 dB. The true velocity is 10 cm/s.

- the standard deviation on the estimate is lower for the autocorrelation estimator at low SNRs. As the SNR increases the standard deviation approaches zero for both estimators. The cross-correlation estimator approaches zero faster than the autocorrelation estimator,
- the performance of the autocorrelation estimator for different values of the parameters is more unambiguous.

Both estimators have some advantages and disadvantages, so the choice of which to use depends on the situation. The computational load has previously been of much concern due to the limitations of the electronics. With the advances in electronics in the last decade this problem is of less concern. If the optimum f_{prf} is used, and the aim is to obtain an estimate with high accuracy that is stable to different choices of the parameters, then the autocorrelation estimator should be employed. If the number of estimates along the RF-line is of concern, the cross-correlation estimator should be used. The employment of a wideband excitation pulse increases the axial resolution, so more estimates are usually computed along the axial direction.

6.4.2 Performance on simulated data

The performance on the synthetic data indicated that N_s should be 2 pulse lengths. As higher values of N_s were not investigated, the best choice of N_s could be even higher. Therefore the performance on the simulated data has been investigated for a range of N_s values. The HP filter was employed for echo-canceling, so the performance of the autocorrelation and the cross-correlation estimators can be compared. This procedure will be employed for all estimators, which are introduced and evaluated in the following. The SNR in the data set is 20 dB. The velocity range from -50 cm/s to 50 cm/s was investigated in steps of 1 cm/s.

The RMS error as a function of N_s is plotted in Fig. 6.18. The RMS error decreases as N_s increase. A high value of N_s should be used, if the aim is to obtain the lowest error as possible. The investigations have not been carried out for values of N_s over 7 pulse lengths. A visual inspection of the estimated velocity

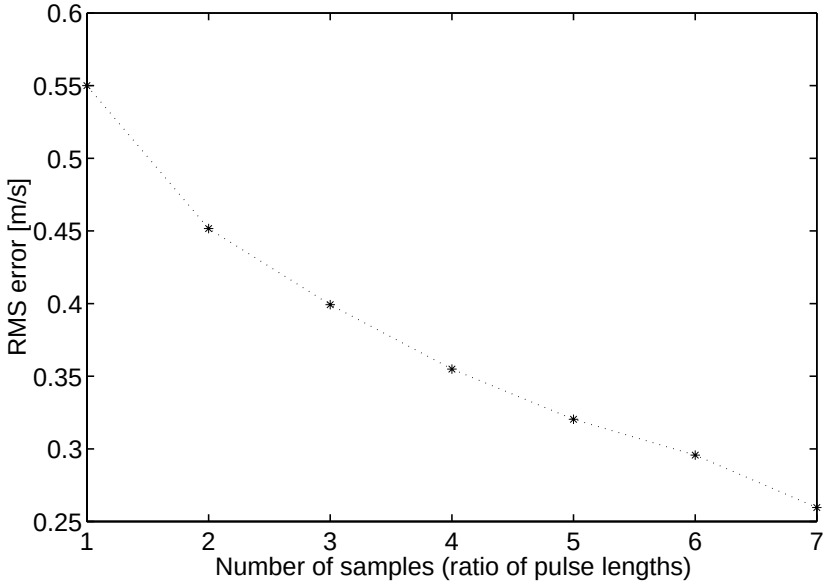

Figure 6.18: The RMS error ([m/s]) as a function of N_s for the cross-correlation estimator. The SNR is 20 dB.

profiles reveals that a high value of N_s also has a negative influence on the estimation. Figure 6.19 shows the problem. Only estimates within the vessel are shown. Non-zero estimates are also present outside the vessel, so a discrimination algorithm must used to determine, which of the estimates should be displayed. Estimates, which are represented by the maximum and minimum value of the velocity scale, take values above or below the maximum and minimum value, respectively. As N_s increase, the estimator fails to produce good estimates in part of the vessel in the frame, which contains the systolic phase. The estimates are close to 0, which are not consistent with the actual velocity in the vessel. The influence is especially pronounced in the upper, left part of the vessel. This is not desirable, as the aim is to produce accurate estimates across the full spatial extent of the vessel. The problem decreases for lower values of N_s. The increased RMS error at low values of N_s is mainly due to the occurrence of more estimates, which deviate significantly in amplitude from the true value. They are a result of the amplitude problem discussed earlier. Some are still present in the systolic frame in Fig. 6.19, but many have been removed. By comparing the estimates obtained when N_s are equal to 3 and 7 pulse lengths, this decrease in the number of highly deviating estimates shows. Figure 6.20 shows the estimated velocity profiles for the systolic frame and a diastolic frame, when N_s are equal to 3 pulse lengths. It is the same two frames, which were plotted to show the performance of the autocorrelation estimator. The incorrect estimates occur as single and grouped errors. A group consists of two or more estimates, which are neighbors along the lateral and/or axial directions in the image. Some kind of post-processing filter must be applied to reduce the amplitude of these estimates prior to displaying them. The incorrect estimates occur mostly along the posterior wall and the lower half of the vessel (below the center axis of the vessel). The velocities are underestimated. An objective measure for the number of highly deviating estimates has been determined. It is the same measure used for the autocorrelation estimator. For the cross-correlation estimator a total of 14.7 % of the estimates take values outside the velocity range from -10 cm/s to 80 cm/s.

Apart from the highly deviating estimates, the cross-correlation estimator is able to produce estimates, which follow the overall trends of the velocity variation across the vessel and throughout the cardiac cycle. In Fig. 6.21 a set of lines from the systolic and diastolic frame in Fig. 6.20 are shown separately. The variations about the true velocities vary for the different frames. The lowest variation mostly occurs along the center axis of the vessel, where the estimates are a little underestimated. An overestimation is seen along the vessel walls. Post-processing is required to minimize this variation prior to displaying the estimates. In Appendix C the estimates for all 10 frames are available from a postscript-file, which is enclosed on CD-

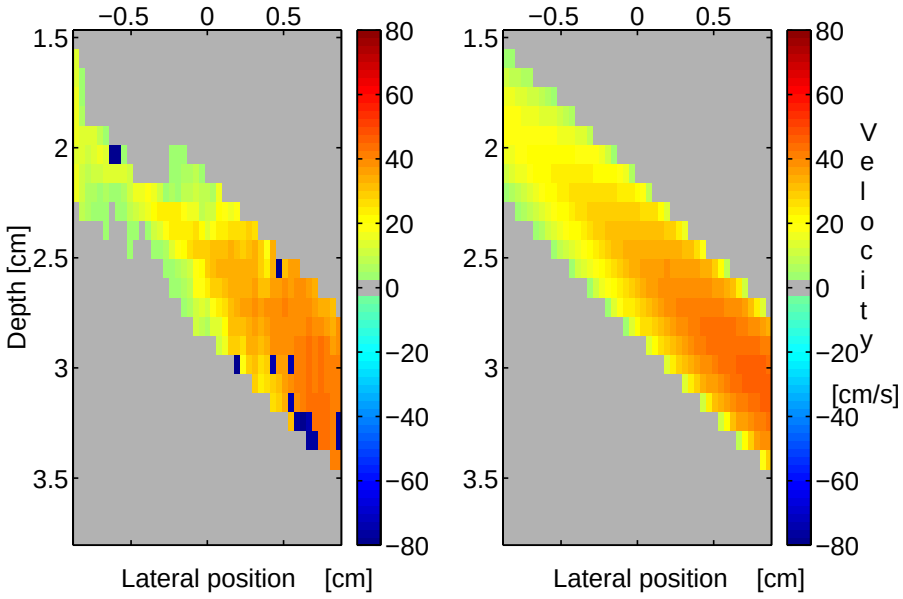

Figure 6.19: Cross-correlation estimator: The estimated (left) and the true (right) velocities for the systolic frame, when N_s equal 7 pulse lengths. The SNR is 20 dB.

rom.

The amplitudes of the variation and the distribution of under-/overestimated velocities differ from what is experienced with the autocorrelation estimator. Overall the autocorrelation estimator produces estimates, which follow the variations of the true velocities better than the cross-correlation estimator. The autocorrelation estimator out performs the cross-correlation estimator, when no aliasing occur. This conclusion is based on the RMS error, the visual inspection of the images, and the measure of the number of highly deviating estimates.

6.5 Extended autocorrelation estimator

The autocorrelation estimator has been preferred in most commercial scanners previously due to the high computational load of the cross-correlation estimator. To overcome the aliasing problem of the autocorrelation estimator, Lai and Torp [56] have developed a new estimator that combines the autocorrelation and the cross-correlation estimators. The phase estimate from the autocorrelation estimator may be off by an integer number n_p of 2π:

$$\phi_{true} = \phi_{autocor} + n_p 2\pi. \tag{6.16}$$

As the cross-correlation estimator can handle any search range, a set of possible true phase shifts for a range of $n_p = [..., -2, -1, 0, 1, 2, ...]$ can be evaluated by the cross-correlation estimator. The maximum of the resulting cross-correlation function gives the estimate of the correct phase-shift. The estimator is called the Extended Autocorrelation method (EAM), and the steps involved are listed below:

- compute an initial estimate of the phase shift employing the autocorrelation estimator,
- determine a set of possible values of the phase shift (a total of N_p) by adding and subtracting an integer number of 2π,
- compute the temporal shifts, which correspond to the set of possible phase shifts,

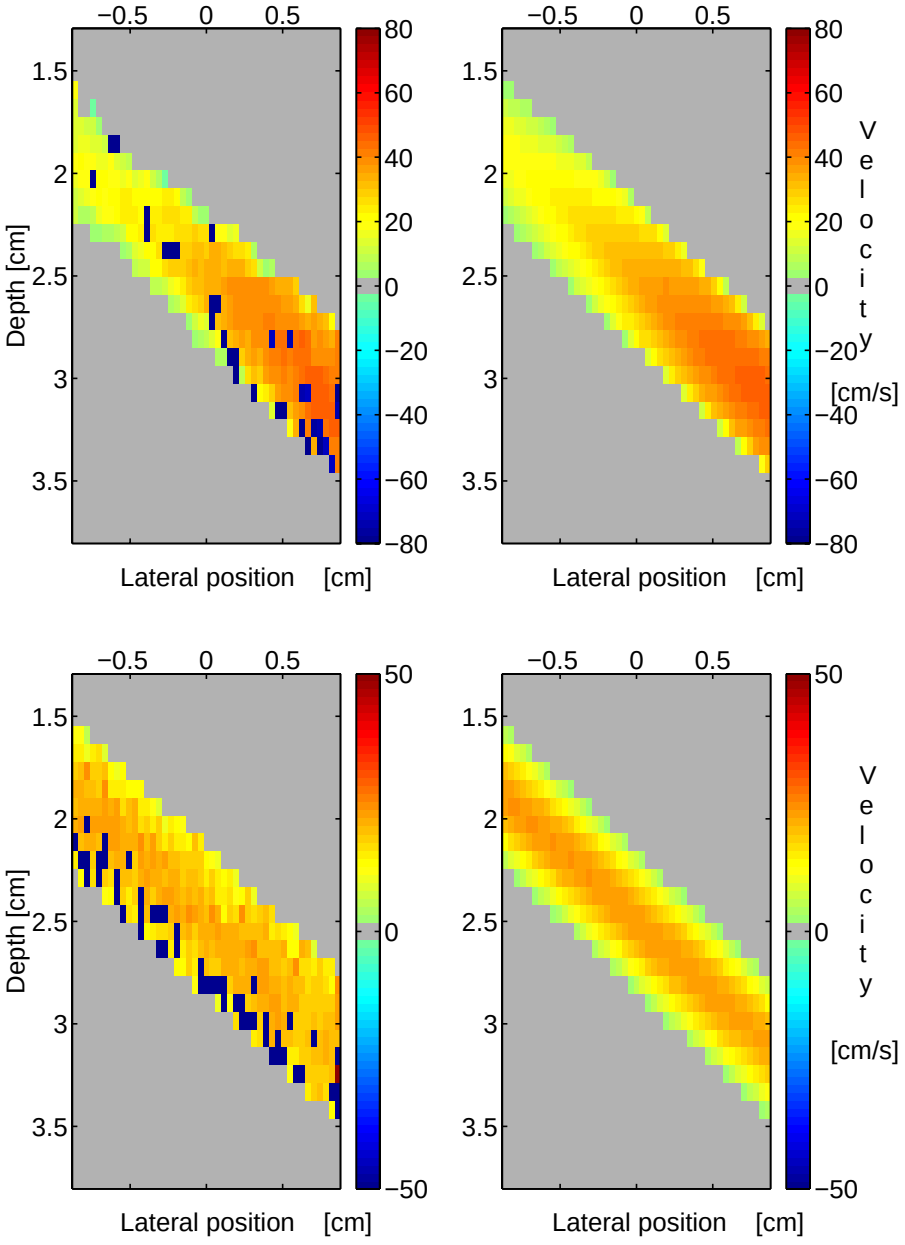

Figure 6.20: Cross-correlation estimator: The estimated (left) and the true (right) velocities for a systolic (upper two plots) and a diastolic frame (lower two plots), when N_s equal 3 pulse lengths. The SNR is 20 dB.

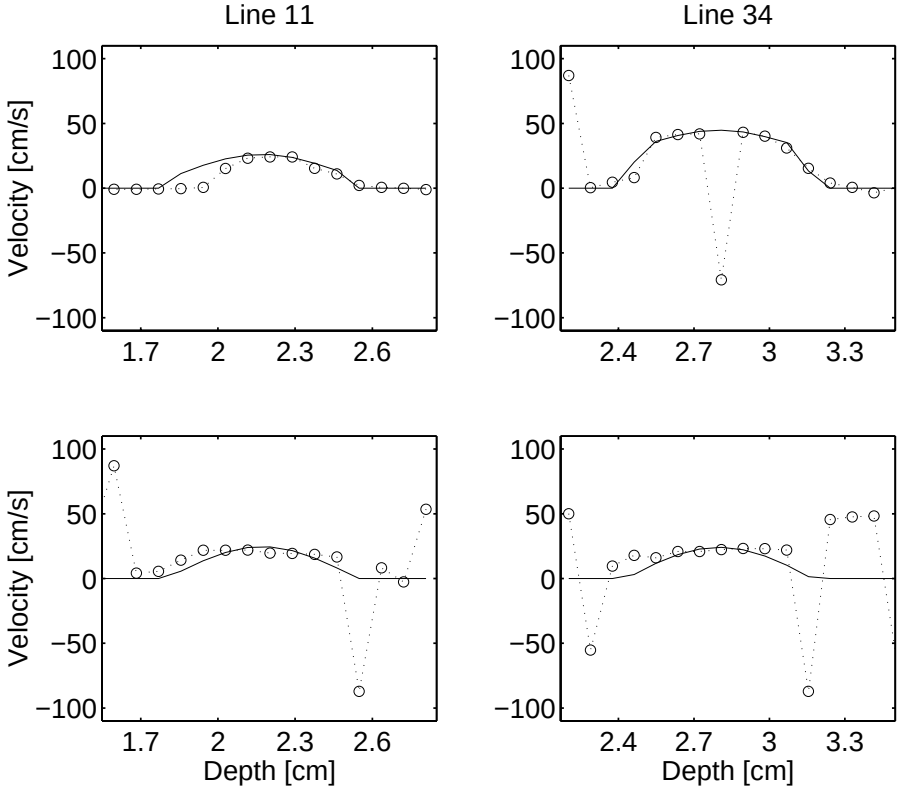

Figure 6.21: The cross-correlation estimator: Plots of the estimates for line 11 and 34 in the images of the systolic (2 upper plots) and diastolic frame (two lower plots).

- perform the cross-correlation analysis for the set of possible temporal shifts - including the temporal shift of the initial phase estimate ($n_p = 0$),
- determine the maximum of the cross-correlation function and the corresponding value of the temporal shift,
- compute the velocity estimate based on the new estimate of the temporal shift.

An estimator combining the advantages of the two methods has been obtained. The computational load has been lowered quite a lot compared to the load for the cross-correlation estimator as $N_p << N_{v-steps}$. The number of multiplications and additions employed are:

$$\begin{aligned} N_{m,EAM} &= 4N_s(N_{l,e}-1)+1+N_s(N_{l,e}-1)N_p \\ N_{a,EAM} &= 3N_s(N_{l,e}-1)+(N_s-1)(N_{l,e}-1)N_p. \end{aligned} \tag{6.17}$$

These numbers are obtained by combining (6.9) and (6.14) and substituting $N_{v-steps}$ with N_p. To obtain an accurate initial estimate of the velocity a long pulse should be emitted. This is not optimum from a cross-correlation point of view. A conflict exists with respect to the choice of the excitation pulse. In the following the focus will be put on getting a good initial estimate of the velocity, so the data set generated with a long excitation pulse will be employed in the performance evaluation.

6.5.1 Performance on synthetic data

The performance of the estimator on the synthetic data was evaluated for the following values of the estimator parameters:

- number of lines: $N_l \in [3, 6, 9, 12, 15, 18, 21, 24]$,
- sampling frequency: $f_s \in [15, 20, 30, 40, 60]$ MHz,
- number of samples: $N_s \in [0.25, 0.5, 0.75, 1.0, 1.25, 1.5, 1.75, 2.0]$ times the length of the emitted pulse. The length in samples is dependent on the sampling frequency.

Three possible phase shifts were investigated: $n_p = [-1, 0, 1]$. In this context an estimate is defined as good, if the bias is less than 2 cm/s, and the standard deviation is less than 1 cm/s.

The performance on the synthetic data shows that the aliasing problem of the autocorrelation estimator can be circumvented by performing the subsequent cross-correlation analysis. The choice of estimator parameters, which gives good estimates, are more restricted though. The estimation of the velocity 30 cm/s gives most restrictions. The initial estimate is incorrect due to the limitation of the autocorrelation estimator. The subsequent cross-correlation analysis only performs well for all SNRs and $N_l \geq 6$ (9 for the regression line filter), when N_s are 0.25 pulse lengths. A lower variance can be obtained, if N_s are increased but then only a subset of the values of N_l can be employed. A good estimate cannot be obtained for $N_s > 1.25$ pulse lengths for any value of N_l, when the SNR is 0 dB and no echo-canceling filter is applied. The application of the HP filter stabilizes the estimation a little. No good estimates can be obtained, when $N_s > 1.5$ pulse lengths for any value of N_l. The regression line filter only works well for all SNRs and $N_l \geq 9$, when N_s equals 0.25 pulse lengths. In general more combinations of N_l and N_s give good estimates, as the SNR increases. The performance for the velocity 40 cm/s is very similar to the performance on velocities below 30 cm/s. The overall best choice of N_s for the velocities 10, 20, and 40 cm/s lies around one pulse length. The level of variation on the standard deviations for different choices of the parameters is on the order of a few millimeters per second or less. The loss of working with less samples than the best choice is therefore very limited. The following trends can be determined for the cases, when N_s and N_l are chosen appropriately:

- the estimate is biased, and the level is dependent on the estimator parameters. The bias is positive and takes values in the range from 3.5-8.5 % of the true velocity for the given data set. No unambiguous relation between the bias and the parameters can be determined,
- the performance is independent of the sampling frequency,
- the standard deviation on the estimates decreases as the SNR increases,
- the standard deviation decreases as the number of lines are increased, as long as N_s and N_l are chosen appropriately. The value of N_s, which gives the overall best performance, is lower, when 21 and 24 lines are employed in the estimation, compared to when N_l are in the range from 6-18 lines.

The effect of performing the echo-canceling is not unambiguous. An increase as well as a decrease in the standard deviation can be obtained. No unambiguous relation between the level of the standard deviation and the parameters has been determined. The differences in the standard deviations even out as the SNR increases. The combinations of N_l and N_s, which give good performance, are almost identical for the different filters. Under some circumstances more or less combinations will work for the different filters. As the HP echo-canceling filter produces good estimates for more combinations of the parameters, it is to preferred over the regression line filter.

Figures 6.22-6.24 show examples of the performance of the estimator, when the different parameters are varied. The HP echo-canceling filter was applied prior to the velocity estimation. When one parameter is varied, the others are kept constant at: the SNR is 10 dB, the number of lines are 9, the sampling frequency is 30 MHz, and the number of samples are equal to one pulse length. Please refer to Appendix B for tables containing the performance for the range of combinations of the parameters, the velocity values, and the echo-canceling filters.

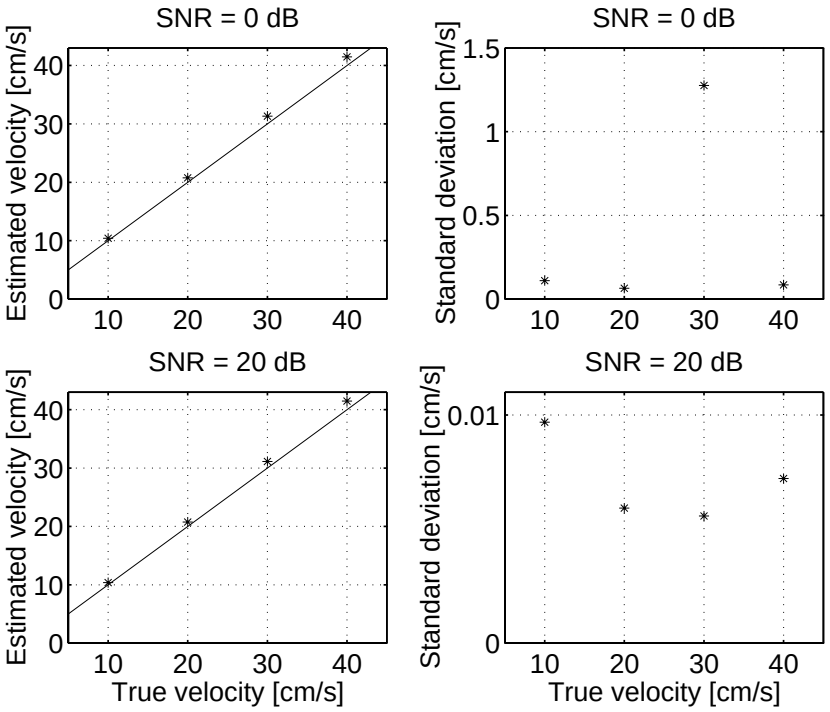

Figure 6.22: The extended autocorrelation estimator: the true (—) and the estimated (*) velocities along with the standard deviation for a SNR of 0 and 20 dB. HP echo-canceling filter was applied. Nine lines was employed. The sampling frequency is 30 MHz, and the number of samples are equal to one pulse length.

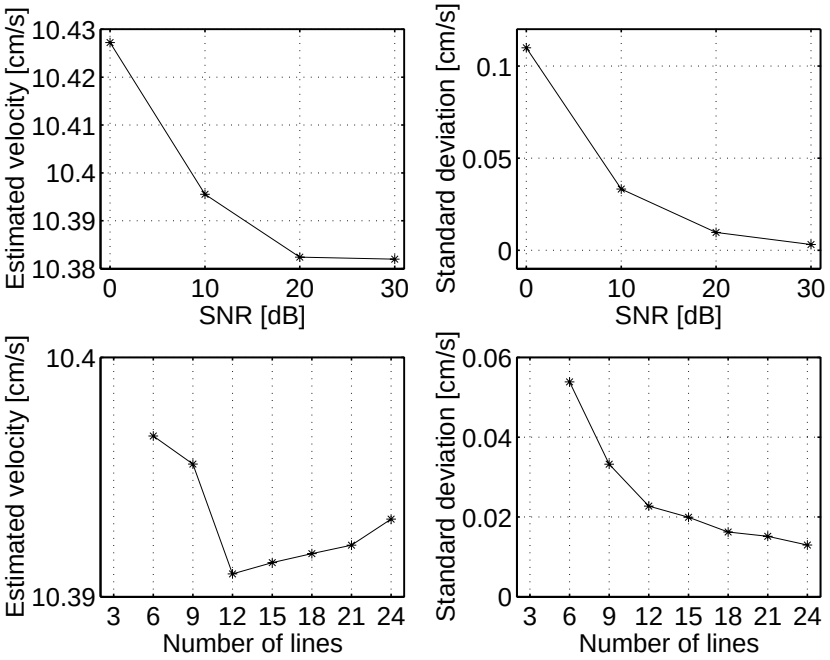

Figure 6.23: Performance of the extended autocorrelation estimator as a function of the number of lines and the SNR. HP echo-canceling filter applied. The sampling frequency is 30 MHz, and the number of samples are equal to one pulse length. The true velocity is 10 cm/s.

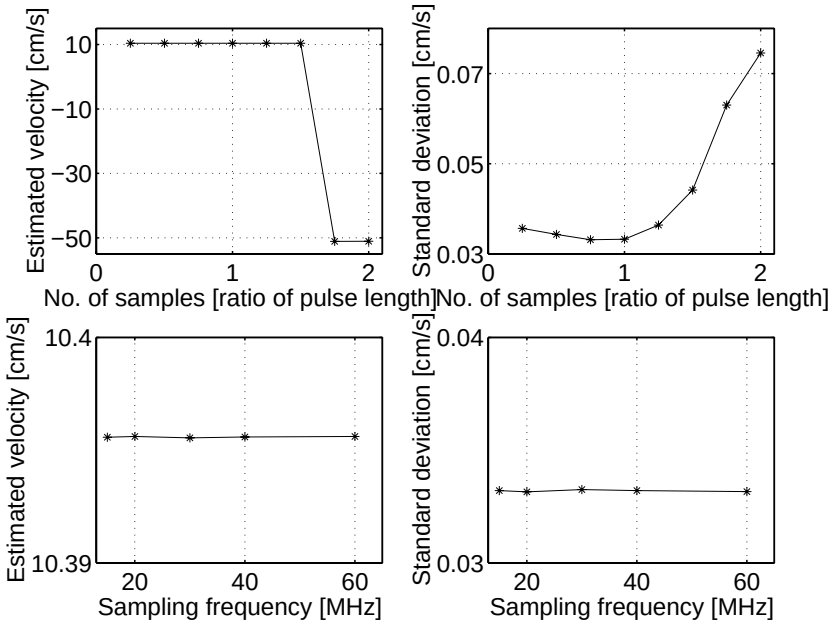

Figure 6.24: Performance of the extended autocorrelation estimator as a function of the number of samples and the sampling frequency. HP echo-canceling filter applied. The SNR is 10 dB, and 9 lines were employed. The true velocity is 10 cm/s.

The EAM estimator out performs the autocorrelation estimator, as it can produce good estimates for the full range of velocities. The levels of the velocity estimates and the standard deviations are similar (almost identical) for the velocities 10 and 20 cm/s. The choice of parameters, which give good performance, are more limited though.

The performance of the cross-correlation estimator is very dependent on the choice of the parameters. The EAM estimator is less dependent hereof (at least when the velocity is different from 30 cm/s), and since the EAM estimator can handle the full velocity range, it should be preferred over the cross-correlation estimator.

6.5.2 Performance on simulated data

When the extended autocorrelation estimator was applied to the synthetic data, the same number of samples were employed in the autocorrelation and the cross-correlation analysis. In principle the number of samples employed could be different for the two steps in the estimation. This approach will be pursued in the evaluation of the performance on the simulated data. N_s are kept constant at one pulse length for the autocorrelation analysis, whereas N_s are varied over the range from 0.25-6 pulse lengths in the cross-correlation analysis.

The initial estimates computed by the autocorrelation estimator are equal to the ”correct” estimates, as the f_{prf} has been chosen, so no aliasing will occur. The subsequent cross-correlation analysis is therefore not really needed but will be performed, if the EAM estimator is employed. Under these circumstances it is possible to determine, how the subsequent cross-correlation analysis influences the estimation. Inspection of the computed estimates reveals that the subsequent cross-correlation analysis introduces quite a few velocity estimates, which deviate significantly from the true velocity. This is due to the amplitude problem of the cross-correlation estimator, where the zero-crossings and peaks in the segments match but the amplitude levels vary (see discussion in Section 6.4). The number of 2π-investigations, which produce a correct output, have been determined. In the following this measure will be referred to as the number of correct

2π-investigations. This measure is plotted as a function of the number of samples employed in the cross-correlation analysis in Fig. 6.25. The estimator is applied to the simulated data with a SNR of 10 and 20 dB. The performance increases slowly as the number of samples are increased. In the current study 4 and 6 pulse lengths equal 6.2 and 9.3 mm, respectively, so the segment length exceeds the extent of the vessel. At 6 pulse lengths and a SNR of 20 dB only 61.4 % of the investigations produce a correct estimate. The discussion in the following relates to the results obtained, when N_s equal 6 pulse lengths. Inspections of the 2D plots of the velocity estimates reveal that the majority of the incorrect estimates extent several pixels laterally and/or axially. Examples of the estimated velocity profiles for a systolic and a diastolic frame are plotted in Fig. 6.26. It is the same two frames used to display the performance of the autocorrelation and the cross-correlation estimators. Non-zero estimates are present both inside and outside the vessel, but only the estimates within the vessel are displayed. Velocities plotted with the colors, which represent the maximum and minimum values on the velocity scale, take values above or below these limits. Of the 10 simulated frames the performance on the systolic frame represents the worst case. A total of 56.9 % of the 2π-investigations turn out wrong. In general the majority of the incorrect velocity estimates along the anterior wall are overestimated, whereas an underestimation is seen along the posterior wall. The incorrect estimates within the vessel are mostly overestimated. A comparison between frames shows that a portion of the incorrect estimates are repeated in subsequent frames. Figure 6.27 shows the true and the estimated velocities for two lines from the systolic and diastolic frame. The performance measure for the number of deviating estimates, which was introduced for the autocorrelation estimator, has also been determined for the EAM estimator. A total of 41.2 % of the estimates take values outside the range from -10 cm/s to 80 cm/s.

Post-processing of the estimates is required, if the EAM estimator should be employed for blood velocity estimation. Lai and Torp suggests [56] to apply a post-processing filter, which compares the phase estimate in a given location to the phase estimates of its neighbors in time (between frames) and space (within frame). The incorrect estimates will be off by an integer number of 2π. Therefore an integer number of 2π must be subtracted or added until the phase estimate lies in the same range of values as its neighbors. The filter is named the 2D-tracking filter. The filter has been implemented and applied. The mean of the phase estimates in the spatial and temporal neighborhood of the velocity of interest is computed. The spatial neighbors include the neighbors along the axial and lateral direction. The mean is subtracted from the phase value being tracked, and the resulting value is compared to a threshold value. The outcome of the comparison determines whether a subtraction/addition of 2π should be performed. The filter has been applied to all frames. The first and last axial line of estimates in the image are not filtered, because a full spatial neighborhood does not exist. As no temporal neighbors exist for the first frame, this frame was filtered with a 2D tracking filter, which only employs the spatial neighbors. The filter was applied to the estimated profiles obtained with N_s equal to 6 pulse lengths. After filtering 78.8 and 78.0 % of the estimates are identical to the correct estimates, when the SNR is 10 and 20 dB, respectively. The performance of the EAM estimator (including the 2D tracking) has improved 16-19 %, and the largest improvement is obtained for a SNR of 10 dB. Inspection of the velocity profiles confirms that some of the highly deviating estimates have been removed, but also new incorrect estimates have been produced. Fig. 6.28 shows examples of the resulting velocity profiles for the systolic and the diastolic frame from Fig. 6.26. Only the velocity estimates within the vessel are displayed. The problem of the incorrect estimates have not been resolved fully but minimized. As the ”correct” estimates are identical to the estimates obtained with the autocorrelation estimator, the trends with respect to the variations about the true velocities are the same and will not be repeated here.

The simulated data generated by emitting a long pulse have been used in the above evaluation. This is optimum for the autocorrelation estimator, so an initial estimate with low variance is obtained. From a cross-correlation point of view a short pulse (a wideband pulse) should be emitted. The optimum choice of excitation pulse collides. The performance of the EAM estimator on the data generated by emitting a short pulse has therefore also been evaluated. In Fig. 6.29 the number of correct 2π-investigations $N_{2\pi}$ (in

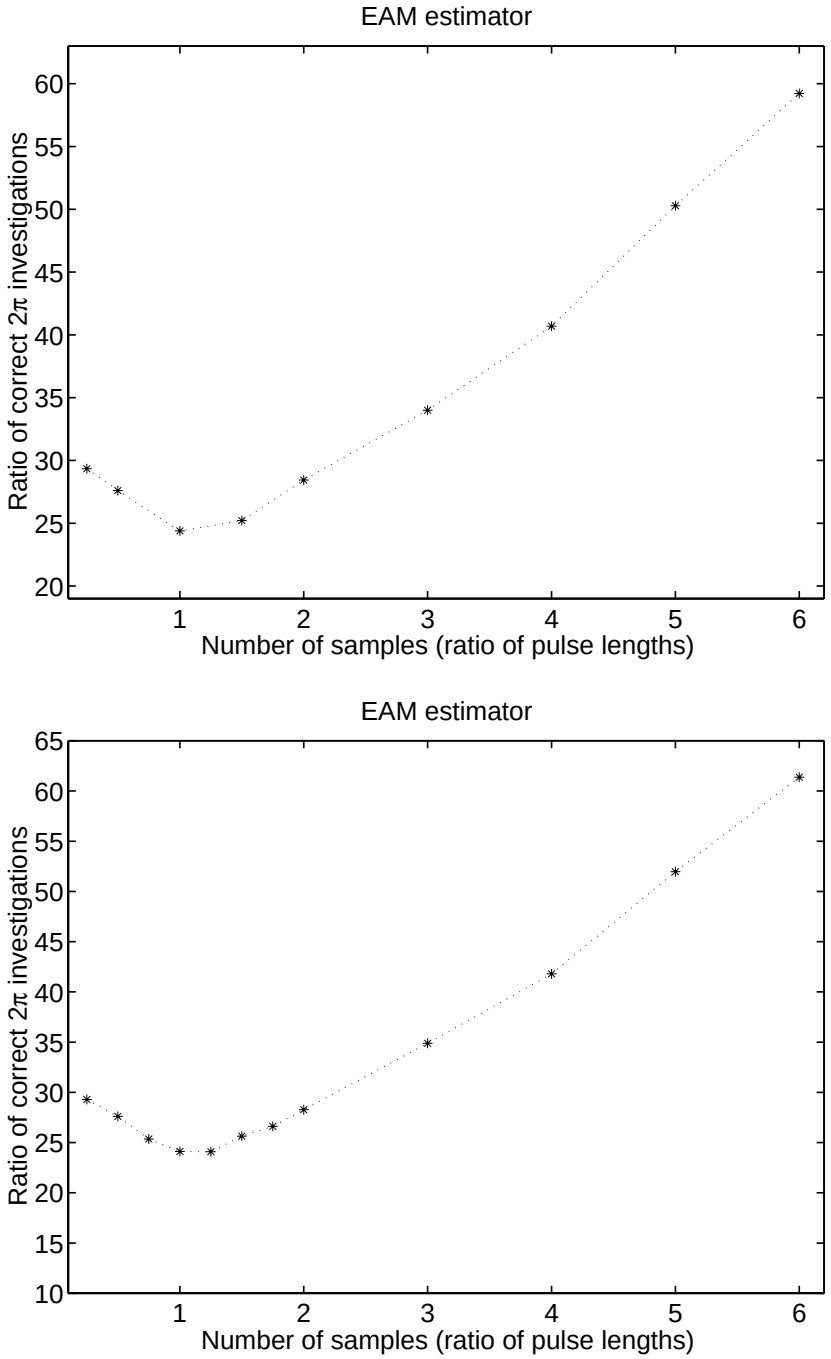

Figure 6.25: Number of correct 2π-investigations (in %) as a function of the number of samples employed for the cross-correlation analysis with the EAM estimator. The SNR is 10 and 20 dB in the top and bottom plot, respectively.

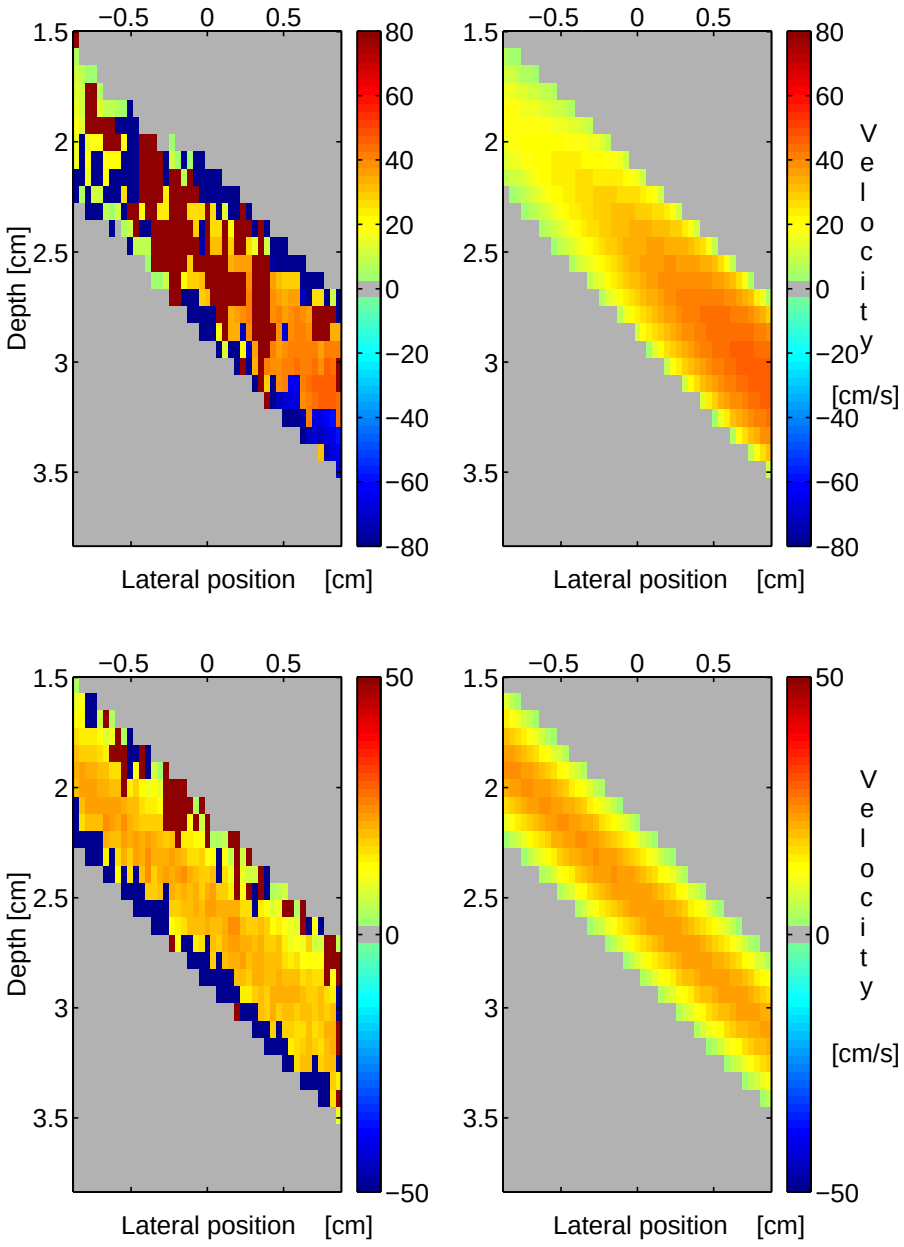

Figure 6.26: EAM estimator: The estimated (left) and the true (right) velocities of a systolic (upper two plots) and diastolic frame (lower two plots). The SNR is 20 dB, and N_s (for the cross-correlation analysis) are 6 pulse lengths.

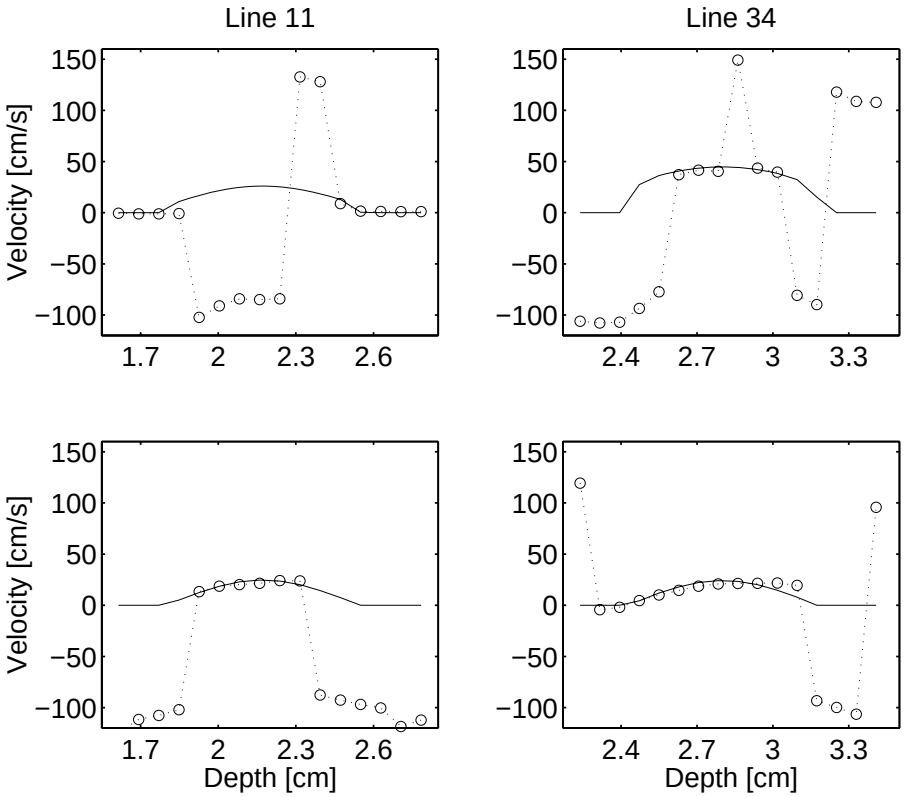

Figure 6.27: EAM estimator: The estimates for line 11 and 34 in the images of the systolic (upper 2 plots) and diastolic frame (lower 2 plots).

%) as a function of the number of samples employed for the cross-correlation analysis are plotted. The SNR is 10 and 20 dB, respectively. $N_{2\pi}$ grows exponentially and reaches a plateau around 5 pulse lengths. With this approach 76.9 % and 83.6 % of the 2π-investigations turn out correct, when $N_{\frac{\lambda}{2}}$ equal 5 pulse lengths, and the SNR is 10 and 20 dB, respectively. The performance of the 2π-investigations has increased with 25-30 %. This improvement is relative to the performance of the EAM estimator on data with a long excitation pulse, and when no 2D tracking is performed. The performance is similar to the performance of the EAM estimator on data generated with a long pulse, when the 2D tracking is applied. The best performance of the EAM estimator is obtained on the data generated with a short pulse, as the basis for the cross-correlation analysis has improved. Five pulse lengths equal 4.3 mm, so the correlation analysis is performed over a shorter spatial range than was the case for the data set generated with a long pulse. In Fig. 6.30 the estimated and true velocities for the systolic and the diastolic frame are plotted. Only the velocity estimates within the vessel are plotted. It is the same two frames used to show performance previously. Most of the incorrect velocity estimates along the posterior wall take values below the true velocity, whereas the estimates along the anterior wall are overestimated. Still some incorrect estimates show up in consecutive frames. The majority of these estimates still group. The performance can be improved, if the 2D tracking filter is applied. The number of correct 2π-investigations increase to 90.0 and 89.8 %, when the SNR is 10 and 20 dB, respectively. Examples of the resulting images of the estimated velocity profiles are plotted in Fig. 6.31. The non-erroneous estimates computed with the EAM estimator, when it was applied to the data set generated from a long and short excitation pulse, have been compared (see Fig. 6.26 and 6.30). The latter estimates fluctuate more, when the course across the axial extent of the vessel is investigated. The velocity values are lower and thereby further from the true velocities. The employment of a short pulse has degraded the performance of the autocorrelation estimation, which was to be expected.

The best performance of the EAM estimator is obtained, if it is applied to data generated with a short pulse, and a 2D tracking filter is applied prior to displaying the estimates. The best performance is deter-

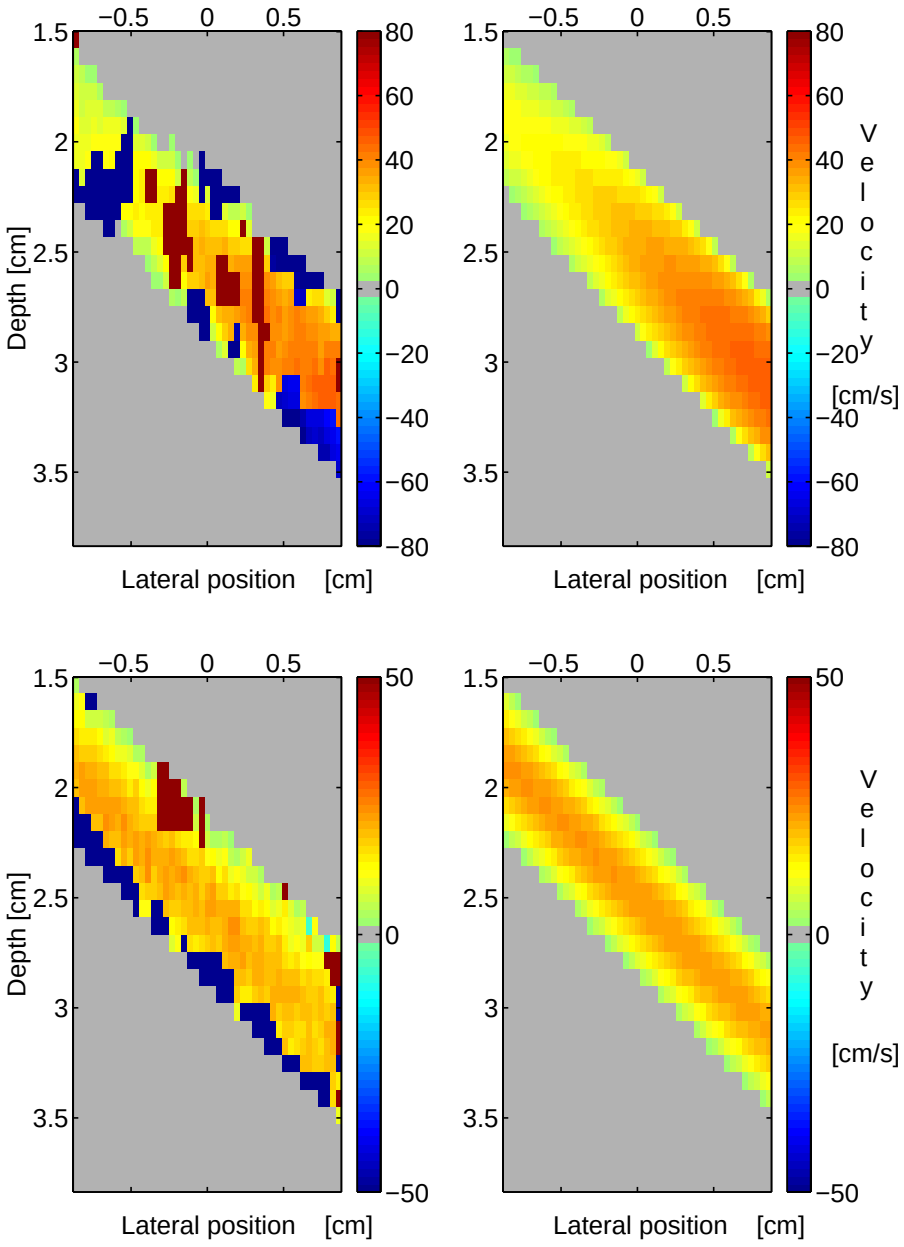

Figure 6.28: EAM estimator: The estimated (left) and the true (right) velocities of a systolic (upper two plots) and diastolic frame (lower two plots) after application of the 2D tracking filter. The SNR is 20 dB, and N_s (for the cross-correlation analysis) are 6 pulse lengths.

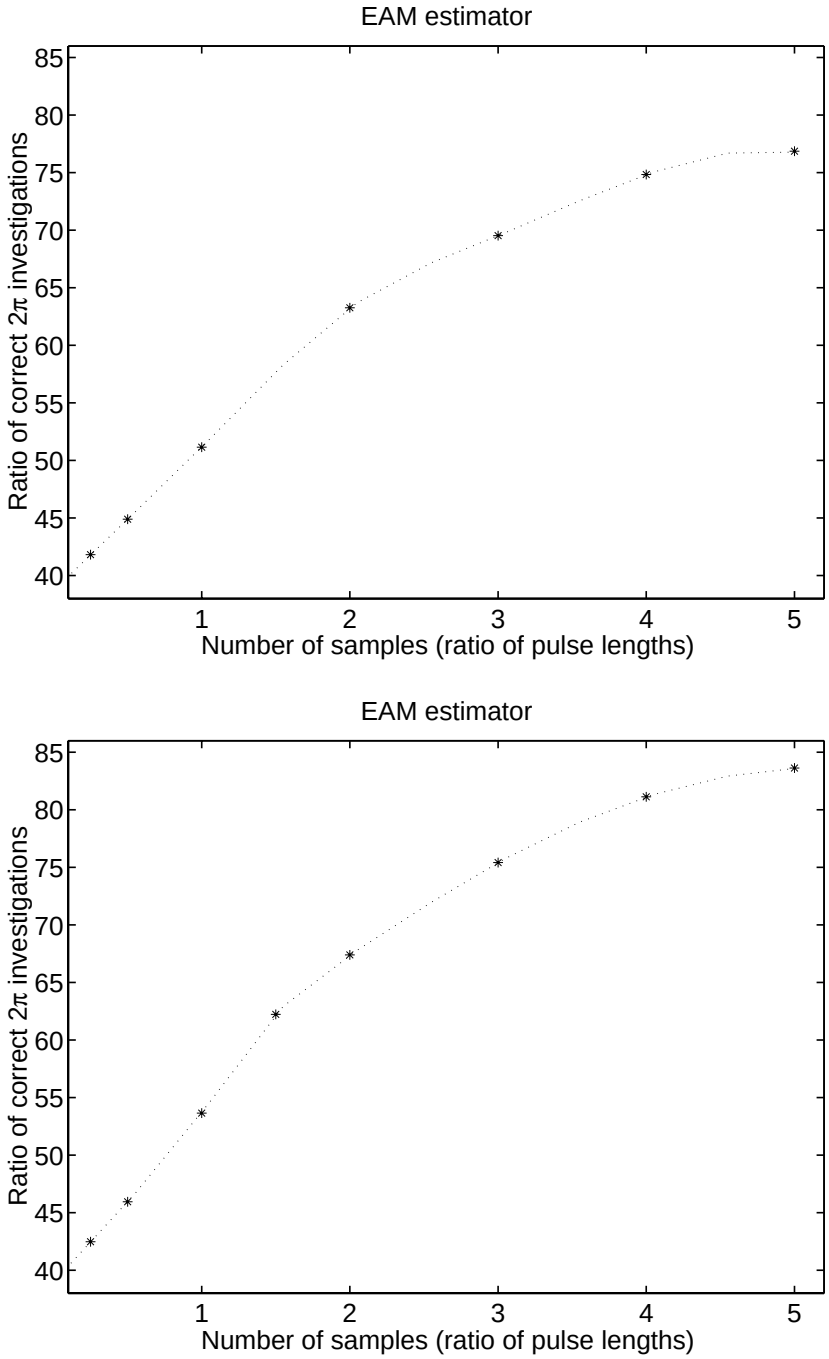

Figure 6.29: Number of correct 2π-investigations (in %) as a function of the number of samples employed for the cross-correlation analysis with the EAM estimator. The simulated data generated from emission of a short pulse are used. The SNR is 10 and 20 dB in the top and bottom plot, respectively.

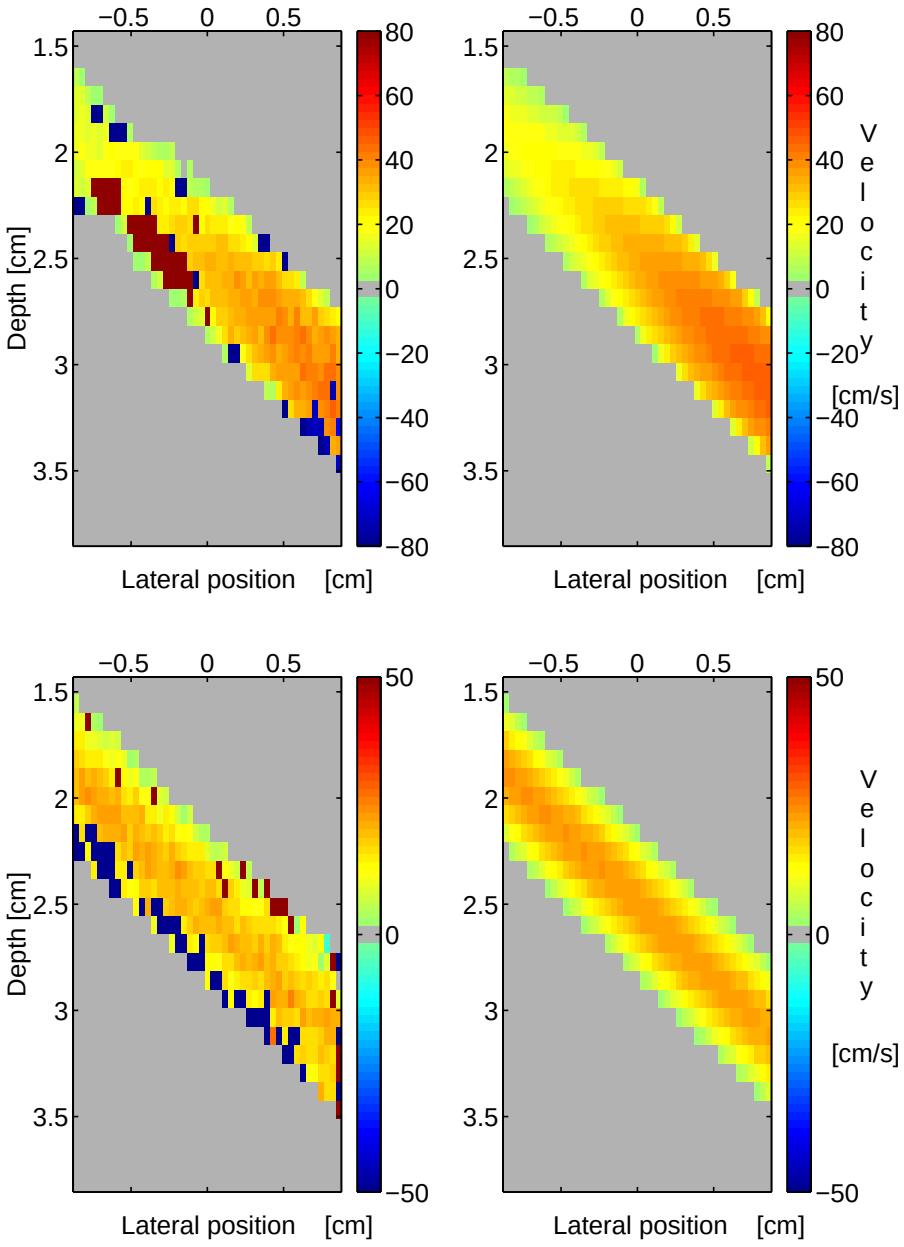

Figure 6.30: EAM estimator: The estimated (left) and the true (right) velocities of a systolic (upper two plots) and a diastolic frame (lower two plots), when the estimator is applied to data generated with a short pulse. The SNR is 20 dB, and N_s (for the cross-correlation analysis) equal 5 pulse lengths.

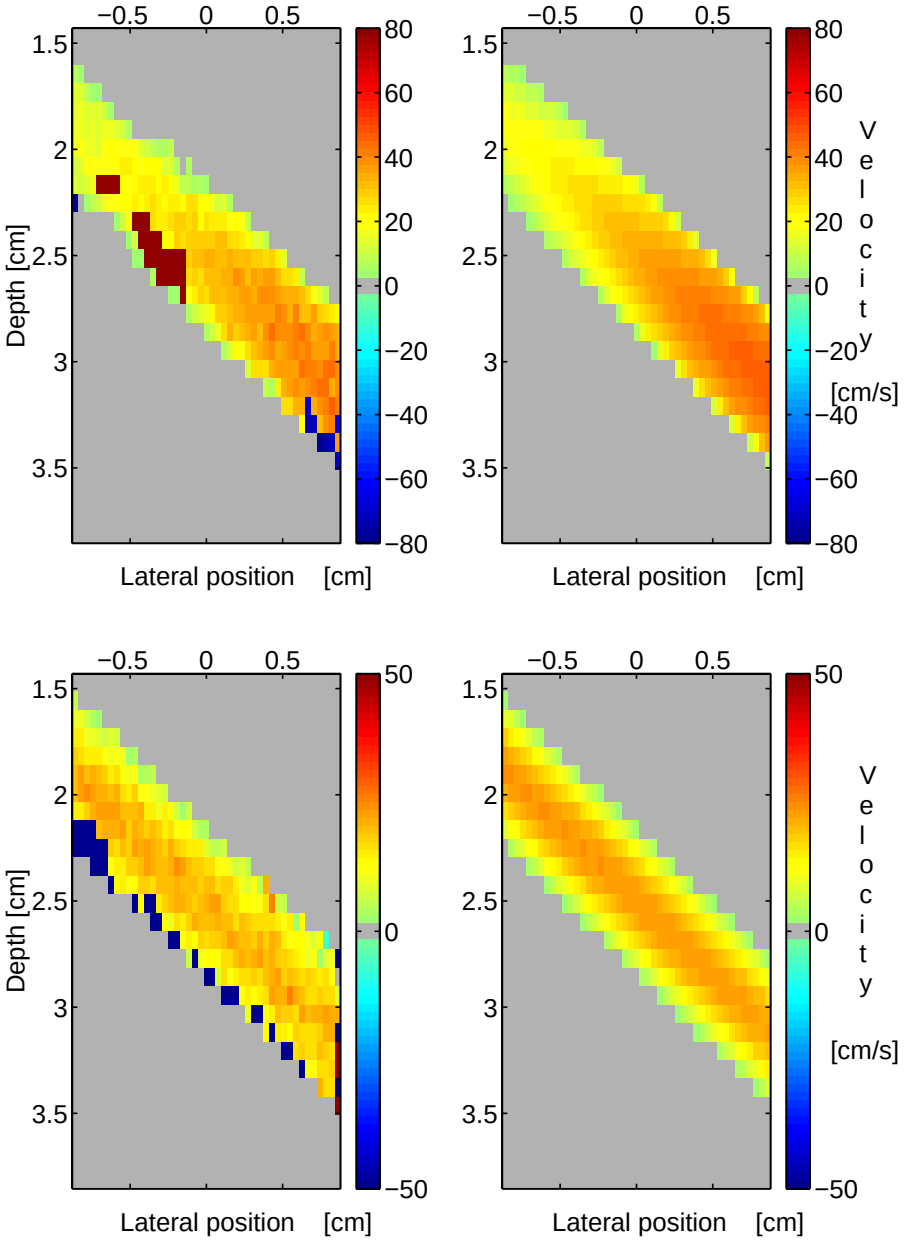

Figure 6.31: EAM estimator: The estimated (left) and the true (right) velocities of a systolic (upper two plots) and a diastolic frame (lower two plots), when the estimator is applied to data generated with a short pulse, and 2D tracking is performed. The SNR is 20 dB, and N_s (for the cross-correlation analysis) equal 5 pulse lengths.

Excitation pulse	SNR (dB)	Number of samples (fraction of pulse length) 0.5	1	2	3	4	5
Long	10	0.9	0.92	0.89	0.86	0.82	0.76
	20	0.9	0.92	0.89	0.85	0.8	0.74
Short	10	0.8	0.76	0.66	0.6	0.55	0.53
	20	0.79	0.73	0.61	0.53	0.46	0.43

Table 6.2: The RMS error ([m/s]) as a function of the number of samples used in the cross-correlation analysis with the EAM estimator. The estimator is applied to data generated with a long and a short excitation pulse, respectively. The SNR is 10 and 20 dB, respectively.

mined by means of the RMS error and the number of correct 2π-investigations. A low error and a high number of correct 2π-investigations are desirable. A total of 16.5 % of the computed velocity estimates take values outside the range from -10 cm/s to 80 cm/s. This measure is a factor of 2.5 lower than the same measure, when the EAM estimator was applied to data generated with a long pulse. Table 6.2 lists the RMS error for the EAM estimator, when it was applied to the data set generated with a long and a short pulse, respectively. The values represent the errors prior to applying the 2D tracking filter, as these determine the performance of the estimator itself. The incorrect estimates result in the high values of the RMS error. The estimated velocity profiles with the EAM estimator on all 10 frames are enclosed in Appendix C. The results obtained, when the estimator was applied to the data generated from a short and long pulse, are included. No post-processing has been applied to the estimated velocity profiles.

The discussion of the EAM estimator in the following and in the subsequent sections is strictly related to the performance of the EAM estimator itself. The autocorrelation estimator should be preferred over the EAM estimator, when no aliasing occur. The EAM estimator introduces quite a few new erroneous estimates, and they appear in all frames throughout the cardiac cycle. Some can be eliminated by applying the 2D tracking filter, but still the advantages of the EAM estimator seem to be counteracted by the limitations of the cross-correlation analysis.

The performance of the EAM and cross-correlation estimators are similar, when the estimators use 5 and 3 pulse lengths, respectively. This conclusion is based on the RMS error, the measure of the number of highly deviating estimates, and the visual inspection. The conclusion is valid, when the EAM estimator is applied to the data generated with a short excitation pulse. Both estimators introduce some estimates, which deviate significantly from the true velocity. These incorrect estimates occur more often for the EAM estimator and seem to group together more. The advantage of the EAM estimator is that the ”correct” estimates follow the variations across the vessel and throughout the cardiac cycle well and better than is the case for the cross-correlation estimator. A post-processing filter should be applied to the minimize the variations and the values of the estimates, which deviate significantly.

6.6 The Butterfly Search Technique

In 1995 Alam and Parker [57] proposed another blood velocity estimator, which also tries to match patterns between consecutive lines. A perfect match corresponds to the situation, where the amplitude values in corresponding positions in the segments under investigation are equal. A mathematical measure of equality between samples is the variance. If two values are equal, the variance will be zero. In the RF-signals noise is present, so a perfect match will never occur. The effect of decorrelation adds to the mismatch between the segments. Still some similarity will be present, and a match between segments in consecutive

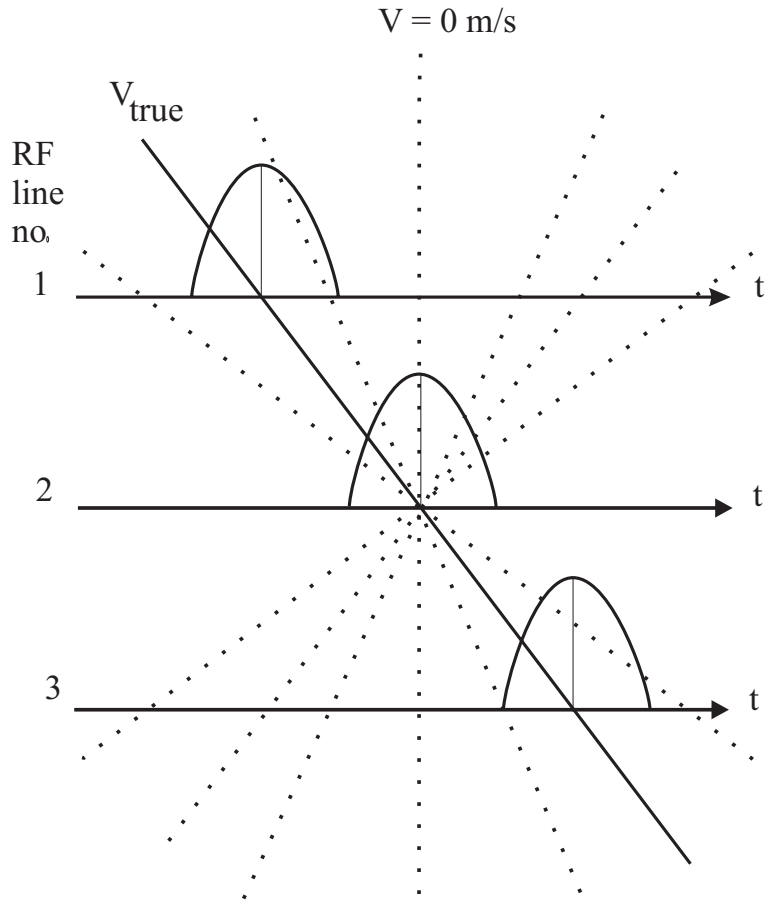

Figure 6.32: BST estimator: Envelope detected response from single scatterer moving away from the transducer along with the trajectory lines representing different velocities.

RF-lines will be characterized by having a low variance. This is the idea behind the estimator developed by Alam and Parker. For a set of sample shifts (corresponding to a set of velocities) the shifted segment in the consecutive line is compared to the original segment by means of a variance analysis. The minimum variance corresponds to matching segments, and an estimate of the velocity has been determined. By employing this estimator the amplitude problem of the cross-correlation estimator will be eliminated, as the mismatch in amplitudes results in a high variance. The analysis can be performed on the real RF-signals, the envelope detected RF-signals, or the complex demodulated (I and Q) RF-signals [57]. The method has been named the Butterfly Search Technique (BST), as the search is performed along a set of trajectory lines that forms a butterfly shape. The slope of the trajectory lines is a function of the velocity. In Fig. 6.32 the search approach is indicated on envelope detected data from a single scatterer. In the plot the RF-line in the middle (line number 2) is used as the reference but in principle any of the lines can be used here fore. A short pulse should be emitted to minimize signal decorrelation, and averaging over a set of samples and a set of lines should be performed to increase the accuracy on the estimate.

The computational load of the BST estimator is much higher than for the autocorrelation estimator, but it can be directly implemented in hardware [57]. The search can be performed by sampling through the data set, and then pass the values through a variance processor. The analysis for a range of velocities can be performed by parallel processing. With this approach the resolution on the velocity estimate is determined by the sampling frequency, as no interpolation is carried out on the computed set of variance values. The variance value for each investigated velocity is obtained by performing the following computations:

- the mean of the sample values for the set of RF-lines is determined for the range of samples *n* in the

segment of length N_s:

$$\mu(n) = \frac{1}{N_{l,e}} \sum_{l=1}^{N_{l,e}} r_{cfm}(n,l),$$

- the variance values for each position in the segment n is determined, and the N_s values are summed to obtain one variance value for the segment:

$$\sigma^2 = \sum_{n=1}^{N_s} \frac{1}{N_{l,e}-1} \sum_{l=1}^{N_{l,e}} (r_{cfm}(n,l) - \mu(n))^2.$$

The computations are performed on the echo-canceled data, but the subscript has been omitted. The values of σ^2 as a function of the investigated velocities give the basis for determining the velocity estimate. The sample shift related to the minimum variance value gives the estimate of the velocity. The number of additions and multiplications used to obtain the set of variance values are:

$$\begin{aligned} N_{m,BST} &= N_s N_{v-steps} + N_s N_{l,e} N_{v-steps} \\ N_{a,BST} &= 2(N_s - 1) N_{l,e} N_{v-steps} + N_{l,e} N_s N_{v-steps}, \end{aligned} \tag{6.18}$$

where $N_{v-steps}$ represents the number of investigated velocities. The computation of the mean includes a normalization with the number of values used. The factor $1/N_{l,e}$ can be determined prior to performing the variance analysis, and then multiplied on to the sum of sample values. The first term in the $N_{m,BST}$ represents this multiplication. The pre-processing, which is required to determine the enveloped detected data or the I and Q signals, has not been included in $N_{m,BST}$ and $N_{a,BST}$. This further increases the computational load.

6.6.1 Performance on synthetic data

In the current study the search approach by sampling through data will not be employed. A set of discrete velocities will be investigated as were the case for the cross-correlation estimator. The estimator will be applied to the envelope detected data. The estimator parameters were varied as follows:

- number of lines : $N_l \in [3, 6, 9, 12, 15, 18, 21, 24]$,
- sampling frequency : $f_s \in [15, 20, 30, 40, 60]$ MHz,
- number of samples : $N_s \in [0.25, 0.5, 0.75, 1.0, 1.25, 1.5, 1.75, 2.0]$ times the length of the emitted pulse. The length in samples is dependent on the sampling frequency.

The velocity range from -50 cm/s to 50 cm/s was investigated in steps of 1 cm/s. The estimated velocities can only take one of the discrete values investigated, since no interpolation of the function, which represents the variance values as a function of the discrete velocities, is performed. A finite resolution on the velocities is therefore dictated by the choice of the step size. A good performance is defined as an estimation, where the mean is within ± 2 cm/s of the true velocity, and the standard deviation is less than 1 cm/s. The best performance is obtained, when the standard deviation takes its minimum value, and the mean is within $\pm$ 2 cm/s. The following trends can be derived from the results:

- the BST estimator does not suffer from aliasing problems,
- the mean approaches the true velocity as the SNR increases, when the true velocity is 10 cm/s. For the velocities 20, 30, and 40 cm/s the estimates approach a value biased by +1 cm/s,

- the standard deviation decreases as the number of samples are increased, when no echo-canceling and the HP echo-canceling filter are used. A slight increase (less than 0.1 cm/s) is seen for some combinations of the parameters, when $N_s > 1.25$. The trend is not as unambiguous for the regression line filter,

- the standard deviation decreases as the number of lines are increased, when no echo-canceling and the HP echo-canceling filter are used. For the regression line filter this trend is not seen for all combinations of the parameters,

- the standard deviation on the estimates decreases and reaches 0 as the SNR increases,

- the performance is independent of the sampling frequency, when N_l and N_s are chosen, so a good performance is obtained,

- the choice of the segment length (N_s), which gives good performance, gets more limited as the SNR decreases. The choice of N_s moves towards 2 pulse lengths,

- the employment of the HP echo-canceling filter increases the standard deviation. This is also the case for the regression line filter for low values of N_l and N_s. The difference in the standard deviations evens out as N_l and N_s increases, and the velocity is below 30 cm/s. For some combinations of the parameters estimates with a lower standard deviation are obtained after application of the regression line echo-canceling filter. The difference decreases as the SNR increases.

If the regression line filter is employed, a minimum of 15 lines and $N_s \geq 1.25$ pulse lengths must be employed to obtain a good and stable performance for all SNRs and velocity levels. A minimum of 12 lines and $N_s \geq 1.5$ pulse lengths must be used, when the HP filter is applied. The demands decrease as the SNR increases, when the HP filter is employed. If a standard deviation of 2 cm/s can be accepted, a good performance with the HP filter can be obtained, when 9 lines are used. The performance for the range of combinations of the parameters, the velocity values, and the echo-canceling filters, are enclosed in Appendix B. Figures 6.33-6.35 show examples of the performance of the estimator, when the different parameters are varied. The HP echo-canceling filter was applied prior to the velocity estimation. When one parameter is varied, the others are kept constant at: the SNR is 10 dB, the N_l is 9, the sampling frequency is 30 MHz, and N_s are 2 pulse lengths.

The standard deviations on the estimates computed with the BST estimator are a factor of 10-40 times higher than the same measure for the autocorrelation estimator, when the SNR is 0 dB. The performance of the estimators are only compared for the velocities 10 and 20 cm/s. As the SNR increases, the standard deviation approaches 0 for both estimators. As the SNR increases, the bias on the BST estimates is higher for velocities above 10 cm/s but lower, when the velocity is equal to 10 cm/s. The autocorrelation estimator is to be preferred if the computational load and a high accuracy at low SNRs are of concern. The BST estimator will eliminate the aliasing problem and increase the number of estimates obtainable along the RF-line.

The BST estimator is more stable to different choices of the estimator parameters than the cross-correlation estimator. The standard deviation on the BST estimates is higher for a SNR of 0 dB for most combinations of the parameters, which give good performance of both estimators. The mean and the standard deviation are more stable for different choices of N_l, N_s, and f_s as the SNR decreases. The BST estimator can work - and work well - at lower sampling frequencies than the cross-correlation estimator. The BST estimator is to be preferred over the cross-correlation estimator.

Both the BST and the EAM estimators only work well for a limited range of the estimator parameters. When the parameters are chosen appropriately both estimators can handle velocities above the aliasing bound of the autocorrelation estimator. The estimates are biased, and the bias takes a positive value. The

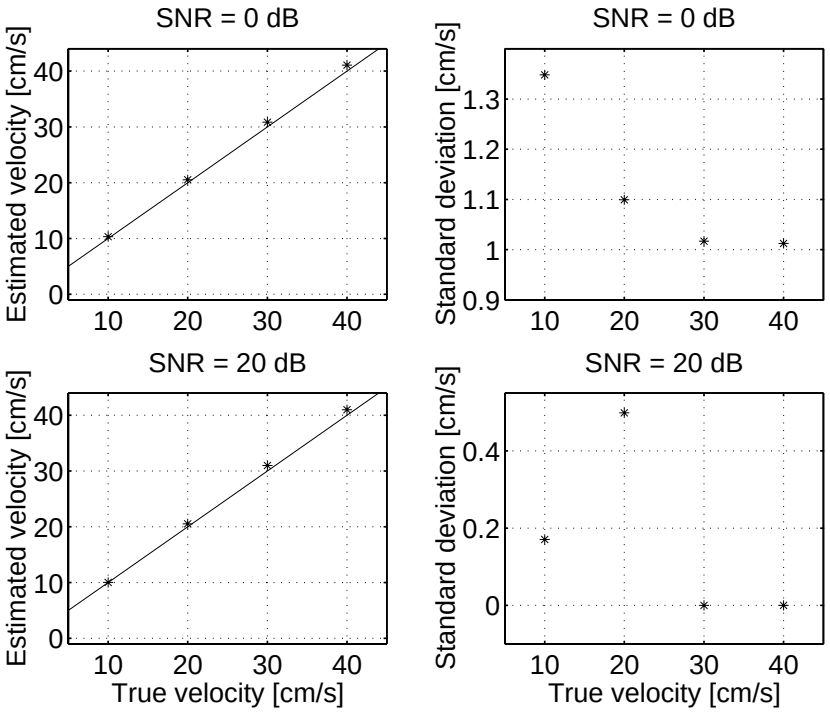

Figure 6.33: The Butterfly search technique: the true (—) and the estimated (*) velocities along with the standard deviation for a SNR of 0 and 20 dB. HP echo-canceling filter applied. The number of lines are 9, f_s is 30 MHz, and N_s are 2 pulse lengths.

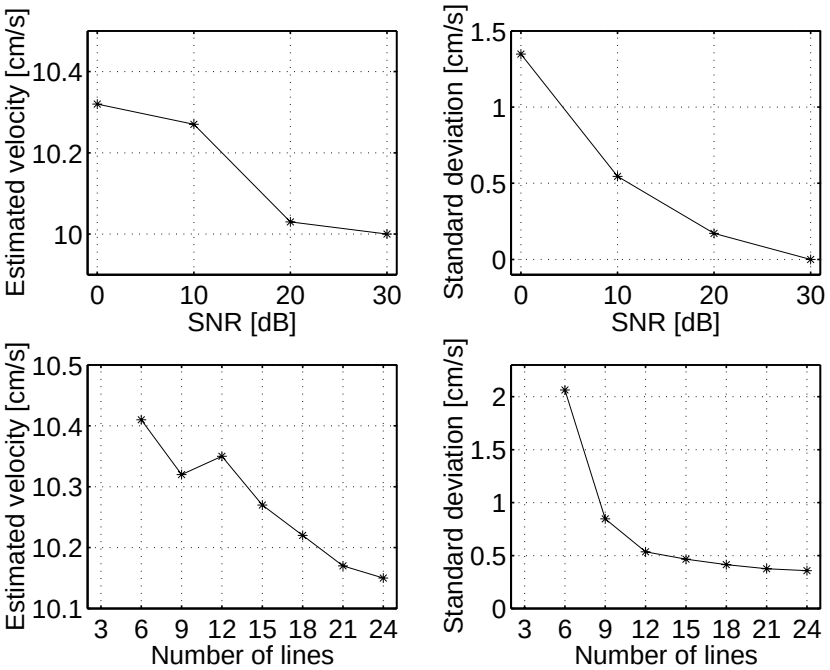

Figure 6.34: Performance of the Butterfly search technique as a function of the number of lines and the SNR. HP echo-canceling filter applied. The sampling frequency is 30 MHz, and N_s are 2 pulse lengths. The true velocity is 10 cm/s.

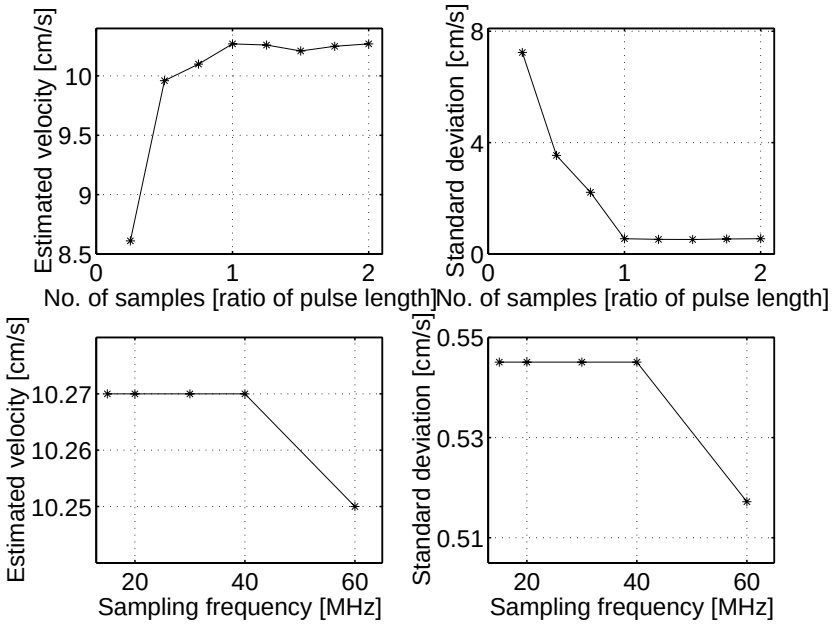

Figure 6.35: Performance of the Butterfly search technique as a function of the number of samples and the sampling frequency. HP echo-canceling filter applied. The number of lines are 9, and the SNR is 10 dB. The true velocity is 10 cm/s.

standard deviations on the estimates obtained with the EAM estimator are a factor of 4-10 lower, when the SNR is 0 dB. One should keep in mind that the standard deviations are below 1 cm/s for both, when the parameters are chosen to give good performance. As the SNR increases, the standard deviation on the BST estimates approaches zero, whereas a non-zero standard deviation is still obtained with the EAM estimator. The bias is slightly higher (but less than 1 cm/s) for the EAM estimator, when the velocities exceed 20 cm/s. The EAM estimator should be preferred over the BST estimator, when the aim is to obtain the lowest standard deviation on the estimates for any SNR.

6.6.2 Performance on simulated data

In the following the performance of the BST estimator will be determined. The echo-canceling was performed with the 2^{nd} order HP filter. This choice is made, because the investigations on the synthetic data showed that 1) the regression line filter requires more than the available 8 lines to perform well, and 2) a comparison of the performance of the autocorrelation, the cross-correlation, and the BST estimators can be performed. The velocity range from -50 cm/s to 50 cm/s was investigated in steps of 1 cm/s.

The performance of the BST estimator has been determined for a range of N_s values. The RMS error as a function of N_s is plotted in Fig. 6.36. The RMS error decreases as N_s increases. Inspection of the velocity estimates reveals that the BST estimator has the same problem as the cross-correlation estimator. It is not able to compute good estimates across the full extent of the vessel. The problem is most pronounced in the systolic frame, which is plotted in Fig. 6.37. Minimization of this deficiency is obtained by decreasing N_s, which on the other hand results in an increase in the RMS error. To obtain estimates across the full spatial extent of the vessel, the accuracy on the estimates has to be down weighted. The estimated velocities for the systolic frame and a diastolic frame are plotted in Fig. 6.38, when N_s are equal to 3 pulse lengths. It is the same two frames, which have been used to show the performance of the estimators discussed in the previous sections. Only the velocity estimates within the vessel are shown. Estimates that are plotted with the maximum and minimum value of the velocity scale take values above or below these border values. Inspection of all the velocity estimates obtained, when N_s equal 3 pulse lengths, reveals that the velocity

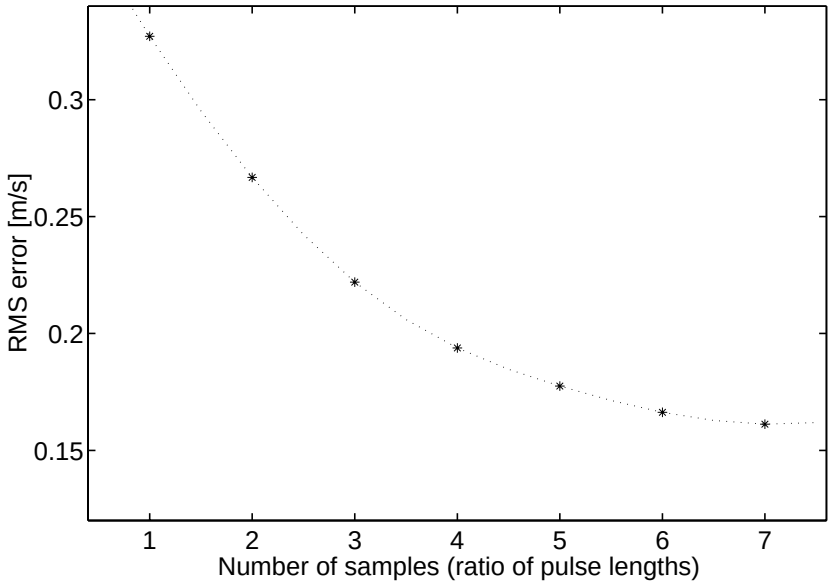

Figure 6.36: RMS error ([m/s]) as a function of N_s for the BST estimator. The SNR is 20 dB.

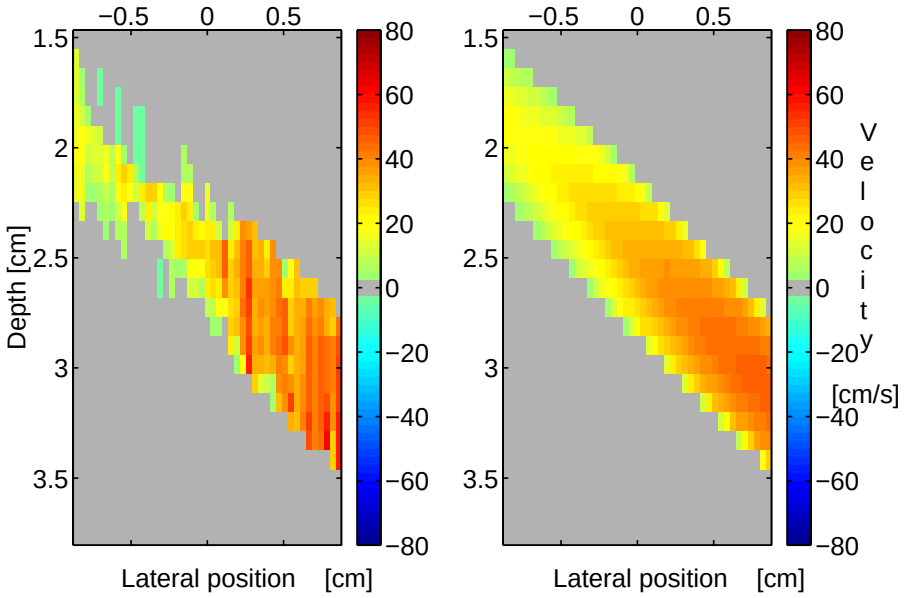

Figure 6.37: BST estimator: The estimated (left) and the true (right) velocities for the systolic frame, when N_s equal 7 pulse lengths. The SNR is 20 dB.

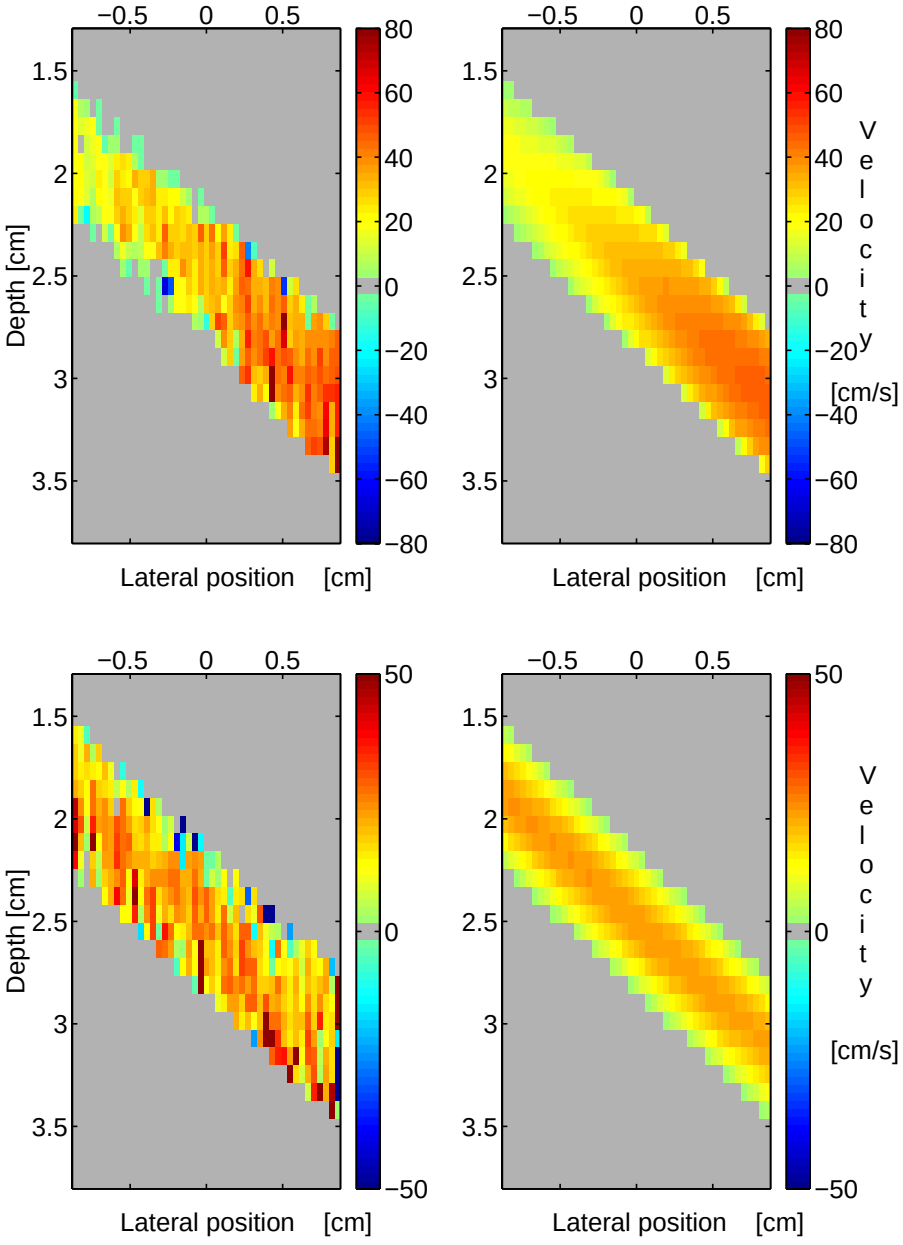

Figure 6.38: BST estimator: The estimated (left) and the true (right) velocities for a systolic (upper two plots) and a diastolic frame (lower two plots), when N_s equal 3 pulse lengths. The SNR is 20 dB.

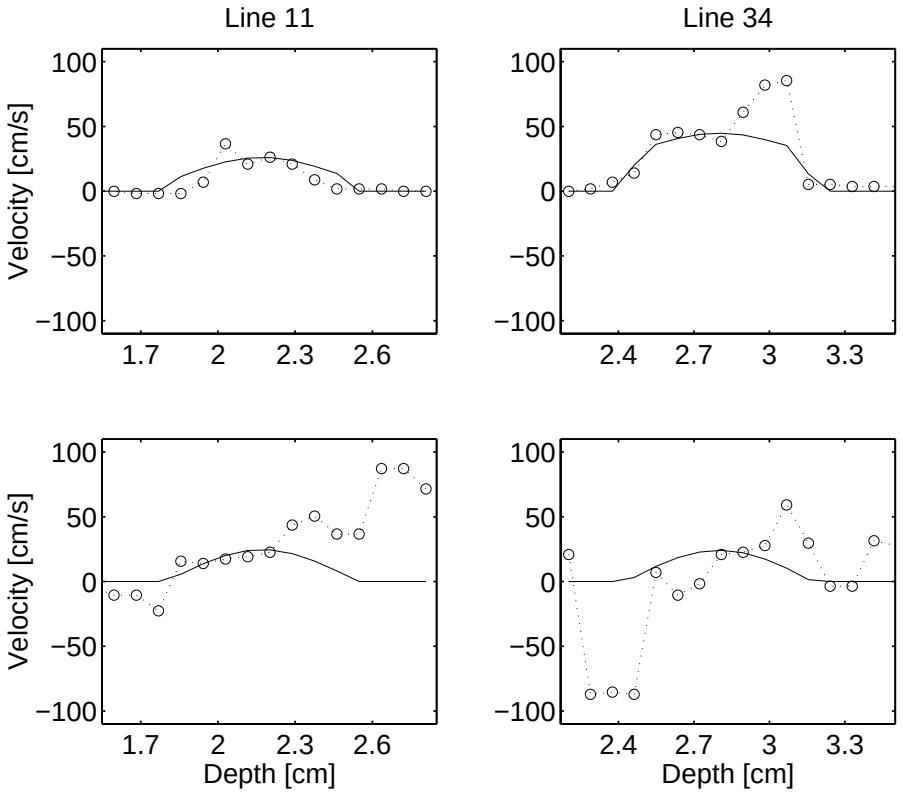

Figure 6.39: BST estimator: Plot of line 11 and 34 in the images for the systolic (upper 2 plots) and diastolic frame (lower 2 plots). The SNR is 20 dB, and N_s are 3 pulse lengths.

estimates fluctuate about the true velocities. Both over- and underestimation are seen throughout the vessel and the frames. There exists a tendency of overestimation along the posterior vessel wall. For the remaining estimates the variation is not systematic but random. The estimates do not follow the velocity variations across the axial extent of the vessel very well. Some estimates occur that deviate significantly from the true value, and they occur as both single and grouped errors. These incorrect estimates take values, which are both over- and underestimated. Only very few of them repeat themselves in the consecutive frame. In Fig. 6.39 the estimates along two lines (axially) for the systolic and diastolic frame are plotted. The fluctuations about the true velocities and the existence of highly deviating estimates are seen in these plots. Post-processing is required prior to displaying the estimates to minimize the variation and the amplitude of the incorrect estimates. A total of 6.9 % of the estimates take values outside the velocity range from -10 cm/s to 80 cm/s. The estimated velocity profiles over the cardiac cycle have been combined into one postscript-file, which is enclosed on CD-rom. Please refer to Appendix C for information on how to locate and access this file.

The performance of the autocorrelation estimator out performs the BST estimator, when no aliasing occur. This conclusion is based on the value of the RMS error, the measure of the number of highly deviating estimates, and the inspection of the estimated velocity profiles. For the autocorrelation estimator the variations about the true velocity are systematic, which is not the case for the BST estimator. Still the BST estimator has some advantages over some of the other estimators evaluated, as it only produce few highly deviating errors. The overall trends with respect to the velocity levels throughout the cardiac cycle is also determined. The inability to follow the variations across the vessel is a drawback, and a post-processing filter should be employed to minimize these variations. If this is possible, the BST estimator will be beneficial to employ, if aliasing errors occur.

The BST estimator out performs the cross-correlation estimator. This conclusion is based on the follow-

ing. The RMS error of the BST estimator is lower, and the number of highly deviating estimates are a factor of 2 lower. The cross-correlation estimator computes estimates that follow the true variations across the axial extent of the vessel better, when only the estimates that do not deviate significantly are considered. So both estimators have advantages and disadvantages. The cross-correlation estimator should be preferred, if the highly deviating estimates can be removed through post-processing.

The BST estimator also out performs the EAM estimator, when the conclusion is based on the RMS error and the number of highly deviating estimates. If the highly deviating estimates of the EAM estimator are removed by post-processing, the EAM estimator (employed on data generated with a short excitation pulse) should be preferred. This conclusion is based on the fact that the non-highly deviating estimates are closer to the true velocities and follow the variations of the velocity throughout the vessel and the cardiac cycle better.

6.7 Extended autocorrelation estimator employing variance

The cross-correlation analysis suffers from the amplitude problem discussed in Section 6.4. This highly degraded the performance of the EAM estimator (see Section 6.5). The BST estimator tries to come about the amplitude problem by determining the variance between samples from consecutive lines instead. The analysis in Section 6.6 shows that less highly deviating estimates are obtained with the BST estimator. A new extended autocorrelation estimator is suggested here. It combines the autocorrelation estimator and the Butterfly Search Technique. An initial guess of the velocity is obtained by employing the autocorrelation estimator. The set of possible phases are evaluated by employing the Butterfly Search Technique on the real RF-data or the envelope detected data. The new estimator is named the Autocorrelation and Butterfly (AB) estimator, and the steps are as follows:

- compute an initial estimate of the phase shift employing the autocorrelation estimator,
- determine a set of possible values of the phase shift by adding and subtracting an integer number of 2π (see (6.16)),
- compute the temporal shifts, which correspond to the set of possible phase shifts,
- perform the variance analysis for the set of possible temporal shifts - including the temporal shift for the initial phase estimate,
- determine the minimum variance value and the corresponding temporal shift,
- compute the velocity estimate based on the new estimate of the temporal shift.

The decorrelation between the signals in consecutive RF-lines influences the performance of the variance analysis and thereby the performance of the AB estimator.

The computational load of the AB estimator is higher than for the EAM estimator due to the additional additions and multiplications needed to compute the variance. The number of multiplications $N_{m,AB}$ and additions $N_{a,AB}$ performed to compute the variance values for N_p possible phase shifts are:

$$\begin{aligned} N_{m,AB} &= 4N_s(N_{l,e}-1)+1+N_{l,e}N_sN_p+N_sN_p \\ N_{a,AB} &= 3N_s(N_{l,e}-1)+2(N_{l,e}-1)N_sN_p+N_{l,e}N_sN_p. \end{aligned} \tag{6.19}$$

These numbers are obtained by combining (6.9) and (6.18), where $N_{v-steps}$ is substituted with N_p. The computations performed to get the envelope detected signals are not included in $N_{m,AB}$ and $N_{a,AB}$. The

autocorrelation estimator is applied to the echo-canceled, real RF-signals. The BST estimator works on both the real and envelope detected signals, and the 2π-investigations will be performed with both approaches. The two approaches will be referred to as the AB1 and the AB2 estimators, respectively.

6.7.1 Performance on synthetic data

The AB1 and the AB2 estimators will be evaluated for the same parameter set, which were used for the EAM estimator:

- number of lines : $N_l \in [3, 6, 9, 12, 15, 18, 21, 24]$,
- sampling frequency : $f_s \in [15, 20, 30, 40, 60]$ MHz,
- number of samples : $N_s \in [0.25, 0.5, 0.75, 1.0, 1.25, 1.5, 1.75, 2.0]$ times the length of the emitted pulse. The length in samples is dependent on the sampling frequency.

Three possible phase shifts were investigated: $n_p = [-1, 0, 1]$. The data set generated with a long excitation pulse will be used, since a long pulse is optimum for the autocorrelation estimator. The same number of samples are used in the computation of the initial phase shift and the variance value for each segment. In this context an estimate is defined as good, if the bias is less than 2 cm/s, and the standard deviation is less than 1 cm/s.

The results obtained with the AB1 estimator will be discussed first. The AB1 estimator does not suffer from aliasing problems for many combinations of the parameters N_l and N_s, when no echo-canceling or a HP echo-canceling filter is used. The subsequent variance analysis corrects for the initial incorrect estimate. The regression line filter does not go well with the AB1 estimator. A non-aliased estimation is only obtainable for $N_l \geq 9$ and N_s equal to 0.25 pulse lengths, when the velocity is 30 cm/s and the SNR is 0 dB. The limitations on the choices of N_l and N_s might become a problem in an *in-vivo* situation. The HP filter should be applied instead, and the results for this situation is discussed in the following. The estimation of the velocity 30 cm/s gives the most restrictions with respect to the choice of the parameters N_l and the N_s. The application of the HP filter prior to estimation has a positive effect on the estimation. The estimator is capable of performing a good estimation for more combinations of N_l and N_s, when the velocity is 30 cm/s. It is not possible to get a good estimation for any value of N_l, when $N_s \geq 1.25$ pulse lengths, the SNR is 0 dB, and the velocity is 30 cm/s. As the SNR increases, more combinations of N_l and N_s result in a successful estimation. If the estimator should be able to work at all SNRs, the range of N_l's, and all velocities (except 40 cm/s), the number of samples should be equal to 0.25 pulse lengths. Estimates with a slightly lower standard deviation can be obtained for other values of N_s, if $N_l \geq 12$. The difference on the standard deviations is on the order of 10^{-2} cm/s or less, so the difference is really only slightly lower. The velocity 40 cm/s unfortunately sets up slightly different restrictions, when 15 and 18 lines are used. In this case N_s should take the value 0.5 or 0.75 pulse lengths as a minimum. So the choice of N_s is dependent on the value of N_l. The incorrect estimates span the range from -85 cm/s to 40 cm/s with standard deviations in the range from 1.5 to 65 cm/s. For a few combinations of N_l and N_s a low value of the sampling frequency causes the estimation to fail. A sampling frequency above 20 MHz ensures good performance. The following trends exist for the AB1 estimator, when the parameters N_s and N_l are chosen appropriately (a good estimate has been computed):

- the estimate is biased. The velocity estimates are overestimated, and the level of the bias is dependent on the estimator parameters. The bias takes values in the range from 4-10 % of the true velocity,
- the performance is independent of the sampling frequency,
- the standard deviation on the estimates decreases as the SNR increases,

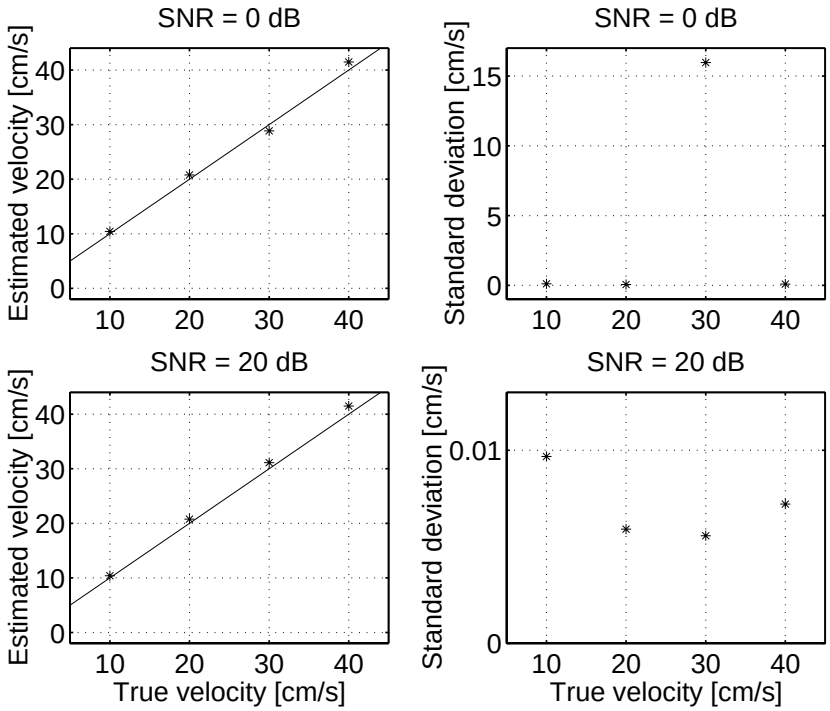

Figure 6.40: The AB1 estimator: the true (—) and the estimated (*) velocities along with the standard deviation for a SNR of 0 and 20 dB. HP echo-canceling filter was applied. Nine lines were employed. The sampling frequency is 30 MHz, and the number of samples are equal to one pulse length.

- the standard deviation decreases as the number of lines are increased.

Figures 6.40-6.42 show examples of the performance of the AB1 estimator. When one parameter is varied, the others are kept constant at: the SNR is 10 dB, the number of lines are 9, the sampling frequency is 30 MHz, and the number of samples are equal to one pulse length. Tables containing the performance for the range of combinations of the parameters, the velocities, and the echo-canceling filters are enclosed in Appendix B.

The results obtained with the AB2 estimator will be discussed in the following. Only results obtained after echo-canceling with the HP filter will be discussed to be able to compare the performance of the two estimators. The AB2 estimator is more stable to variations in the values of N_l and N_s than the AB1 estimator, since:

- the estimates and standard deviations obtained with the AB1 and the AB2 estimators are identical for the combinations of N_l and N_s that produce good estimates with the AB1 estimator,
- good estimates are obtained for combinations of N_l and N_s, which were not possible with the AB1 estimator,
- the incorrect estimates for the velocity equal to 30 cm/s span the range from 29 to 50 cm/s with standard deviations in the range from 1.1 to 21 cm/s. The mean and standard deviation span a narrower range of values, than were the case for the AB1 estimator. The 2π-investigations performed with the AB2 estimator turn out successful for quite a lot of the 100 realizations of the data set. If the definition of a good estimate is changed, so higher values of the bias and standard deviation are allowed, some of the remaining combinations of the N_s and N_l will produce good estimates,
- the restrictions on the choice of parameters introduced for the velocity 40 cm/s do not exist for the AB2 estimator.

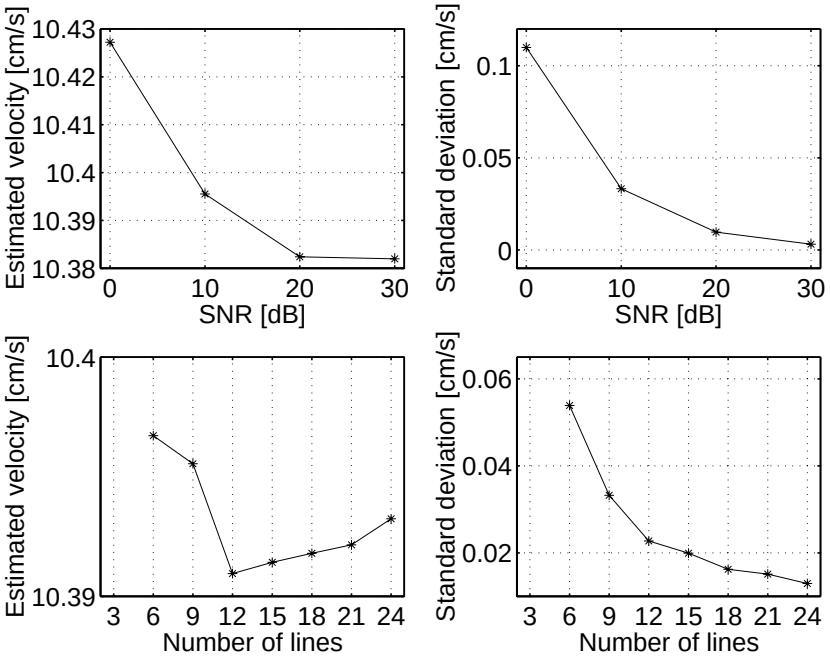

Figure 6.41: Performance of the AB1 estimator as a function of the number of lines and the SNR. HP echo-canceling filter applied. The sampling frequency is 30 MHz, and the number of samples are equal to one pulse length. The true velocity is 10 cm/s.

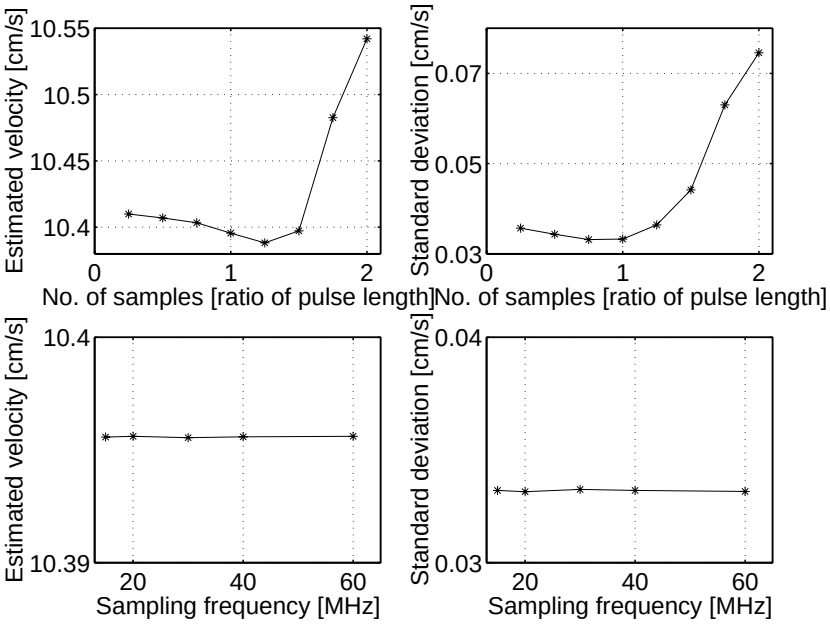

Figure 6.42: Performance of the AB1 estimator as a function of the number of samples and the sampling frequency. HP echo-canceling filter applied. The SNR is 10 dB, and 9 lines were employed. The true velocity is 10 cm/s.

For the AB2 estimator to perform well for all SNRs, all values of N_l, and all velocities the number of samples employed in the estimation should equal the number of samples within 0.25 pulse lengths. A slight improvement on the accuracy is obtained, if N_s equals 0.5 pulse lengths, and $N_l \geq 9$. The trends with respect to the bias, and the relations between the standard deviation and the parameters f_s, N_l, and the SNR are the same for the AB1 and the AB2 estimators.

The same combination of parameters gives the best performance of the two estimators, when the velocities 10, 20, and 30 cm/s are considered. The AB2 estimator can handle the velocity 40 cm/s for a wider range of values of the parameters. For the given data set the AB2 estimator is to be preferred over the AB1 estimator.

The performance of the EAM and the AB estimators on the synthetic data set is identical. The best performance is obtained for the same combination of parameters, and the mean and standard deviations are identical. Based on this observation the EAM estimator should be preferred over the AB estimator, if the computational load is of concern. Otherwise the AB estimator should be used, since it is more stable to variations in the choice of parameters.

The mean and the standard deviation on the estimates are identical for most combinations of the parameters, when the performance of the AB and the autocorrelation estimators are compared for velocities below 30 cm/s. Only the AB estimator can handle the velocities 30 and 40 cm/s. Therefore the AB estimator should be preferred over the autocorrelation estimator, since it is able to produce good estimates for the full range of velocities.

The AB estimator performs well for more combinations of the parameters than the cross-correlation estimator. Both estimators can handle velocities above 20 cm/s. Estimates with a zero standard deviation can be obtained with the cross-correlation estimator for high SNRs, which is not possible with the AB estimator. For lower SNRs the standard deviations for the two estimators are more similar. Still the AB estimator should be preferred over the cross-correlation estimator, since it is more stable to variations in the SNR and the choice of parameters.

A comparison of the results for the AB and the BST estimators reveals that both estimators can handle velocities above 20 cm/s. The AB estimator can produce good estimates for more combinations of the parameters than the BST estimator, and the standard deviation at low SNRs is lower for the AB estimator. At higher SNRs the BST estimator produces estimates with a standard deviation of zero, which is not possible with the AB estimator. Based on the performance at low SNRs the AB estimator should be preferred over the BST estimator.

6.7.2 Performance on simulated data

The performance of the AB1 and the AB2 estimators is evaluated in the following. The evaluations are carried out on both data sets (short and long emitted pulse). The initial estimate computed by the autocorrelation estimator is the ”correct” estimate. The idea of performing the autocorrelation estimation and the subsequent variance analysis with different values of N_s is investigated. Samples equal to one pulse length is used to compute the autocorrelation estimate. The number of samples used in the variance analysis are varied. The performance is evaluated by determining the number of correct 2π-investigations.

First, the performance on the data set generated with a narrow band pulse is evaluated, when the AB1 estimator is employed. In Fig. 6.43 the number of correct 2π-investigations $N_{2\pi}$ (in %) as a function of the number of samples employed for the variance analysis are plotted. The SNR is 10 and 20 dB, respectively. The best performance is obtained, when the number of samples equal 0.6-0.65 pulse lengths. The number of correct 2π-investigations are 68.1 % and 63.7 % for a SNR of 20 and 10 dB, respectively. As the SNR increases a better performance is obtained. Still 30-36 % of the 2π-investigations turn out wrong, and this

is a problem.

The performance of the AB2 estimator has been determined, and the number of correct 2π-investigations as a function of the number of samples employed are plotted in Fig. 6.44. The number of correct 2π-investigations increases, as the number of samples employed for the variance analysis increase. For N_s equal to 5-6 pulse lengths the performance converges to 92 %, when the SNR is 20 dB. The variance analysis is not reliable unless a large number of samples are employed. One should remember that 4 and 6 pulse lengths equal 6.2 and 9.3 mm's. The diameter of the vessel is 6 mm. The performance decreases as the SNR decreases, and a higher value of N_s must be employed to obtain the maximum number of correct 2π-investigations. The AB2 estimator out performs the AB1 estimator, when N_s exceed one pulse length, and the AB2 estimator should be preferred over the AB1 estimator for blood velocity estimation. The performance of the AB2 estimator is discussed in the following. Although the 2π-investigations turn out correct in the majority of the investigations, some erroneous estimates still exist. The 2D plots of the velocity estimates have been investigated, when N_s equal 5 pulse lengths. Quite a few of the incorrect estimates group together axially. For a number of lines incorrect estimates are obtained across the full axial extent of the vessel. Only few single errors exist. The incorrect velocity estimates along the anterior and posterior vessel wall are mostly under- and overestimated, respectively. Examples of the estimates on a systolic and diastolic frame are plotted in Fig. 6.45. The same two frames, which have been used to show the performance of the estimators discussed in the previous sections, are used here. Only the velocity estimates within the vessel are displayed. Estimates that are plotted with the maximum and minimum value of the velocity scale take values above or below these border values. In Fig. 6.46 the estimates for two axial lines, which are taken from the systolic and diastolic frame in Fig. 6.45, are plotted. The measure for the number of highly deviating estimates, which was determined for the previous evaluated estimators, will also be used to determine the performance of the AB2 estimator. A total of 9.0 % of the estimates take values outside the velocity range from -10 cm/s to 80 cm/s. As the "correct" estimates are equal to the estimates obtained with the autocorrelation estimator, the trends with respect to the variations about the true velocities are the same. This discussion will not be repeated here.

Data obtained after emission of a narrow band pulse is to be preferred, if a good initial estimate is to be computed with the autocorrelation estimator. The variance analysis performs best, when a wideband pulse is emitted. A conflict with respect to choosing the excitation pulse exists - just as was the case for the EAM estimator. The performance of the AB2 estimator is determined for the data set that favors the BST estimator, and the results are discussed in the following. Figure 6.47 shows the number of correct 2π-investigations as a function of N_s. The AB2 estimator performs slightly better on the data set, which was generated from a short excitation pulse. For N_s equal to 5 pulse lengths a total of 89.5 and 96.3 % of the 2π-investigations turn out correct, when the SNR is 10 and 20 dB, respectively. The performance for a SNR of 10 dB can be increased, if N_s are increased. A total of 3.8 % of the estimates take values outside the velocity range from -10 cm/s to 80 cm/s, when the SNR is 20 dB. The estimated velocity profiles for a systolic and diastolic frame are plotted in Fig. 6.48, when N_s equal 5 pulse lengths. Only the velocity estimates within the vessel are displayed, and it is the same two frames used to show the performance of the previously evaluated estimators. The majority of the remaining incorrect estimates show up in the last axial line (to the right) in the images. Some single and grouped errors are seen, and they are mostly located along the vessel wall. It will be beneficial to apply the 2D tracking filter (see Section 6.5.2) prior to displaying the estimates, so some of the incorrect estimates are removed. The velocity profiles obtained with the AB2 estimator, when it was applied to the data set generated from a long and short excitation pulse, have been compared. The trends with respect to the non-highly deviating estimates, which were seen with the EAM estimator, also exist for the AB2 estimator. The estimates, which arise from the application of the AB2 estimator to the data generated with a short pulse, fluctuate more, when the course across the axial extent of the vessel is investigated. The velocity values are lower and thereby further from the true velocities. The basis for the autocorrelation estimation has been degraded, and the estimates come with a higher inaccuracy.

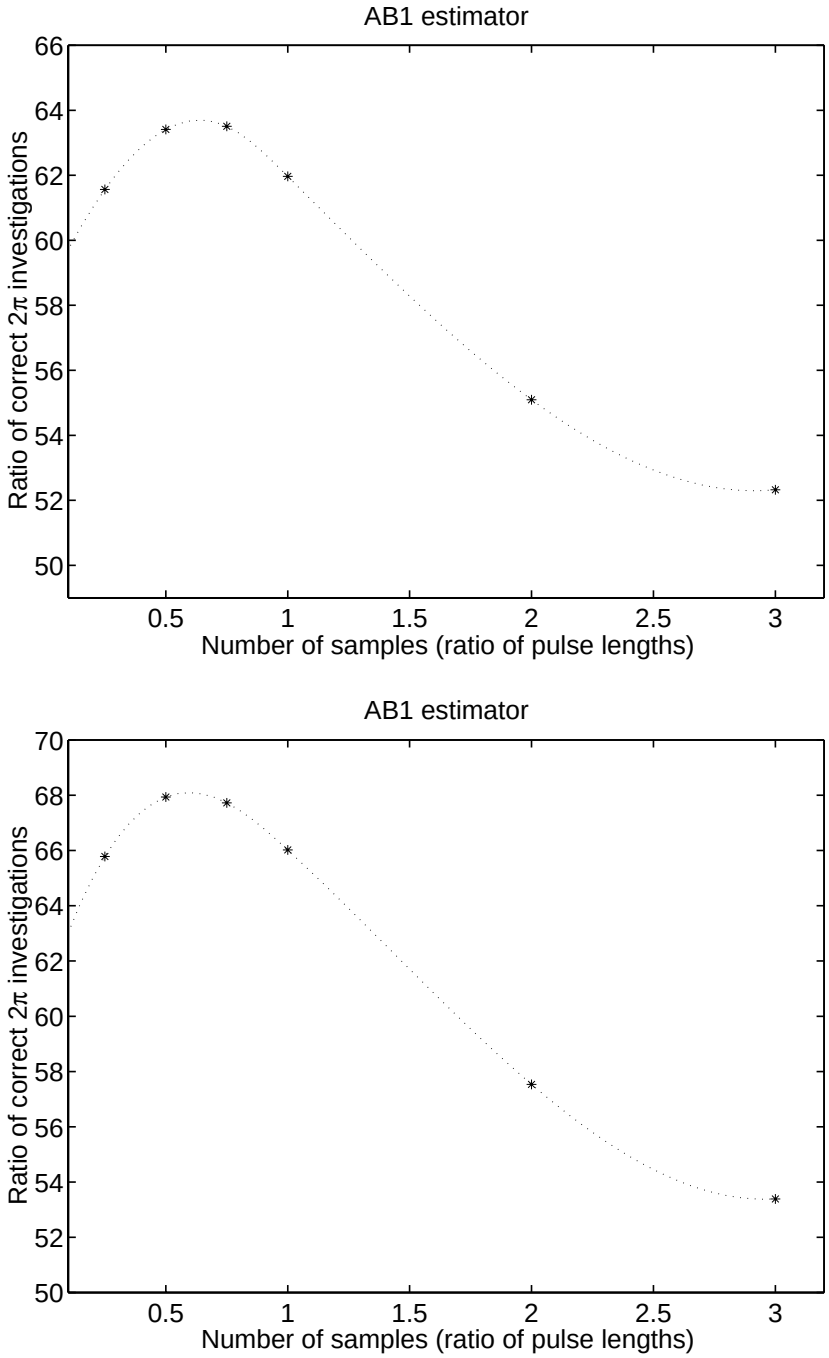

Figure 6.43: Number of correct 2π-investigations (in %) as a function of the number of samples used in the variance analysis with the AB1 estimator. The SNR is 10 (top) and 20 dB (bottom), respectively.

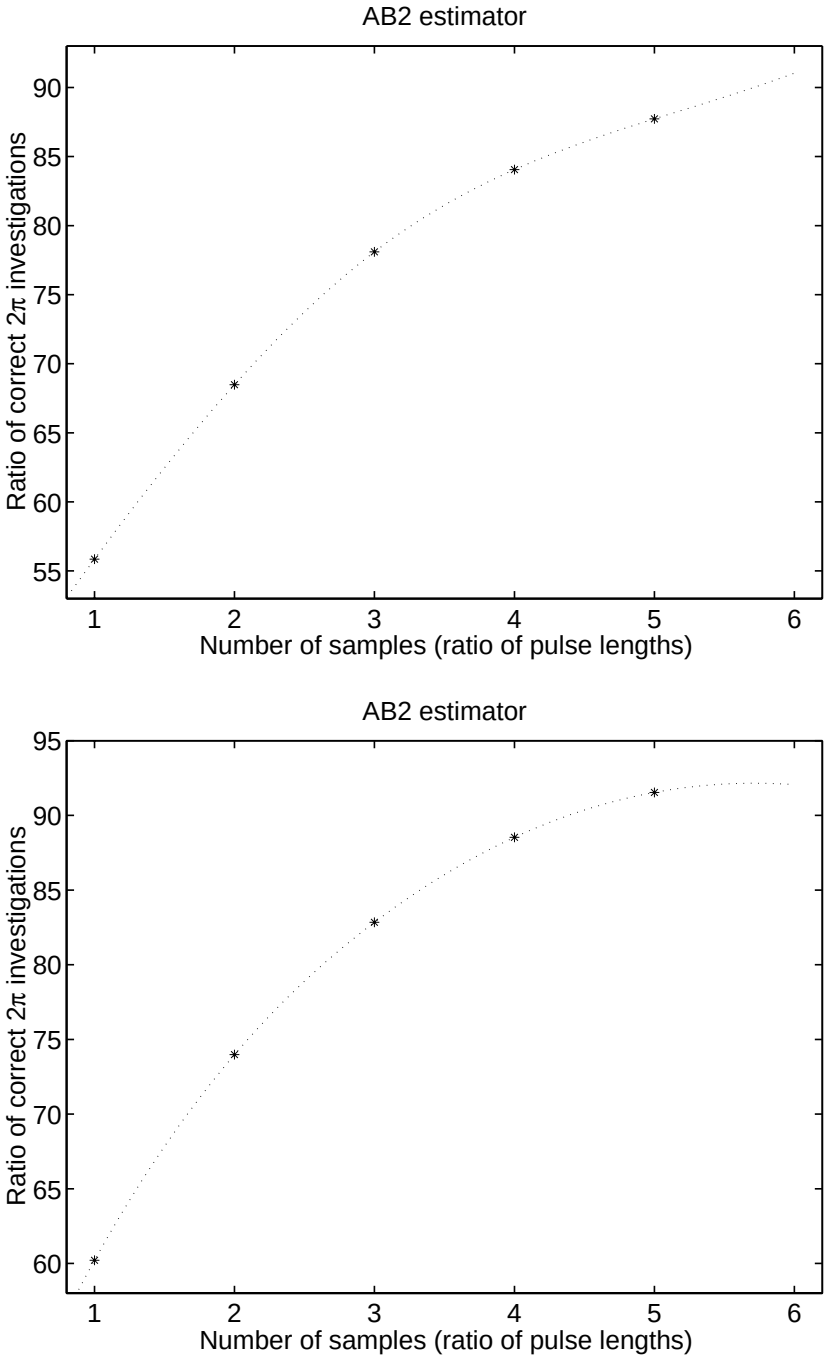

Figure 6.44: Number of correct 2π-investigations (in %) as a function of the number of samples used in the variance analysis with the AB2 estimator. The top and bottom plots shows the results for a SNR of 10 and 20 dB, respectively.

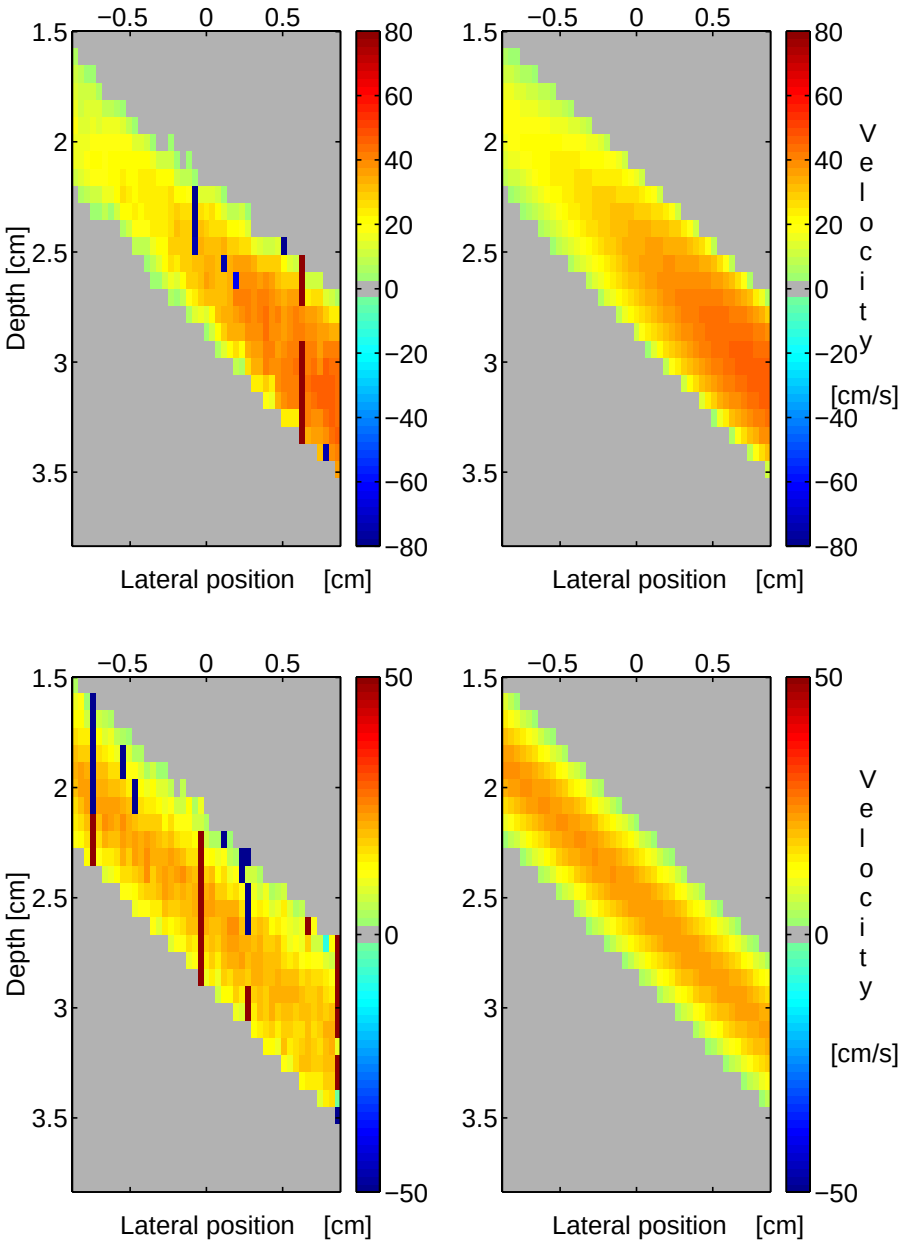

Figure 6.45: AB2 estimator: The estimated and true velocities of a systolic (upper two plots) and diastolic frame (lower two plots), when the data set is generated from a long excitation pulse. The SNR is 20 dB, and N_s (for the variance analysis) are 5 pulse lengths.

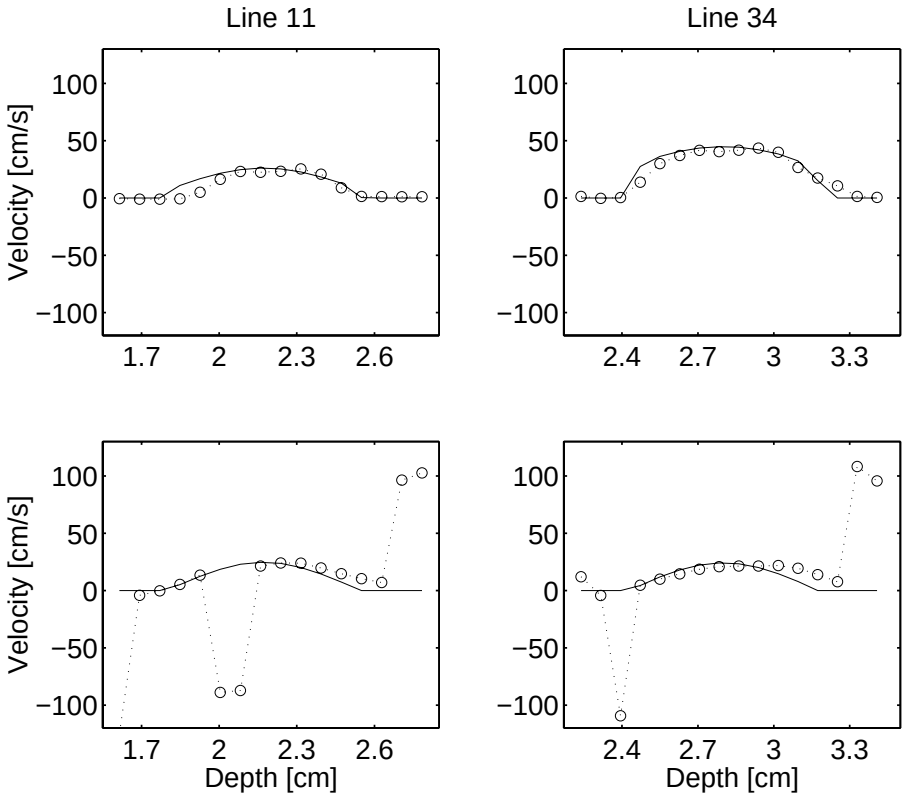

Figure 6.46: AB2 estimator: The estimates for line 11 and 34 in the images of the systolic (upper 2 plots) and diastolic frame (lower 2 plots). The SNR is 20 dB.

The performance (with respect to the number of correct 2π-investigations) of the AB1 estimator also improves, when it is applied to the data set generated from a short excitation pulse. Still, the AB2 estimator out performs and should be preferred over the AB1 estimator.

In Appendix C the images, which contain the velocity profiles, are included for all 10 frames in the cardiac cycle.

The RMS error for the AB2 estimator as a function of N_s (for the variance analysis) are listed in Table 6.3. These RMS errors relate to the performance, when the estimator are applied to the data set generated with a long and a short pulse, respectively.

The autocorrelation estimator out performs the AB estimator, when no aliasing occur. The RMS error is

Excitation pulse	SNR (dB)	Number of samples (ratio of pulse lengths) 0.25	0.5	1.0	2.0	3.0	4.0	5.0
Long	10	-	-	0.73	0.62	0.53	0.45	0.39
	20	-	-	0.69	0.57	0.46	0.38	0.33
Short	10	0.69	0.66	0.61	0.53	0.46	0.41	0.36
	20	0.56	0.53	0.46	0.36	0.29	0.25	0.22

Table 6.3: The RMS error ([m/s]) as a function of the number of samples used in the variance analysis with the AB2 estimator. The results are listed, when the estimator is applied to the data set generated with a long and a short pulse, respectively. The SNR is 10 and 20 dB, respectively.

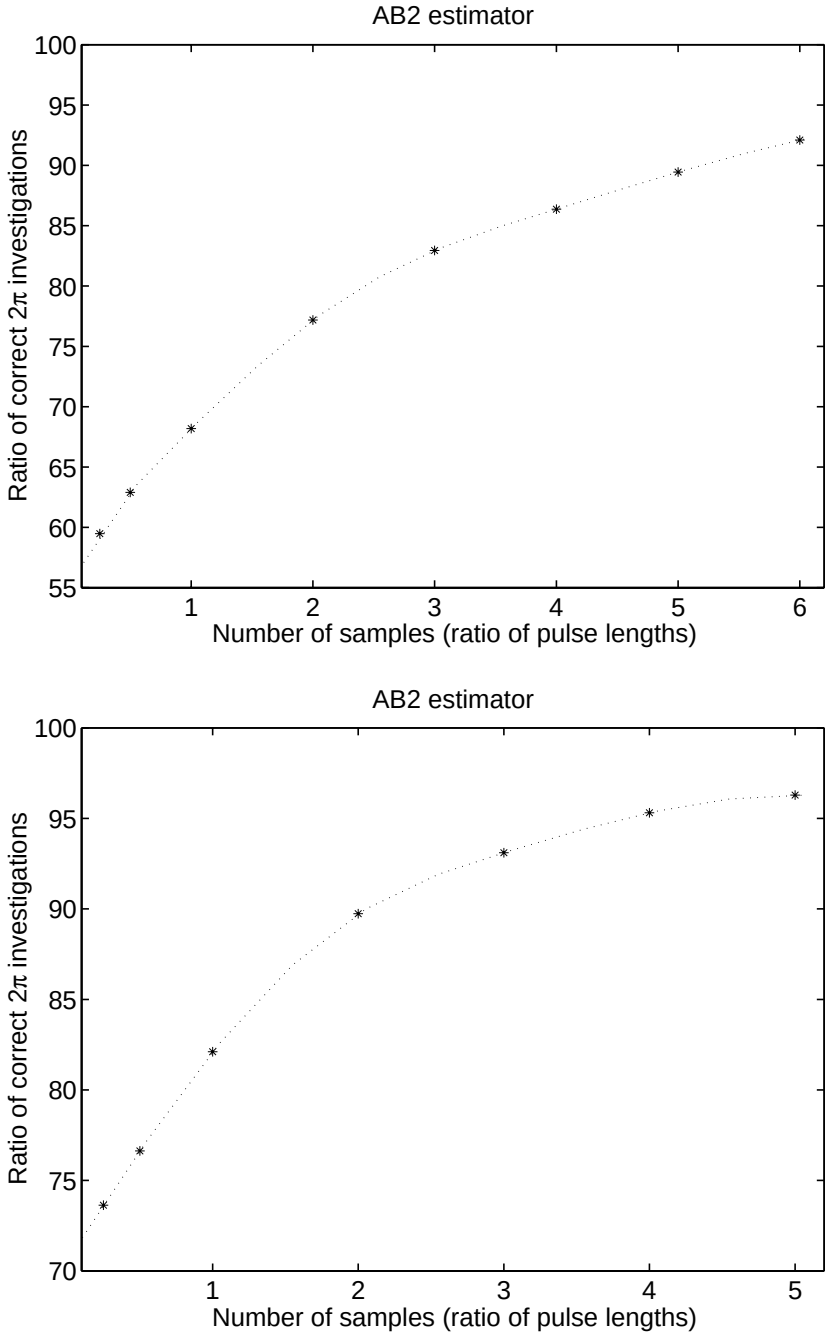

Figure 6.47: Number of correct 2π-investigations (in %) as a function of the number of samples used in the variance analysis with the AB2 estimator. The top and bottom plots shows the results for a SNR of 10 and 20 dB, respectively. A short excitation pulse was used.

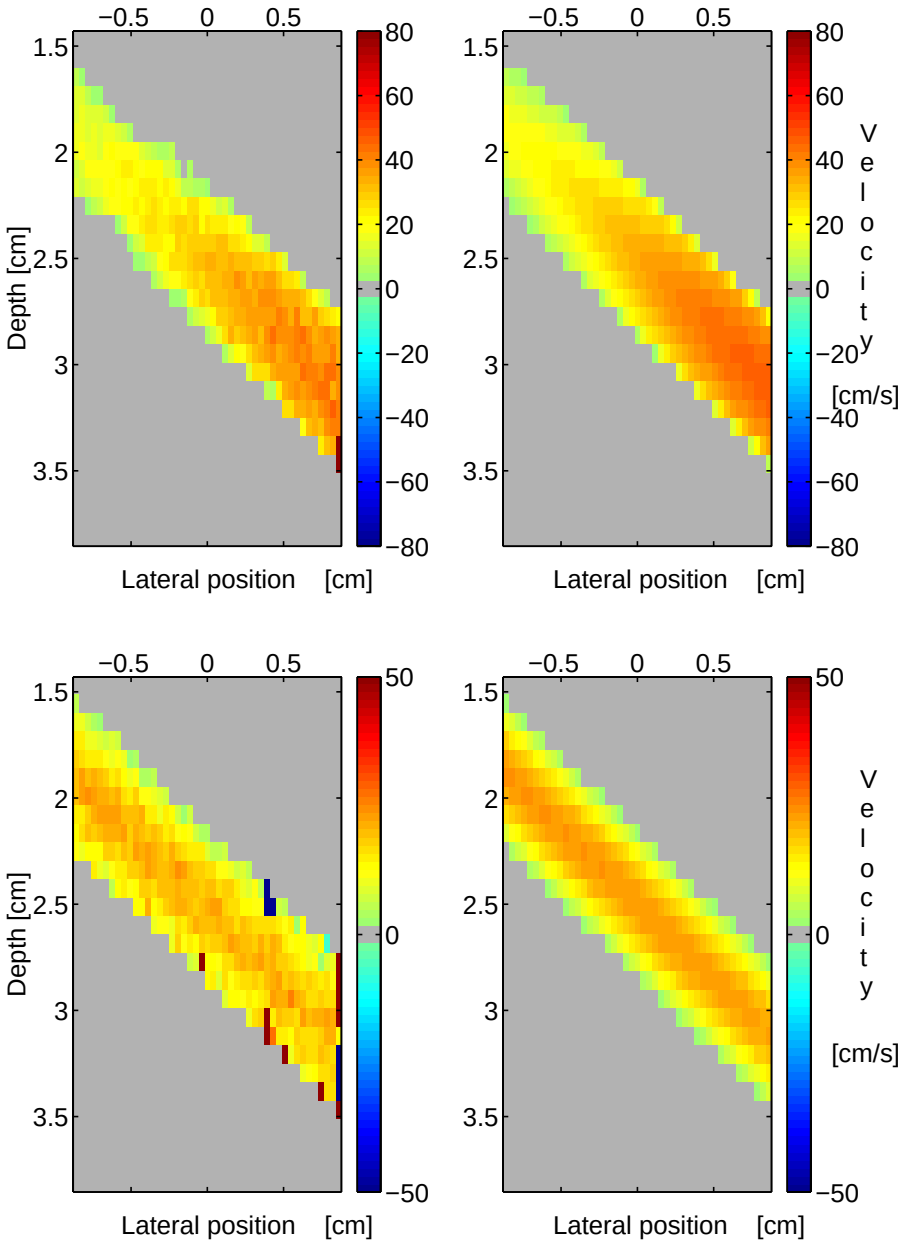

Figure 6.48: AB2 estimator: The estimated (left) and the true (right) velocities of a systolic (upper two plots) and diastolic frame (lower two plots). The SNR is 20 dB, and the data set generated with a short pulse is used. The number of samples used in the variance analysis are equal to 5 pulse lengths.

lower, and hardly any highly deviating velocity estimates are seen. The performance of the AB2 estimator comes close to the performance of the autocorrelation estimator, though. If (some of) the highly deviating estimates can be removed by proper post-processing, the AB2 estimator should be preferred over the autocorrelation estimator, as it is designed to handle the aliasing problem.

The AB2 estimator out performs the cross-correlation estimator. This conclusion is independent of the choice of data set, as the RMS error is lower for both data sets. Fewer highly deviating estimates are obtained with the AB2 estimator, and the estimates follow the velocity variations throughout the vessel and the cardiac cycle more closely. Post-processing of the estimates should be performed for both estimators prior to displaying the estimates.

Both the AB2 and the EAM estimators were developed to overcome the limitation of the autocorrelation estimator with respect to aliasing. None of them perform as well as the autocorrelation estimator, when no aliasing is present. Both estimators produce deviating estimates, which are off by an integer number of 2π. The analysis with the cross-correlation estimator or the BST estimator fails. A comparison reveals that the AB2 estimator out performs the EAM estimator. The introduction of a variance analysis (inherited from the BST estimator) instead of the cross-correlation analysis improves the investigation of the set of possible 2π phases. This conclusion is based on the values of the RMS errors, the measure of the number of highly deviating estimates, and the inspection of the computed velocity estimates. Still post-processing is required to minimize the error.

The performance of the BST and the AB2 estimators are similar, when the AB2 estimator is applied to the data generated from a short excitation pulse. The conclusion is based on a comparison of the RMS errors and the measures for the number of deviating estimates. The estimation with the BST estimator is performed with N_s equal to 3 pulse lengths. Deviating estimates occur for both estimators and must be removed by means of post-processing. The visual inspection of the obtained velocity estimates shows that the AB2 estimator produces estimates, which follow the velocity variations better. Based on this observation the AB2 estimator should be preferred over the BST estimator, if the AB2 estimator is applied to data generated with a short excitation pulse.

6.8 Wideband Maximum Likelihood estimator

The estimator described in this section is inspired by techniques developed for radar. The field of detection and estimation is of much concern in radar. Objects (*e.g.* airplanes, missiles) must be detected, and features (*e.g.* velocity and direction) must be estimated. Algorithms have been developed based on statistics, which are capable of performing the detection and estimation. A thorough discussion of these are available from the books on detection and estimation by Van Trees [33], [34]. The methods are developed for complex signals and will be used for this type of signals in this study. Ferrara et al. [48], [58] employed this theory and developed an estimator applicable for estimation on RF-signals. It is named the Wideband Maximum Likelihood estimator (MLE), and the estimator will be derived in the following. The derivation is split up into a number of steps. Otherwise the discussion easily becomes unclear. The basic principles of estimation and detection will be discussed first in Section 6.8.1. The expansion for the situation at hand will be introduced in Section 6.8.2.

6.8.1 Basic principles of detection and estimation theory

The objective of performing detection and estimation is to determine the presence of one or more objects and estimate some properties for these objects. If each of the objects (*e.g.* airplane, group of scatterers) emit a characteristic signal, $\sqrt{E}s(t)$, this can be acquired and used for the detection and estimation. The signal

can be self generated or a reflection of a transmitted signal from an observer. The variable E represents the energy of the received signal, and it is assumed that $\int_0^T s^2(t) = 1$. The following discussion will investigate the situation, when only one object is present. The derived algorithms can be extended to the situation of more objects [33], [34]. The presence of the object is not known a priori, so the acquired signal, $r_c(t)$, can either contain noise only or the emitted signal added noise. Two situations - equal to two hypothesis (H_0, H_1) in statistics - can exist:

$$r_c(t) = \begin{cases} \sqrt{E}s(t) + n(t) & 0 \leq t \leq T : H_1 \\ n(t) & 0 \leq t \leq T : H_0, \end{cases} \tag{6.20}$$

where T represents the temporal length of an observation. It is desirable to reduce the dimensionality of the signal vector $r_c(t)$ to ease the subsequent detection and estimation process [33], [34]. If $s(t)$ is known, it is beneficial to perform the reduction through a series expansion of $r_c(t)$ [33], [34]:

$$\begin{aligned} r_c(t) &= \lim_{K\to\infty} \sum_{i=1}^{K} q_i \psi_i(t) \\ & \qquad 0 \leq t \leq T, \end{aligned} \tag{6.21}$$

where q_i are the coefficients of the series, and ψ_i are a set of orthonormal functions. If the first orthonormal function, ψ_1, is set equal to $s(t)$, the coefficients become:

$$q_1 = \begin{cases} \int_0^T (\sqrt{E}s(t) + n(t))s^*(t)dt &= \sqrt{E} + n_1 : H_1, \\ \int_0^T n(t)s^*(t)dt &= n_1 : H_0. \end{cases} \tag{6.22}$$

$$q_i = \begin{cases} \int_0^T (\sqrt{E}s(t) + n(t))\psi_i(t)dt &= n_i : H_1, \\ \int_0^T n(t)\psi_i(t)dt &= n_i : H_0. \end{cases} \tag{6.23}$$

Only q_1 will contain information related to $s(t)$, since all ψ_i are orthogonal to $s(t)$ for $i > 1$. Therefore q_1 represents the measure (the sufficient statistic), which is needed to perform the detection and estimation. Given the probability density of q_1 under the two hypothesis, a statistical solution based on the likelihood ratio $LR(Q_1)$ can be obtained [33]:

$$LR(Q_1) = \frac{p_{q_1|H_1}(Q_1|H_1)}{p_{q_1|H_0}(Q_1|H_0)}, \tag{6.24}$$

where Q_1 represents an observation of q_1, and $p_{q_1|H_0}$ and $p_{q_1|H_1}$ are the probability density functions under H_0 and H_1, respectively. The likelihood ratio determines the ratio of the probability values for the observation under the two hypothesis. The ratio performs a comparison of the probability values, and the output expresses which hypothesis is more likely. A decision criteria is introduced as a threshold value η for the ratio. The detection problem is then solved by comparing the likelihood ratio to the threshold:

$$LR(Q_1) \underset{H_0}{\overset{H_1}{\gtrless}} \eta. \tag{6.25}$$

The computation of q_1 is equal to a correlation analysis between the acquired signal, $r_c(t)$, and the reference signal, $s(t)$.

The likelihood ratio can also be employed for the estimation of properties of the object [34]. One property could be the distance from the observer to the object of interest. Consider the situation where the observer transmits a signal. As this signal reaches the object, the transmitted signal is reflected. The reflected signal will reach the observer, and the time of arrival is related to the distance. As the distance is not known a priori, the acquisition takes place over a time window T_w ($T_w >> T$). In this long signal the reflected signal is present within a temporal interval $[t_1, t_1 + T]$, and the determination of t_1 equals the estimation of

the distance. A search through the long signal must be performed for the range of possible values of t_1. Although not stated in the above discussion of the detection problem a search through a long signal is also required as the distance is not known a priori. For each investigated interval $[t, t+T]$ q_1 is computed, and the presence of the reflected signal within the investigated interval is determined. At some point the signal is detected, and the temporal value t is the estimate of the temporal location t_1. The likelihood ratio takes its maximum value [33], [34], when the signal is detected, so the estimate of the temporal location $\hat{t}_1$ is determined as:

$$\hat{t}_1 = \arg\max_t(LR(Q_1(t))), \tag{6.26}$$

where t takes values in the range from 0 to $T_w - T$. An estimator based on this theory is named a maximum likelihood estimator.

A statistical approach for detection and estimation has been derived above. It requires knowledge of:

- the signal of interest, $s(t)$,
- the distribution for q_1 under H_0 and H_1, respectively.

The detection and estimation are then based on the likelihood ratio.

6.8.2 Estimation of blood velocity

The maximum likelihood estimation scheme derived above can also be used for estimation of the blood velocities in ultrasound RF-signals. The situation is slightly more complicated though, as a large number of small objects (the scatterers) are present and contribute to the acquired signal. As discussed in Section 6.1, the acquired signal consists of the sum of contributions from the individual scatterers distributed in space. Therefore the (average) velocity of a group of scatterers will be determined, rather than the velocity of each scatterer.

The first step in the estimation was to reduce the dimensionality of the signal vector. A choice of the orthonormal functions, ψ_i, is required. If ψ_1 was chosen to be identical to the signal of interest, an estimator based on q_1 alone could be obtained. As the properties of the scatterers and the attenuation are not known a priori, it is not possible to determine the response from a group scatterers. The signal $s(t)$ cannot be modeled. Even if $s(t)$ could have been modeled, it will be very difficult to determine the blood velocities by processing one RF-line only, as the Doppler shift is negligible compared to the spectrum changes from attenuation. Only the position of the scatterers could have been determined. Instead several RF-signals should be acquired and used to determine the shift in position between acquisitions, which gives a basis for estimating the velocity. The acquisition of several RF-lines also makes it possible to determine an approximative model for $s(t)$. If it is assumed that the response from a group of scatterers does not change between acquisitions, the same response will be present in all RF-signals. The location of the response in each RF-signal is shifted, as the scatterers have moved between acquisitions. The response in the first RF-line can be used as a model for $s(t)$ and be used to perform the correlation analysis. The correlation analysis requires that a set of samples are employed. The first RF-line, which now acts as the reference line, is split up in a number of segments, and a velocity estimate is determined for each segment. The reference segment is compared to segments in all RF-lines - including the first RF-line:

$$q_{1,l} = \sum_{k=0}^{N_s-1} r_{c,cfm}(1, k + i_{seg}N_s) r^*_{c,cfm}(l, k + i_{seg}N_s + n \cdot (l-1)), \tag{6.27}$$

where n gives the temporal shift in position of the segments in the RF-signals in number of samples. The parameter n is a function of the investigated velocity. A total of $N_{l,e}$ values of q_1 are obtained from each

correlation analysis, and these observations are referred to as $Q_{1,l}$. The position of the segments in the RF-lines are determined by the velocity, which currently is being evaluated. In Section 6.8.1 the correlation was performed over a range of temporal values, which represented the temporal location in the signal. The temporal location is related to the velocity, so in the following the $q_{1,l}$ and the likelihood ratio will be defined as a function of velocity. The velocity variable is named v_p. Each value of $Q_{1,l}$ tells, if the reference signal has been detected in the RF-line under investigation.

The probability density of each q_{1} under H_1 is a complex Gaussian distribution with a zero mean [33], [34], [48], [51], [58]. The variance equals the energy of the reference signal, which includes the energy of the response, E_r, and the noise, N_0. The probability density of the sum of the $q_{1,l}$ will also be a complex Gaussian distribution, when the individual $q_{1,l}$ are assumed statistically independent. The probability density of $q_{1,s} = q_{1,1} + ... + q_{1,N_{l,e}}$ is:

$$p_{q_{1,s}|H_1}(Q_{1,s}|H_1) = \frac{1}{\pi(E_r+N_0)N_{l,e}} \exp\left(-\frac{|Q_{1,s}(v_p)|^2}{(E_r+N_0)N_{l,e}}\right), \tag{6.28}$$

where $N_{l,e}$ represent the number of lines available for the estimation after echo-canceling. The probability density of $q_{1,s}$ under H_0 is:

$$p_{q_{1,s}|H_0}(Q_{1,s}|H_0) = \frac{1}{\pi N_0 N_{l,e}} \exp\left(-\frac{|Q_{1,s}(v_p)|^2}{N_0 N_{l,e}}\right). \tag{6.29}$$

As the probability density of $q_{1,s}$ is known under H_0 and H_1, the likelihood ratio can be derived:

$$\begin{aligned} LR(Q_{1,s}(v_p)) &= \frac{p_{q_{1,s}|H_1}(Q_{1,s}|H_1)}{p_{q_{1,s}|H_0}(Q_{1,s}|H_0)} \\ &= \frac{(\pi(E_r+N_0)N_{l,e})^{-1} \exp\left(-\frac{|Q_{1,s}(v_p)|^2}{(E_r+N_0)N_{l,e}}\right)}{(\pi N_0 N_{l,e})^{-1} \exp\left(-\frac{|Q_{1,s}(v_p)|^2}{N_0 N_{l,e}}\right)}. \end{aligned} \tag{6.30}$$

By taking the logarithm and rearranging the terms the following relation is obtained:

$$\ln(LR(Q_{1,s}(v_p))) = \ln(\frac{N_0}{E_r+N_0}) + \frac{E_r}{(E_r+N_0)N_0 N_{l,e}}|Q_{1,s}(v_p)|^2. \tag{6.31}$$

The parameters N_0, E_r, and $N_{l,e}$ are constants. They only contribute with an offset value and a scaling of $|Q_{1,s}(v_p)|^2$, so $|Q_{1,s}(v_p)|^2$ represents the sufficient statistic (the measure), which is needed to perform an estimation of v_p. If $|Q_{1,s}(v_p)|^2$ is computed (using (6.27) and summing the $N_{l,e}$ values) for the range of velocities, the maximum of $|Q_{1,s}(v_p)|^2$ gives the estimate of the (average) velocity for a group of scatterers:

$$\hat{v}(x,z,t_f) = \arg\max_{v_p}(|Q_1(v_p)|^2). \tag{6.32}$$

The derived scheme for estimation can be employed to determine estimates of the blood velocity. A short excitation pulse should be employed to minimize the influence of velocity spread, which will degrade the performance of the estimator. The correlation analysis tries to find a signal, which is identical to the reference signal. Due to the decorrelation a perfect match does not exist.

The computational load of the estimator is higher than for the cross-correlation estimator, as the correlation analysis is performed on the complex data. The number of additions $N_{a,MLE}$ and multiplications $N_{m,MLE}$ performed to obtain the value of $|Q_{1,s}|^2$ for $N_{v-steps}$ velocity values are:

$$\begin{aligned} N_{m,MLE} &= 4N_s N_{l,e} N_{v-steps} + 4N_{v-steps} \\ N_{a,MLE} &= 2(N_s-1)N_{l,e}N_{v-steps} + 3N_{v-steps} + (N_{l,e}-1)N_{v-steps}. \end{aligned} \tag{6.33}$$

These numbers have been obtained by counting the number of multiplications and additions performed to compute $Q_{1,l}$ in (6.27) and $|Q_{1,s}|^2$ for the range of investigated velocities.

6.8.3 Performance on synthetic data

The performance of the maximum likelihood estimator (MLE) was determined on the synthetic data set generated with a short excitation pulse. The estimator parameters were varied as follows:

- number of lines : $N_l \in [3, 6, 9, 12, 15, 18, 21, 24]$,
- sampling frequency : $f_s \in [15, 20, 30, 40, 60]$ MHz,
- number of samples : $N_s \in [0.25, 0.5, 0.75, 1.0, 1.25, 1.5, 1.75, 2.0]$ times the length of the emitted pulse. The length in samples is dependent on the sampling frequency.

The velocity range from -50 cm/s to 50 cm/s was investigated with a resolution of 1 cm/s. No interpolation of the likelihood ratio is performed prior to the determining the maximum. The velocity resolution on the estimates is restricted by the choice of the step size. A good performance on the estimation is obtained, when the mean lies within $\pm$ 2 cm/s of the true velocity, and the standard deviation is less than 1 cm/s. The following trends exist, when the velocities 10, 30, and 40 cm/s are evaluated, and a good performance is obtained:

- the maximum likelihood estimator does not suffer from aliasing problems,
- the estimates are biased. The bias decreases to 0 cm/s for the estimation of the velocity 10 cm/s, when N_l increase. For the velocities beyond 10 cm/s the bias converges to +1 cm/s as N_l increase. This trend holds for all values of N_s,
- the standard deviation decreases and reaches 0 as N_l increase. The zero standard deviation is obtained even for low values of N_l, and no performance improvement is obtained, if N_l are increased. The lower value of N_l, which gives zero standard deviation, is dependent on the SNR and the choice of echo-canceling filter. As the SNR increases the limit decreases,
- the choice of N_s only plays are role for low values of N_l and the SNR, where the standard deviation varies for the different values of N_s,
- the performance is independent of the choice of sampling frequency for most combinations of N_l and N_s. The sampling frequency should be higher than 15 MHz, when the SNR and N_l take a value in the lower range, to ensure a good performance.

The MLE estimator performs very well on the velocities 10, 30, and 40 cm/s, where a standard deviation close to or equal to zero can be obtained even at low SNRs and low values of N_l. For a velocity of 20 cm/s this can only be obtained for high SNRs. The estimate is still biased, and the bias takes a positive value. For most combinations of N_l and N_s the bias approaches +1 cm/s, as the SNR increases. For some choices of N_s the bias goes to zero, when the number of lines used are low. An overall good performance on the estimation of the velocity 20 cm/s is obtained, when N_s take a value in the range 1-1.5 pulse lengths. For all 4 velocities the following can be concluded. Employment of the regression line filter requires that more than 3 lines are available. Otherwise the subsequent estimation fails. If a bias of zero for the velocity 10 cm/s should be obtained, a minimum of 15 lines must be employed. The HP filter is able to produce the zero bias for the velocity 10 cm/s, when only 6 lines is employed. The levels of the standard deviations for the three echo-canceling filters are very similar. The standard deviation after application of the HP filter takes values higher, lower, and equal to the standard deviations obtained, when no echo-canceling was applied. The difference in the levels of the standard deviations are on the order of a few millimeter per second for these two filters. The standard deviations are even more similar, when the results obtained with the regression line filter and no echo-canceling filter are compared. So the performance of the estimator is

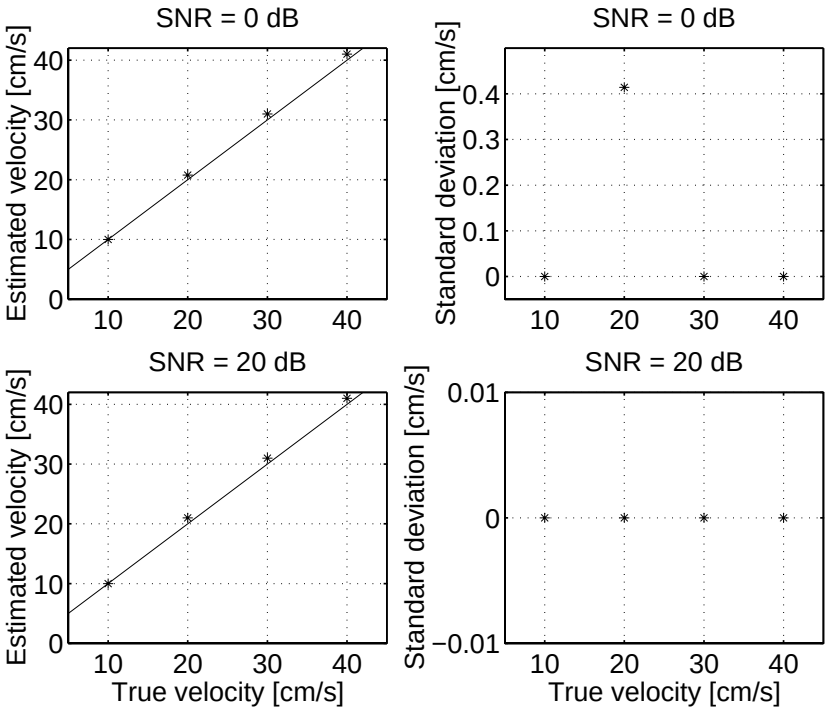

Figure 6.49: The maximum likelihood estimator: the true (—) and the estimated (*) velocities along with the standard deviation for a SNR of 0 and 20 dB. Nine lines were employed. The sampling frequency is 30 MHz, and the number of samples are equal to one pulse length.

not influenced significantly by the introduction of the echo-canceling filters for the given data. Please refer to Appendix B to see tables containing the performance for the range of the parameters, the velocities, and the echo-canceling filters. Examples of the performance are plotted in Figures 6.49-6.51, when the different parameters are varied. The HP echo-canceling filter was applied prior to the velocity estimation. When one parameter is varied, the others are kept constant at: the SNR is 10 dB, N_l are 9, the sampling frequency is 30 MHz, and N_s are equal to one pulse length.

The maximum likelihood estimator out performs all of the estimators discussed previously for the velocities 10, 30, and 40 cm/s, when the SNR is low and N_l is above 6 lines. Estimates with a standard deviation of 0 cm/s can be obtained under these conditions.

The MLE estimator does not suffer from aliasing problems, and therefore the MLE estimator should be preferred over the autocorrelation estimator. When the velocity is 20 cm/s or N_l is low, the lowest standard deviation on the estimate is obtained with the autocorrelation estimator.

The maximum likelihood estimator performs well for most combinations of the parameters. So overall the MLE should be preferred over the cross-correlation estimator.

Both the MLE and the EAM estimators can handle the full velocity range. For low SNRs and a velocity of 20 cm/s the EAM estimator produces estimates with a lower variance than the MLE estimator. At higher SNRs the MLE estimator out performs the EAM estimator, as estimates with a zero standard deviation are obtained. Overall the MLE estimator should be preferred over the EAM estimator.

The performance of the BST and the MLE estimators is very similar. Both can handle the full range of velocities, and they produce estimates with a zero standard deviation as the SNR increases. The MLE estimator works well for more combinations of the parameters, which give the MLE estimator some advantages over the BST estimator. The maximum likelihood estimator should be preferred over the BST estimator.

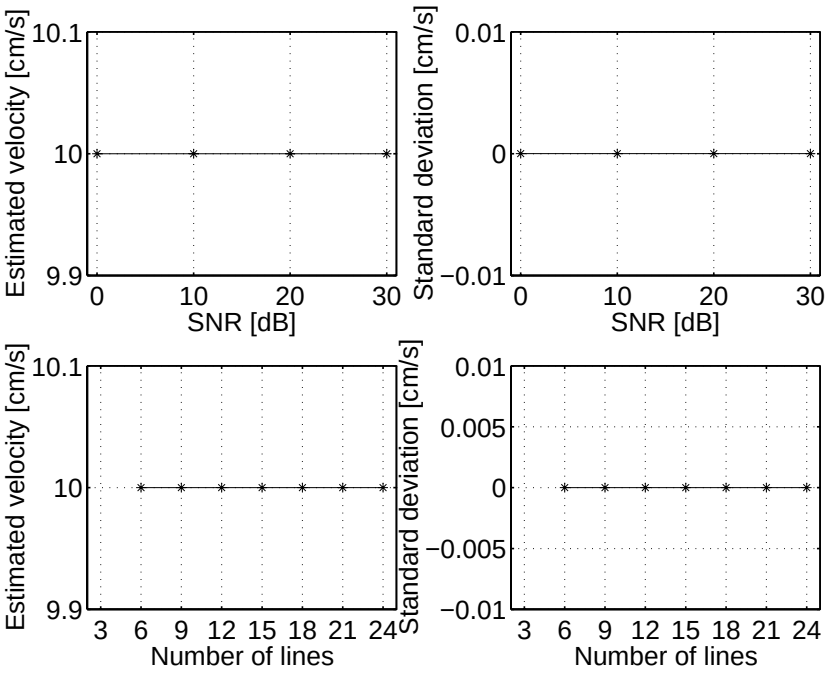

Figure 6.50: Performance of maximum likelihood estimator as a function of the number of lines and the SNR. HP echo-canceling filter applied. The sampling frequency is 30 MHz, and the number of samples are equal to one pulse length. The true velocity is 10 cm/s.

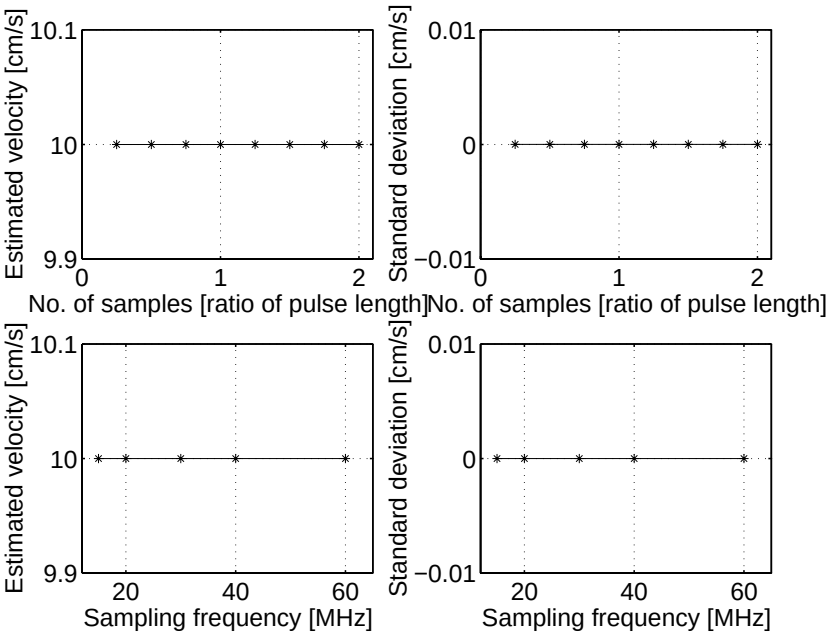

Figure 6.51: Performance of maximum likelihood estimator as a function of the number of samples and the sampling frequency. HP echo-canceling filter applied. The SNR is 10 dB, and 9 lines were employed. The true velocity is 10 cm/s.

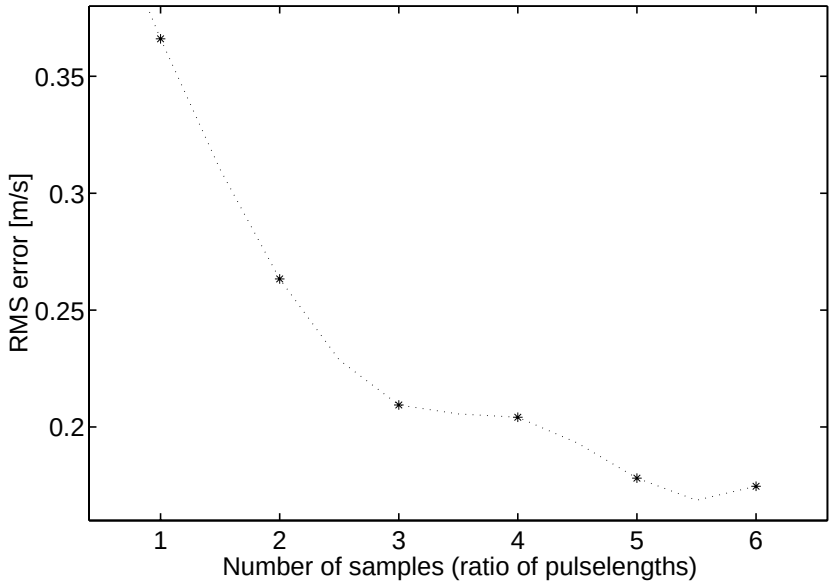

Figure 6.52: RMS error ([m/s]) as a function of N_s for the MLE estimator. The SNR is 20 dB.

The AB estimator performs very similar to the EAM estimator. Therefore the same conclusion will be drawn: overall the MLE estimator should be preferred over the AB estimator.

6.8.4 Performance on simulated data

The performance of the MLE estimator has been evaluated on the data set generated with a short pulse. The SNR is 20 dB, and the HP filter was applied for echo-canceling. The velocity range from -50 cm/s to 50 cm/s was investigated with a resolution of 1 cm/s. The RMS error as a function of N_s is plotted in Fig. 6.52. The error decreases, as N_s increase, and reaches a value of 0.17 for N_s equal to 6 pulse lengths. The estimator is not able to produce estimates across the full axial extent of vessel, and this problem increases as N_s increase. The same problem was experienced with the BST and the cross-correlation estimators. Figure 6.53 shows the problem for the systolic frame, when N_s equal 6 pulse lengths. A lower value of N_s must be used to minimize the problem. In Fig. 6.54 examples of the estimated velocity profiles for a systolic and a diastolic frame are plotted. The number of samples used are equal to 3 pulse lengths. Again the performance on the same two frames, which have been used to show the performance of estimators discussed in the previous sections, are plotted. Only the velocity estimates within the vessel are shown. Estimates that are plotted with the maximum and minimum value of the velocity scale take values above or below these border values. The problem has not been resolved but minimized.

Inspection of all computed estimates reveals that some estimates occur, which deviate significantly from the true velocity. These velocity estimates are underestimated, and they are mostly found along the posterior vessel wall. More than 50 % of them group together axially and/or laterally. The remaining estimates fluctuate about the true velocities. The estimates along the vessel wall are mostly overestimated, whereas an underestimation is seen along the center axis of the vessel. This conclusion holds for all frames except the systolic frame, where the velocity estimates are mostly underestimated. The level of overestimation is higher than the underestimation, so the velocity estimates across the axial extent of the vessel do not vary as much as the true velocity profile. The MLE estimator does not follow the velocity variations across the spatial extent of the vessel very well. In Fig. 6.55 a selection of the axial lines in the systolic and diastolic frame in Fig. 6.54 are plotted separately. The problem of determining the velocities along the vessel wall shows clearly in the lower two plots. A file, which contains the velocity estimates of all 10 frames, have

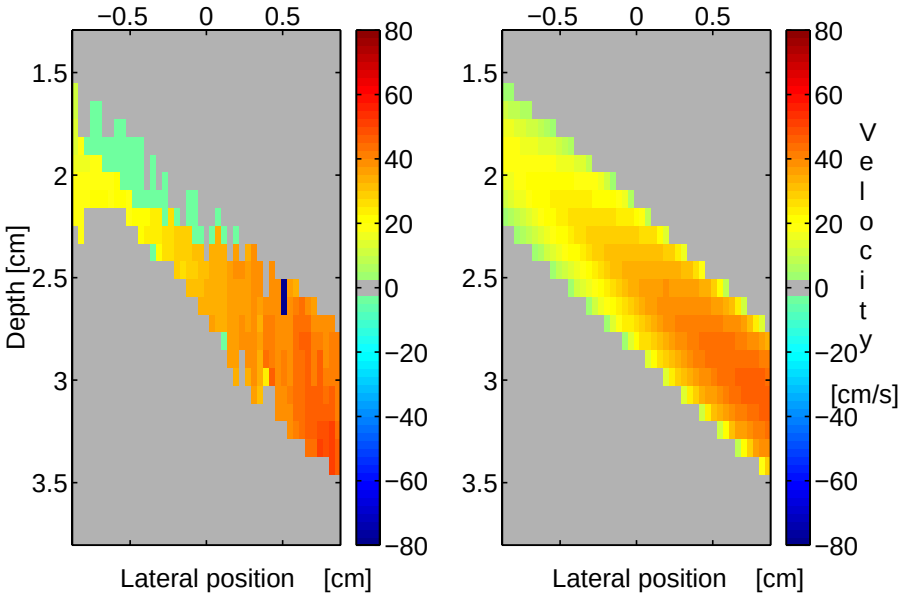

Figure 6.53: MLE estimator: The estimated (left) and the true (right) velocities for the systolic frame, when N_s equal 7 pulse lengths. The SNR is 20 dB.

been generated, and it can be accessed from the enclosed CD-rom (see Appendix C). The measure of the number of highly deviating estimates has been determined. A total of 4.1 % of the estimates take values outside the velocity range from -10 cm/s to 80 cm/s.

A post-processing filter should be applied to minimize the amplitude of the incorrect estimates and resolve the problem of overestimation along the vessel wall. The resulting velocity distributions should be more consistent with the true velocity distributions.

The autocorrelation estimator should be preferred over the MLE estimator, when no aliasing occur. The RMS error is lower, and hardly any deviating estimates occur. The autocorrelation estimator follows the velocity variations across the vessel and throughout the cardiac cycle more closely than the MLE estimator. The MLE estimator has the advantage of being able to handle the aliasing problem. If a post-processing filter can be determined, which can remove (or minimize the amplitude of) the highly deviating estimates one should consider using the MLE estimator.

The MLE estimator out performs the cross-correlation estimator, when the RMS error and the measure of the number of highly deviating estimates are used to compare performance. The conclusion is drawn for the estimates obtained, when N_s are equal to 3 pulse lengths in the estimation. Both estimators produce estimates, which deviate significantly from the true velocity. The cross-correlation estimator is able to follow the velocity variations across the extent of the vessel better than the MLE estimator. Both estimators require that a post-processing filter is applied to minimize the variations about the true velocities.

A better performance on velocity estimation is obtained, if the MLE estimator is used instead of the EAM estimator. A lower RMS error is obtained, and the MLE estimator does not introduce as many highly deviating estimates as the EAM estimator. If these estimates can be removed by a post-processing filter, the EAM estimator should be preferred over the MLE estimator, as the ”correct” estimates follow the variations across the vessel and throughout the cardiac cycle better.

The RMS error for the BST and the MLE estimators is very similar, and both estimators produce some estimates, which deviate significantly from the true value. The fluctuations about the true velocities are not systematic for the BST estimator, which result in a very noisy image of the velocity profile. The velocity

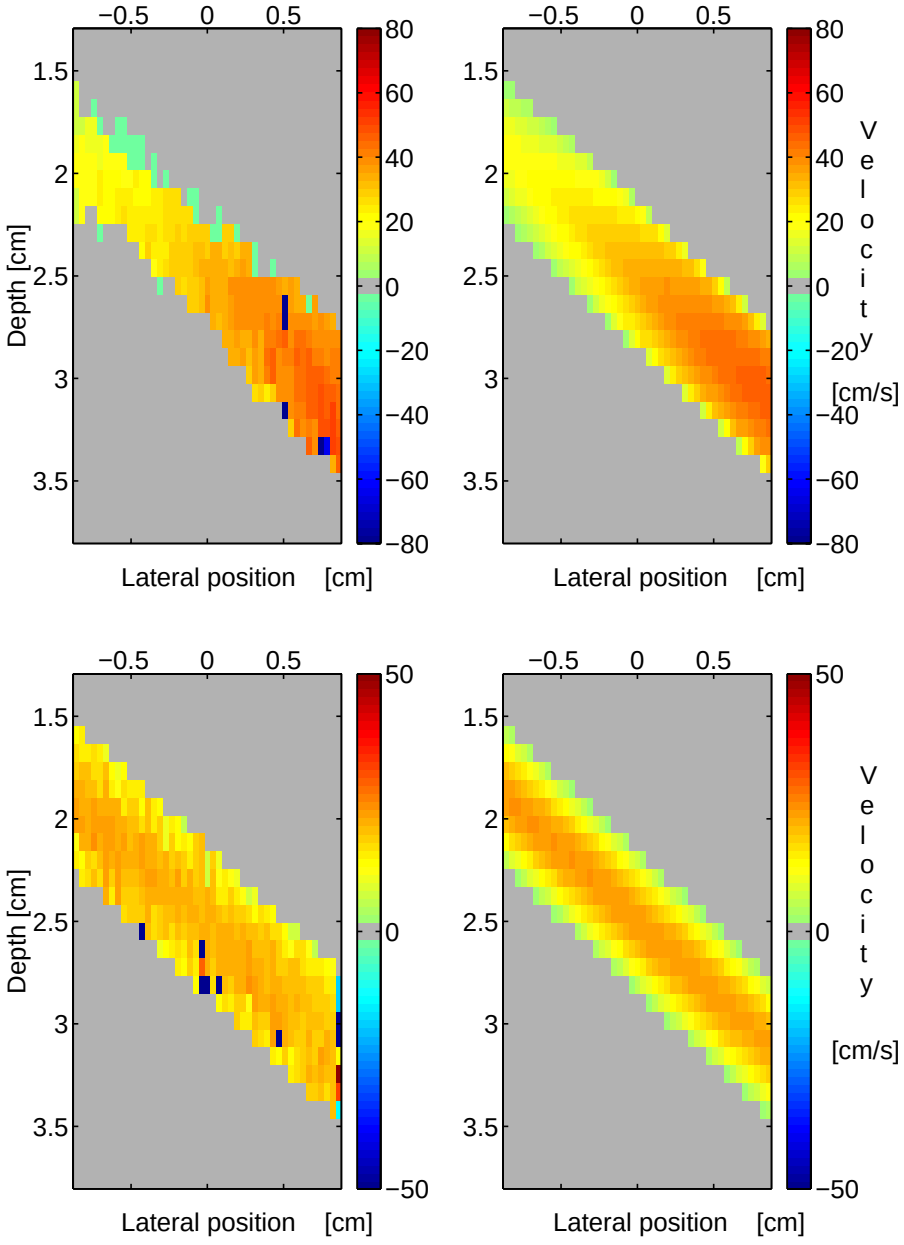

Figure 6.54: MLE estimator: The estimated (left) and the true (right) velocities for a systolic (upper two plots) and a diastolic frame (lower two plots), when N_s equal 3 pulse lengths. The SNR is 20 dB.

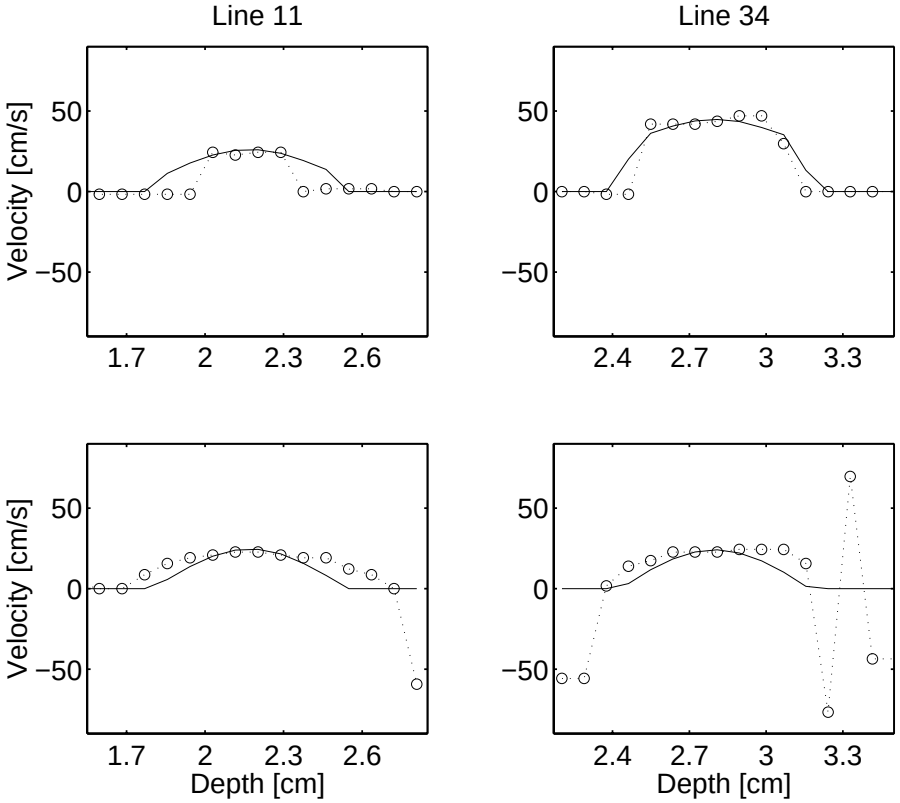

Figure 6.55: MLE estimator: Plot of line 11 and 34 in the images for the systolic (upper 2 plots) and diastolic frame (lower 2 plots). The SNR is 20 dB.

profile for the MLE estimator is more smooth, which is beneficial when consecutive frames are displayed after each other at a high frame rate. The number of highly deviating estimates are slightly lower with the MLE estimator. Overall the MLE estimator should be preferred over the BST estimator.

The performance of the MLE and the AB2 estimators is similar, when the AB2 estimator is employed on data generated with a short pulse. The RMS error is almost the same, when the MLE estimator employs 3 pulse lengths in the estimation. Estimates that deviates significantly in amplitude are produced by both estimators. The number of highly deviating estimates are very similar. The AB2 estimator produces estimates, which are more consistent with the true estimates, as they follow the variations across the vessel and throughout the cardiac cycle well. Based on this observation the AB2 estimator should be preferred over the MLE estimator.

6.9 Maximum likelihood estimator including spatial and temporal correlation

All of the estimators discussed above focused at determining the velocity for each segment individually. An estimate is computed and assigned to the corresponding location of the segment in the RF-line. A spatial and temporal correlation between the velocities in the vessel are not considered. If a correlation exists the variations between the velocity levels in a bounded neighborhood are restricted. The mechanics of non-turbulent, fluid motion predicts [24] that a temporal and spatial correlation exist. The velocity levels are similar in a spatially and temporally bounded neighborhood, and the transition from one velocity level to another can be described by a continuous function. An estimate that deviates significantly in amplitude

from its neighbors can be considered as an incorrect estimate. Examples of incorrect estimates have been seen for most of the estimators investigated here. With the autocorrelation estimator aliased estimates could be obtained. The cross-correlation analysis produced incorrect estimates due to the amplitude problem. Incorporation of the correlation property in the estimation will be beneficial. In the following an estimator based on maximum likelihood theory, which includes the correlation property, is derived. A maximum likelihood estimator was derived in Section 6.8.2, where a maximum likelihood function was determined from the probability density for the first coefficient in the series expansion. This approach is also used for the estimator developed here, but the employed probability density under H_1 is expanded with an a priori probability density.

The velocity is a function of time and spatial location: $v(x,z,t_f)$, where (x,z) determine the spatial location along the lateral and axial direction, respectively. The axial location in an RF-line was referred to by the time of acquisition t in the previous sections. The two variables are related through: $t = 2z/c$, and the spatial variable is used in the following. The variable t_f represents the time instant, where a frame is generated and is related to the frame rate through:$t_f = n_F T_{frame}$. The variables n_F and T_{frame} represent a discrete, integer value and the time between two consecutive frames are displayed, respectively. The flow is three-dimensional but in this context the third dimension will not be considered, as velocity estimates are not computed along the y direction. Only the velocity component along the axial direction is estimated, so $v(x,z,t_f)$ is one-dimensional.

The existence of temporal and spatial correlation introduces some restrictions on the velocity variations in a bounded neighborhood. This introduces an a priori knowledge of the velocity level in a given location, if the velocities in the neighborhood are known. It has to be similar in value to its neighbors in time and space. If the MLE estimator is employed, the likelihood ratio (LR) is determined for a range of velocities, and the maximum of the LR gives the estimate of the velocity. Given the a priori knowledge of the velocities in the neighborhood, the velocity in the location currently being estimated will be restricted to span a narrower range of velocities. The range is determined by the velocity values of its neighbors. This restriction can be introduced in the estimation by expanding the probability density under H_1 with an a priori probability density function p_a. The probability density function sets up restrictions for when neighboring velocities can be considered similar. The expansion of the probability density under H_1 introduces additional information to the estimation process, so a better basis for the estimation is obtained. The joint probability density becomes:

$$p(q_1, v_p(x,z,t_f)) = p_a(v_p(x,z,t_f))p_{q_1|H_1}, \tag{6.34}$$

where $v_p(x,z,t_f)$ determines the value of the velocity currently being evaluated.

So far the actual definition of similarity has not been given. The range of possible variations of the velocities in a bounded neighborhood must be investigated, and a probability density function for the a priori knowledge must be determined. The true velocities are given for the simulated data employed in this chapter, which makes it possible to investigate the temporal and spatial velocity variations in the 2D images of the velocity profiles. The spatial variations along the axial and lateral directions will be considered. The variations are expressed by means of the difference between the velocities in two neighboring locations:

$$\begin{aligned} v_{dx}(x,z,t_f) &= v(x+\Delta x,z,t_f) - v(x,z,t_f) \\ v_{dz}(x,z,t_f) &= v(x,z+\Delta z,t_f) - v(x,z,t_f) \\ v_{dt}(x,z,t_f) &= v(x,z,t_f - T_{frame}) - v(x,z,t_f), \end{aligned} \tag{6.35}$$

where Δx and Δz determine the lateral and axial distance between neighbors. A histogram analysis of v_{dx}, v_{dz}, and v_{dt} results in the set of probability densities, which are plotted in Fig. 6.56. The values of Δx and Δz are 0.4 mm and 0.8 mm. The obtained densities are only valid for the carotid artery under the given simulation conditions. The probability densities are approximately Gaussian distributed. The probability density for the axial derivatives show the least resemblance with a Gaussian distribution, because of the drop in probability for values of $|v_{dx}| < 8$ cm/s. The temporal probability density is shifted slightly

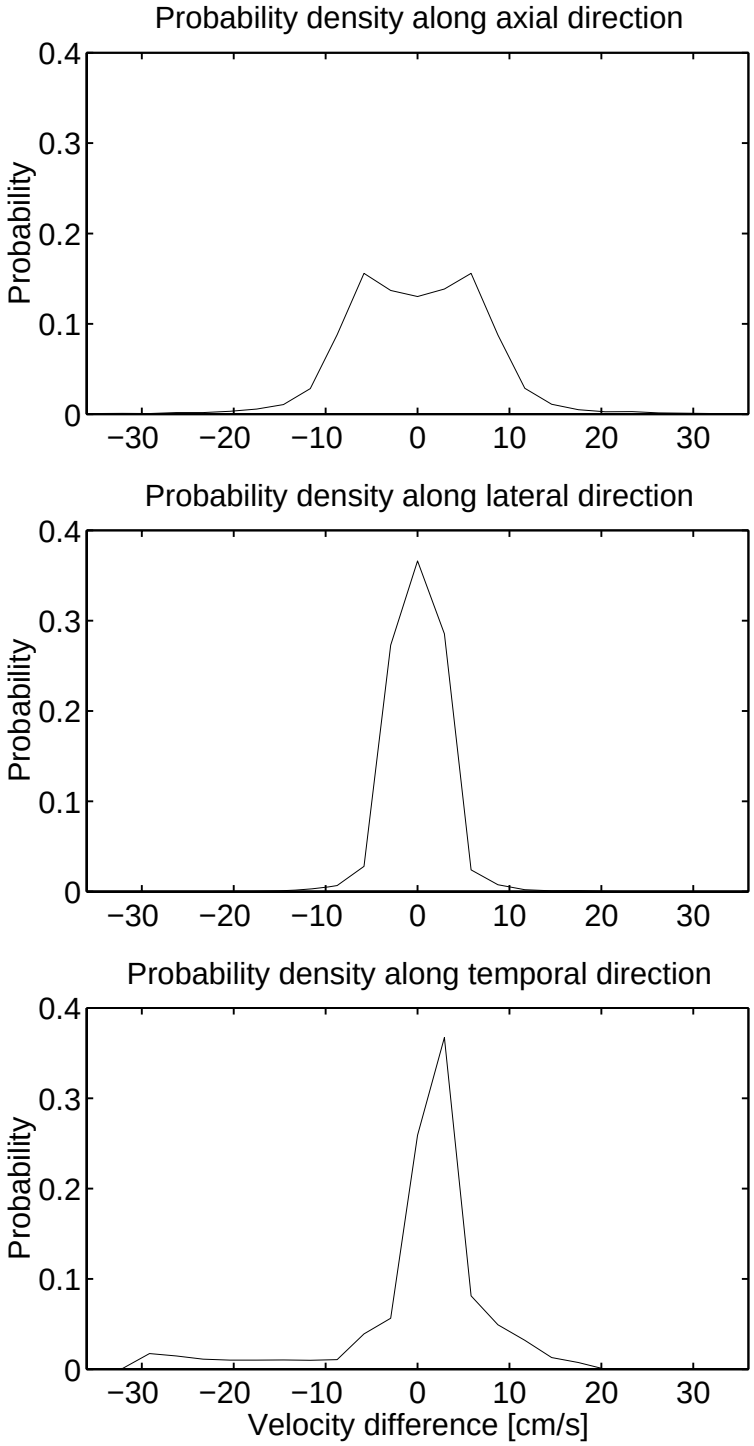

Figure 6.56: Plots of the axial (top), lateral (middle), and temporal (bottom) variations in the velocity profiles in the 2D images.

towards positive velocity changes. The high, negative values of v_{dt} resemble the variations, when the present and previous frame contain part of the systolic and the diastolic phase, respectively. The positive velocity variations resemble the conditions for the frames from the diastolic phase. The latter has a longer temporal duration, and therefore small changes are seen more often in the cardiac cycle. The mean is very close to zero. The width of the distribution is dependent on the temporal resolution and will decrease as the frame rate increases. The reason here fore is that the amplitude of the changes will be lower at a higher frame rate, as the variations in the velocity throughout the cardiac cycle are sampled more often. In general the width of the density functions will be dependent on the temporal and spatial resolution, which makes the modeling of the densities dependent hereof. The above investigations tell that the spatial and temporal velocity variations are restricted. A measure of similarity is obtained by computing the difference, and the probability densities are approximately Gaussian. A priori knowledge of the velocity variations is present and should be included in the probability density of $q_{1,s}$ under H_1. The functionality of the a priori density is to compare the velocity $v_p(x,z,t_f)$ currently being investigated to the values of its neighbors and determine, if $v_p(x,z,t_f)$ is likely or not.

In this study the probability densities for the variations will be approximated by Gaussian distributions with a zero mean. The value of the variance depends on whether the density is related to the spatial or temporal variations. The a priori density p_a is defined as:

$$p_a(v_p(x,z,t)) = \frac{1}{Z}\exp\left(-\frac{\zeta_1 C_1(x,z,t_f)}{\sigma_1^2} - \frac{\zeta_2 C_2(x,z,t_f)}{\sigma_2^2}\right), \tag{6.36}$$

where Z is a normalization constant, which assures that $\int p(q_1,v_p)dq_1 dv_{dx}dv_{dz}dv_{dt} = 1$. The parameters ζ_1 and ζ_1 are scaling factors. σ_1^2 and σ_2^2 are the variances of the temporal and spatial distributions. The terms C_1 and C_2 contain the similarity investigation along the temporal and spatial direction, respectively. Before defining these terms, a discussion of the neighborhood is performed. The RF-data are acquired according to a predefined scheme, which determines when RF-lines are acquired for the different lateral positions. When data are available, the processing can be initiated. The choice of acquisition and processing scheme are manifold, and it determines, which spatial neighbors are available and can be employed. In the following it is assumed that:

- the set of RF-lines for each lateral position are processed after each other (line by line from left to right), and
- each line is split up in a number of segments, and the segments are processed after each other (from first to last segment).

With this choice only two spatial neighbors (along the axial and lateral directions) within the same frame are available, when the estimation is carried out: $v(x-\Delta x,z,t_f)$ and $v(x,z-\Delta z,t_f)$. Estimates from the previous frame are used to make a complete neighborhood, which contains information around the location under investigation. The employed neighborhood V_n becomes:
$V_n = [v(x-\Delta x,z,t_f), v(x+\Delta x,z,t_f - T_{frame}), v(x,z-\Delta z,t_f), v(x,z+\Delta z,t_f - T_{frame}), v(x,z,t_f - T_{frame})]$. A full neighborhood does not exist for the first and last segment in each line, and the first and last line in the image. In the following the estimates for these spatial locations will be computed with the MLE estimator. This approach is also employed for the first frame, as no temporal neighbors exist.

Based on the definition of the neighbors, the terms $C_1(x,z,t_f)$ and $C_2(x,z,t_f)$ are defined as:

$$\begin{aligned} C_1(x,z,t_f) &= (v(x,z,t_f - T_{frame}) - v_p(x,z,t_f))^2 + (v(x+\Delta x,z,t_f - T_{frame}) - v_p(x,z,t_f))^2 \\ &\quad + (v(x,z+\Delta z,t - T_{frame}) - v_p(x,z,t))^2 \\ C_2(x,z,t_f) &= (v(x-\Delta x,z,t_f) - v_p(x,z,t_f))^2 + (v(x,z-\Delta z,t_f) - v_p(x,z,t_f))^2. \end{aligned} \tag{6.37}$$

The joint probability density for $q_{1,s}$ under H_1 becomes:

$$p_{q_{1,s}|H_1}(Q_{1,s},v_p|H_1)=\frac{1}{Z}\frac{1}{\pi(E_r+N_0)N_{l,e}}\exp\left(-\frac{\zeta_1 C_1(x,z,t_f)}{\sigma_1^2}-\frac{\zeta_2 C_2(x,z,t_f)}{\sigma_2^2}\right)\exp\left(-\frac{|Q_{1,s}(v_p)|^2}{(E_r+N_0)N_{l,e}}\right). \tag{6.38}$$

The probability density of $q_{1,s}$ under H_0 is unchanged:

$$p_{q_{1,s}|H_0}(Q_{1,s},v_p|H_0)=\frac{1}{\pi N_0 N_{l,e}}\exp\left(-\frac{|Q_{1,s}(v_p)|^2}{N_0 N_{l,e}}\right). \tag{6.39}$$

The likelihood ratio for the current problem becomes:

$$\begin{aligned} LR(Q_{1,s},v_p) &= \frac{p_{q_{1,s}|H_1}(Q_{1,s}|H_1)}{p_{q_{1,s}|H_0}(Q_{1,s}|H_0)} \\ &= \frac{(Z\pi(E_r+N_0)N_{l,e})^{-1}\exp\left(-\frac{\zeta_1 C_1(x,z,t_f)}{\sigma_1^2}-\frac{\zeta_2 C_2(x,z,t_f)}{\sigma_2^2}\right)\exp\left(-\frac{|Q_{1,s}(v_p)|^2}{(E_r+N_0)N_{l,e}}\right)}{(\pi N_0 N_{l,e})^{-1}\exp\left(-\frac{|Q_{1,s}(v_p)|^2}{N_0 N_{l,e}}\right)}. \end{aligned} \tag{6.40}$$

If all the exponentials are combined into one, and the logarithm of the LR is computed the following relation is obtained:

$$\begin{aligned} \ln(LR(Q_{1,s},v_p)) &= \ln(\frac{N_0}{Z(E_r+N_0)})-\frac{\zeta_1 C_1(x,z,t_f)}{\sigma_1^2}-\frac{\zeta_2 C_2(x,z,t_f)}{\sigma_2^2} \\ &\quad -|Q_{1,s}(v_p)|^2\frac{1}{N_{l,e}}\left(\frac{1}{E_r+N_0}-\frac{1}{N_0}\right) \\ &= \ln(\frac{N_0}{Z(E_r+N_0)})-\frac{\zeta_1 C_1(x,z,t_f)}{\sigma_1^2}-\frac{\zeta_2 C_2(x,z,t_f)}{\sigma_2^2}+\frac{1}{N_{l,e}}\frac{E_r}{(E_r+N_0)N_0}|Q_{1,s}(v_p)|^2. \end{aligned} \tag{6.41}$$

The first term in (6.41) represents a constant value and therefore only adds an offset to the likelihood ratio. The last three terms represent the sufficient statistic. Determination of (6.41) for a range of velocity values requires knowledge of E_r, N_0, ζ_1, and ζ_2. The factors ζ_1 and ζ_2 scale the contributions from C_1 and C_2. If C_1 and C_2 should play any role in the sum of terms, the scale factors will take values which to some extent compensate out the amplitude differences between C_1, C_2, and $Q_{1,s}$. In this study ζ_1 and ζ_2 will be defined as:

$$\begin{aligned} \zeta_1 &= \kappa_1\frac{E_r(E_r+N_0)}{N_0} \\ \zeta_2 &= \kappa_2\frac{E_r(E_r+N_0)}{N_0}, \end{aligned} \tag{6.42}$$

where κ_1 and κ_2 are a new set of scale factors. These definitions are introduced in (6.41). By rearranging terms, ignoring the first term and the common constants for the last terms, the sufficient statistic in the form of the likelihood ratio (LR_S) can be expressed as:

$$\ln(LR_S(Q_{1,s},v_p))=\frac{1}{N_{l,e}(E_r+N_0)^2}|Q_{1,s}(v_p)|^2-\frac{\kappa_1 C_1(x,z,t_f)}{\sigma_1^2}-\frac{\kappa_2 C_2(x,z,t_f)}{\sigma_2^2}. \tag{6.43}$$

The values of the variables κ_1, κ_2, σ_1^2, and σ_2^2 are dependent on the temporal and spatial resolution. The exact values for the individual variables as a function of the resolution will not be investigated in this context, and therefore the variables are combined as:

$$\begin{aligned} \Gamma_1 &= \kappa_1/\sigma_1^2 \\ \Gamma_2 &= \kappa_2/\sigma_2^2. \end{aligned} \tag{6.44}$$

The velocity estimate is:

$$\begin{aligned}\hat{v}(x,z,t_f) &= \arg\max_{v_p}\left(\ln(LR_S(Q_{1,s},v_p))\right)\\ &= \arg\max_{v_p}\left(\frac{1}{N_{l,e}(E_r+N_0)^2}|Q_{1,s}(v_p)|^2-\Gamma_1 C_1(x,z,t_f)-\Gamma_2 C_2(x,z,t_f)\right).\end{aligned} \tag{6.45}$$

The value of $\ln(LR_S(Q_{1,s},v_p))$ is computed for the range of velocities investigated. Each value is determined by:

- computing the values of $Q_{1,l}$. The definition of $Q_{1,l}$ is given in (6.27),
- computing $Q_{1,s}$ by summing the $Q_{1,l}$, and then performing the squaring to obtain $|Q_{1,s}(v_p)|^2$,
- determining C_1 and C_2 for the velocity under investigation, and then
- performing the summing of the terms within the brackets in (6.45).

An estimator, which is based on maximum likelihood theory and incorporates the temporal and spatial correlation between the blood velocities, has been derived in the above. It will be named the CMLE estimator, where the C refers to incorporation of the correlation property. The performance of the estimator is influenced by decorrelation and the accuracy on the neighboring velocity estimates. The latter influences the terms C_1 and C_2.

The similarity investigations by means of C_1 and C_2 increase the computational load of the estimator compared to the ordinary maximum likelihood estimator introduced in Section 6.8.2. The computations performed in (6.27), (6.37), and (6.45) along with the summing and squaring operation to obtain $|Q_{1,s}|^2$ determines the number of additions $N_{a,CMLE}$ and multiplications $N_{m,CMLE}$ performed to obtain (6.45) for $N_{v-steps}$:

$$\begin{aligned}N_{m,CMLE} &= 4N_sN_{l,e}N_{v-steps}+12N_{v-steps}+N_s+2\\ N_{a,CMLE} &= 2(N_s-1)N_{l,e}N_{v-steps}+13N_{v-steps}+(N_{l,e}-1)N_{v-steps}+(N_s-1).\end{aligned} \tag{6.46}$$

6.9.1 Determination of the estimator parameters

The values of Γ_1 and Γ_2 must be determined before the estimator can be employed. In the following these scale factors are determined for the simulated data set used in this chapter. This data set give the velocity profiles for the carotid artery for one choice of the temporal and spatial resolution. The factors are specific for this situation. In order for the estimator to be applicable for the estimation of the velocities in other blood vessels, the values should be determined for other vessels and thereby velocity profiles. Additionally, the influence of different settings of the temporal and spatial resolution should be determined. A set of scale factors, which are dependent on the vessel and the resolution, will most likely occur. This is not to be seen as a limitation. A look-up table can be implemented, which contains this information. The spatial and temporal resolution are specified by the scanner, so this information is given. An input from the clinician can determine the anatomical site and thereby the settings for the vessels in this region.

The RMS error is used as the measure for the performance, and the error is determined for a range of values of Γ_1 and Γ_2. The choice of the number of samples used in the correlation analysis will be inherited from the MLE estimator and are set equal to 3 pulse lengths. Table 6.4 lists the RMS error, when Γ_1 and Γ_2 take values in the range from 0 to 5. The error of the first frame is included in the total RMS error, so the performance of the CMLE estimator can be compared with other estimators. The RMS error decreases as the values of the scale factors increase. For the investigated combinations of Γ_1 and Γ_2 the minimum

Γ_2 \ Γ_1	0	1	2	3	4	5
0	0.2092	0.1306	0.1219	0.1199	0.1198	0.1195
1	0.1399	0.1219	0.1201	0.1181	0.1182	0.1183
2	0.1228	0.12	0.1181	0.118	0.118	0.1182
3	0.1209	0.1181	0.1181	0.1181	0.118	0.1181
4	0.1202	0.1182	0.1181	0.1181	0.1179	0.118
5	0.1187	0.1182	0.1181	0.1181	0.1179	0.1178

Table 6.4: The RMS error ([m/s]) as a function of Γ_1 and Γ_2.

RMS error is obtained for $(\Gamma_1, \Gamma_2) = (5, 5)$. Inspection of the RMS errors reveals that the performance is degraded only by 0.25 %, if $(\Gamma_1, \Gamma_2) = (2, 2)$ are used instead. For values of Γ_1 and Γ_2 above 1 the RMS error is nearly constant.

The influence of the a priori probability density on the estimation is plotted in Fig. 6.57. The values of the sufficient statistic are plotted as a function of v_p for the MLE and the CMLE estimators. The sufficient statistic for the MLE estimator has two high peaks. The maximum occurs for a velocity of -50 cm/s, whereas the second peak is located at a velocity of 11 cm/s. The true velocity is equal to 12.6 cm/s. The velocity at the second peak is closer to the true velocity and should have been the output of the estimation. This result is obtained with the CMLE estimator. The velocity -50 cm/s is far from the values of the neighboring velocities, and the a priori density assigns a low probability to this velocity. This causes the value of LR_S to decrease, as the terms $\Gamma_1 C_1$ and $\Gamma_2 C_2$ take high values and therefore contribute to the sum. The true velocity estimate is not obtained, but the introduction of the correlation property has produced a more correct estimate. The course of the LR_S for the CMLE estimator is more flat. A clear peak is present, but it does not stick out as much as was the case for the MLE estimator.

6.9.2 Performance on simulated data

The performance of the CMLE estimator has not been determined for the synthetic data set, since the data were not designed to represent a spatial and temporal distribution of velocities. In the following the performance of the CMLE estimator on the simulated data will be evaluated. The data set generated with a short excitation pulse are employed, and the HP echo-canceling filter was applied prior to the estimation. The SNR is 20 dB. The investigated velocities v_p range from -50 cm/s to 50 cm/s in steps of 1 cm/s. The number of samples used in the correlation analysis are set equal to 3 pulse lengths. This is inherited from the performance evaluations of the MLE estimator.

Figure 6.58 shows plots of the estimated velocity profiles for a systolic and diastolic frame. It is the same two frames used in the previous sections to display the performances. Only the velocity estimates within the vessel are plotted. The systolic frame is the first frame, and therefore the velocity estimates has not been determined with the CMLE estimator. The estimated velocities have been computed with the MLE estimator. The velocity estimates in the diastolic frame have been computed with the CMLE estimator. No highly deviating estimates are seen, when the velocity estimates along the image edge are discarded. The latter has not been determined with the CMLE estimator, as a full neighborhood does not exist. The introduction of the correlation property in the estimator has removed the highly deviating estimates produced by the MLE estimator. This is verified by comparing Figures 6.54 and 6.58. It can be concluded that the correlation property contains valuable information for the estimation, and it should be incorporated in the estimation.

Inspection of all 10 frames reveals that no estimates, which deviate significantly from its neighbors, are

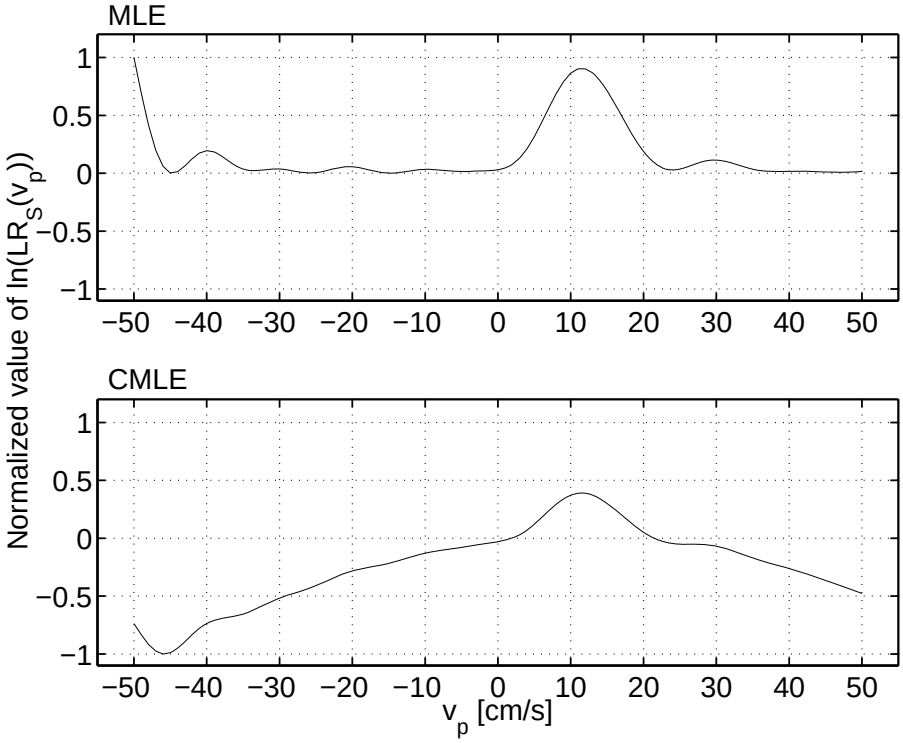

Figure 6.57: The value of the likelihood ratio for the span of investigated velocities v_p, when the MLE (top) and CMLE (bottom) estimators are used, respectively. The scaling factors Γ_1 and Γ_2 in the CMLE estimator are equal to (2,2).

obtained with the CMLE estimator. The remaining erroneous estimates are along the image edge, which was processed by the MLE estimator. A total of 1.0 % of the estimates take values outside the velocity range from -10 cm/s to 80 cm/s. The non-deviating estimates obtained with the MLE and the CMLE estimators are identical for more than 90 % of the estimates. The difference on the velocities for the remaining 10 % of the estimates is on the order of ± 2 cm/s. As most of the estimates are identical, the CMLE estimator suffers from the same problem as the MLE estimator. They are not able to produce estimates, which follow the velocity variations across the spatial extent of the vessel well. The estimates along the center axis of the vessel are underestimated, whereas the estimates along the vessel wall are mostly overestimated. Figure 6.59 shows this problem. The estimated velocity profiles are not as smooth as the true profile, so post-processing should be applied to reduce the variation. Still, the introduction of the temporal and spatial correlation between the velocities in a bounded neighborhood has been very beneficial for the outcome of the estimation. The estimated velocity profiles with the CMLE estimator on all 10 frames are enclosed in Appendix C.

The autocorrelation estimator out performs the CMLE estimator, when no aliasing occurs. The RMS error is lower, and the estimates follow the variation across the axial extent of the vessel better. Still, the performance of the CMLE estimator is quite good, as it does not produce any highly deviating estimates. The RMS errors would be close, if the errors in the first frame and along the image edges were not included in the RMS error. The measure of the number of highly deviating estimates is very similar for the two estimators. The CMLE estimator therefore seems applicable for blood velocity estimation.

The CMLE estimator performs better than the cross-correlation estimator, as the RMS error is lower, and no highly deviating estimates are produced. The advantage of the cross-correlation estimator is that it is capable of producing estimates, which follow the variation across the axial extent better. Both the CMLE and the cross-correlation estimators perform a cross-correlation analysis, but the analysis is performed on

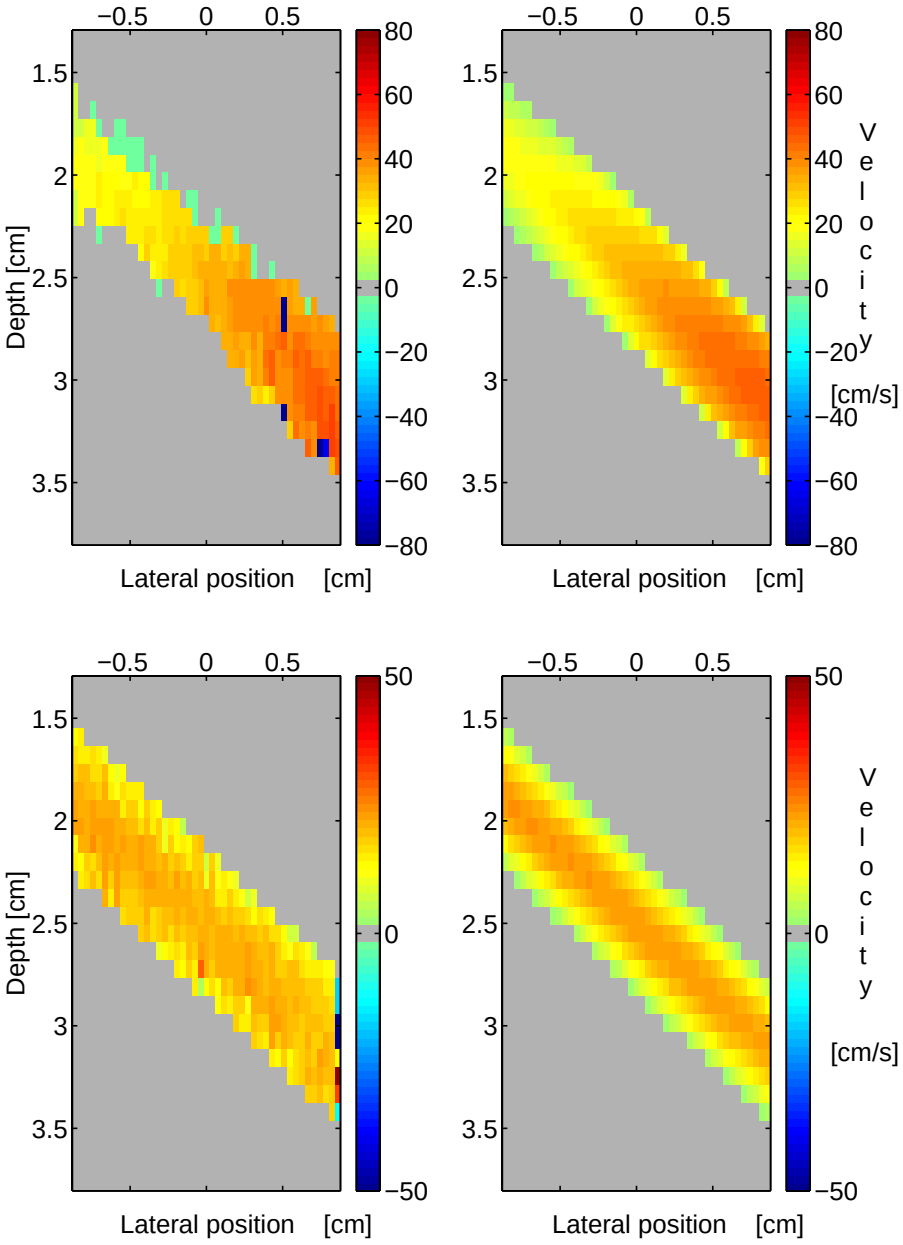

Figure 6.58: CMLE estimator: The estimated (left) and the true (right) velocities for a systolic (upper two plots) and a diastolic frame (lower two plots), when N_s equal 3 pulse lengths. Both Γ_1 and Γ_2 are equal to 2. The SNR is 20 dB.

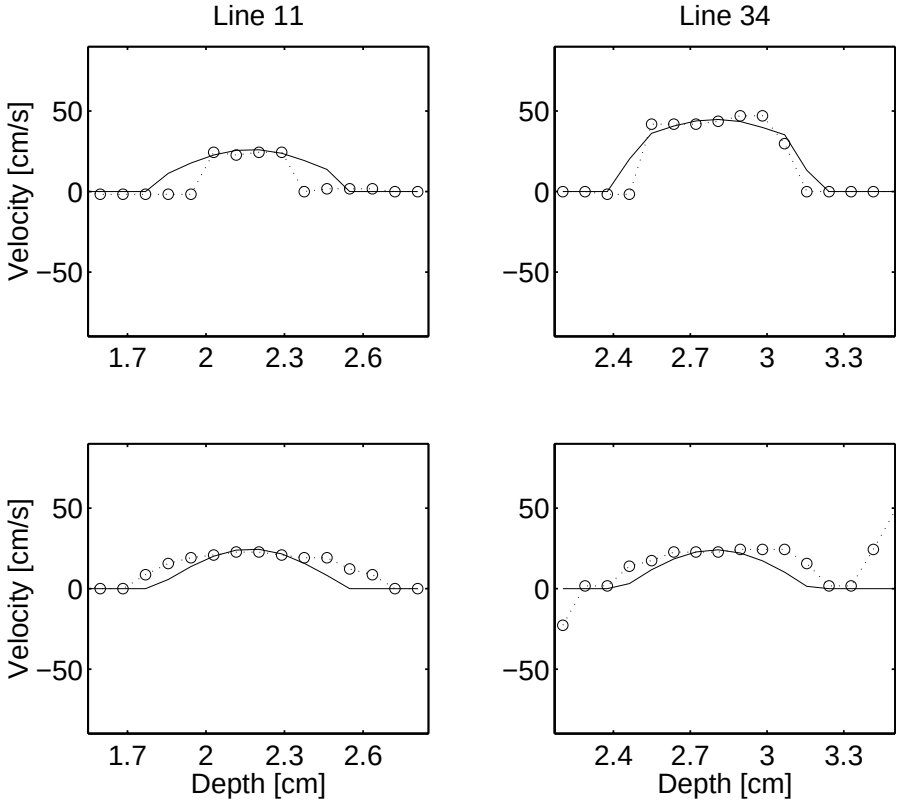

Figure 6.59: CMLE estimator: Plot of line 11 and 34 in the images for the systolic (upper 2 plots) and diastolic frame (lower 2 plots). Both Γ_1 and Γ_2 are equal to 2. The SNR is 20 dB.

the complex and real signals, respectively. Given this fact it should be possible to include the spatial and temporal correlation in the cross-correlation estimator. This could possibly reduce the number of highly deviating estimates. Inspection of the estimated velocity profiles reveals that more highly deviating estimates are produced with the cross-correlation estimator (in its present form). A comparison of the measures of the number of highly deviating estimates results in the same conclusion. Based on the results, the CMLE estimator should be preferred over the cross-correlation estimator, when the performance evaluation is based on the RMS error and the number of highly deviating estimates.

The CMLE estimator out performs the EAM estimator, as no highly deviating estimates are produced, and the RMS error is lower. The advantage of the EAM estimator is that the estimates follow the variations across the axial extent of the vessel better. Still, the CMLE estimator should be preferred.

The RMS error and the number of highly deviating estimates are higher for the BST estimator than the CMLE estimator. In addition the fluctuations of the velocity estimates across the spatial extent of the vessel are more random with the BST estimator, so the CMLE estimator should be preferred for blood velocity estimation.

The AB2 estimator produces rather good estimates, as it is able to follow the velocity variations across the axial extent of the vessel. Still the CMLE estimator should be preferred over the AB2 estimator. The RMS error is about 50 % lower, and no highly deviating estimates are produced. When the estimates obtained with the AB2 estimator are post-processed with the 2D-tracking filter, the AB2 estimator gets to be more applicable for blood velocity estimation. Under these circumstances the AB2 estimator probably should be preferred over the CMLE estimator.

A comparison of the CMLE and the MLE estimators reveals, that the RMS error has been reduced by

about 45 %. In addition most of the highly deviating estimates have been removed. The remaining deviating estimates is due to the employment of the MLE estimator for the estimates in the first frame, and along the image edges. There is no doubt that the CMLE estimator should be preferred over the MLE estimator. The spatial and temporal correlation among the velocities contain valuable information for the estimation.

6.10 Summary

This chapter has been concerned with the introduction and evaluation of a selection of blood velocity estimators. In the following the estimators and their performance on synthetic and simulated data will be summarized. The estimation is performed on recorded RF-signals, which have been pre-processed to minimize the noise content and to remove responses originating from the tissue. The latter process is referred to as echo-canceling, and two echo-canceling filters have been employed and evaluated on the synthetic data. The filters were the high-pass (HP) filter and the regression line filter. Both filters filter out movement at low frequencies. The number of lines used in the HP filter determine the width of the transition band between stop and pass band. The removal of low frequencies is beneficial, as the tissue movements occur at low frequencies. Unfortunately, part of the blood also moves at low frequencies, so valuable information from the blood signal is removed and limits the blood velocities, which can be determined. The filter employs a set of RF-lines to compute one filtered value, so RF-lines are lost in the filtering. Therefore a low filter order is often used, which then again degrades the performance of the filter. A simple 2^{nd} order filter has been employed here. The second filter is the regression line filter. If sample values in consecutive lines are identical (or at least very similar), the relation between the samples can be described by a straight line with a very low slope. By fitting a line to the samples and then subtract it from the samples, the tissue components will be filtered out. No RF-lines are lost. The influence of the two filters on the estimation has been determined. A successful estimation can be performed after echo-canceling with both filters in most cases. This conclusion is valid for the investigated velocities. The regression line filter did not go well with the AB1 estimator though, and the HP filter should be preferred for this estimator. No unambiguous relations for the influence on the standard deviations have been determined. The influence is dependent on the choice of the estimator parameters. Under some circumstances the filters stabilize the estimation, and for other it degrades the performance. For the given data set the differences in the standard deviations were on the order of a few millimeter per second, so no significant difference in the performance can be determined. The regression line filter seems to work best, when the number of lines used in the filter take a high value. This limits is usability, when only a limited set of lines are available for estimation.

A total of seven blood velocity estimators have been introduced and evaluated here. All estimators aim at determining the movement of the scatterers between acquisitions. The scattered responses from the scatterers are fairly similar in consecutive acquisitions, so similar patterns are seen in consecutive RF-lines. The position of the patterns in the RF-signals are temporally shifted due to the movement. An estimate of the velocity is obtained, when an estimate of the movement is determined.

First, the autocorrelation estimator was introduced. This estimator determines the movement of the scatterers by determining the phase shift between consecutive RF-lines. The obtained velocity estimates are biased due to the influence of noise. A long excitation pulse should be used to obtain an estimate with a low standard deviation. An inverse tangent operation is included in the estimation, which puts an upper bound on the velocities that can be determined. The bound is dependent on the choice of pulse repetition frequency and the center frequency. Aliased estimates are obtained, if the true velocity exceeds the maximum velocity detectable. This problem was verified, when the performance of the estimator on the synthetic data was determined. The non-aliased estimates were biased as expected. The velocity estimates are overestimated. The level of the bias is dependent on the SNR and the choice of the parameters in the estimation. The standard deviation decreases, as the number of lines used in the estimation increase, and the SNR increases. The performance was independent on the choice of the sampling frequency. The performance on simulated

data, which resembled RF-signals obtained at the carotid artery, was determined. The results showed that the autocorrelation estimator computes estimates, which follow the velocity variations across the axial extent of the vessel, and throughout the vessel and the cardiac cycle well. This is valid, as long as the pulse repetition frequency and the center frequency are chosen, so no aliasing occurs. The true velocity profiles take values in the velocity range from 0 cm/s to 50 cm/s. A measure of the number of highly deviating estimates was determined. Only 0.4 % of the estimates take values outside the velocity range from -10 cm/s to 80 cm/s. The RMS error on the estimation over the 10 frames is 0.06 m/s for a SNR of 20 dB. The autocorrelation estimator has been very popular in the past, as the computational load is low. The computational load has previously been of much concern. The advances in electronics makes it possible to consider using algorithms, which are computationally more demanding, if they are able to out perform the autocorrelation estimator.

A tracking of the moving patterns can be performed with a cross-correlation analysis. The cross-correlation function is determined for a set of temporal shifts (and thereby a set of velocities). The temporal shift, which relates to the maximum of the cross-correlation function, determines the estimate of the temporal shift. The computation of the cross-correlation for a range of shifts increases the computational load of the estimation. The patterns in the consecutive lines are not identical due to decorrelation. This influences the performance of the estimator. A short excitation pulse should be emitted, as the bandwidth influences the standard deviation on the estimate. The cross-correlation estimator does not suffer from the aliasing problem. It can handle any temporal shift and thereby any velocity. A large number of samples should be employed in the computation of the cross-correlation. For the simulated data an upper limit on the number of samples exists for the current data set. As the number of samples increases, the estimator fails to produce good estimates across the full axial extent of the vessel. When the number of samples are equal to 3 pulse lengths, the RMS error is 0.4 m/s, when the SNR is 20 dB. The estimator produces both over- and underestimated estimates. The cross-correlation estimator suffers from the amplitude problem, which can cause a false detection of the velocity. This problem was experienced, and estimates, which deviate significantly from the true velocity, occur in the estimated velocity profiles for the simulated data. A total of 14.7 % of the estimates take values outside the velocity range from -10 cm/s to 80 cm/s. A post-processing filter must be applied to minimize the amplitude of these estimates. The non-deviating estimates follow the variations across and throughout the vessel and the cardiac cycle well but not as well as the autocorrelation estimator.

The advantages of the autocorrelation and the cross-correlation estimators have been combined in the Extended Autocorrelation Method (EAM). An initial estimate is determined with the autocorrelation estimator, which can be off by an integer number of 2π due to the aliasing problem. A subsequent cross-correlation analysis is performed for the set of possible true phase shifts. The limitation of the autocorrelation estimator is circumvented, as the cross-correlation estimator can investigate any temporal shift and thereby velocity. The computational load related to the cross-correlation analysis is minimized due to computation of an initial velocity estimate. The performance evaluations on both data sets reveal that the EAM estimator is capable of overcoming the aliasing problem. Unfortunately the amplitude problem of the cross-correlation introduces quite a few highly deviating estimates in the velocity profiles obtained from the simulated data. These must be removed through post-processing of the estimates. The cross-correlation analysis performs best, when a wideband pulse is emitted, whereas a narrow band pulse should be used with the autocorrelation estimator. This mismatch influences the performance. If a narrow band pulse is used, an accurate initial estimate is obtained, but a total of 41.2 % highly deviating estimates are obtained. The RMS error is 0.74 m/s, when the SNR is 20 dB and the number of samples used in the cross-correlation analysis are 5 pulse lengths. The accuracy on the initial estimate decreases, if a wideband pulse is employed. But this choice improves the basis for the cross-correlation analysis. Less highly deviating estimates are obtained. Still, quite a few exist and must be removed through post-processing. About 17 % of the total number of estimates are incorrect, when the SNR is 20 dB. The number of samples used for the cross-correlation analysis should be 5 pulse lengths, when the estimation is carried out on the data generated with the wideband pulse. In this

case the RMS error is 0.43 m/s, when the SNR is 20 dB. The advantages of the EAM estimator with respect to resolving the aliasing problem of the autocorrelation estimator is counteracted by the limitations of the cross-correlation analysis.

The cross-correlation estimator tries to determine, if patterns are similar by calculating the cross-correlation value. Similarity can also be expressed by means of the variations between samples in consecutive lines. The BST estimator employs this feature by performing a variance analysis. A low value of the variance resembles that the compared segments are similar. Any temporal shift can be investigated, so the estimator does not suffer from aliasing problems. The performance of the estimator is influenced by the decorrelation. A wideband excitation pulse should be employed. The performance on the synthetic data reveals that the estimates are biased, and the bias takes a positive value. The variance analysis should be performed for several samples, and the sum of variance values for a segment is used to determine the velocity estimate. Low standard deviations are obtained as the SNR increases. Inspection of the velocity profiles computed from the simulated data reveals that an upper limit on the number of samples used for the variance analysis exists. As the number of samples increases the estimator fails to produce estimates for the full axial extent of the vessel. A choice was made, and the number of samples were set equal to 3 pulse lengths. The problem is not fully resolved with this choice of the number of samples, but it has been minimized. The estimator produces less highly deviating estimates than was seen with the cross-correlation and the EAM estimators. A total of 6.9 % of the estimates take values outside the velocity range from -10 cm/s to 80 cm/s. The RMS is 0.22 m/s, when SNR is 20 dB. The estimates do not follow the velocity variations across the axial extent of the vessel very well. A random variation about the true velocities occurs. This is a problem, as it is very difficult to extract valuable information from this ”noisy” profile. The variations are due to the limitations of the estimator - not the actual velocity distribution. The velocity profiles must be post-processed before they are displayed. When comparing the introduced estimators capability to follow the velocity variations in the vessel, the BST estimator has the poorest performance.

The idea of combining the autocorrelation and the cross-correlation estimators is smart, as the advantages of each are exploited and the computational load is minimized. The amplitude problem limited the performance of the EAM estimator. A new estimator, which combines the autocorrelation and the BST estimators, has been suggested and evaluated. It has been named the Autocorrelation and Butterfly estimator (AB). Although the BST estimator could not determine the variations across the vessel very well, it was able to produce estimates within the right velocity range. Few highly deviating estimates were produced, and therefore it seems beneficial to employ it together with the autocorrelation estimator. The performance evaluation on both the synthetic and simulated data confirms this. The best performance is obtained, if the variance analysis is performed on the enveloped detected data. The number of samples employed for the variance analysis should take a value around 5-6 pulse lengths, when the estimator is applied to the simulated data. The BST estimator works best, when a wideband pulse is employed, whereas the autocorrelation estimator should be applied to data generated from a long pulse. This mismatch influences the performance of the AB estimator. A less accurate initial estimate is obtained, if a short pulse is employed, but only very few highly deviating estimates are obtained. At a SNR of 20 dB, a total of 4 % of the estimations produce highly deviating estimates. In this case the RMS error is 0.22 m/s. The number of highly deviating estimates increase to 8 %, if the AB estimator is applied to the data generated with a long pulse. The RMS error is 0.33 m/s, when the SNR is 20 dB. The highly deviating estimates should be removed (or at least reduced) through post-processing. The employment of the variance analysis instead of the cross-correlation analysis in the investigations of a set possible true phase shifts is beneficial. The problem of highly deviating estimates has not been resolved fully with the AB estimator, but the number of highly deviating estimates have been lowered significantly. The AB estimator is to be preferred over the EAM estimator. The AB estimator does not suffer from the aliasing problem, and it only produces few highly deviating estimates. The AB estimator can almost match the autocorrelation estimator, and it out performs the cross-correlation and BST estimators.

The MLE estimator employs maximum likelihood theory to determine the velocity estimates. A set of

samples in consecutive RF-lines are correlated for each investigated velocity. A probability density can be derived for the correlation values, and an estimator based on the likelihood ratio arises. The correlation analysis is performed on the complex signals. The MLE estimator performs very well on the synthetic data. The estimator does not suffer from aliasing problems. The estimates are biased, and the bias is positive. A zero standard deviation can be obtained even at low SNRs, and when only few RF-lines are used in the estimation. Overall the estimator out performs all estimators discussed so far. A good performance is also obtained on the simulated data. The choice of the number of samples to be used in the correlation analysis is limited, if good estimates across the full axial extent of the vessel should be obtained. In this study the number of samples were set equal to 3 pulse lengths. The problem is not resolved but minimized with this choice of the number of samples. In this case the RMS error is 0.21 m/s, when the SNR is 20 dB. A total of 4.1 % highly deviating estimates are obtained for the simulated data. The number of these estimates are less than what was seen with the cross-correlation and the EAM estimators. The velocity estimates do not follow the variations across the axial extent of the vessel well. The estimates are very similar across the axial extent. This is to be preferred over the random fluctuations of the velocity estimates, which were experienced with the BST estimator. The AB estimator matches the performance of the MLE estimator and the former should be preferred.

None of the above estimators employ the features of fluid mechanics in the estimation, which predicts that the velocities are correlated in time and space. The velocities in a spatial and temporal bounded neighborhood are similar, and transitions between the different velocity levels occur smoothly. By comparing the velocity value v_p under investigation (in a correlation analysis) to the velocity values in a spatial and temporal neighborhood, it can be determined, if v_p is likely or not. A new estimator based on maximum likelihood theory has been developed here. The probability density used with the MLE estimator has been expanded with an a priori probability density, which determines if v_p is likely or not. A set of scale factors are included in the a priori density, which weight the contributions from the temporal and spatial neighbors. The values of the scale factors are dependent on the temporal and spatial resolution. The new estimator has been named the CMLE estimator. The CMLE estimator does not suffer from aliasing problems. No highly deviating estimates are obtained with this estimator, so the estimator out performs all previously discussed estimators. The number of samples used in the estimation was inherited from the MLE estimator and were set to 3 pulse lengths. In this case an RMS error of 0.12 m/s is obtained, when the scale factors were used, which gave the lowest error. The SNR is 20 dB in this case. The estimates do not follow the variations across the axial extent of the vessel well. The estimates are more similar across the vessel. The same problem was experienced with the MLE estimator. Still, the introduction of the correlation property in the estimator has improved the blood velocity estimation. The correlation property contains valuable information for the estimation, and it should be incorporated in the estimation scheme. The basic idea of introducing the correlation property in the estimation can probably also be employed for the cross-correlation estimator. This idea should be pursued and evaluated.

All presented estimators are able to perform blood velocity estimation, but the accuracy on the estimation varies for the different estimators. A low standard deviation is desirable, and therefore some estimators are to be preferred over others. The computational load has previously been of much concern, as the electronics were limited in their performance. This problem limited the choice of estimators, which could be used, if real-time processing should be obtained. With the advances in the electronics new estimators, which are computationally more demanding, should be considered. The new estimators should resolve some of the problems experienced with the previously employed estimators. The two new estimators presented here are able to resolve some of the experienced problems and out perform most of the other estimators. Especially the correlation property between the velocities in a spatial and temporal neighborhood contained valuable information for the estimation, and this aspect should be incorporated in the estimators. A clinical evaluation of the AB and the CMLE estimators should be carried out in the future, before a final conclusion can be drawn on the feasibility of using these estimators for blood velocity estimation. But the presented results seem very promising. The employment of the CMLE estimator requires further investigations into the

influence of the velocity profile (*e.g.* carotid or femoral artery) and the spatial and temporal resolution on the values of the scaling parameters. The main contribution to the field of blood velocity estimation obtained from this study is the aspect and the importance of incorporating the correlation between velocities in time and space. The incorporation of this property into the estimation should be pursued, and it seems possible to include it in existing estimators such as the maximum likelihood and the cross-correlation estimators.

Chapter 7

Post-processing of blood velocity estimates

The blood velocity estimators produce estimates with a certain level of inaccuracy. The standard deviation on the estimates is influenced by the measurement noise, the velocity spread, and the signal alteration introduced by de-noising and clutter filters. The characteristics of the employed estimator also influences the estimates. In case of the cross-correlation estimator highly deviating estimates were obtained because of the amplitude problem. The autocorrelation estimator can produce aliased estimates due to the limitations of the inverse tangent operation in the estimator. A noisy and non-smooth appearance of the velocity distribution is obtained, which is not consistent with the actual velocity in the vessel. The level of noise varies over the image and between consecutive images. The human visual system is sensitive to these rapid variations. When the images are displayed after each other at a high frame rate, the observers focus gets distracted from the important information. Post-processing of the estimates should be performed prior to displaying the estimates, and the applied filter should minimize the variation. A median filter has been used previously, and it will be discussed and evaluated in Section 7.1. A new post-processing filter based on optical flow theory has been developed in this study. Applying the theory of fluid mechanics introduces restrictions on the variations. Neighboring estimates in time and space are highly correlated, since transitions must occur smoothly. This property is employed. The filter is derived and evaluated in Section 7.2. In Chapter 6 a 2D-tracking filter was introduced, which was used for post-processing of the velocity estimates obtained with the EAM and the AB estimators (see Section 6.5 and 6.7). As this filter is specific for these two estimators, it will not be introduced and evaluated in this chapter. The two filters discussed in the following are independent of the employed blood velocity estimator.

7.1 Post-processing filter based on median filter

Investigation of the blood velocity distributions in the human cardiovascular system reveals that the velocities are correlated in time and space. This was verified for the carotid artery in Chapter 6. Neighboring velocities are similar in amplitude. The correlation property makes it possible to derive post-processing filters, which can reduce the variations in the estimated velocity distributions. The level of similarity must be determined by some means. This can be done by comparing the individual estimates with their neighbors. If the deviation is too high, the estimate is replaced with one, which is more similar to the velocities in the neighborhood. A less noisy and more smooth velocity distribution should be obtained.

In image processing the non-linear median filter is often employed for smoothing. The filter rearranges a set of values $\vec{V}^e = [v_1^e, v_2^e, ..., v_N^e]$, so that the values are arranged according to an increasing amplitude order. The output $\hat{v}^c$ of the filter is the central value in the resulting, rearranged row of values$\vec{V}_o^e$ [59], [60]. The variable names and superscripts are chosen to relate the discussion to the situation at hand, where a

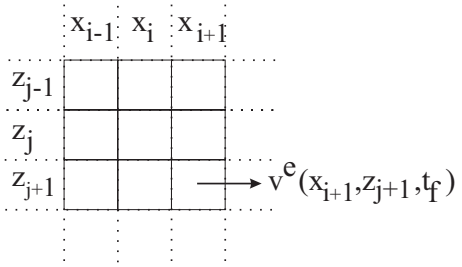

Figure 7.1: Definition of the spatial coordinate system in the 2D image.

set of estimated velocities v are given and should be processed. The filter employs the computed velocity estimates and produce an estimate of the correct velocity. An example of median filtering is given to clarify the definition of the filter:

$$\begin{aligned} \vec{V}^e &= [1,3,13,7,9] \\ \vec{V}_o^e &= [1,3,7,9,13] \\ \hat{v}^c &= 7. \end{aligned} \tag{7.1}$$

The filter is very useful for noise suppression and preservation of edges [59]. Each pixel in the image is filtered, and the set of values involved in the filtering are:

- the value of the pixel of interest for the current filtering, $v^e(x_i,z_j,t_f)$, where (x_i,z_j) are the spatial coordinates in a 2D image, and t_f represents the time instant, where the image was generated,
- the values of the pixels in the neighborhood of $v^e(x_i,z_j,t_f)$.

The definition of the spatial coordinate system in the 2D image for a given time instant t_f is given in Fig. 7.1. A neighborhood can extend in both time and space. Examples of neighbors are:
$v^e(x_{i-1},z_{j-1},t_f), v^e(x_{i-1},z_j,t_f),..,v^e(x_i,z_{j-1},t_f), v^e(x_i,z_j,t_f),...,v^e(x_i,z_j,t_f-T_{frame})$, where T_{frame} is the time between the generation of two consecutive frames. The common definition of a two-dimensional median filter states [59] that all neighbors along the vertical, the horizontal, and the diagonal axes are employed. In this study a modified two-dimensional median filter will be employed, which only employs the spatial neighbors along the vertical (axial) and horizontal (lateral) axes in the image. The number of values, N_m, used define the order of the median filter. If the value of the pixel under investigation deviates significantly from its neighbors, the amplitude ordering will place it as one of the outer elements in the rearranged vector. The pixel value will be replaced by one of the neighboring values, and the noisy estimate has been removed. The rearranging according to amplitude serves as the similarity investigation. The velocity level for the pixel under investigation should lie within an amplitude range defined by its neighbors. A high deviation will be experienced when aliasing errors occur. If $(N-1)/2$ neighboring estimates are erroneous, a median filter of order N or higher is required to remove all the errors. Smoothing is also obtained, when only small deviations are seen. The velocity estimate under investigation is replaced by the value of the velocity of one of the neighbors, if it does not take the central position in $\vec{V}_o^e$.

In this study two median filters, which employ the spatial neighbors, will be evaluated. The first filter, $M1$, is a 3^{rd} order filter, which uses the two neighbors $v^e(x_i,z_{j-1},t_f)$ and $v^e(x_i,z_{j+1},t_f)$ along with the pixel value $v^e(x_i,z_j,t_f)$. This filter acts along the axial direction in the image. The second filter, $M2$, employs the immediate neighbors axially and laterally: $v^e(x_{i-1},z_j,t_f)$, $v^e(x_i,z_{j-1},t_f)$, $v^e(x_i,z_{j+1},t_f)$, and $v^e(x_{i+1},z_j,t_f)$ along with the pixel value $v^e(x_i,z_j,t_f)$. The filter will only be applied to the image once.

Parameter	Value
Center frequency of pulse	5.0 MHz
No. of elements	128
Pulse length	1.5 / 6 cycles
Geometric focus	17 mm
Pulse repetition frequency	4 kHz
Sampling frequency	40 MHz
Radius of vessel	3 mm
Angle between vessel and transducer	35^o

Table 7.1: Choice of parameters for the simulated data used in the performance evaluation of the median filter.

SNR	RMS_{before}	$M1$	$M2$
0	0.125	11.0	27.1
5	0.096	8.4	21.8
10	0.076	5.0	15.2
15	0.061	2.2	9.9
20	0.054	0.0	6.0
30	0.049	-0.8	3.9
40	0.048	-0.4	4.1

Table 7.2: The RMS ([m/s]) error before and the improvement in % after application of the median filters for a range of SNRs.

7.1.1 Performance on simulated and *in-vivo* data

The performance of the median filters has been evaluated on simulated data, which resemble RF-signals obtained at the carotid artery. The simulation was performed with the simulation program Field II [26], [27]. Table 7.1 lists the simulation parameters. The transducer is modeled as a linear array. The focusing and apodization scheme matches the setup of a B-K Medical 3535 scanner, when it is connected to the linear array. Tissue motion due to pulsation is included, and the blood motion is modeled using Womersley's pulsatile blood flow model (see Chapter 4). Eight RF-lines were acquired at each lateral position. Three seconds of data (3 cardiac cycles) have been simulated at a frame rate of 10 frames/s. This gives blood velocity estimates across half the imaging range of the transducer. The choice of the simulation parameters ensures that no aliasing errors occur. The filters capability of minimizing the low amplitude, noisy variations can be evaluated. The performance for a range of SNRs is investigated. The RF-signals were de-noised with the matched filter (see Section 5.1), and a 2^{nd} order HP echo-canceling filter was applied prior to the estimation (see Section 5.2.1). The autocorrelation estimator (see Section 6.3) was employed to obtain the blood velocity estimates v^e. The performance is determined by computing the RMS error before and after the application of the median filter. Table 7.2 lists the RMS errors before and the improvements in % after application of the median filters. An improvement is obtained with both median filters, when the SNR is below 30 dB. The level of improvement increases as the SNR decreases. The RMS error increases after application of the $M1$ filter, when the SNR is 30 and 40 dB. Additional noise variations have been introduced in the image. The best performance is obtained with the $M2$ filter.

In Fig. 7.2 the result of the median filtering with the $M2$ filter is plotted for a frame, which is taken from the diastolic phase of the cardiac cycle. The top plot shows the velocity distribution prior to the filtering, and the bottom plot shows the result of the smoothing with the median filter. The true velocity distribution

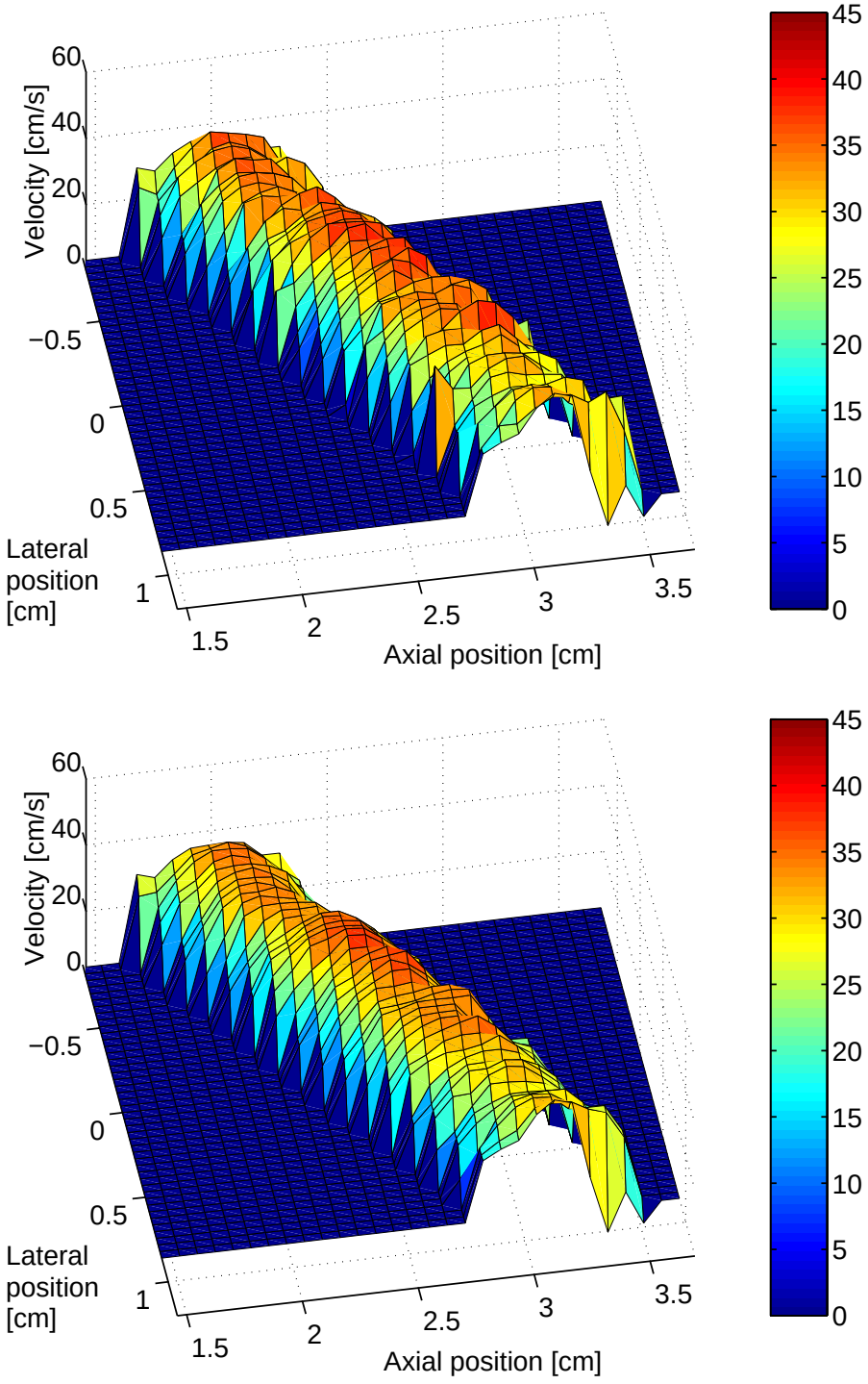

Figure 7.2: The velocity profile before (top) and after (bottom) application of the M2 filter on simulated data.

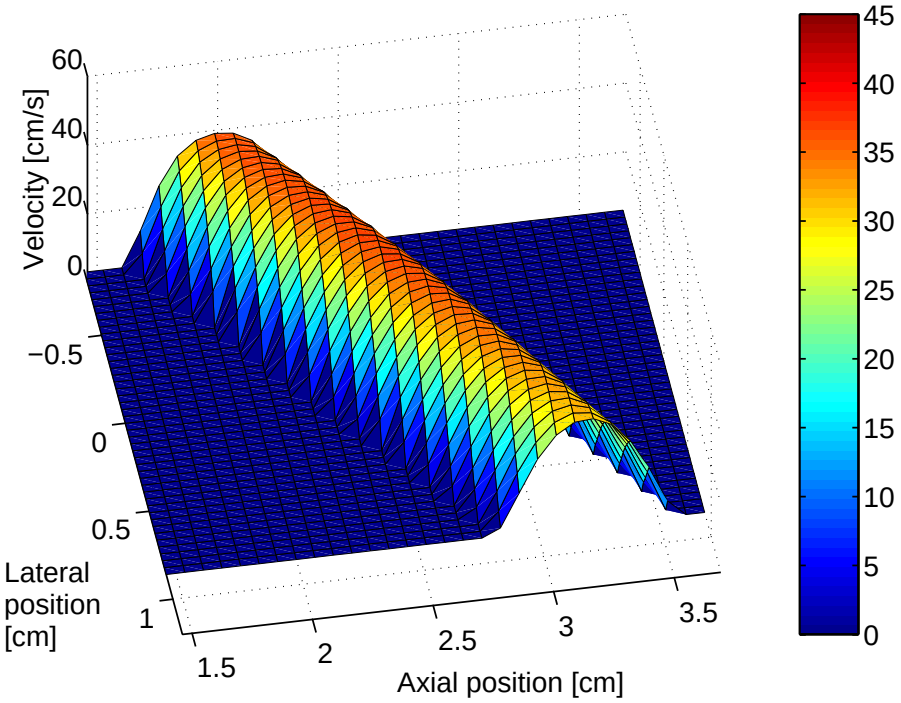

Figure 7.3: The true velocity profile for the diastolic frame in Fig. 7.2.

is plotted in Fig. 7.3. An improvement can be seen. The resulting velocity distribution is not as smooth as the true velocity distribution, but it is more consistent with the true profile.

The filter has been applied to *in-vivo* data acquired with a dedicated sampling system, which has a 30 MHz sampling frequency and 12 bits resolution [61]. Data from the carotid artery were recorded with a 7.5 MHz convex array. The vessel lies at an angle of 35º. The frame rate was 18 frames/s, and 10 seconds of data were recorded. The 2^{nd} order HP echo-canceling filter is used for the echo-canceling prior to the estimation. The estimates are obtained with the autocorrelation estimator. A scan conversion is performed prior to the post-processing, so the velocity estimates are given for the rectangular imaging grid. Figure 7.4 shows an example of the performance of the $M2$ filter. An improvement is obtained. Some of the transitions between velocity levels are still very steep though, which represents a problem. These noisy variations will attract the eye and distract the observer. Other methods for minimization of the variations should be investigated.

7.2 Post-processing filter based on optical flow theory

The median filter represents a simple filter, which uses that the velocity estimate is confined to lie within the amplitude range spanned by its neighbors. No assumptions on the relations between the velocities in a bounded spatial and temporal neighborhood are made. No restrictions on the transitions between the velocities in a neighborhood are given. Therefore the steep transitions between velocity levels can occur. A filter, which employs the spatial and temporal correlation and introduces assumptions on the transitions, is introduced in the following. The mechanics of non-turbulent, fluid motion introduces restrictions on the possible flow patterns for blood. This aspect was discussed in Chapter 6 and verified for the carotid artery. The transition from one velocity to another in a neighboring point in time and space must follow a continuous and smooth function. The smoothness property is the link to introducing restrictions on the variations possible between neighboring velocity estimates in time and space. A filter, which incorporates the smoothness property, can be derived from statistics. The filter computes an estimate of the true velocities

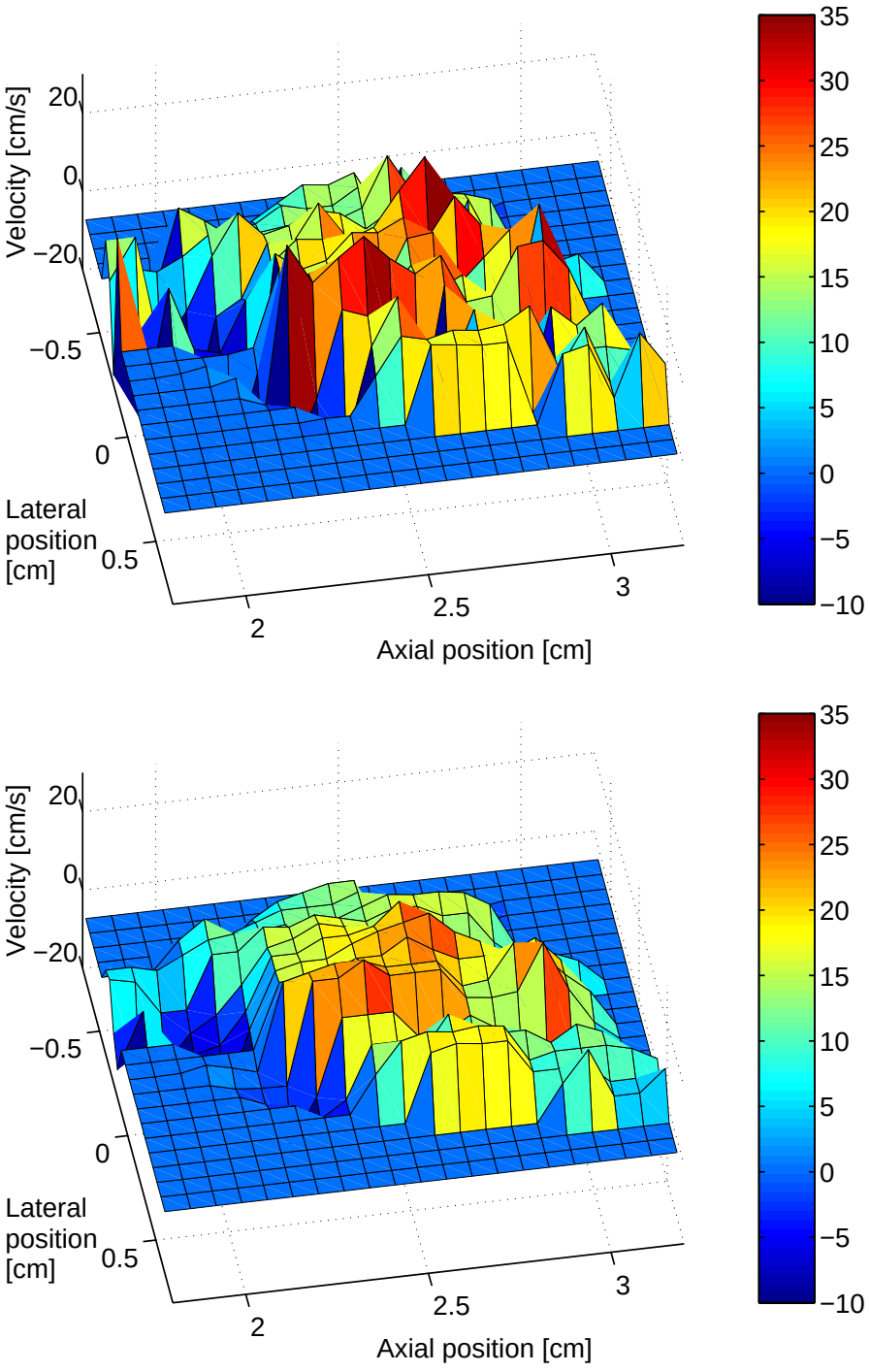

Figure 7.4: The velocity profile before (top) and after application of the $M2$ filter (bottom) on *in-vivo* data.

$\vec{V}^c = [\vec{v}^c(x_1, z_1, t_f), ..., \vec{v}^c(x_N, z_M, t_f)]$ in the image. The available information for the filter is the estimated velocities, $\vec{V}^e = [\vec{v}^e(x_1, z_1), ..., \vec{v}^e(x_N, z_M)]$, for the present and previous image, and the smoothness property.

The filter is designed by employing Bayesian theory [62]. A conditional, posterior probability density function, $p(\vec{V}^c|\vec{V}^e)$, for the true velocities is derived:

$$p(\vec{V}^c|\vec{V}^e) = \frac{p(\vec{V}^c)p(\vec{V}^e|\vec{V}^c)}{p(\vec{V}^e)}. \tag{7.2}$$

$p(\vec{V}^c)$ is the a priori probability density, and $p(\vec{V}^e|\vec{V}^c)$ is the model specific probability. $p(\vec{V}^e)$ is the probability density of the estimated velocities. This factor is not dependent on the true velocities, and therefore does not influence the estimation of the true velocities. The expressions for $p(\vec{V}^c)$ and $p(\vec{V}^e|\vec{V}^c)$ are derived in the following.

An a priori knowledge is given on the true estimates, when the smoothness property is accepted. It has to be within a certain range relative to the neighboring velocities to fulfill the property. Applying the theory of optical flow [63] from image processing makes it possible to define a set of mathematical relations, which determines, when the transitions between velocity levels obey the smoothness property. One set of relations are the spatial and temporal derivatives. A smooth transition will be characterized by having small derivatives, as the velocity levels in neighboring locations will be fairly similar. One way of formulating the smoothness constraint is by using a Markov random field (MRF) model [63], [64], [65]. The Markov property states that the true velocity in a given location (x, z, t_f) depends on the velocities in a finite neighborhood of (x, z, t_f). By implementing the derivatives as finite differences the Markov property is obeyed:

$$\begin{aligned}
\vec{v}_{dx}(x, z, t_f) &= \vec{v}^c(x + \Delta x, z, t_f) - \vec{v}^c(x, z, t_f) \\
\vec{v}_{dz}(x, z, t_f) &= \vec{v}^c(x, z + \Delta z, t_f) - \vec{v}^c(x, z, t_f) \\
\vec{v}_{dt}(x, z, t_f) &= \vec{v}^c(x, z, t_f - T_{frame}) - \vec{v}^c(x, z, t_f),
\end{aligned} \tag{7.3}$$

where $\vec{v}_{dx}, \vec{v}_{dz}$, and $\vec{v}_{dt}$ denote the spatial and temporal derivatives, and Δ describes a spatial distance between neighbors. As an MRF model has been used to describe the local relations, the Hammersfield-Clifford theorem [63], [66] states that the distribution of the derivatives is a Gibbs distribution. The resulting probability density function is:

$$p(\vec{V}^c(t_f)) = \frac{1}{Z}\exp(-\alpha E_1(t_f) - \gamma E_2(t_f)), \tag{7.4}$$

where Z is a normalization factor, which assures that $\int p(\vec{V}^c)d\vec{V}^c = 1$. The variables α and γ are scale factors that weight the contributions from the spatial and temporal derivatives, respectively. $E_1(t_f)$ and $E_2(t_f)$ are energy terms defined by:

$$\begin{aligned}
E_1(t_f) &= \int\int (||\vec{v}_{dx}(x, z, t_f)||^2 + ||\vec{v}_{dz}(x, z, t_f)||^2) dx dz \\
E_2(t_f) &= \int\int ||\vec{v}_{dt}(x, z, t_f)||^2 dx dz.
\end{aligned} \tag{7.5}$$

Two energy terms are used with different scaling factors to allow for the level of spatial and temporal correlation to be different. An a priori probability density has been obtained based on the a priori knowledge saying that transitions should occur smoothly. The a priori probability density assigns a high probability to a choice of the true velocities close to the levels of the neighboring true velocities and vice versa. The chosen definition of the derivatives represents a first-order neighborhood [63].

In the above definition of the smoothness constraints the physical situation at hand was not discussed. The constraints have been chosen merely from a mathematical point of view [63], and the spatial and temporal velocity variations are assumed Gaussian distributed. The investigations in Chapter 6 show that this is only approximately true. Still, the assumption will be employed in the following.

The smoothness property is not the only information available. Although the velocity estimates are encumbered with uncertainty, their values give an indication of what interval of possible velocities the true velocity belongs to. This can be used to define a conditional probability density $p(\vec{V}^e|\vec{V}^c)$, which introduces a relation between the estimates and the true velocities. A relation describing a measure of error is introduced. A Gibbs distribution is often assumed for the error distribution and will be used here. The energy term is defined by:

$$\begin{aligned} E_3(t_f) &= \beta \int\int (\omega_1(x,z,t_f)(v_1^c(x,z,t_f) - v_1^e(x,z,t_f))^2 + \ldots \\ &\quad + \omega_D(x,z,t_f)(v_D^c(x,z,t_f) - v_D^e(x,z,t_f))^2) dx dz, \end{aligned} \tag{7.6}$$

where β is a weighting parameter like α and γ. The index D indicates the dimension of the velocity vector. The scale factor $\omega_i(x,z,t_f)$ ($i = [1,..,D]$) is introduced to account for ones faith in the velocity estimates. If the estimate is encumbered with high uncertainty, it is not a good indicator for the level of the true velocity, and its influence in the post-processing should be weighted down. When employing Kasai's autocorrelation method (see Section 6.3) for estimating the velocities, a measure of the variance on the estimate can be determined. In this case one could set $\omega_i(x,z,t_f)$ proportional to the inverse of the standard deviation. The different components in the velocity vector might have been obtained with different estimators, and therefore ω is dependent hereof. The weighting parameters are restricted by $\alpha+\beta+\gamma = 1$, and each of them takes a value between 0 and 1.

At this point a posterior, conditional probability density for the true velocities has been derived. An estimate of the true velocities, $\hat{v}^c(x,z,t_f)$ can be obtained by maximization of the obtained a posteriori density, $p(\vec{V}^c|\vec{V}^e)$, with respect to $\vec{V}^c$. In statistics this estimate is referred to as the MAP estimate [33]. As the posterior density is expressed by an exponential, the maximization of (7.2) equals minimization of the sum $E = \alpha E_1 + \gamma E_2 + \beta E_3$. The energy terms are computed by integrating over the whole image, which makes the optimization very cumbersome. Besag [67] has derived a method termed the Iterated Conditional Mode (ICM) to ease the optimization. Through iterations the global posterior probability in (7.2) is maximized by maximizing the local posterior probability. Rather than working on the whole image, the maximization process is carried out on each of the pixels on an iterative basis. The term E in the exponential represents a quadratic form [33], [62]. When the quadratic form is positive-definite, it is ensured that only one minimum exists [63]. The single minimum and the Markov property ensure that the ICM method will converge to the estimates obtained, if the global posterior distribution was maximized. A simple filter is obtained, which computes an estimate of the true velocity, $\hat{v}^c$, in a given location from the values of the velocity in the neighboring locations in space and time. The velocity estimates $\hat{v}^e$ in the neighborhood are used as initial guesses of the true velocities. The best filtering and thereby estimate of the true velocity is obtained, if the neighboring velocities are true, or at least as close to the true value as possible. With this in mind the new, filtered estimate in a given location should be used in the subsequent filtering of its neighbors, as soon as it has been determined [66]. This assumption is fully valid, if one can ensure that a better and more true estimate is obtained in each iteration. This is not always the case, and then the filtering order is not indifferent. Consider the following: the estimation of $\hat{v}_k^c(x,z,t_f)$ is followed by the estimation of $\hat{v}_k^c(x+\Delta x,z,t_f)$, where k represents the iteration number. One iteration in the filtering of the image will then follow the procedure (written as pseudo computer code):

```
for j = 1 : number of rows in image
    for j = 1 : number of columns in image
        perform filtering of pixel in location (x_i, z_j)
    end
end
```

If a poor estimate of $\hat{v}_k^c(x,z,t_f)$ is computed, this will influence the estimation of $\hat{v}_k^c(x+\Delta x,z,t_f)$ negatively. A defective estimate of $\hat{v}_k^c(x+\Delta x,z,t_f)$ is obtained, which again will influence the estimation of $\hat{v}_k^c(x+$

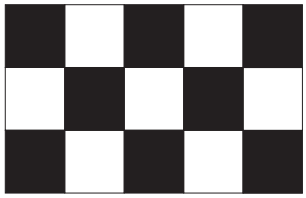

Figure 7.5: Chessboard pattern.

$2\Delta x, z, t_f$). The initial poor estimate gets to influence all other estimates, so the error will spread. The influence of a poor estimate can be reduced by employing a different filtering order [66], which matches the distribution of black and white squares (equal to image pixels) on a chessboard (see Fig. 7.5). First, the estimates of $\hat{v}^c$ are computed for the velocities in all the locations indicated by black (white). Then the filtering is performed on the velocities in all the remaining locations, which are represented by white (black) pixels. Here the estimates from the first filtering are used in the second filtering. Each iteration consists of two filterings. The poor estimate of $\hat{v}_k^c(x,z,t_f)$ will still influence $\hat{v}_k^c(x+\Delta x,z,t_f)$, but the error will not be passed on to $\hat{v}_k^c(x+2\Delta x,z,t_f)$ and the rest of the image. In most commercial scanners today only the velocity along the axial direction is estimated, so the velocity vector is one-dimensional ($D=1$). The filter equations for this situation for iteration $k+1$ become:

$$\begin{aligned}\hat{v}_{k+1}^c(x,z,t_f) &= \frac{1}{4\alpha+\beta\omega+\gamma}\cdot \\ &\quad (\ \alpha(v_k^c(x-\Delta x,z,t_f)+v_k^c(x+\Delta x,z,t_f)+v_k^c(x,z-\Delta z,t_f)+v_k^c(x,z+\Delta z,t_f)\ ) \\ &+ \gamma v^c(x,z,t_f-T_{frame}) \\ &+ \beta\omega(x,z,t_f)v^e(x,z,t_f)\ ), \end{aligned} \tag{7.7}$$

when the first filtering is performed, and:

$$\begin{aligned}\hat{v}_{k+1}^c(x,z,t_f) &= \frac{1}{4\alpha+\beta\omega+\gamma}\cdot \\ &\quad (\ \alpha(v_{k+1}^c(x-\Delta x,z,t_f)+v_{k+1}^c(x+\Delta x,z,t_f)+v_{k+1}^c(x,z-\Delta z,t_f)+v_{k+1}^c(x,z+\Delta z,t_f)\ ) \\ &+ \gamma v^c(x,z,t_f-T_{frame}) \\ &+ \beta\omega(x,z,t_f)v^e(x,z,t_f)\ ), \end{aligned} \tag{7.8}$$

for the second filtering. The number of iterations required are dependent on the situation and will be discussed in Section 7.2.2.

In the above it has been assumed that the same scale factors are used for all images. Investigations of the velocity profile throughout the cardiac cycle reveal that the velocity levels and the levels of the temporal and spatial derivatives vary over the cardiac cycle. Therefore it might be beneficial to let the scale factors vary over the cardiac cycle. The value of the scale factors become dependent on time: $\alpha(t_f), \beta(t_f)$, and $\gamma(t_f)$. This aspect is investigated in this study.

The filter is applied to the whole image. A complete neighborhood does not exist for the edge pixels, as one or more neighbors do not exist. These pixels can either be left un-filtered, or a modified filter, which does not use the missing pixels, can be used. In this study these pixels will not be filtered.

7.2.1 Determination of filter parameters

The optimum scale factors can be determined by minimization of the absolute error:

$$\hat{\Theta} = \arg\min_{\Theta} \sum_{f=1}^{F}\sum_{j=1}^{N}\sum_{i=1}^{M} ||v^c(x_i,z_j,t_f) - \hat{v}^c(x_i,z_j,t_f)||, \tag{7.9}$$

SNR	0	5	10	15	20	30	40
α	0.77	0.89	0.80	0.39	0.22	0.15	0.13
β	0.00	0.00	0.13	0.59	0.77	0.85	0.87
γ	0.23	0.11	0.07	0.02	0.01	0.00	0.00

Table 7.3: The best choice of the scale parameters (α, β, γ) for a range of SNRs ([dB]).

where Θ is a vector, which consists of the scale parameters (α, β, γ). A set of F 2D images must be available, where the true and the estimated velocities are known. The integration has been substituted with a summation, as the 2D images consist of a finite number of pixels. The absolute error was preferred over the RMS error for the determination of the scale factors. This choice was based on investigations. The squaring operation in the computation of the RMS error causes high amplitude errors to have more weight in the sum of errors. The optimization thereby puts more weight on eliminating the high amplitude errors, which proved to be inexpedient. Optimization using the RMS error eliminates the influence from the estimates $v^e(x,z,t_f)$ in the filtering, as the value of β approaches or is set equal to 0. This result was obtained even at higher SNRs, where the standard deviation on the estimates is low. The information in the estimates is discarded, which is not desirable. Instead the absolute error was employed for optimization, which weights the errors equally.

The simulated data used for evaluating the median filter will be employed for the determination of the scale parameters for the statistical filter. The temporal resolution is dictated by the frame rate, which is 10 frames/s. The spatial resolution Δ along the axial and lateral direction equals 0.8 mm and 0.4 mm, respectively. The scale parameters have been determined for a range of SNRs. The results, when the scale parameters are kept constant over the cardiac cycle, are listed in Table 7.3. The value of the scale parameters are dependent on the SNR. At low SNRs the filter only uses the neighboring velocities in time and space. The estimated velocities, V^e, have a high uncertainty, and therefore they should not contribute much in the filtering. An averaging over the spatial and temporal neighbors is performed, where the contribution from the spatial neighbors is weighted higher than the temporal neighbors. As the SNR increases, the uncertainty on the estimate decreases. The estimated velocities are close to the truth, and therefore should play a big role in the post-processing. The spatial neighbors influence the post-processing more than the temporal neighbor. This is to be expected, as the spatial neighbors originate from the same frame, and the velocities are similar. The temporal correlation is dependent on frame rate. For the current scan situation the results show that the temporal correlation is low compared to the spatial correlation due to the low frame rate. At higher frame rates one should expect an increase in the temporal correlation. The importance of the temporal and spatial neighbors decreases with increasing SNR. At high SNRs the temporal influence disappears. In practice one will never set any of the scale parameters to zero. Instead a low but non-zero value will be used.

As discussed previously it might be beneficial to let the scale parameters vary over the cardiac cycle. This was investigated, and the best choice of the scale parameters for each frame are listed in Tables 7.4-7.6. The scale parameters have not been determined for frame 1, as it is the first frame in the set of frames, so the temporal correlation cannot be included. The results clearly show that the best choice of the scale parameters varies over the cardiac cycle. Frame 11 and 21 contain the systolic phase of the cardiac cycle, where the velocity changes fast to reach the peak velocity within a short period of time. Therefore the amplitudes of the spatial derivatives are high, and the spatial correlation is low. The spatial neighbors should contribute less to the filtering, and therefore α is low. The temporal derivative will be high too, as the previous frame contained velocity estimates from the last part of the diastolic phase, where the velocity levels are lower. The temporal correlation will be low, and this explains why γ is set equal to 0. The filtering mainly relies on the estimates $\vec{V}^e$ to produce the new estimates of the velocities. The influence from the estimates $\vec{V}^e$ increases as the SNR increases for all frames. The level of temporal and spatial correlation varies for the different frames and the SNR, and the choice of the scale parameters α and γ varies. The

		SNR [dB]						
Frame		0	5	10	15	20	30	40
2	α	0.8	0.32	0.16	0.09	0.13	0.12	0.11
	β	0.2	0.68	0.83	0.9	0.87	0.88	0.89
	γ	0	0	0	0	0	0	0
3	α	0.98	0.52	0.26	0.2	0.15	0.17	0.17
	β	0	0.48	0.74	0.8	0.85	0.83	0.83
	γ	0.02	0	0	0	0	0	0
4	α	0.84	0.66	0.4	0.24	0.17	0.16	0.17
	β	0	0.18	0.47	0.7	0.76	0.76	0.75
	γ	0.16	0.16	0.13	0.06	0.07	0.08	0.08
5	α	0.53	0.41	0.21	0.09	0.06	0.06	0.06
	β	0	0.18	0.46	0.71	0.76	0.76	0.75
	γ	0.47	0.41	0.33	0.2	0.18	0.18	0.19
6	α	0.57	0.64	0.51	0.25	0.15	0.13	0.14
	β	0	0	0	0.44	0.54	0.57	0.55
	γ	0.43	0.36	0.49	0.31	0.31	0.3	0.31
7	α	0.83	0.84	0.86	0.41	0.2	0.23	0.2
	β	0	0	0	0.23	0.47	0.46	0.52
	γ	0.17	0.16	0.14	0.36	0.33	0.31	0.28
8	α	0.58	0.68	0.45	0.32	0.21	0.13	0.12
	β	0	0	0	0	0.01	0.14	0.15
	γ	0.42	0.32	0.55	0.68	0.78	0.73	0.73
9	α	0.52	0.45	0.34	0.38	0.25	0.14	0.13
	β	0	0	0	0	0	0.4	0.39
	γ	0.48	0.55	0.66	0.62	0.75	0.46	0.48
10	α	0.57	0.67	0.71	0.67	0.54	0.29	0.33
	β	0	0	0	0	0	0.1	0.13
	γ	0.43	0.33	0.29	0.33	0.46	0.61	0.54
11	α	0.3	0.19	0.11	0.09	0.07	0.08	0.08
	β	0.7	0.81	0.89	0.91	0.93	0.92	0.92
	γ	0	0	0	0	0	0	0

Table 7.4: The best choice of the scale parameters for the frames 2-11 for a range of SNRs ([dB]).

Frame		SNR [dB] 0	5	10	15	20	30	40
12	α	0.91	0.51	0.25	0.11	0.12	0.12	0.13
	β	0	0.45	0.7	0.87	0.86	0.86	0.86
	γ	0.09	0.04	0.05	0.02	0.02	0.02	0.01
13	α	1	0.59	0.37	0.21	0.18	0.18	0.18
	β	0	0.41	0.63	0.79	0.82	0.82	0.82
	γ	0	0	0	0	0	0	0
14	α	0.98	0.5	0.28	0.18	0.13	0.13	0.14
	β	0	0.44	0.65	0.73	0.8	0.79	0.77
	γ	0.02	0.06	0.07	0.09	0.07	0.08	0.09
15	α	0.53	0.28	0.16	0.09	0.07	0.08	0.08
	β	0	0.31	0.6	0.66	0.78	0.78	0.78
	γ	0.47	0.41	0.24	0.25	0.15	0.14	0.14
16	α	0.56	0.59	0.39	0.16	0.08	0.07	0.07
	β	0	0	0.26	0.59	0.75	0.71	0.69
	γ	0.44	0.41	0.35	0.25	0.17	0.22	0.24
17	α	0.56	0.56	0.45	0.28	0.15	0.09	0.07
	β	0	0	0	0.22	0.38	0.49	0.51
	γ	0.44	0.44	0.55	0.5	0.47	0.42	0.42
18	α	0.67	0.62	0.34	0.21	0.11	0.08	0.09
	β	0	0	0	0	0	0	0
	γ	0.33	0.38	0.66	0.79	0.89	0.92	0.91
19	α	0.47	0.52	0.49	0.35	0.22	0.18	0.16
	β	0	0	0	0	0.21	0.12	0.17
	γ	0.53	0.48	0.51	0.65	0.57	0.7	0.67
20	α	0.71	0.66	0.64	0.62	0.54	0.61	0.23
	β	0	0	0	0	0.03	0.08	0.54
	γ	0.29	0.34	0.36	0.38	0.43	0.31	0.23
21	α	0.28	0.17	0.09	0.07	0.05	0.05	0.05
	β	0.72	0.83	0.91	0.93	0.95	0.95	0.95
	γ	0	0	0	0	0	0	0

Table 7.5: The best choice of the scale parameters for the frames 12-21 for a range of SNRs ([dB]).

		SNR [dB]						
Frame		0	5	10	15	20	30	40
22	α	0.77	0.59	0.3	0.23	0.21	0.21	0.21
	β	0	0.26	0.6	0.68	0.69	0.7	0.7
	γ	0.23	0.15	0.1	0.09	0.1	0.09	0.09
23	α	0.79	0.87	0.49	0.24	0.18	0.17	0.17
	β	0	0.13	0.51	0.76	0.82	0.83	0.83
	γ	0.21	0	0	0	0	0	0
24	α	0.8	0.53	0.24	0.12	0.14	0.13	0.13
	β	0	0.27	0.67	0.82	0.8	0.81	0.79
	γ	0.2	0.2	0.09	0.06	0.06	0.06	0.08
25	α	0.42	0.57	0.2	0.1	0.09	0.07	0.06
	β	0	0.02	0.51	0.66	0.66	0.71	0.71
	γ	0.58	0.41	0.29	0.24	0.25	0.22	0.23
26	α	0.59	0.56	0.4	0.12	0.09	0.07	0.06
	β	0	0	0.12	0.63	0.67	0.69	0.7
	γ	0.41	0.44	0.48	0.25	0.24	0.24	0.24
27	α	0.55	0.53	0.5	0.45	0.15	0.07	0.06
	β	0	0	0.02	0.05	0.43	0.61	0.62
	γ	0.45	0.47	0.48	0.5	0.42	0.32	0.32
28	α	0.63	0.7	0.42	0.26	0.17	0.06	0.04
	β	0	0	0	0	0.1	0.04	0.09
	γ	0.37	0.3	0.58	0.74	0.73	0.9	0.87
29	α	0.56	0.57	0.53	0.22	0.16	0.1	0.12
	β	0	0	0	0	0	0.2	0.18
	γ	0.44	0.43	0.47	0.78	0.84	0.7	0.7

Table 7.6: The best choice of the scale parameters for the frames 22-29 for a range of SNRs ([dB]).

temporal correlation is higher than the spatial correlation for some frames, and the opposite for other frames. The level of the temporal and spatial correlation can change for the same frame, as the SNR changes. The importance of the spatial neighbors decreases with increasing SNR. Again, in an implementation a scale parameter will never be set equal to zero. A low but non-zero value will be used. In Fig. 7.6 the values of the scale parameters are plotted as a function of the frame number for a SNR of 15 dB. The values fluctuate throughout the cardiac cycle, and some fluctuation is also seen between the 3 cardiac cycles. The latter is due to the influence from the noise and the value of the frame rate. The frame rate is actually 9.87 frame/s in the current simulation, so the velocity distributions in the so-called systolic frames (frame 11 and frame 21) will not be 100 % identical. The same holds for the rest of the frames, so the velocity distribution will not be identical in any two frames. Implementation of the filter therefore becomes very complicated. The exact content in the image with respect to the velocity levels and the position in the cardiac cycle must be known, so the proper set of scale parameters can be used. The value of the scale parameters will be dependent on the choice of the spatial and temporal resolution. Therefore the scale parameters must be determined for all possible settings of the resolution, if only the absolute best performance is accepted. The post-processing has become very complicated. It will probably be possible to pursue this approach but it does not seem very attractive. Instead a model, which follows the overall trends in the variation, could be used. A model will be derived in the following for the scale factors, when the SNR is 15 dB. The scale parameter α shows the least variation of the three, and only for two frames does it deviate a lot. Therefore α will be modeled as a constant, which is equal to the mean of all estimated values of α. Before moving on to modeling γ and β one should remember that $\alpha+\beta+\gamma=1$ at all time instances. Additionally, none of the scale factors should take the value zero at any time instance. The fluctuations of β and γ will be modeled by linear functions, which have an increasing and decreasing slope, respectively. Other functions (*e.g.* a sinusoid) might be usable too. In this study a simple function has been chosen, where the relations between the scale parameters and some of the properties (SNR, resolution) can be introduced in a simple way. The model for the scale factors are:

$$\begin{aligned} \alpha &= 0.24 \\ \beta &= 0.7 - 0.066 \cdot (f-1) \\ \gamma &= 0.06 + 0.066 \cdot (f-1), \end{aligned} \tag{7.10}$$

where f represents a frame number from 1-10, which relates to the frame rate for the current simulation. The first frame contains the initial systolic phase in the cardiac cycle. In Fig. 7.7 the models for the scale factors for each frame are plotted. The optimum values of the scale factors are repeated, so a comparison can be performed. The modeled scale factors take values that are either higher or lower than the optimum values. Still the overall trends are represented by the model. As the SNR decreases, the fluctuation of α increases and the mean value increases. If the same approach for the modeling of the scale parameters is employed, the value of α increases, which causes the slopes of the linear relations for β and γ to decrease.

7.2.2 Performance on simulated and *in-vivo* data

As the true velocities are known, a measure of the performance of the filter can be obtained by computing the RMS error before and after application of the filter. In this study only one iteration is performed. This choice has been made for two reasons. The improvement obtained after just one iteration is quite high, which will become clear in the following. This argument alone does not justify to perform one iteration only. The generated images have a finite spatial resolution, so some variation might be present and should be preserved. The flow profile for the femoral artery will contain some variations, as the velocities take both positive and negative values as shown in Fig. 7.8. One should be careful not to remove this valuable information. It has therefore been decided to perform one iteration only in this study. Then a question arises with respect to the filtering order. Should the filter be applied to the black or white pixels first? Is the performance independent on this choice? The answer to the last question is no, and the discussion in the following will make this clear. Consider the following situation. The velocity in a white pixel deviates from

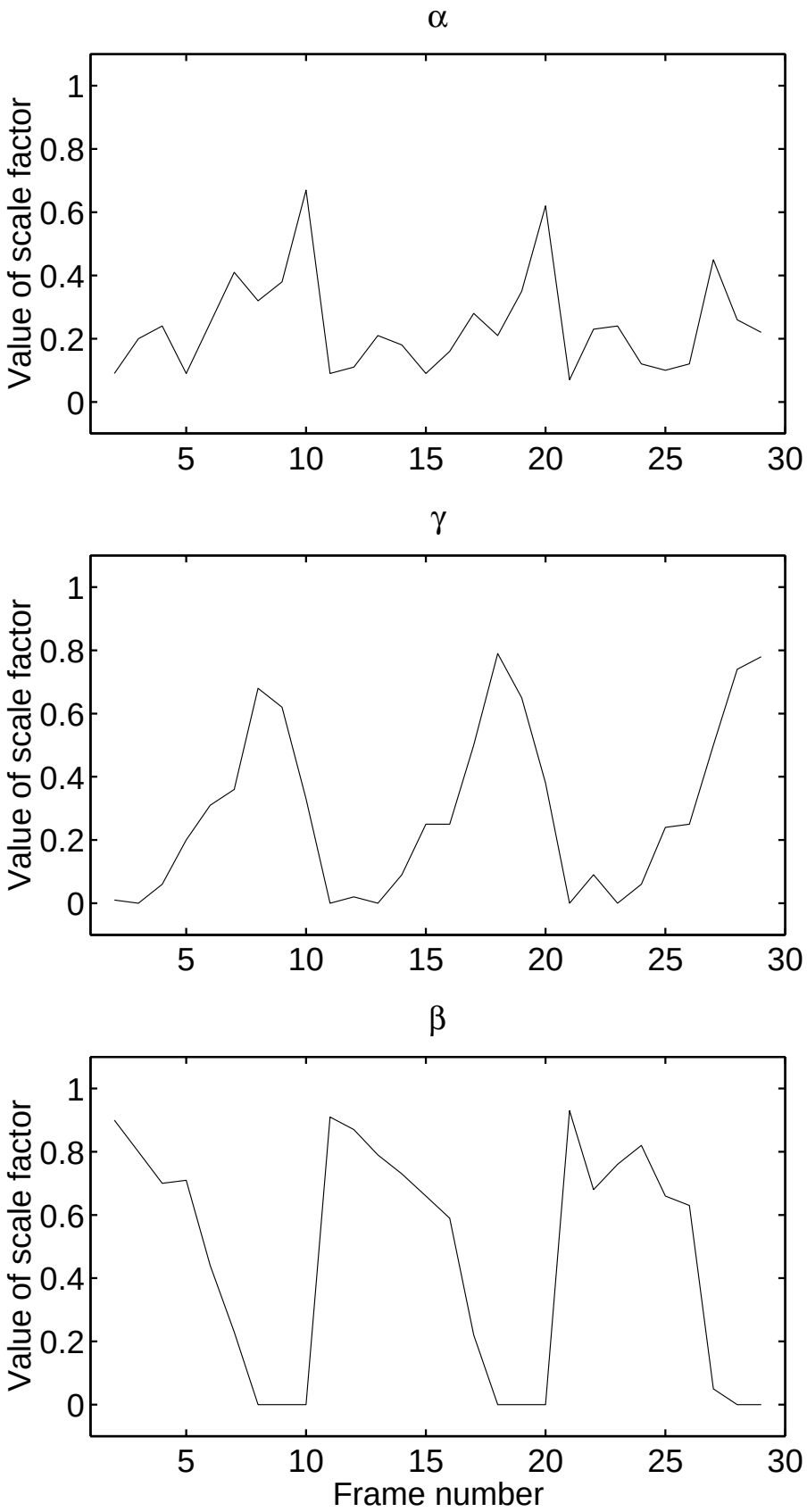

Figure 7.6: The values of the scale parameters as a function of frame number for a SNR of 15 dB.

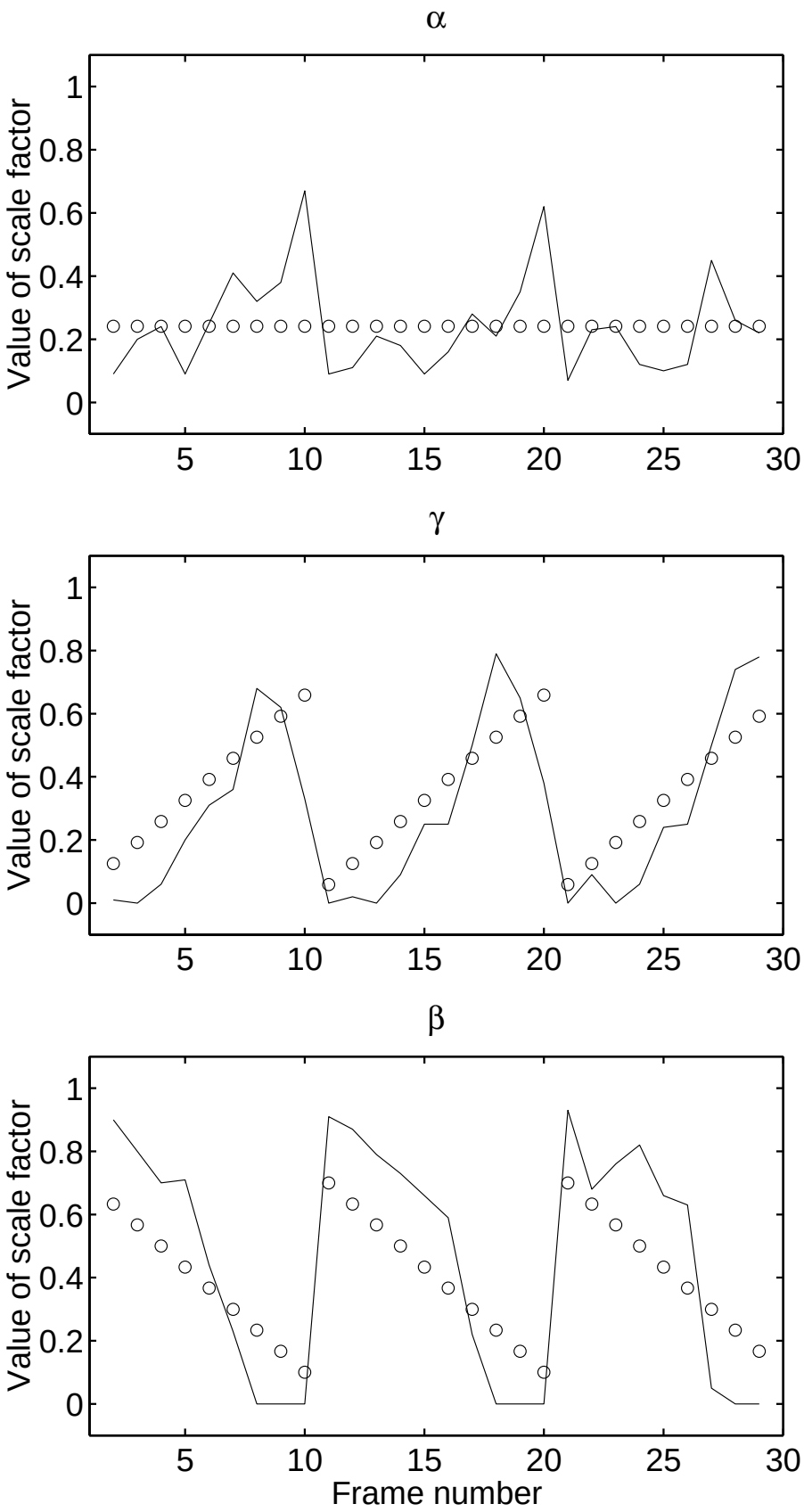

Figure 7.7: Model of the scale parameters (o) as a function of frame number for a SNR of 15 dB. The best choices of the scale parameters are indicated with the solid line (—).

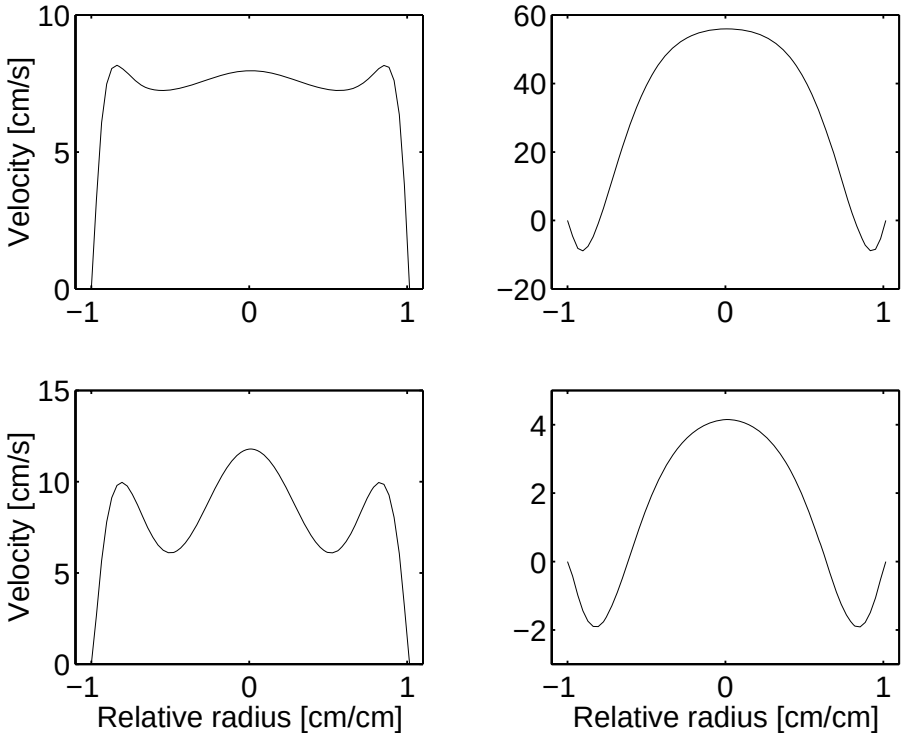

Figure 7.8: The velocity profile at 4 time instances (0, 0.25, 0.5, 0.75 s) for the femoral artery based on Womersley's model (see Chapter 3).

its neighbors. It can either be a wrong estimate (*e.g.* an aliased estimate), or the true estimate, which arises due to turbulence or the properties of the velocity profile for the given vessel. An example of the latter could be an estimate obtained from the femoral artery. If the filter is applied first on the white pixels, the filter's estimate of the velocity in this pixel will be closer to the velocity values of the neighbors. The original deviating estimate will influence the filtering of its neighbors in the black pixels less, as it has already been filtered. This is beneficial if the original estimate is wrong but information will be removed, if the variation should be present. If the black pixels were filtered first, the deviating estimate gets to influence its neighbors, and the valuable information or wrong estimate is preserved. As the nature of the deviating velocity estimate is unknown a priori, both approaches must be evaluated. In this study the filtering is performed twice, and the resulting estimates are the average of the two evaluations.

Table 7.7 lists the RMS error before and the improvement in % obtained after application of the filter, $Stat1$, when the same set of scale parameters (see Table 7.3) are used for all frames, and ω is equal to one. The results show that improvements are obtained for all SNRs and range from 15-53 %. The improvement is highest for low SNRs. A choice of which set of scaling factors to use must be made, if the level of SNR is unknown a priori. Results of using the scale factors for 15 dB on all the data sets are listed as $Stat2$ in Table 7.7. The improvement is slightly smaller than for the first case. For high SNRs it seems as if the $Stat2$ filter performs better than the $Stat1$ filter, which of course is not true. The reason for these results is that the performance evaluation is carried out using the RMS error, whereas the scale parameters were determined by employing the absolute error. If the absolute errors were listed instead of the RMS errors, one will see that the performance of the $Stat1$ filter is better than the $Stat2$ filter for all SNRs.

The performance of the statistical filter and the M1 and M2 median filters has been compared. The improvement obtained with the median filters are repeated in the last two columns in Table 7.7. The statistical filter out performs the median filters for all SNRs. The improvement is a factor of 2 higher at low SNRs, and it approaches a factor of 4 as the SNR increases. Plots of the original velocity profile and the resulting velocity profile after application of the $Stat2$ filter on the simulated data are shown in Fig. 7.9. The true

SNR	RMS_{before}	$Stat1$	$Stat2$	$M1$	$M2$
0	0.125	52.6	46.0	11.0	27.1
5	0.096	44.3	40.0	8.4	21.8
10	0.076	34.9	32.4	5.0	15.2
15	0.061	26.6	26.6	2.2	9.9
20	0.054	20.6	21.1	0.0	6.0
30	0.049	16.9	17.6	-0.8	3.9
40	0.048	15.8	16.5	-0.4	4.1

Table 7.7: The RMS error ([m/s]) before and the improvement in % after application of the statistical and median filters.

velocity profile was plotted in Fig. 7.3. A more smooth profile has been obtained, which more closely resembles the true velocity profile. The filter was applied to the acquired *in-vivo* data introduced in Section 7.1.1. An example of the original and filtered CFM image is plotted in Fig. 7.10, when the $Stat2$ filter was used. A more smooth profile has been obtained with the $Stat2$ filter. The steep transitions obtained with median filtering have been removed.

The above discussion considered the performance, when the same set of scale parameters were used for all frames. The investigations in Section 7.2.1 clearly revealed that the value of the scale parameters vary as a function of the frame number and thereby the temporal position in the cardiac cycle. A better performance by means of a lower error will be obtained, if the scale parameters vary with time. The complexity of the time variation was reduced by modeling the variation in a more simple form, which will be easier to implement and control for different settings. The feasibility of the model is determined by comparing the absolute errors after application of the filter with time-varying ($Stat2_{ef}$) and constant ($Stat2$) scale factors for each frame. The absolute error (AE) is employed as it was the basis for determining the scale parameters. It will not give misleading improvement values as is the case for the RMS error. The absolute errors are compared by computing:

$$R_{abs} = \frac{AE_c - AE_{ef}}{AE_{ef}}, \tag{7.11}$$

for each frame, where AE_c and AE_{ef} are the error after application of the $Stat2$ and the $Stat2_{ef}$ filters, respectively. Figure 7.11 shows plots of R_{abs} (in %) for the SNRs 0, 10, 20, and 30 dB. For a positive value of R_{abs} the best performance is obtained, when the filtering is performed with the $Stat2_{ef}$ filter. The sign and the amplitude of R_{abs} vary as a function of frame number and SNR. Employment of the $Stat2_{ef}$ filter does not always give the lowest error. For certain frames the $Stat2$ filter is to be preferred over the $Stat2_{ef}$ filter. The three cardiac cycles approximately span the frames 1-10, 11-20, and 21-30 (frame 30 not simulated). The following trends exist:

- the best performance for the first 4 frames in the cardiac cycle is obtained with the $Stat2$ filter,
- the best performance for the next 5 frames is obtained with the $Stat2_{ef}$ filter.

This means that the $Stat2_{ef}$ filter performs best on the frames at the end of the diastolic phase. For a SNR of 0 dB the $Stat2_{ef}$ filter lowers the error quite a bit for these frames. The summed absolute errors over all frames for the $Stat2$ and the $Stat2_{ef}$ filters have been compared. The results reveal that the overall improvement, when the $Stat2_{ef}$ filter is employed, ranges from 1.7-5.0 %, when the SNR is varied from 0-40 dB. The improvement decreases as the SNR increases. If the exact values of the scale factors for each frame are used, the improvement ranges from 3.1-5.4 %. The scale parameters for the 15 dB case are used for all data sets (independent of the SNR). The largest improvement is obtained for a SNR of 20 dB, and the lowest for 0 dB. The employment of the simple linear model for the scale parameters slightly degrades the overall improvement obtained by using time-varying scale parameters. The levels of the improvement (both when

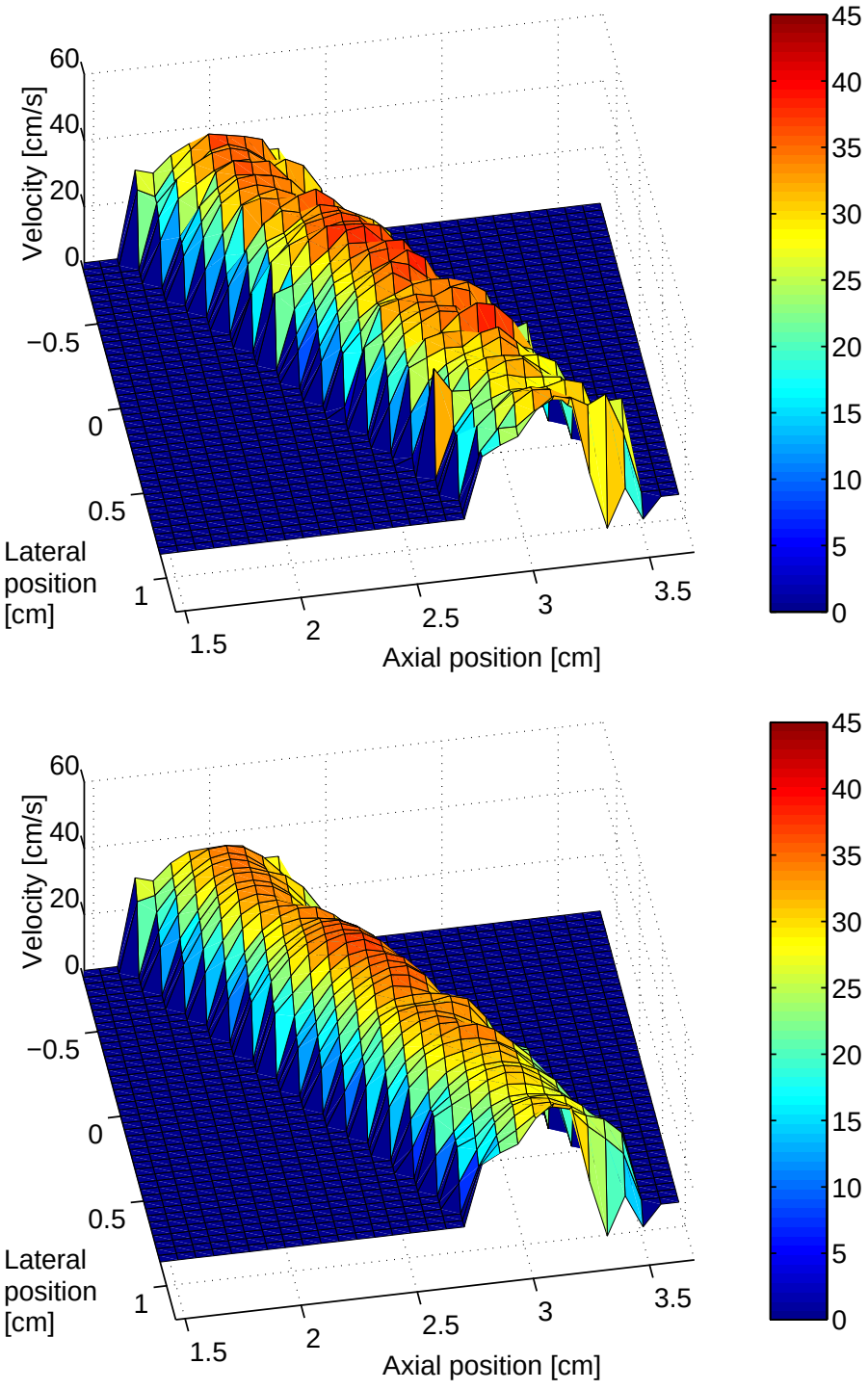

Figure 7.9: The velocity profile before (top) and after (bottom) application of the post-processing filter *Stat*2 on simulated data.

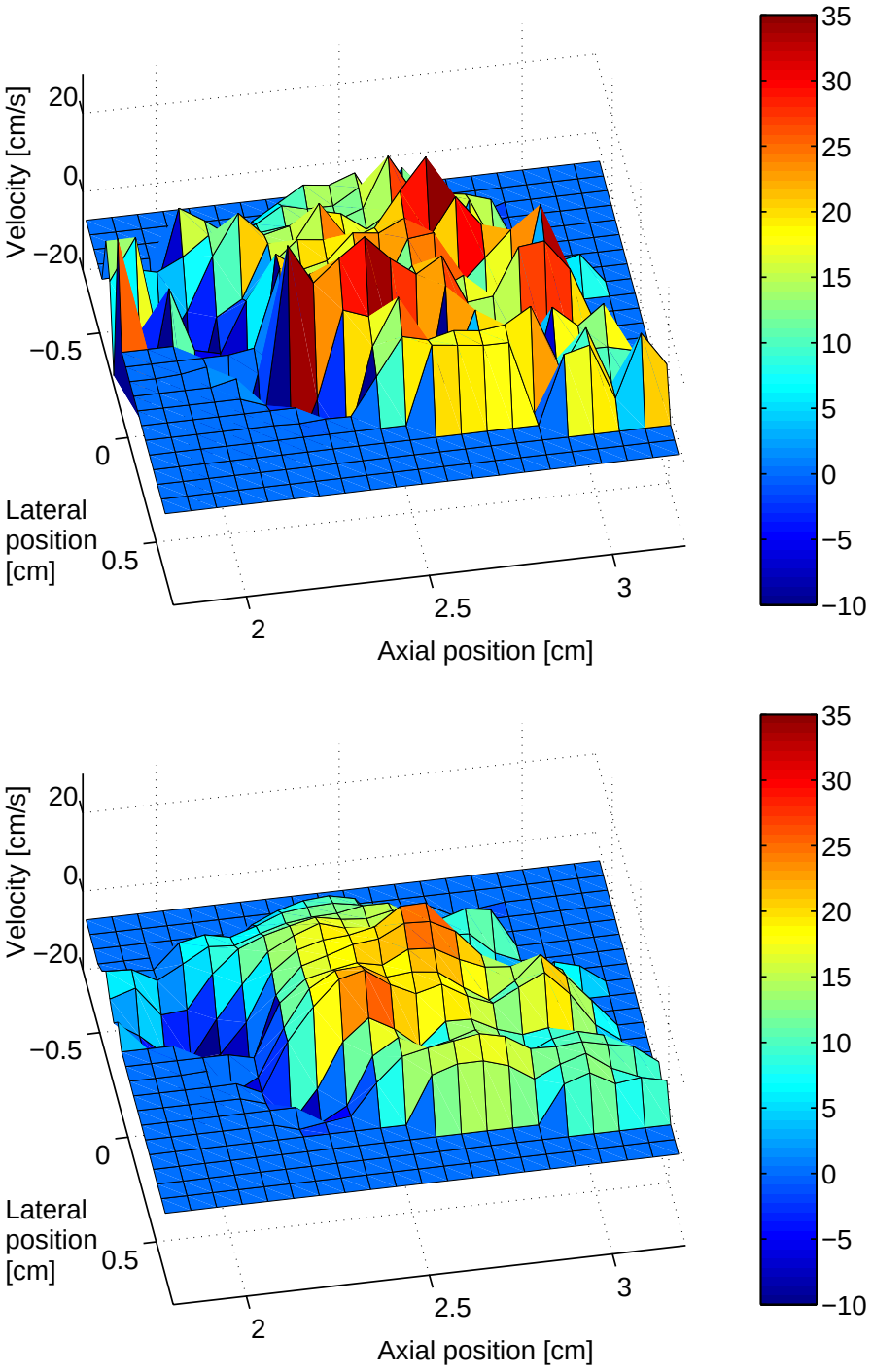

Figure 7.10: The velocity profile before (top) and after (bottom) application of the post-processing filter *Stat*2 on *in-vivo* data.

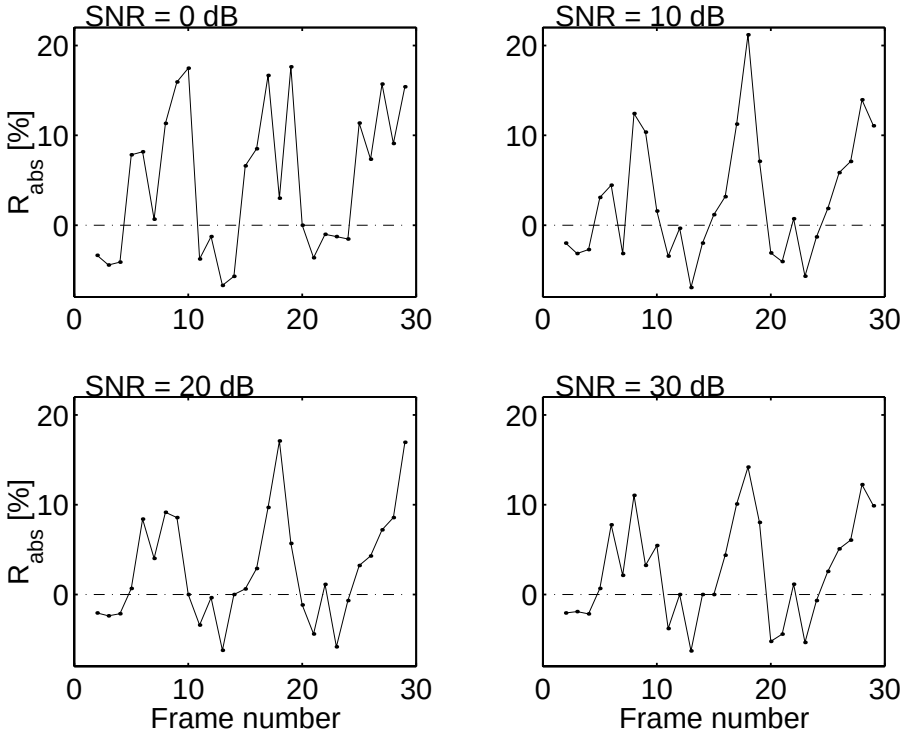

Figure 7.11: Ratio of the absolute errors, when the $Stat2_{ef}$ and the $Stat2$ filters are used, as a function of frame number.

using the model and the exact time-varying values of the scale parameters) are so low that it does not seem worth introducing the time-varying scale parameters. Employment of the time-varying scale parameters requires a determination of the position in the cardiac cycle, which can be done by 1) recording the ECG-signal and synchronizing the processing to this signal, or 2) inspection of the magnitudes of the spatial and temporal derivatives to determine the position in the cardiac cycle. Given the above investigations the scale parameters determined by minimizing the absolute error over all frames should be used in the filter, when the SNR in the RF-signals is not determined prior to the processing.

7.3 Summary

Post-processing of the velocity estimates must be performed, so velocity profiles can be displayed, which are more consistent with the true profile. Two post-processing filters have been introduced and evaluated here. A median filter can be applied to reduce the noisy variations, and the performance of two median filters have been determined on simulated data resembling RF-signals from the carotid artery. The best performance was obtained, when the filter employed all 4 spatial neighbors along the lateral and axial directions in the image. The resulting velocity profiles are more consistent with the true velocity profiles. The RMS error on the velocity estimates was lowered by 3.9-27.1 %. The highest improvement was obtained at low SNRs. The median filter was applied to *in-vivo* data from the carotid artery. The obtained velocity profiles still contain some steep transitions between velocity levels, which is not desirable.

The second post-processing filter represents a new approach, which employs Bayesian image analysis to derive a filter based on statistics. The filter incorporates features of fluid flow. These features introduce restrictions on the variations allowed between the velocities in neighboring spatial and temporal locations. A posterior probability density function is determined. It consists of an a priori density term, which sets up restrictions for the variations, and a model specific term. The latter incorporates the information available

from the given estimates prior to the post-processing. The posterior density is maximimzed on an iterative basis. In each iteration a new estimate of the velocity is computed as a linear combination of the original estimate and the velocity estimates in the spatial and temporal neighborhood. The scale factors in the filter vary for different levels of the SNR. This should be employed, if the SNR is determined prior to acquiring and processing data for blood velocity estimation. Otherwise one set of values should be used for all. In this study the parameters determined for the 15 dB case were used. When the same set of scale factors are used throughout the cardiac cycle, the improvements on the RMS error are 16.5-46.0 % on the simulated data. The highest improvement is obtained for low values of the SNR. The filter was applied to *in-vivo* data from the carotid artery. A more smooth velocity profile was obtained after the post-processing. The scale parameters vary as a function of the temporal location in the cardiac cycle. If a simple linear model for the variation of the scale parameters for a SNR of 15 dB are used on all data sets (independent on SNR) only very little overall improvement is obtained. It does not seem worth introducing the time-varying scale parameters under these circumstances.

The results above show that the statistical filter out performs simple median filters and produces less noisy velocity images. The filtering is computationally very simple. Memory capacity has to be set aside for storing the previous CFM image though. The temporal and spatial correlation property between the velocities contain valuable information for the post-processing of the estimates and therefore should be incorporated in the post-processing filter.

The values of the scale factors are dependent on the spatial and temporal resolution in the images. The temporal resolution is determined by the frame rate. In this study the scale factors have been determined for one realization of the possible set of resolution values. More realizations should be investigated to determine the importance and influence of the resolution on the values of the scale factors. In this study the scale factors were determined for a frame rate of 10 frames/s. Still, a successful post-processing of the *in-vivo* data, where the frame rate is 18 frames/s, was performed.

The performance of the statistical filter has been evaluated on the velocity profile of the carotid artery. This profile is very smooth and does not contain both positive and negative velocities in neighboring locations. Investigations are to be carried out, which determine the scale parameters and the performance of the filter on other velocity profiles. Data from the femoral artery are of interest, as both positive and negative velocities are seen in neighboring locations. These variations should not be removed by the filter. One unique filter, which can handle all velocity profiles, might not exist. This is not seen as a limitation of this approach. An input from the clinician, which determines the anatomical site being scanned, will enable employment of different filters for different anatomical locations. The aspect of employing processing schemes, which are specific for an anatomical site, is already used in todays scanners. In case of the statistical post-processing filter, the basic algorithm will be identical for all situations, but the scale factors will vary with the anatomical site.

Highly deviating estimates are produced by some estimators, and the performance of the statistical filter should be evaluated under these circumstances. The filters capability of minimizing the amplitude of these estimates should be determined. The number of iterations performed in the filtering might have to be more than one under these circumstances. A measure for ones faith in the estimates should be determined and included. A relation (or lookup table) between this measure and the scaling factor ω should be determined. In this way the highly deviating estimates get to influence the outcome of the filtering less. This should result in new, filtered estimates, which are more consistent with the true velocities.

The discussion and investigations in this chapter reveal that it is beneficial to incorporate the features of fluid mechanics in the post-processing algorithm. One filter, which incorporates the spatial and temporal correlation between the blood velocities, has been derived here. Other filters should also be considered, but they should all incorporate the correlation property.

Chapter 8

Conclusion

The discussion in the following summarizes the work and results obtained within this Ph.D. project. The project has mainly been concerned with developing algorithms, which are to be used in the processing of acquired ultrasound RF-signals. The aim of the processing is to obtain estimates of the blood velocities in the human cardiovascular system. The processing can be split up in three main steps. First, the RF-signals are pre-processed to improve the basis for the estimation. Then the actual estimation is carried out, and estimates of the velocity profile in the vessels are achieved. The computed estimates come with a level of inaccuracy, which results in a noisy and non-smooth appearance of the velocity profiles. Post-processing of the estimates is therefore performed, before the estimates are displayed. New algorithms to be used in these processing steps have been investigated.

Apart from the development of new algorithms, the issue of performance evaluation has also been addressed. A proper set of data are required to evaluate the performance of an algorithm. Simulated data are often preferred, since they are well-defined. The data must be representative of the *in-vivo* situation. The features of the *in-vivo* situation and especially the features, which will influence the performance, should be incorporated. Tissue motion is one feature of importance, and it is induced by breathing, the beating of the heart, and the pulsation of the vessel walls. The aspect of tissue motion and the incorporation hereof in the generation of simulated data have been investigated. The presence of tissue motion was verified through inspection of *in-vivo* data. The tissue motion is on the order of a few millimeter per second close to the motion inducer. Models have been derived for each motion contributor. Each model consists of two terms. The first describes the temporal course of the motion next to the inducer. This is determined by the motion pattern of the inducer (*e.g.* heart beat rate, breathing rate, level of breathing). The second term describes the damping of the motion in space. As the distance increases from the inducer to a point in space, the level of the motion decreases. Simulations have been performed to verify the models. A comparison between the *in-vivo* and simulated data reveals a good qualitatively agreement.

Given a proper basis for the performance evaluation the development and evaluation of new algorithms were carried out.

Non-zero estimates are computed for both the blood and tissue regions. Only the blood velocity estimates are of interest in CFM-mode. A discriminator must be applied that determines, which segments of the RF-signals that carry blood velocity information. If the discrimination is performed prior to the actual blood velocity estimation, the computational load can be decreased, as only segments, which carry blood velocity information, should be processed by the estimators. Two new discriminators have been developed within this project. They are based on maximum likelihood theory and neural networks, respectively. A set of features, which distinguish segments that do and do not carry blood velocity information, have been determined. The features are I) the energy content in the segments before and after echo-canceling, and II) the amplitude

variations between segments in consecutive RF-lines before and after echo-canceling. A performance evaluation of the discriminators shows that these features contain valuable information for the discrimination. The discriminators process the values of the features and computes a probability value, which determines whether the segment under investigation carry blood velocity information. The results were compared to a simple amplitude discriminator, which has previously been used in commercial scanners. This discriminator bases its classification on the average amplitude value in the segment. All three discriminators have a high success rate on determining the segments, which do not carry blood velocity information. The number of correctly classified segments are above 91 %. The amplitude discriminator has a poor performance on the segments, which do carry blood velocity information. Less than 50 % of these segments are classified correctly. The new methods can rectify this problem to some extent. The incorporation of more features and the employment of more advanced algorithms result in a better basis for the discrimination. The success rate on the discrimination increases significantly. For SNRs above 0 dB the success rate reaches a minimum of 91 %. As the SNR increases above 10 dB, more than 94 % of the segments, which carry blood velocity information, can be classified correct. It can be concluded that it is beneficial to incorporate more features and to employ more advanced algorithms in the discrimination. Further investigations into this area should be carried out. This includes determining more or other features, which distinguish the information content in the segments well.

Several blood velocity estimators have been developed in the past. None of them incorporate the features of fluid mechanics, which predicts that the velocities are correlated in time and space. The possibility of incorporating this aspect has been investigated. An estimator based on maximum likelihood theory has been derived, which incorporates the correlation property by introducing an a priori probability density in the distribution describing the acquired signals. The functionality of the a priori distribution is to determine, if the velocity value under investigation is likely, when the velocities in a bounded spatial and temporal neighborhood are known. The performance of this new estimator (the CMLE estimator) has been evaluated and compared to a selection of the previous developed estimators. The introduction of the correlation property has a positive effect on the estimation. No estimates, which deviate significantly from its neighbors, are computed. This is consistent with the true velocity profiles. The estimated velocity profiles comply with the features of fluid mechanics. The occurrence of deviating estimates is often experienced with the other estimators, so the correlation property contains valuable information for the estimation. The estimator is not able to follow the fine variations across the axial extent of the vessel, but the velocity estimates follow the overall variations throughout the cardiac cycle well. None of the evaluated estimators perform perfectly in the sense of computing exact estimates. Different trends are experienced, and each of them have their advantages and disadvantages. These have been determined and discussed in this project. But overall the CMLE estimator can compete with and out perform quite a few of the previously developed estimators. This conclusion is based on a comparison of the RMS errors and the measure of the number of highly deviating estimates. The work carried out in this project has determined that the flow physics should be incorporated in the estimation scheme.

A second blood velocity estimator has been developed in this project. It combines two of the previously developed estimators in order to minimize the computational load, overcome some of the limitations of the individual estimators, and exploit the advantages of the individual estimators. The idea of combining two estimators is not new. The EAM estimator combines the autocorrelation and the cross-correlation estimators. The estimator presented here combines the autocorrelation and the BST estimators. It has been named the AB estimator. The reason for combining the autocorrelation estimator with the BST or the cross-correlation estimators is to overcome the aliasing problem of the autocorrelation estimator. This can be achieved with the EAM and AB estimators, but unfortunately the estimators also introduce estimates, which deviate significantly from the true velocities. When inspecting the estimated velocity profiles the AB estimator out performs the EAM estimator. The number of highly deviating estimates are on the order of 4 %. The same measure for the EAM estimator is a factor of 4 higher. The combination of the autocorrelation and the BST estimators has been advantages for the estimation. The problems of the EAM estimator is

due to the limitations of the cross-correlation analysis, and these has been overcome to some extent by the variance analysis performed with the BST estimator. Post-processing of the estimates, which incorporates the features of fluid mechanics, can remove some of the highly deviating estimates and thereby improve the performance of the AB and the EAM estimators. The non-highly deviating estimates follow the variations across the axial extent of the vessel and throughout the cardiac cycle well. This makes the AB estimator a very powerful estimator, which should be considered used for blood velocity estimation. The AB estimator out perform most of the estimators discussed and evaluated. This conclusion is based on a comparison of the RMS error and the measure of the number of highly deviating estimates. The visual inspection of the velocity profiles supports this conclusion.

The velocity estimates come with a level of inaccuracy, which results in a noisy and non-smooth appearance of the velocity profiles. When the individual frames are shown right after each other at a high frame rate, this noise attracts the eye and removes the observers attention from the important information. Post-processing is performed before the estimated velocity profiles are displayed. The features of fluid mechanics should be incorporated in the post-processing filter. This idea has been pursued, and a filter based on optical flow theory has been derived. The filter employs the estimated velocity values in a temporal and spatial neighborhood along with the estimate in the location currently being filtered to produce a new estimate. The filter relation is linear, and a set of scaling factors weight the contributions for the spatial and temporal neighbors and the original estimate. The performance has been evaluated on simulated data for the carotid artery. The velocity profiles are smoothened by the filter, and the resulting, filtered velocity profiles are more consistent with the true velocity profiles. The filter out performs post-processing performed with median filters. The RMS error has been improved by a factor of 2-4. Incorporation of the features of fluid mechanics has been beneficial for the post-processing.

The above discussion can be summarized in two sentences. The outcome of this Ph.D. project is a set of algorithms, which should be considered employed in the pre-processing of the RF-signals, the actual estimation of the blood velocity estimates, and the post-processing of the estimates. The features of the RF-signals and the blood flow, which have been incorporated in the new algorithms, contain valuable information for the processing.

Bibliography

[1] B-K Medical Denmark. Gentofte, Denmark.

[2] Siemens A/S Denmark.

[3] J. A. Jensen. *Estimation of Blood Velocities Using Ultrasound: A Signal Processing Approach*. Cambridge University Press, New York, 1996.

[4] L. E. Kinsler, A. R. Frey, A. B. Coppens, and J. V. Sanders. *Fundamentals of Acoustics*. John Wiley & Sons, New York, third edition, 1982.

[5] G. S. Kino. *Acoustic Waves, Devices, Imaging, & Analog Signal Processing*. Prentice-Hall, Englewood Cliffs, N.J., 1987.

[6] D. H. Johnson and D. E. Dudgeon. *Array Signal Processing, Concepts and Techniques*. Prentice-Hall, 1993.

[7] D. E. Dudgeon and R. M. Mersereau. *Multidimensional digital signal processing*. Prentice Hall, 1984.

[8] P. N. Burns, J. E. Powers, and T. Fritzsch. Harmonic imaging: New imaging and doppler method for contrast enhanced us. *Radiology*, 185(P):142, 1992.

[9] P. N. Burns, J. E. Powers, and T. Fritzsch. Harmonic imaging: Principles and preliminary results. *Angiology*, pages S63–S74, 1996.

[10] A. D. Pierce. *Acoustics, An Introduction to Physical Principles and Applications*. Acoustical Society of America, New York, 1989.

[11] G. E. Trahey and D. Zhao. Quality factors for phase aberration correction in medical ultrasound. In *Proc. SPIE - Int. Soc. Opt. Eng.*, volume 1231, pages 40–49, 1990.

[12] W. F. Walker and G. E. Trahey. A fundamental limit on the performance of correlation based phase correction and flow estimation techniques. *IEEE Trans. Ultrason., Ferroelec., Freq. Contr.*, 41:644–654, 1994.

[13] H. Baba, R. Shinomura, Y. Miwa, N. Nakata, and J. Harada. Clinical evaluation of real-time phase-aberration correction system. In *Proc. IEEE Ultrason. Symp.*, 2000.

[14] Y. Li and B. Robinson. Phase aberration correction using near-field signal redundancy-two-dimensional array algorithms. In *Proc. IEEE Ultrason. Symp.*, 2000.

[15] B. Robinson and C. Cooley. Synthetic dynamic transmit focus. In *Proc. IEEE Ultrason. Symp.*, 2000.

[16] B. Haider. Synthetic transmit focusing for medical ultrasonic imaging. In *Proc. IEEE Ultrason. Symp.*, 2000.

[17] A. Despopoulos and S. Silbernagl. *Color Atlas of Physiology*. Thieme, 1986.

[18] C. G. Caro, T. J. Pedley, R. C. Schroter, and W. A. Seed. Mechanics of the circulation. In A.C. Guyton, editor, *Cardiovascular Physiology*. Medical and Technical Publishers, 1974.

[19] W. W. Nichols and M. F. O'Rourke. *McDonald's Blood Flow in Arteries, Theoretical, Experimental and Clinical Principles*. Lea & Febiger, Philadelphia, 1990.

[20] S. Timoshenko. *Strength of Materials, Part II : Advanced theory and problems*. D. van Nostrand Company, 1956.

[21] L. G. Napolitano and G. M. Carlomagno. Momentum and energy transfer in blood flows through deformable pipes. *AGARD Proc*, CP-65-70:17.0–17.9, 1970.

[22] J. M. Evans, R. Skidmore, J. D. Baker, and P. N. T. Wells. A new approach to the noninvasive measurement of cardiac output using an annular array Doppler technique. II ; Practical implementation and results. *Ultrasound Med. Biol.*, 15:179–187, 1989a.

[23] J. M. Evans, R. Skidmore, N. P. Luckman, and P. N. T. Wells. A new approach to the noninvasive measurement of cardiac output using an annular array Doppler technique. I ; Theoretical considerations and ultrasonic fields. *Ultrasound Med. Biol.*, 15:169–178, 1989b.

[24] R. W. Fox and A. T. McDonald. *Introduction to fluid mechanics*. John Wiley and Sons, 1985.

[25] N. Dreijer. Diagnostic ultrasound. Brüel & Kjær, 1983.

[26] J. A. Jensen. Field: A program for simulating ultrasound systems. *Med. Biol. Eng. Comp.*, 10th Nordic-Baltic Conference on Biomedical Imaging, Vol. 4, Supplement 1, Part 1:351–353, 1996b.

[27] J. A. Jensen. Users' guide for the Field II program. Technical report, Dept. of Information Technology, Technical University of Denmark, 1998.

[28] A. M. Badawi, A. M. Hashem, A-BM. Yossef, and M. Abdel-Wahab. Invivo quantification of motion in liver parenchyma and its application in shistosomiasis tissue characterization. *Proc. SPIE - Int Soc Opt Eng*, 2424:602–610, 1995.

[29] A. I. El-Fallah, M. B. Plantec, and K. W. Ferrara. Ultrasonic measurement of breast tissue motion and the implications for velocity estimation. *Ultrasound Med. Biol.*, 23:1047–1057, 1997.

[30] O. Bonnefous. Stenoses dynamics with ultrasonic wall motion images. In *Proc. IEEE Ultrason. Symp.*, pages 1709–1712, 1994.

[31] J. A. Jensen and J. Mathorne. Sampling System for In Vivo Ultrasound Images. In *Med. Imag. V Symp.*, volume SPIE Vol. 1444, pages 221–231, 1991.

[32] K. Conradsen. *En introduktion til statistik - bind 1B*. IMM - Technical University of Denmark, 1995.

[33] H. L. Van Trees. *Detection, Estimation and Modulation Theory, Part I: Detection, estimation, and linear modulation theory*. Wiley, 1971.

[34] H. L. Van Trees. *Detection, Estimation and Modulation Theory, Part III: Radar-sonar signal processing and Gaussian signals in noise*. Wiley, 1971.

[35] A. P. G. Hoeks, J. J. W. van de Vorst, A. Dabekaussen, P. J. Brands, and R. S. Reneman. An efficient algorithm to remove low frequency Doppler signal in digital Doppler systems. *Ultrason. Imaging*, 13:135–145, 1991a.

[36] S. Bjaerum and H. Torp. Statistical evaluation of clutter filters in color flow imaging. *Ultrasonics*, 38:376–380, 2000.

[37] L. A. F. Ledoux, P. J. Brands, and A. P. G. Hoeks. Reduction of the clutter component in doppler ultrasound signals based on singular value decomposition: a simulation study. *Ultrason. Imaging*, pages 1–18, 1997.

[38] A. P. Kadi and T. Loupas. On the performance of regression and step-initialized IIR clutter filters for color Doppler systems in diagnostic medical ultrasound. *IEEE Trans. Ultrason., Ferroelec., Freq. Contr.*, 42:927–937, 1995.

[39] R. Rojas. *Neural Networks - A Systematic Introduction*. Springer Verlag, 1996.

[40] C. M. Bishop. *Neural Networks for Pattern Recognition*. Oxford University Press, 1995.

[41] I. A. Wright, N. A. J. Gough, F. Rakebrandt, M. Wahab, and J. P. Woodcock. Neural network analysis of Doppler ultrasound blood flow signals : a pilot study. *Ultrasound Med. Biol.*, 23:683–690, 1997.

[42] L. Kahl, R. Orglmeister, and K. J. G. Schmailzl. A Neural Network Based Classifier for Ultrasonic Raw Data of Myocardium. In *Proc. IEEE Ultrason. Symp.*, pages 1173–1176, 1997.

[43] T. Binder, M. Sűssner, D. Moertl, T. Strohmer, H. Baumgartner, G. Maurer, and G. Porenta. Artificial neural networks and spatial temporal contour linking for automated endocardial contour detection on echocardiograms: A novel approach to determine left ventricular contractile function. *Ultrasound Med. Biol.*, 25:1069–1076, 1999.

[44] E. J. Feleppa, W. R. Fair, T. Liu, A. Kalisz, K. C. Balaji, C. R. Porter, H. Tsai, V. Reuter, W. Gnadt, and M. J. Miltner. Three-Dimensional Ultrasound Analyses of the Prostate. *Mol Urol*, 4:133–139, 2000.

[45] J. S. Bridle. Probabilistic interpretation of feedforward classification output networks, with relationships to statistical pattern recognition. In F. F. Souli and J. Hrault, editors, *Neurocomputing : Algorithms, Architectures and Applications*, pages 227–236. Springer Verlag, 1990.

[46] J. Larsen. Neural Classifier 1.0 Software Documentation. Technical report, Dept. of Mathematical Modelling, Technical University of Denmark, Denmark, 1998.

[47] J. Larsen. http://www.imm.dtu.dk/.

[48] K. W. Ferrara and V. R. Algazi. A new wideband spread target maximum likelihood estimator for blood velocity estimation – Part I: Theory. *IEEE Trans. Ultrason., Ferroelec., Freq. Contr.*, 38:1–16, 1991a.

[49] J. A. Jensen. A new calculation procedure for spatial impulse responses in ultrasound. *J. Acoust. Soc. Am.*, pages 3266–3274, 1999.

[50] K. W. Ferrara and V. R. Algazi. A Statistical Analysis of the Received Signal from Blood During Laminar Flow. *IEEE Trans. Ultrason., Ferroelec., Freq. Contr.*, 41:185–198, 1994.

[51] K. Conradsen. *En introduktion til statistik - bind 1A*. IMM - Technical University of Denmark, 1995.

[52] R. F. Wagner, S. W. Smith, J. M. Sandrick, and H. Lopez. Statistics of speckle in ultrasound B-scans. *IEEE Trans. Son. Ultrason.*, 30:156–163, 1983.

[53] C. Kasai, K. Namekawa, A. Koyano, and R. Omoto. Real-time two-dimensional blood flow imaging using an autocorrelation technique. *IEEE Trans. Son. Ultrason.*, 32:458–463, 1985.

[54] S. G. Foster. *A pulsed ultrasonic flowmeter employing time domain methods*. PhD thesis, Dept. Elec. Eng., University of Illinois, Urbana, Ill., 1985.

[55] O. Bonnefous, P. Pesqué, and X. Bernard. A new velocity estimator for color flow mapping. In *Proc. IEEE Ultrason. Symp.*, pages 855–860, 1986.

[56] X. Lai and H. Torp. An extended autocorrelation method for estimation of blood velocity. *IEEE Trans. Ultrason., Ferroelec., Freq. Contr.*, 44:1332–1342, 1997.

[57] S. K. Alam and K. J. Parker. The butterfly search technique for estimation of blood velocity. *Ultrasound Med. Biol.*, 21:657–670, 1995.

[58] K. W. Ferrara and V. R. Algazi. A new wideband spread target maximum likelihood estimator for blood velocity estimation – Part II: Evaluation of estimators with experimental data. *IEEE Trans. Ultrason., Ferroelec., Freq. Contr.*, 38:17–26, 1991b.

[59] W. K. Pratt. *Digital Image Processing*. John Wiley & Sons, Inc., 1991.

[60] M. Sonka, V. Hlavac, and R. Boyle. *Image processing, analysis and machine vision*. Chapman Hall, 1994.

[61] J. A. Jensen, O. Holm, L. J. Jensen, H. Bendsen, H. M. Pedersen, K. Salomonsen, J. Hansen, and S. Nikolov. Experimental ultrasound system for real-time synthetic imaging. In *Proc. IEEE Ultrason. Symp.*, volume 2, pages 1595–1599, 1999.

[62] J. Besag. Toward bayesian image analysis. *J. Appl. Stat.*, 16:395–407, 1989.

[63] R. Larsen, K. Conradsen, and B. E. Ersbøll. Estimation of dense image flow fields in fluids. *IEEE Transactions on Geoscience and Remote Sensing*, 36:256–264, 1998.

[64] J. Konrad and E. Dubois. Bayesian estimation of motion vector fields. *IEEE Trans. Pattern Anal. Mach. Intell.*, 14:910–927, 1992.

[65] S. Geman and D. Geman. Stochastic relaxation, gibbs distributions and the bayesian restoration of images. *IEEE Trans. Pattern Anal. Mach. Intell.*, PAMI-6:721–741, 1984.

[66] R. Larsen and A. Rosholm. Motion flow detection using ICM-optimization on a massive parallel computer. Technical report, Dept. of Mathematical Modelling, Technical University of Denmark, 1994.

[67] J. Besag. On the statistical analysis of dirty pictures. *J. Roy. Stat. Soc. B.*, 48:259–302, 1986.

Appendix A

Papers presented and published within the Ph.D. project

A copy of the papers presented and published during the Ph.D. project are available from the directory ”MSchlaikjer_Papers” on the enclosed CD-rom in Appendix D. The format of the papers is PostScript (*.ps).

The papers are:

”Tissue motion in blood velocity estimation and its simulation”, presented at the IEEE International Ultrasonics Symposium, Sendai, Japan, 1998.
Authors: M. Schlaikjer, S. Torp-Pedersen, J. A. Jensen, and P. F. Stetson.
Proc. IEEE Ultrasonic Symp., pages 1495-1499, 1998.
Name of postscript-file: ieee_uffc_symp1998.ps .

”Simulation of RF data with tissue motion for optimizing stationary echo canceling filters”, presented at the Ultrasonics International ’99 and 1999 Congress on Ultrasonics, Copenhagen, Denmark, 1999.
Authors: M. Schlaikjer, S. Torp-Pedersen, and J. A. Jensen.
To be published in Ultrasonics, 2002.
Name of postscript-file: UI_WCU_1999.ps .

”Neural Network for RF Decomposition in Ultrasound”, presented at the International ICSC Symposium on Neural Computation, Berlin, Germany, 2000.
Authors: M. Schlaikjer and J. A. Jensen,
Proc. of Neural Computation, pages 628-633, 2000.
Name of postscript-file: nc2000.ps .

”Pre- and Post-processing Filters for Improvement of Blood Velocity Estimation”, presented at the IEEE International Ultrasonics Symposium, San Juan, Puerto Rico, 2000.
Authors: M. Schlaikjer, S. Torp-Pedersen, and J. A. Jensen.
Proc. of IEEE Ultrasonic Symp., vol.2, pages 1531-1536, 2000.
Name of postscript-file: ieee_uffc_symp2000.ps .

”Joint Probability Discrimination between Stationary Tissue and Blood Velocity Signals”, presented at the IEEE International Ultrasonics Symposium, Atlanta, Georgia, 2001.
Authors: M. Schlaikjer and J. A. Jensen.
To be published in Proc. of IEEE Ultrasonic Symp., 2001.
Name of postscript-file: ieee_uffc_symp2001a.ps .

”A New Maximum Likelihood Blood Velocity Estimator Incorporating Spatial and Temporal Correlation”, presented at the IEEE International Ultrasonics Symposium, Atlanta, Georgia, 2001.
Authors: M. Schlaikjer and J. A. Jensen.
To be published in Proc. of IEEE Ultrasonic Symp., 2001.
Name of postscript-file: ieee_uffc_symp2001b.ps .

Appendix B

Performance of the blood velocity estimators on synthetic data

In Chapter 6 a selection of blood velocity estimators were introduced and evaluated. The performance on the synthetic data was determined for a range of values of the parameters:

- the sampling frequency (f_s),
- the number of samples used in the estimation,
- the number of RF-lines available,
- the SNR.

The influence of the echo-canceling filter was determined, as the evaluation was performed for three filters: no echo-canceling filter, the 2^{nd} order HP echo-canceling filter, and the regression line echo-canceling filter. Four velocities - $v = [10, 20, 30, 40]$ cm/s were investigated. A listing of the mean and the standard deviation for all the combinations of the parameters, the echo-canceling filters, and the velocities will take up hundreds of pages. Therefore it has been decided to include the generated tables on the enclosed CD-rom (see Appendix D). For each combination of the parameters the mean μ and the standard deviation σ are listed as $\mu \pm \sigma$.

A directory structure has been designed to make it easier to read the results. The results are located in the directory /VelEstimators/SyntheticData. The tables for each estimator are located in their own subdirectory:

AutocorEst	:	The results for the autocorrelation estimator.
CrosscorEst	:	The results for the cross-correlation estimator.
EamEst	:	The results for the EAM estimator.
BstEst	:	The results for the BST estimator.
AbEst	:	The results for the AB1 estimator.
MleEst	:	The results for the MLE estimator.
CmleEst	:	The results for the CMLE estimator.

The file names are related to the name of the estimator, the SNR, and the velocity investigated. An example hereof is ”tablesab0dbv1.ps”, which refers to the results obtained with the AB1 estimator, when the true velocity is 10 cm/s, and the SNR is 0 dB. In the tables the following abbreviation for the echo-canceling (Echo-can.) filters are used:

- No echo-canceling filter : None,
- the 2^{nd} order HP echo-canceling filter : HP,
- the regression line filter : Hoeks.

Appendix C

Performance of the blood velocity estimators on simulated data

In Chapter 6 a selection of blood velocity estimators were introduced and evaluated. A selection of the resulting CFM-mode images for each estimator is plotted in the dissertation. The performance on all 10 frames in the cardiac cycle is included on the enclosed CD-rom (see Appendix D). The images of the estimated and true velocity profiles are combined in one PostScript file.

A directory structure has been designed to make it easier to read the results. The results are located in the directory /VelEstimators/SimulatedData. The postscript-files for each estimator are located in their own subdirectory:

AutocorEst	:	The results for the autocorrelation estimator.
CrosscorEst	:	The results for the cross-correlation estimator.
EamEst	:	The results for the EAM estimator.
BstEst	:	The results for the BST estimator.
AbEst	:	The results for the AB2 estimator.
MleEst	:	The results for the MLE estimator.
CmleEst	:	The results for the CMLE estimator.

One postscript-file are present in each directory (except for the AB2 and the EAM estimators, where 2 files are present). The name of the file is ”EstVelFrame1_10??.ps”. The ”??” refers to the name of the estimator, and the following possibilities are present: { Autocor, Ab2, Bst, Crosscor, Eam, Mle, Cmle }. In case of the AB2 and EAM estimator 2 files are present, as the performance on the data set generated from a long and a short pulse is given. The postscript-file, which represents the results with a short pulse, is named ”EstVelFrame1_10??_S.ps”, whereas the file, which contains the results with a long pulse is named ”EstVelFrame1_10??.ps”.

The results were obtained for the simulated data resembling the carotid artery. The SNR is 20 dB, and the 2^{nd} order HP echo-canceling filter was applied prior to the blood velocity information.

Appendix D

Enclosed CD-rom

The CD-rom, which contains the papers presented and published during the Ph.D. project, and the performance results of the blood velocity estimators, is enclosed here. Please refer to Appendix A-C for information on the directory structure and the specific content on this CD-rom.